University of Southampton

SPACE CHARGE MEASUREMENT OF XLPE – A COMPARISION OF AC AND DC STRESSING

By

Yiu Fai Fred Ho, BEng (Hons)

PhD Thesis

DEPARTMENT OF ELECTRONICS AND COMPUTER SCIENCE

September 2001

Abstract

This thesis reports on aspects of the design (i.e. electrical, electronic, mechanical and control software) and construction of the "laser induced pressure propagation (LIPP)" system, which can be used to investigate the space charge formation and evolution within the dielectric material with different sample treatments under both dc and 50 *Hz* ac ageing conditions.

As the space charge distribution in cables is of great interest to the manufacturers and the end users, the newly designed LIPP system was extended so as to be used for planar and coaxial cable structures. The theoretical principles of the LIPP technique for cable geometries and the corresponding data processing method have been developed. From the preliminary results from the XLPE cable samples, the calculated electric stress distribution based on the developed method showed a very good agreement with the theoretical profile. However, due to the limitation imposed by the HV dc power supply and ac transformer in the current system, the applied electric stress is low. Consequently the SNR of the measurement signals in the cable sample is low and the space charge effect was not significant. Therefore, in this project our interests are to study space charge under both dc and ac conditions in the planar sample, the space charge measurement in the cable sample will be left as further work.

Several technical issues related to the LIPP technique have been addressed. These include unexpected sample breakdown within ac ageing period, the high frequency noise, offset of the point on wave voltage, effect of the semicon thickness to measurement resolution and mismatch of the acoustic properties between the semicon and HV metal electrode. In order to ensure the high accuracy and consistence of the newly designed LIPP, two correction factors i.e. variation in laser power and target efficiency, are introduced and verified.

Under dc condition, space charge measurements on XLPE and LDPE plaques with two different treatments and semicon electrodes demonstrated that the degassing process reduces the dc threshold stress for space charge creation in the XLPE samples with XLPE semicons (approxiately 30% reduction), but not with LDPE samples with XLPE semicons. However, by using LDPE semicons with bulk LDPE insulation, there was no indication of space charge up to ~19.2 kV/mm during the ramp rate measurements.

The dc ageing measurements illustrated that the space charge performance of the LDPE samples with LDPE semicons is better than the XLPE samples with XLPE semicons and the LDPE samples with XLPE semicons. Also, the results showed that applying XLPE semicons to LDPE bulk insulation, the cross-linking byproducts from the semicons may diffuse across the XLPE/LDPE interface, and affect the space charge performance.

In the case of ac, a qualitative and simple quantitative appraisal of the stress and charge profiles at the electrode interfaces (i.e. X-plots and *Dev%*) has been introduced and validated enabling the processing of a vast amounts of ac raw data without resorting to a complex mathematical treatise. The results confirmed the existence of space charge in the insulation material subjected to 50 *Hz* ac conditions and showed that space charge effects in XLPE and LDPE with XLPE semicon electrodes are significant when the applied ac stress is above 11.3 kV/mm_{peak} and the fast charge formation (charge injection) is more pronounced than the slow charge under the 50 *Hz* ac electric stress.

List of contents **Page**

List of figures

Acknowledgements

I would like to thank my project supervisors, Dr George Chen and Prof. Tony Davies, for their valuable advice, support, patience and assistance during all stages of this project. I would also like to thank my colleagues, Mr. Roland Caleducutt and Mr. Neil Palmer in the HV Lab for their help and some extremely useful engineering support during the stages of design, set-up and modification of the LIPP system and Mr. Richard Howell in the electronic workshop for his valuable support on the electronic control unit of the LIPP system.

My grateful thanks are also extended to the National Grid, UK and BICCGenernal cables, UK for the funding of this project, in particular like to thank Prof. S. Swingler, Dr. S. J. Sutton for all their advice and encouragement throughout the project.

Eventually, I am indebted to Dr. N. Hampton, Dr. S. Hobdell and Dr. S. Betteridge of BICCGenernal Cables, UK for their many helpful discussions and the supply of samples.

Principle notations

ΔT Electric pulse duration (PEA)

A Surface area of measurement

A_1, A_2 Cross-section area of the liquid host

$A(\upsilon)$ Pressure wave degradation factor

c, υ Velocity of sound

C_a Capacitance of the measurement circuit,

C_b Capacitance of blocking capacitor,

C_o Capacitance of the non-compressed material

C_s Sample capacitance

d Sample thickness

ε_r Relative permittivity

e_{33}^* The apparent piezoelectric coefficient in the thickness direction

$e^{-\alpha(\upsilon)z}$ Pressure wave degradation term

$e_p(t)$ High voltage narrow electric pulse (PEA)

$E(z,t)$ Electric stress distribution

E_{cal} Electric field for calibration

$E_{cal}(z,t) = \frac{V}{R\ln\left(R/r\right)}$ Electric stress at the interface between the front electrode and sample during calibration (Cable geometry)

$F(P)(z,\upsilon)$ The Fourier component of the pressure wave at the angular frequency and at abscissa z

g The pull of gravity

$G(\varepsilon)$ Coefficient that depends on the relationship between the permittivity and the pressure wave

I_{space} Current output from the testing sample

I_{cal} Calibrated current at the target interface

I_{int} peak current at interface

I_0' Calibrated peak current at either the input or output interface

K Equal to the $\varepsilon/\varepsilon_0$

N, n	Laser shot number
P_1	Pressure of the liquid at outlet of the water tank
P_2	Pressure of the liquid inject to the sample
P_0	is the maximum amplitude of the pressure wave at the target interface
P_z	is the mean amplitude of the pressure wave at location z
$p(z,t)$	Pressure wave profile
$\rho(z)$	Space charge density distribution
ρ	The density of liquid
qq	Number of data point per measurement (i.e. 512)
δ	The amount of mechanical displacement carried by the pressure pulse
γ_3	The uniaxial electrostriction coefficient
R_a	Resistance of the measurement circuit,
τ	Width of the pressure wave at location z
τ_{rise}	Typical rise time of the LIPP current pulse
$\tau_{measured}$	Measured signal rise time by the oscilloscope
u_{sa}	Speed of acoustic in the sample
$u_{sa}(\upsilon)$	Velocity of sound in the sample and opposite direction to z abscissa which is frequency dependence
$V_m(t)$	Change in voltage across the capacitor
V_1	Velocity of the liquid at outlet of the water tank
V_2	Velocity of the liquid inject to the sample
V_s	Voltage measurement by the oscillscope
ω	Angular frequency
χ	Pressure independent compressibility of the sample
α_p	Relative temperature dependence of the polarisation
α_x	Relative temperature dependence of the thermal expansion coefficient
α_ε	Relative temperature dependence of the permittivity
z	Distance through the testing sample
z'	The radius reached by the pressure wave front at time t (Cable geometry)
$z_f(t)$	Position of the pressure wave front at time t

$\sqrt{R/z}$ Geometric factor that indicates the strength of the acoustic wave varies with the square root of position z

Ω Ohms (Resistance)

Abbreviations

Ac	Alternating current
Dc	Direct current
HV	High voltage
Hz	Hertz
LDPE	Low density polyethylene
LIMM	Laser intensity modulation method
LIPP	Laser induced pressure propagation
PE	Polyethylene
PEA	Pulsed Electroacoustic method
PPS	Piezoelectically generated pressure step method
SNR	Signal to noise ratio
TPM	Thermal Pulse method
TSC	Thermally stimulated current method
TSM	Thermal Step method
V	Voltage
XLPE	Cross-linked polyethylene

Chapter 1

Introduction and overview

1.1 Introduction

With the requirement of a stable and reliable power transmission system the use of ultra high voltage has been well established. Transmission of electric power from the generator to the customer can be realised through either overhead lines or underground cables.

Within the last thirty years, the overhead line is more heavily favoured to transfer large blocks of electrical power within the power system rather than the underground cables. This is because as far as the economics are concerned, the cost of manufacturing an insulated underground cable is typically above ten times as much as the overhead line for a given capacity. Moreover, the installation and maintenance cost of underground transmission systems are considerably higher than the overhead lines, accounting as much as 40 % of the total capital cost of the entire system [1-2].

In addition, the system fault of an overhead line can be found relatively quicker and repaired at a reasonable cost. Therefore, the overhead line can then be restored to service in a matter of hours. However, for an underground cable, location of the fault within the underground transmission system is time consuming and involves a considerable expense [3-4], hence the cable may be out of service for a week or more.

As the cable is buried under the ground, it is to all intents and purposes placed in a thermal blanket; hence the cable transmission capability becomes thermally limited [5]. However, this is not the case with most overhead lines, which can be cooled by convection in the ambient air. The use of underground cables has been largely limited by the above reasons. However, in the past decade there are clear indications that the conditions just described are changing due to a number of factors:

Firstly, the cost of land purchased in the densely populated urban areas to build pylons to carry the overhead lines have increased dramatically in the last two decades, leading to the overhead power transmission system became prohibitively expensive.

Secondly, in the late 1980's and early 1990's there was heightened awareness by the general public to the environment and the aesthetics of the overhead lines. Underground transmission system has relatively minor aesthetic impact to our living environment compared to the overhead line. Therefore, at some locations where particular environmental sensitivity, such as UK national parks or the pump storage power station at Dinorwig in Wales, the underground cable is used to link the power station to an existing overhead transmission system.

Nevertheless, other than the economic and environmental reasons, the underground power transmission system does however have some technical advantages over the overhead transmission line. The dc power transmission is a non-synchronous transmission technique; therefore it can be used to link two different HV ac systems (i.e. different frequencies). Also, as the cables are entirely in an enclosed system and not exposed to environmental conditions, all the detrimental factors such as rain, ice, wind, lighting strikes, ocean spray, dust and air-borne pollutants, which normally influence the efficient operation of the overhead line are eliminated.

1.2 Development of underground cables

Underground power transmission was first used in the 1880's by Edison (USA) and Ferranti (UK), both for electrical lighting systems. The cables used were solid copper rods, insulated with jute wrapping. Currently, there are two predominant types of solid insulation used for underground cables; these are traditional paper/oil and polymeric insulation. However, in recent years the traditional paper/oil is progressively being replaced by the polymeric insulation.

In recent years there has been a worldwide swing away from paper insulation towards polymeric insulation, although the latter are derived from mineral oil, which seems to have an ever-escalating price. Rather surprisingly the costs of paper and polymeric material have

risen at roughly the same rate in the past twenty years. The reason that the cost of paper has kept pace with that of polymeric material is because the manufacture of paper from wood is a very energy intensive process. The dramatic increase in oil price have an immediate effect on the price of polymeric material but there is a delay with paper price until the increased oil price is reflected in a higher price for electricity [6].

Another factor in the changing pattern of preferred cable types is that it is becoming increase difficult to secure, at a reasonable cost, the skills which are required to joint and terminate the traditional paper/oil cable. This is especially the case in the developing countries. Inevitably, the simpler concept and the reduced level of expertise, which is involved, with the installation of polymeric cables has a significant influence on the swing away from paper cables [7].

There are a various kinds of polymeric material for power cables on the commercial market, for example: butyl rubber (IIR) [8], polyvinyl chloride (PVC) [8], ethylene-propylene rubber (EPR) [8-21], polyethylene (PE) [22-24], and cross-linked polyethylene (XLPE) [24-29]. However, polyethylene and cross-linked polyethylene insulation material seems to be dominating the cable industry worldwide.

Polyethylene was first produced in 1936, and is now one of the cheapest and most widely used polymeric material [30]. Although initial attempts were made in 1943 to use low-density polyethylene as an insulating material for the power cables, it was not until the late 1950's and early 1960's that the use of polyethylene as insulation for power distribution applications became established. The advantages of the polyethylene over the paper/oil type are their lower manufacturing cost [2], their ease of installation and handling [2,31], their high intrinsic electric strength typically above 10^9 *V/m* (intrinsic electric strength is the short term value under ideal test condition, i.e. in the absence of voids, contamination and discharge) [32], high resistivity (typically $>10^{16}$ Ωm^{-1}) [33], low dielectric loss angle ($tan\delta$=0.0001 to 0.001) [31] and good resistance to chemicals as well as the ease of processing. However, as the maximum rated temperature of the polyethylene cable is only 70 ^{O}C, it means that the sustained current rating, overload and short circuit temperatures of this kind of underground cables system are limited.

The temperature stability was improved in the 1960's by converting the thermoplastic polyethylene into a cross-linked thermoset (XLPE), which allows the insulation to operate continuously at a maximum temperature of 90 ^{O}C [34]. Cross-linked polyethylene is now a widely accepted material for the cable manufacture industry. However, due to the premature failure rate for polymer insulated power transmission system (2 x 10^{-6} faults/circuit metre/year) [35] is about 6 times higher than the paper/oil cables (3 x 10^{-7} faults/circuit metre/year) [36], the take up rate over the traditional paper/oil insulated cable has slowed down. At extra high voltage transmission cable such as 400 kV to 750 kV, the insulation is still predominantly paper/oil [31].

1.3 Relationships between space charge and cable failure

In order to reduce the failure rates of the underground transmission cable system, new challenges to the insulation engineers and material scientists have been arisen. It is imperative that there is a better understanding of the factors, which affect the failure of the polymeric insulation. Once these factors are fully understood then it may be possible to design a high voltage polymeric cable that is able to operate with low incidence of failures at any high transmission capacity conditions.

For many years, the majority of published experimental results show evidence that cable failures were mainly assigned to the cable manufacturing process, such as the inclusion of contaminants, cavities and internal defects [37]. For example, the cables that have failed in their first few years of service (almost three quarters of the failures) have been found to be due to some sort of defect [15]. After four years of service the majority of failures are reported to be due to water treeing [15], which can be initiated from water filled voids within the polymer [38].

However, the contribution of trapped charge to cable failures has acquired more interest from many researchers in the past two decades, it has known that when the solid extruded polymeric materials are subjected to a high electric stress for a certain period of time (i.e. ageing), their good electrical insulation properties may become degraded. The trapped and low mobility electrically charged species within the bulk can give rise to "space charge", resulting in localised electric stress enhancement. This can cause further concentration of charge and lead to premature failure of the polymeric material. Moreover, in order to

increase the knowledge of space charge dynamic in the polymeric insulation, much effort has been made and several non-destructive measurement techniques for detecting space charge within the solid polymeric material have been developed. One of the well-known pressure wave propagation (PWP) techniques for space charge measurement was established by Laurenceau et al, which is called "Laser induced pressure propagation" method (LIPP). This technique is not only a reliable non-destructive method, but also has a quite reasonable spatial resolution of the concentration of the space charge in the material.

1.4 Overview of the project

Numerous studies have been carried out using the LIPP system to develop a better understanding of the formation of space charge within solid polymeric materials in the last few decades [39-68]. The majority of work to date has been concentrated on the space charge characteristics under dc electric stresses. However, work on the dynamics and the role of space charge on electrical breakdown under 50 *Hz* ac conditions have only received limited attention and have not been conclusive [69-73], this may due to the technical difficulties to construct an ac LIPP system. As there is an increasing body of opinion that space charge build up can be a contributing factor to electric treeing [74-75] and the majority of XLPE cables will be operating under ac conditions in the immediate future, it is appropriate to investigate the charge trapping and mobility under such conditions.

In this research project, a new version of the LIPP system was designed and developed, which can be used to investigate the space charge formation and evolution within LDPE and XLPE samples with different treatments under dc and 50 *Hz* ac ageing conditions [76]. Comparison between the space charge distributions under both dc and ac ageing with different sample polymers and treatments and semicon electrodes are presented. In addition, as the space charge distribution of cable geometries is of a great interest to the manufacturers and the end users, the newly designed LIPP system was extended to cable structures as well as plaques.

This thesis is divided into eight chapters with appendix; chapter 1 includes the introduction and overview of the project.

In chapter 2, the chemical and physical structure of polyethylene (PE) and cross-linked polyethylene (XLPE) are reviewed. Also, in order to provide a fundamental background for the experimental results presented in this thesis, the basic concepts concerning mechanisms of space charge formation, migration and accumulation in the insulation have also been presented.

In chapter 3, the basic principles and the existing dc LIPP system are given. As the one of the main objectives of this research project, is devoted to the design and construction of the new version LIPP system which can be used to investigate the space charge formation and evolution within polymeric sample with different treatments under both dc and 50 *Hz* ac ageing conditions therefore the ac operation principles, technical design and construction of the newly designed LIPP system are reported. Review is also given to several experimental techniques, which can be used for the determination of the space charge and electric field distributions in the solid polymeric material. The information on the measurement principles, typical resolutions, limitations and the advantages associated with each method are shown in Appendix 1.

Since the newly designed LIPP system will be employed to investigate the space charge effect in the XLPE materials from plaque to cable structures for both dc and ac stress conditions, the relevant theoretical principles in cable geometries for space charge measurement using the LIPP technique is still not well defined and these basic principles constitute a significant part in the data processing. Therefore, in Chapter 4 the basic theoretical principles of LIPP technique, the corresponding data processing methods and the development of the theoretical principles in cable geometry for space charge measurement using LIPP system is described in details.

Chapter 5, prior to the application of the newly designed LIPP system to investigate the space charge evolution in the polymeric insulation, the performance validation of the electronic control system, online laser monitor system are given. In addition, during the stages of the system design, a great deal of time and effort has been spent solving some of the technical problems such as, unexpected sample breakdown during ageing period, the high frequency noise, offset of the point on wave voltage and the effect of the semicon thickness to measurement resolution. Therefore, in order to share this valuable experience

with the other researchers and give ideas for the further develop of the ac LIPP system; details of the problems and the solutions have also been reported.

Chapter 6, reports on the space charge measurements of ~1.5 *mm* thick as-received and degassed XLPE and LDPE plaques with two different kinds of semicon electrodes (carbon loaded XLPE and carbon loaded LDPE). Samples were subjected to dc electric stresses for 24 hours in the region of 25 *kV/mm* (at room temperature). Measurements of charge profiles and stress distributions were made using the newly designed LIPP system. Emphasis has been placed on comparing the space charge characteristics of these two insulation systems with the different semicon electrodes. The effects of sample treatment (i.e. degassing) on the space charge dynamics are also reported.

The XLPE and LDPE samples being tested in this project are purpose designed for HV dc power cable. Therefore, the space charge level under HV dc electric ageing is expected to be lower than the conventional XLPE insulation. To verify this information, comparisons have been made between the purpose designed samples and the conventional insulations, which have been tested previously in another project. The entrance and exit current peaks of the LIPP signal are correlated to the interfacial stresses and the space charge within the bulk insulation, and in order to compare the electric ageing effect between different materials without resorting to a complex mathematical treatise, a simple method, which based on the percentage deviation of the entrance peak is introduced.

Chapter 7, reports on the space charge measurements of ~1.5 *mm* thick as-received and degassed XLPE and LDPE plaques with two different kinds of semicon electrodes subjected to an ac electric stresses at room temperature (25 *°C*). It brings an experimental proof of the presence of space charge in the polymeric insulation under 50 *Hz* ac condition. Emphasis has been placed on establishing a simple method, termed "X-plots" to analyse ac space charge data without resorting to a complex mathematical treatise. Results of the space charge and electric stress distributions of as-received and degassed cross-linked polyethylene (XLPE) plaques that are electrically aged for 24 hours in the region of 25 to 30 kV/mm_{peak} are presented.

In chapter 8, the project conclusions and recommendation of the further work of this PhD project are given.

Chapter 2

Production, physical structure, and space charge mechanism in PE and XLPE insulation

2.1 Introduction

As stated in the previous chapter, in the last decade synthetic polymeric materials are progressively replacing paper/oil for the insulation of underground cables particularly in medium voltage systems. The range of polymeric material available in the cable industry is extensive, and any variations in chemical composition enable specific mechanical, electrical and thermal properties to be obtained. Where appropriate, these properties may be further modified by addition of specific fillers, antioxidant and many other ingredients.

In this chapter, the production and physical structure of polyethylene (PE) and cross-linked polyethylene (XLPE) are reviewed. Also, in order to provide a fundamental background for the experimental results presented in the latter part of this thesis, the basic concepts concerned with the mechanisms of space charge formation, migration and accumulation in the bulk insulation have also been given.

2.2 Polyethylene (PE)

Polyethylene is a non-polar organic material, based upon the elements carbon and hydrogen. It is synthesised through the process of polymerisation, with the ethylene gas molecules with the repeat unit of CH_2 –groups are linked by the covalent bonds as shown in figure 2.1 to form a polymer. The polymer is named by adding the prefix "poly" to the name of the monomer from which it is derived, hence polyethylene from ethylene [77].

However, according to the use of different polymerisation methods, a variety of grades differing in molecular weight and density of the polyethylene can be obtained. Sometimes side chains may occur during the polymerisation process, which will disturb the regular

shape of the macromolecules. In fact, the main chains of the polyethylene have a length of thousands to tens of thousands of CH_2 –groups [78]. These chains may run partly parallel to themselves or to the other chains as shown in figure 2.2.

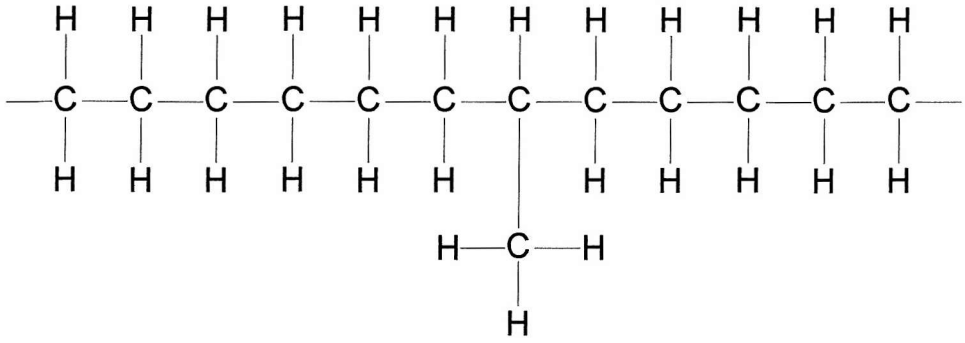

Figure 2.1 Chemical structure of polyethylene

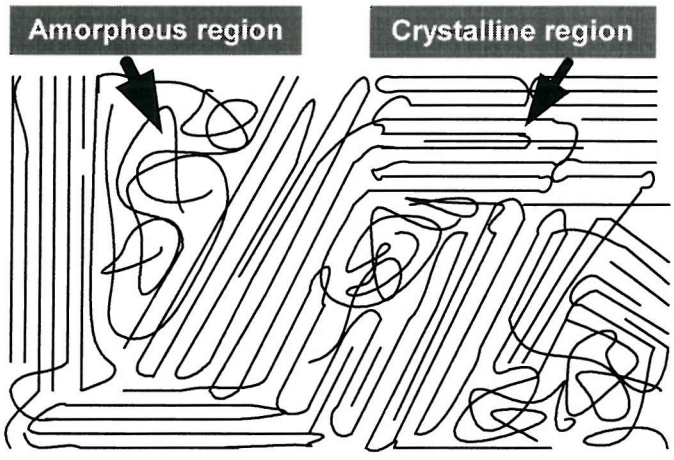

Figure 2.2 Diagram of the polymer crystallinity

The parallel chains region will form the "crystalline part" of the polymer. For another part of their length, where the chains follow an arbitrary path; "amorphous regions" are created. Generally, the conduction of the charge inside the amorphous region of the polymer is far better than that in the crystalline region because the additives such as impurities and anti-oxidants are easily accumulated and the chance for the charge being initiated and trapped within these regions is enhanced [79].

The percentage of the volume that is occupied by the crystalline region is called the "crystillinity or crystalline ratio", which affects the some of the mechanical characteristics of the material, such as density and Young's modulus. The high density of the polyethylene

is a direct consequence of higher crystallinity, which results in the reduction of the chain branching. Polyethylene with 70-80 % crystallinity is called "high-density polyethylene (HDPE)" [80], its density is around 945-960 kg/m^3, and has fewer and shorter chain branches than "low-density polyethylene (LDPE)" [80-81] with typically 45-55 % crystallinity and density of 916-930 kg/m^3. Among other physical properties, melting point of the polymer increases with the crystallinity, the crystalline melting point of the polyethylene increased from 110 ^oC (LDPE) to 130 ^oC (HDPE) as the density is increased from 916 to 960 kg/m^3.

Nowadays, a newer class of polyethylene, which has limited application in the cable industry has been invented which, is called "linear low-density polyethylene (LLDPE)". It is made by a low-pressure manufacturing process, similar to that used for HDPE, but the polymer has purely methyl group side chains [82]

2.3 Polyethylene production - polymerisation

Polyethylene is produced from ethylene gas by a process known as "polymerisation", in which the monomer molecules (i.e. CH_2 –groups) are linked together to produce the polymer chains. To synthesise a polymer chain the monomer must be at least bi-functional that means it can be able to react on two sites of the molecules (i.e. bi-functionality of the ethylene is achieved by opening carbon carbon double bond). The basic idea of polyethylene polymerisation process is shown in figure 2.3, where "n" is the number of monomer units (i.e. CH_2 –groups) in the polymer chain, which is known as the "degree of polymerisation".

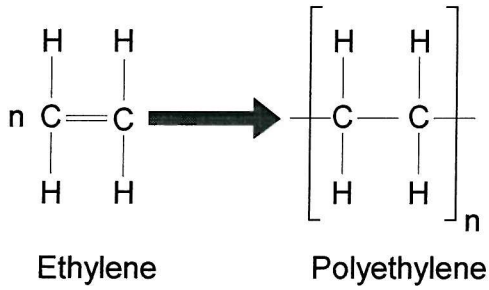

Figure 2.3 Polymerisation of polyethylene

There are two principal processes for the polymerisation, which are "addition polymerisation" and "step growth polymerisation" [80]. Step growth polymerisation describes the process where smaller molecules link together to form large molecules. These

molecules can then link to further monomer or polymer molecules. This type of polymerisation process is typical in the production of polymers such as polyesters. However, in the case of polyethylene, addition polymerisation is applicable, which describes the process where the polymer chain is formed by successive addition of monomer units until to the end of the polymer chain.

2.3A Addition polymerisation of polyethylene

The addition polymerisation is based on a free radical propagation mechanism [81]. The links between the monomer units (i.e. CH_2 –groups) do not occur instantly but in rapid succession. The process is initiated by the free radical (i.e. an atom or molecule with one unpaired electron). These radicals are known as "initiators", which are added to the ethylene gas in trace quantities of 0.1 to 1.0 %. The function of the initiator is to attach itself to an ethylene molecule and causing the carbon carbon double bond to open (reaction 1). The resultant molecule of this reaction is also a free radical, as there is a free unpaired electron on the carbon atom of the ethylene molecule. This new molecule can then react with another monomer in the same manner and the polymer molecule can then continue to grow by adding monomer units one by one to the end of the active chain (reaction 2). Finally, the polymerisation reaction will stop until the end of the active chain-reacts with a molecule that prevents further growth, possibly another free radical or a growing polymer chain (reaction 3). The summaries of the addition polymerisation process in the polyethylene is shown in figure 2.4, where the initiator is denoted by symbol "I", the unpaired electron denoted as "$\bullet$" and the terminator by the symbol "T".

Since the polymerisation reaction of the polyethylene can be terminated at any stage of the production process, therefore the length of the resultant polymer chain can vary and produce a wide range of molecular weight molecules within the polymer. The ratio of high and low molecular weight fraction will affect the physical properties of the polymer. If the range of the molecular weight is broad, then the presence of both low and high molecular weight fractions will cause the polymer to behave differently from a narrow range of molecular weight. For example, the presence of low molecular weight fractions will enhance the melting flow of the polymer. However, in the case of high molecular weight fractions the polymer will has higher physical strength and resistance to chemical attack [81,83].

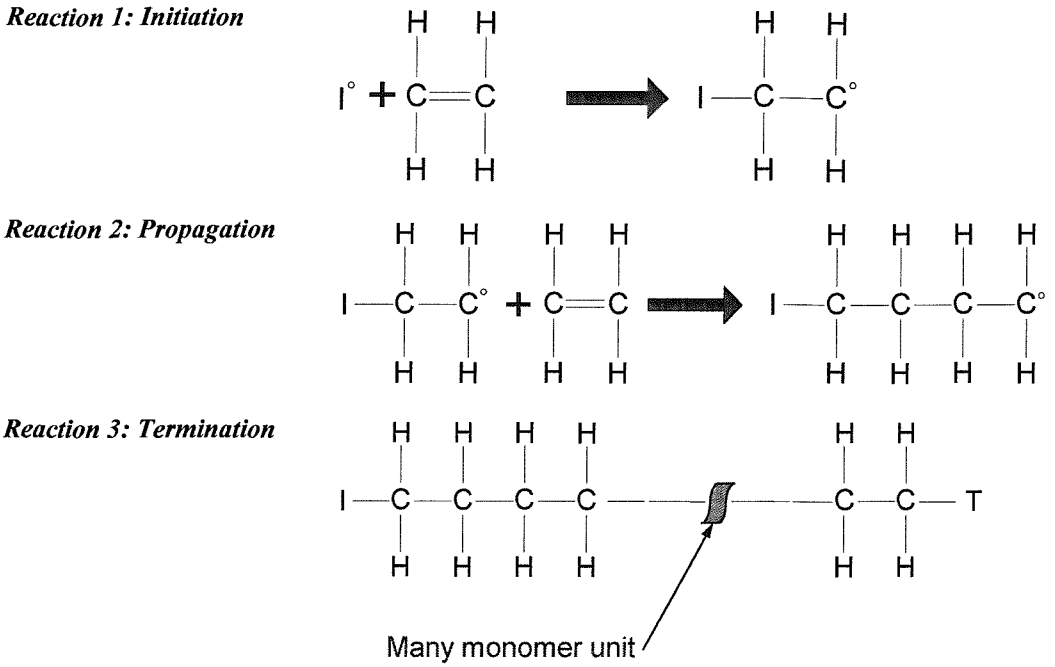

Figure 2.4 Addition polymerisation process of polyethylene [84]

2.4 Cross-linked polyethylene (XLPE)

Despite its excellent electrical properties, the use of the polyethylene as an insulation for power cable has been limited by an upper operational temperature of about 70 ^{O}C, due to its thermoplaticity. However, this constraint of the polyethylene has removed in the 1960's by converting the thermoplastic polyethylene into a cross-linked polyethylene (thermoset), which allows the insulation to operate continuously at a maximum working temperature of 90 ^{O}C.

Broadly speaking, polyethylene can be cross-linked by using two kinds of chemical reactions, such as (1) Dicumyl peroxide crosslinking process and (2) Silane crosslinking process. In order to provide basic ideas how the additives and cross-linking byproducts formed inside the bulk insulation during the cable manufacturing process, both of these cross-linking processes will be described.

2.4A Dicumyl peroxide cross-linking process

Dicumyl peroxide (DCP) is most widely used peroxide in the cable industry to give fast cross-linking without procuring in the extruder. A fairly low proportion (i.e. about 2.5%) of the peroxide is added to the base polymer. The temperature used for the cable extrusion is

between 130 to 150 ^{O}C, and the dicumyl peroxide remains inactive. However, when the temperature is raised to about 180 ^{O}C the dicumyl peroxide will quickly decompose and initiates the cross-linking reaction. Figure 2.5 illustrates the cross-linking mechanism of polyethylene by using dicumyl peroxide. First of all, two cumyloxy radicals are formed by the thermal decomposition of the dicumyl peroxide (reaction 1), then the cumyloxy radicals produced react with the polyethylene chain by abstracting a hydrogen atom (reaction 2).

The polymer chain is now considered as a radical, as it has an unpaired electron on the carbon atom from which the hydrogen atom has been removed. However, cumyl alcohol may also be produced as a decomposition product of the reaction 2, which can then be dehydrated as shown in reaction 3 to form α-methyl styrene and water.

The cumyloxy radical rearranges to form an acetophenone molecule and methyl radical (reaction 4). The methyl radical can then abstract the hydrogen atom from another polyethylene chain (in a similar way to the cumyloxy radical in reaction 5), hence another polyethylene chain radical is produced. Finally, the polyethylene radicals "$R^{\bullet}$" produced from the above reactions are bonded together by a strong covalent bond (reaction 6); hence the cross-linking polyethylene is obtained.

Reaction 1

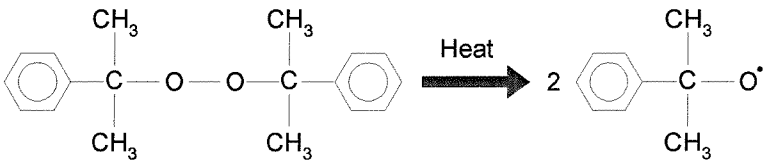

Dicumyl peroxide Cumyloxy radicals

Reaction 2

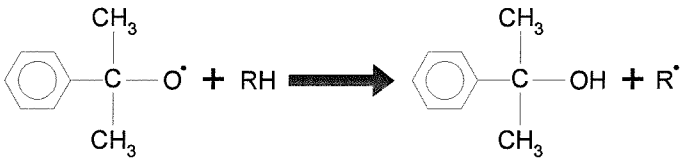

Cumyloxy radicals Cumyl alchol

Reaction 3

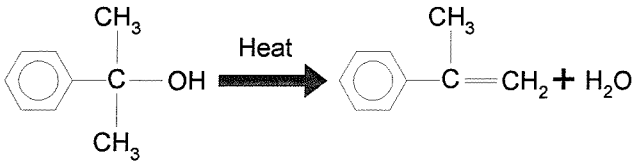

Cumyl alchol α-Methyl styrene Water

Reaction 4

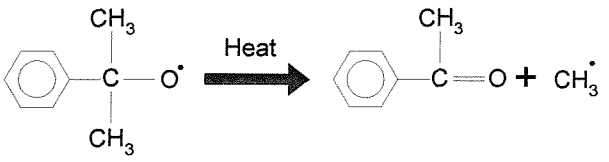

Cumyloxy radicals Acetophenone methyl radicals

Reaction 5

methyl radicals methane

Reaction 6

Crosslinking

Reaction 7

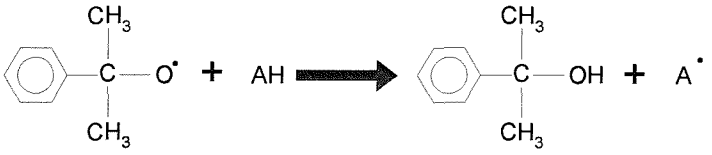

Cumyloxy radicals Cumyl alchol Inert products

Reaction 8

Ethane

where RH = Polyethylene chain

AH = Antioxidant

• = Free radical

Figure 2.5 Schematic cross-linking mechanism of polyethylene by using dicumyl peroxides [85]

Referring to [85], it is important for the peroxide system to choose the suitable antioxidant because they may react with the free radicals during the cross-linking process (reaction 7) to reduce degrees of cross-links. Phenolic antioxidants are particularly reactive and there are two of them, such as Santonox R (Monsanto) and Irganox 1010 (Cib Geigy), which are commonly used by the cable manufacturers. In addition, during the cross-linking process some volatile by-products such as acetophenone, cumyl alcohol, methyl styrene and water are formed within the bulk insulation.

2.4B Silane cross-linking process

Silane cross-linking established in early 1970 by Dow Corning in UK is progressively replacing the conventional peroxide cross-linking method to manufacture low voltage XLPE cables. This process classified as a two components system, for which two materials such as

cross-linkable graft polymer and a catalyst master batch need to be prepared before the cross-linking process. Then these two materials are blended together at the fabricating machine and the mixed product is subsequently cross-linked by immersion in water or low-pressure steam.

Figure 2.6 illustrates the schematic cross-linking mechanism of polyethylene by using silane. Since the polyethylene radicals "$R^{\bullet}$" are constantly regenerated in the cycle by the reactions 3 and 4, therefore the amount of dicumyl peroxide required is smaller compared to the peroxide cross-linking process (typically 0.1 % instead of 2.5 %).

Recently, the above cross-linking process has been further improved by BICC and Maillefer [86]. The improved process introduces all the ingredients together by metering them into the cable extruder, so that the separate grafting stage is eliminated making it easier to ensure that the material is free from contamination. This method can eliminate the problems of limited storage life of the graft polymer, hence reducing processing cost.

Preparation of cross-linkable graft polymer:

Reaction 1

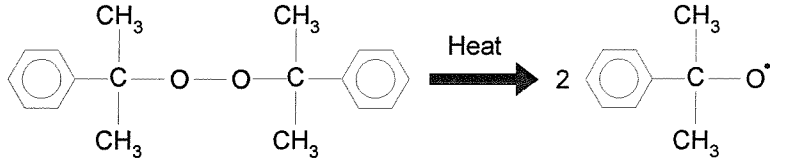

Reaction 2

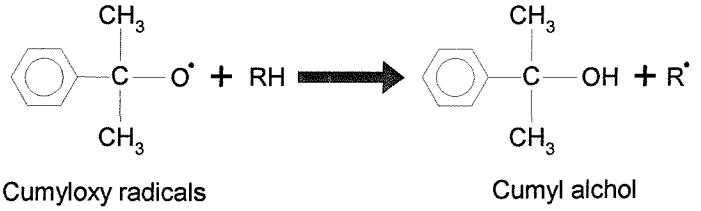

Reaction 3

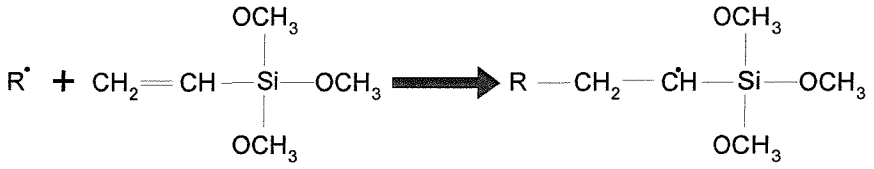

Reaction 4

Crosslinking process using catalyst:

Reaction 5

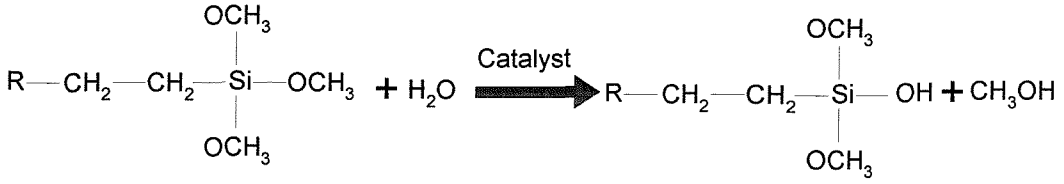

Reaction 6

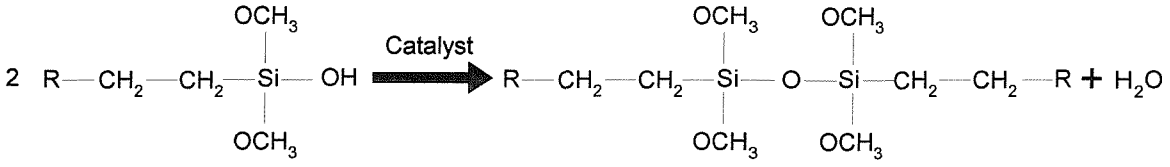

Reaction 7

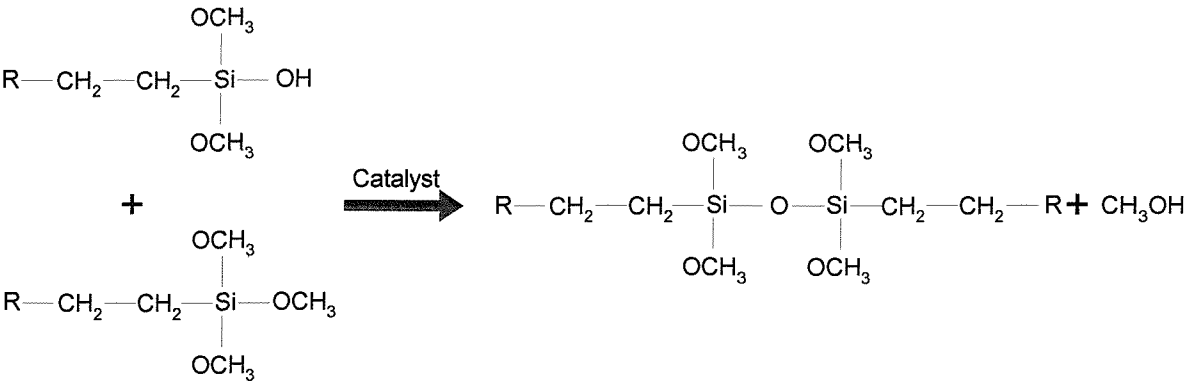

Figure 2.6 Schematic cross-linking mechanism of polyethylene by using silane [86]

2.5 Charge formation and transport in the PE and XLPE insulation

Although the cross-linking in the XLPE material may act as localised charge trapping centres within the bulk insulation, the electrical properties of the polyethylene should still remain relatively unaltered after the cross-linking process [87]. However, the additives and by-products from the cross-linking reaction will act as impurities and significantly affect the electrical properties of the polyethylene [88-90]. In order to provide a fundamental background for the experimental results presented in this thesis, some of the basic concepts concerning the mechanisms of charge formation, migration and accumulation in the PE and XLPE material are given. To study space charge formation and transportation inside the polymeric material, several physical processes are of importance:

1. "*Injection and extraction*", which control the emission or extraction of electrons or holes at the polymer/semicon electrode interface. These processes are strongly dependent on the conditions of the interfaces such as semicon material, surface defects and impurities.

2. "*Ionisation*", which is associated with the electric field assisted dissociation of chemical species such as residues of cross-linking byproducts, additives or other impurities in the polymeric bulk insulation,

3. "*Hopping*", which controls the charge migration within the polymeric bulk insulation,

4. "*Trapping*", the charge created by the above processes accumulates somewhere within the bulk, which is dependent on the availability, depth and the nature of the traps site inside the polymeric bulk insulation.

2.5A Homocharge and heterocharge

The accumulated space charges within the polymeric material can be defined as "homocharge" or "heterocharge" according to its polarity and the polarity of the adjacent electrode as shown in figure 2.7. Homocharge implies space charge of same polarity as the adjacent electrode and the heterocharge implies charge of opposite polarity.

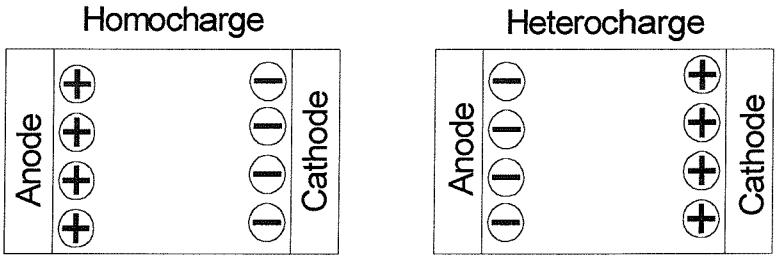

Figure 2.7. Definition of types of space charge near the electrode

Normally, homocharge is formed by trapping of the injected charge near the injecting electrodes. The resulting homocharge distribution will reduce the interfacial stresses and enhance the electric stress within the dielectric bulk.

Heterocharge can be generated by electric field assisted ionisation of the dissociable species in the dielectric material. Under an applied electric field, the charged molecules or ions may migrate towards the electrode with opposite polarity where they may become trapped. The resulting heterocharge distribution will increase the interfacial stresses and reduce the electric stress within the dielectric bulk.

2.5B Electrode process

- ***Injection – homocharge formation***

Generally, when an underground cable is manufactured with PE and XLPE insulation, semiconducting screens (semicons) are normally required over the conductor and insulation for voltages of above 3.6 kV [91]. Semicon screens can provide an equipotential surface on the outside surface of the insulation, eliminating any electric discharges arising from air gaps adjacent to the cable insulation. For example, the coefficient of expansion of polyethylene is approximately 10 times greater than either aluminium or copper conductor [91]. Therefore, when the cable conductor is operating at its maximum temperature of 90 ^{O}C, a sufficiently large air gap may be formed between the insulation and the surface of the conductor, allowing electrical discharges. These discharge sites and any others sites that are formed around a conductor, can be eliminated by applying a semicon layer over the conductor.

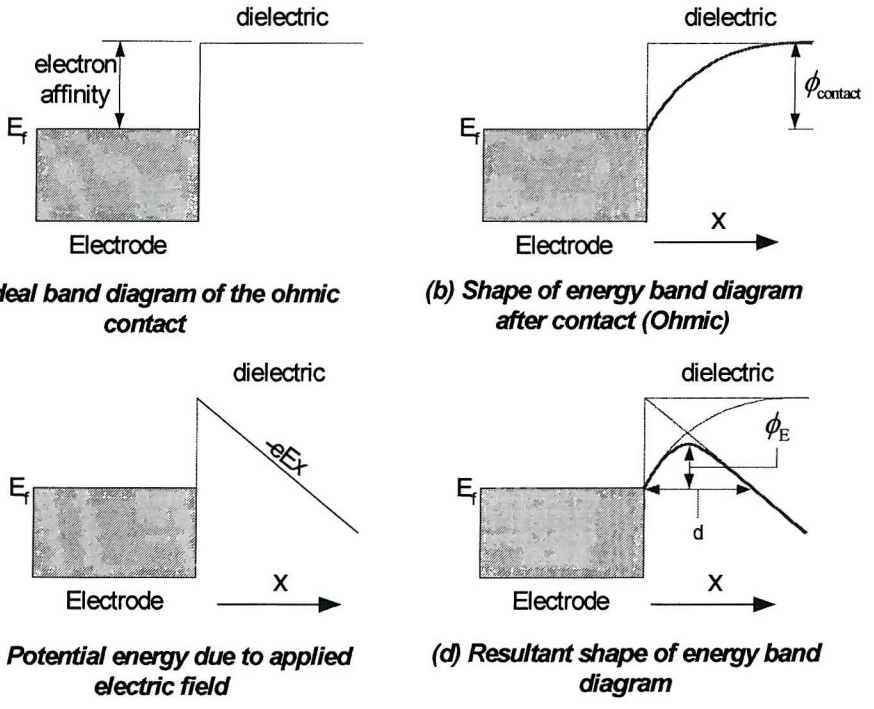

(a) Ideal band diagram of the ohmic contact

(b) Shape of energy band diagram after contact (Ohmic)

(c) Potential energy due to applied electric field

(d) Resultant shape of energy band diagram

Figure 2.8. Modification of the potential barrier at the electrode/dielectric interface by an applied electric field

Depending on the nature of the semicon/polymer interface contact, the charge (i.e. electron or holes) will transfer across the boundary even without the application of an

external electric stress. The charge transfers can be either from the semicon electrode to the polymeric insulation or from the polymeric insulation to the semicon electrode. Basically, two electronic processes, termed "Schottky injection" (thermal excitation over the barrier) and "Fowler-Nordheim tunnelling" are normally used to explain the charge transport between the semicon/polymer interfaces. They are based on the very simple energy band diagram as shown in figure 2.8a.

Considering the interface is an "Ohmic" contact [92], electrons must overcome a potential barrier $\phi_{contact}$ on the interface to enter the polymeric bulk insulation (figure 2.8b). Therefore, as the negative potential ($V=Ex$) is applied to the electrode (i.e. cathode) at temperature T (figure 2.8c), the original height of the potential barrier $\phi_{contact}$ on the interface is reduced to ϕ_E (figure 2.8d). This will increase the probability of an electron having sufficient energy to jump over a potential barrier ϕ_E and encourages electron transfer from the electrode to higher energy states within the bulk insulation, this process is called "Schottky injection" [93-94].

The injection current density J due to the Schottky injection can be expressed as the applied electric stress E and the testing temperature T as shown in equation 2.1, details can be found elsewhere [93-94].

$$J = AT^2 \exp\left[\frac{-\phi_E + \beta_s E^{1/2}}{kT}\right] \text{ ---------- (2.1)}$$

where $A = \dfrac{4\pi em(kT)^2}{h^2}$ is the Richardson – Dushman constant,

k is the Boltzmann constant,

h is the Planck's constant,

$\beta_s = \left(e^3/4\pi\varepsilon_r\varepsilon_0\right)^{\frac{1}{2}}$,

e is the unit of electronic charge,

ε_0 is the permittivity of free space, and

ε_r is the relative permittivity of the dielectric material.

On the other hand, a quantum mechanical process "Fowler-Nordheim tunnelling" is often used as the second explanation for the electrons passing through the potential barrier at the interface. In fact, electrons can exhibit a particle-wave duality. The electric stress E increases the bending over of the conduction band at the interface as shown in figure 2.8d. This results in the width of the potential barrier "d" being reduced, creating a finite probability that the charge penetrates into or escapes from the material through the barrier despite having insufficient energy to surmount them. The generalised formula gives the relationship connecting the tunnelling current density J with the applied voltage V for a barrier of arbitrary shape as shown in equation 2.2, details can be found elsewhere [95-96].

$$J = J_0\left(\bar{\phi}\exp\left(-A\bar{\phi}^{1/2}\right)-\left(\bar{\phi}+eV\right)\exp\left[-A\left(\bar{\phi}+eV\right)^{1/2}\right]\right) \text{ ---------- (2.2)}$$

where $J_0 = \dfrac{e}{2\pi(\beta\Delta s)^2}$ and $A = \dfrac{4\pi\beta\Delta s}{h}(2m)^{1/2}$,

Δs is the width of the barrier at the Fermi level of the cathode,

$\bar{\phi}$ is the means of the barrier height above the Fermi level of the cathode,

h is the Planck's constant,

m is the mass of the electrons,

e is the unit of electronic charge,

β is the function of barrier shape and is usually approximately equal to unity.

In fact, injection of electrons at the cathode and extraction of electrons at the anode are the main mechanism normally used to explain the charge emission at the electrode/ polyethylene interface. However this is not necessarily the case for all polymers. According to the studies of Ieda, some different group of polymer may emit and conduct "holes" across the electrode interface. Table 2.1 shows the summarised dominant injected charge carrier in different polymers [97]. However, due to the complex physical and chemical structure of the polymer the determination of the type of injected charge carrier in different polymers is fraught with complexities and it is still not clear.

Injected carrier	*Polymer*
Electrons	PE, PET, PEN
Holes	EVA, PPX, PTFE, FET

Table 2.1. Summary of injected carrier in different polymer [97]

where PE — Polyethylene
PET — Polyethylene terephthalate
PEN — Polyethylene naphthalene
EVA — Ethylene vinyl acetate
PPX — Poly-xylylene
PTFE — Polytetrafluoroethylene
FET — Fluor ethylene propylene

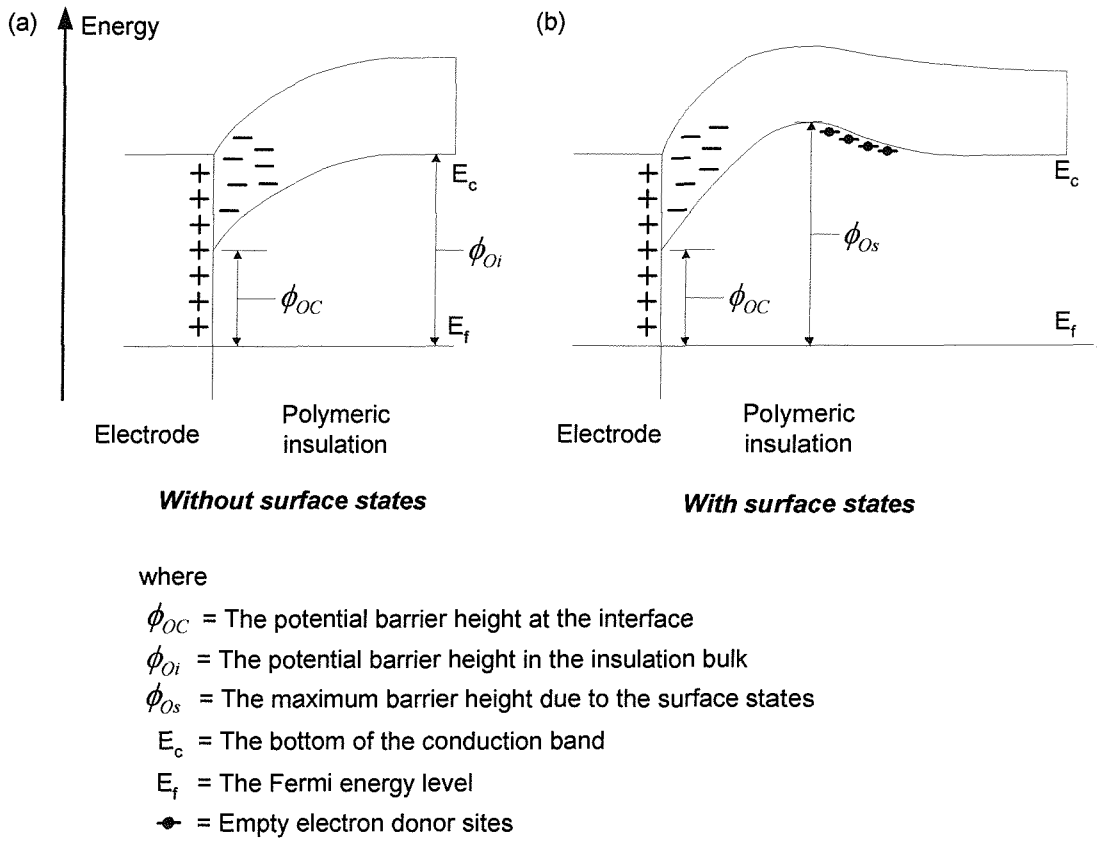

Figure 2.9. Effect of the surface states on the energy band at the interface

In addition to the above electronic processes, another factor, termed "surface states" which concerns the physical condition of the polymer/semicon interface can also influence the charge injection process at the electrode. During the cable manufacturing process, a number

of physical imperfections, which including broken bonds [98], chain branches [99], imperfect contact [98-99], absorbed gas [100], oxidation products [98,101-105] and additives [101,106] may lead to the formation of the acceptor states (i.e. trap states) at the polymer/semicon interface, which is called "surface states".

Considering the "Ohmic" contact as an example, the surface states will act as acceptor states for the negative charge injection from the electrode to create the energy equilibrium. This high, negative, charge concentration becomes trapped close to the interface and causing a formation of a double charge layer. The effect of this double charge layer on the energy band diagram at the interface is shown in figure 2.9. It is noticed that the bending over of the energy band increases the height of the potential barrier from ϕ_{oi} *to* ϕ_{os} at the interface. Hence, the probability of electrons having sufficient energy to be injected into the insulation by Schottky injection may be reduced. However, as the width of the potential barrier is reduced, the probability of fowler-Nordheim tunnelling is enhanced.

2.5C Bulk process

- ***Ionisation -- heterocharge formation***

  As stated in section 2.4, the available PE and XLPE material for the underground cable contain various different organic and inorganic impurities such as catalysts, antioxidants, voltage stabilizers, cross-linking agent and by-products from the production process [88,90]. Under the application of the applied electric stress these impurities within the bulk may be separated into ion pairs by the dissociation process and its reaction is given as,

  $$AB \Leftrightarrow A^{+} + B^{-} \text{ ---------- (2.3)}$$

  Both positive and negative ions present in the polymeric bulk will migrate to the counter electrode under the applied electric stress. For example, the negative ions will move towards the anode by the "hopping process", leading to the build up of the positive charge close to the cathode and negative charge close to the anode, hence resulting in heterocharge formation.

- ***Charge trapping and hopping in the polymer – charge migration***

The semi-crystalline polymeric insulating materials (i.e. PE and XLPE) contain impurities and structural inhomogeneities in the amorphous region, they may cause "traps" in the forbidden band of the polymer, the charge injected from the electrode or created inside the bulk by ionisation process may be trapped there. Generally, a trap for the electron is called an "acceptor" and a trap for holes is called "donor". Other trap, which is able to trap either polarity of the charge, can act as recombination centres. The time that the charge spends in the trap depends on the depth of the trap, defined as the energy needed to liberate the trapped charge.

Referring to the thermally stimulated current (TSC) studies by many researches [98,101,107], it has shown that there are several traps present within the polyethylene material. Summaries of the nature and origin of the carrier traps are shown in table 2.2. More precise descriptions of the TSC technique can be found elsewhere [108]. The depths of the traps found in polyethylene may be classify into two broad groups [5],

I. ***Shallow traps***, energetically located in the region of 0.1 to 0.3 eV below the conduction band. In polyethylene the concentration of the shallow traps has been found in the region of 10^{18} $traps/cm^3$.
II. ***Deep traps***, energetically located in the region of 0.8 to 1.4 eV below the conduction band. In polyethylene the concentration of the shallow traps has been found in the region of 10^{14} $traps/cm^3$.

An occupied electron trap can be drawn in terms of an idealised energy band diagram, called "potential well" as shown in figure 2.10. The slope of the bend in the walls will depend on the force of attraction between the trap and the electron according to the Coulombs law. The trap depth ϕ_D below the conduction band can be considered to be equal to the barrier height inhibiting the movement of the electron, which is therefore equal to the energy required for the electron to escape from the trap.

Peak temperature (^{O}K)	Trap depth (eV)	Region	Origin
130	0.1-0.3	Lamellar surface	Defect
180	0.24	Amorphous	Defect
250	0.8-1.0	Amorphous	Defect
250-310	1.0-1.4	Amorphous/Crystalline interface	Defect
310-330	1.2-1.4	Crystalline	Defect/oxidation products

Table 2.2. Summaries of the charge traps in polyethylene [108]

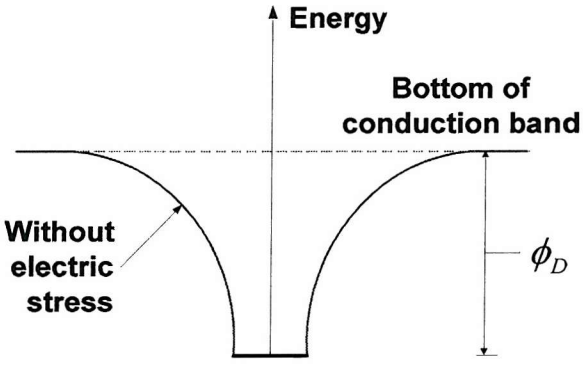

Figure 2.10. Potential well of the electron trap

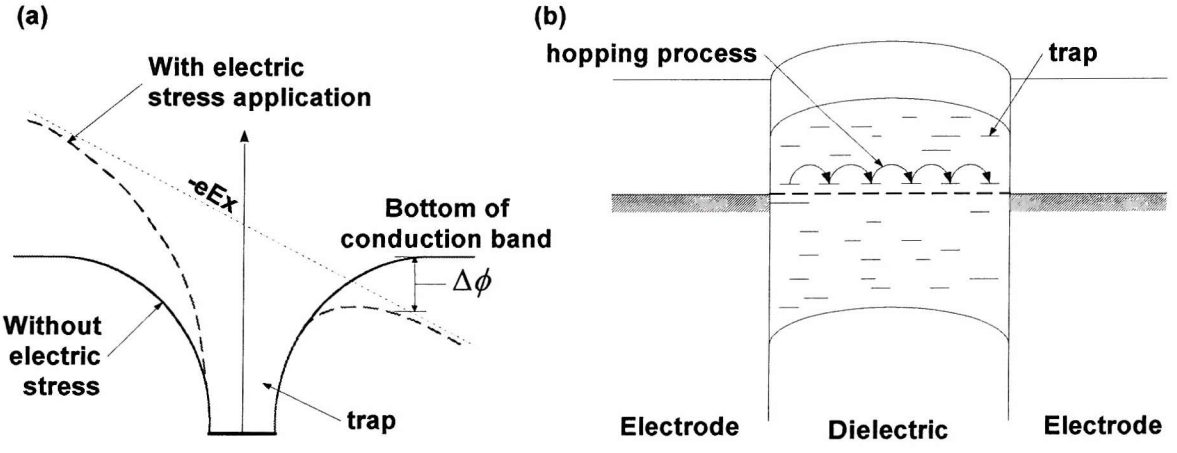

Figure 2.11. Schematic diagrams of the (a) Poole-Frenkel effect and (b) hopping process in the dielectric material

Figure 2.11 shows a schematic diagram of the charge migration process within the dielectric bulk, termed "hopping". When an electric stress is applied, it will interact with

the potential barrier of the trap, the height of the barrier between the traps is then lowered "$\Delta\phi$" by "Poole-Frenkel effect" and the probability of trapped electrons and ions having sufficient energy to escape the trap become higher. This means that the charges are transported through the insulation by hopping [109-110] from one trap to another (i.e. charge migration).

The relationship between the applied electric stress and the current density J is given in equation 2.3, details can be found elsewhere [111-112].

$$J = J_0 \exp\left[\frac{\beta_{PF} E^{1/2}}{2kT}\right] \text{ ---------- (2.3)}$$

where J_0 is a constant, and $\beta_{PF} = 2\beta_s = \left(e^3/\pi\varepsilon_r\varepsilon_0\right)^{\frac{1}{2}}$.

Normally, it is difficult to distinguish the Schottky and Poole-Frenkel effect as the experimental data may fit both mechanisms equally well. The Schottky injection mechanism should depend upon the semicon electrode material whilst the Poole-Frenkel effect is determined by the bulk insulation [113].

2.5D Relationship between space charge and heterogeneity of dielectric material

In this thesis, we have concerned ourselves with ideal dielectric samples, which are entirely homogeneous. However, in the practical case, a dielectric material like cross-linked polyethylene (XLPE) is always likely to have heterogeneous regions with the presence of second phase materials. For example, the stabilisers added to the polymers to prevent thermal degradation are usually dispersed second phase materials. Impurities such as traces of monomer, solvent, and water may also make the practical polymeric system heterogeneous.

When a dielectric material is composed of two or more phases (i.e. heterogeneous dielectrics) a type of polarisation occurs as a result of the accumulation of virtual charge at the interface, (both phases having different dielectric constants). For the polymeric material, charge carriers usually exist that can migrate for some distance through the dielectric bulk. When the charge carriers are impeded in their motion, either because they become trapped in the material (or at the interface) or because they cannot be freely discharged (or replaced

at the electrodes), space charge may be built up at the macroscopic interfaces. Such a distortion appears to an observer as an increase in the capacitance of the sample and may be indistinguishable from the real rise of dielectric constant. In fact, a polymer crystal inevitably has a large number of defects such as impurities and additives within the bulk. Free charge carriers migrating through the crystal under the influence of an applied field may be trapped by a defect. The effect of this will be creation of localised dipole moments. This phenomenon is given the name Maxwell-Wagner effect or interfacial polarisation.

2.6 Conclusions

In this chapter, the chemical and physical structure of polyethylene (PE) and cross-linked polyethylene (XLPE) are reviewed. To show how the additives and byproducts being formed inside the PE and XLPE insulation during the sample preparation process, the chemical processes for manufacturing sample are given.

In addition, to provide a fundamental background for the experimental results presented in the later part of this thesis, the basic concepts concerning mechanisms of space charge formation (i.e. injection and ionisation), migration (i.e. tunnelling and hopping) and accumulation (i.e. charge trapping) in the dielectric insulation are presented.

Chapter 3

Space charge measurement: Laser induced pressure propagation method

3.1 Introduction

Historically, measurements of trapped charge within solid insulation have been difficult to execute and interpret. The simple but destructive method is to cut the dielectric into slices and measure the charge in each slice using charge sensitive powders. Red coloured lead oxide (Pb_3O_4) was used to detect positive charges and yellow-white coloured sulphur (S) used to detect negative charge. However, as it is clear that direct, reliable, non-destructive, quantitative measurement of space charge distribution would be better way of understanding the space charge dynamic in solid dielectric materials Therefore, several non-destructive space charge measurement principles have been developed in the last twenty years. To save listing too many authors a comprehensive bibliography on non-destructive techniques for space charge measurements is given in Appendix 1.

The method used for the space charge measurement in this project was the laser induced pressure propagation technique (LIPP), which was developed by P. Laurenceau et al in 1977 and widely use by J. Lewiner [114-122]. Work in the past decade has been devoted to determining the space charge characteristics under dc electric stresses [39-68]. Work on the dynamics and the role of space charge on electrical breakdown under 50 *Hz* ac a condition have only received limited attention and has not been conclusive [69-73]. The difficulty of an ac measurement system over the dc one lies in how to construct a discharge free HV insulation system and design an automatic data acquisition technique to ensure a direct correlation between the instantaneously applied electric stress and the measurement taken. As there is an increasing body of opinion that space charge build up can be a contributing factor to electric tree initiation of high voltage insulation [74-75] and because the majority of polymeric cables will be operating under ac conditions in the immediate future, it is appropriate to extend the LIPP system to investigate the charge trapping and mobility under ac.

In this chapter, the basic principles of the LIPP system and the existing dc LIPP arrangement are reviewed. One of the main objectives of this research project is devoted to design and construct a new version LIPP system which can be used to investigate the space charge formation and evolution within a polymeric material with different treatments under both dc and 50 *Hz* ac ageing conditions. Therefore, the operational principles, technical design and construction of the newly designed LIPP system are given. In addition, as the space charge distribution of cable geometries is of great interest to the manufacturers and the end users, the newly designed LIPP system was modified, which allows space charge measurement in the coaxial cable sample.

3.2 LIPP principle and the existing dc LIPP system

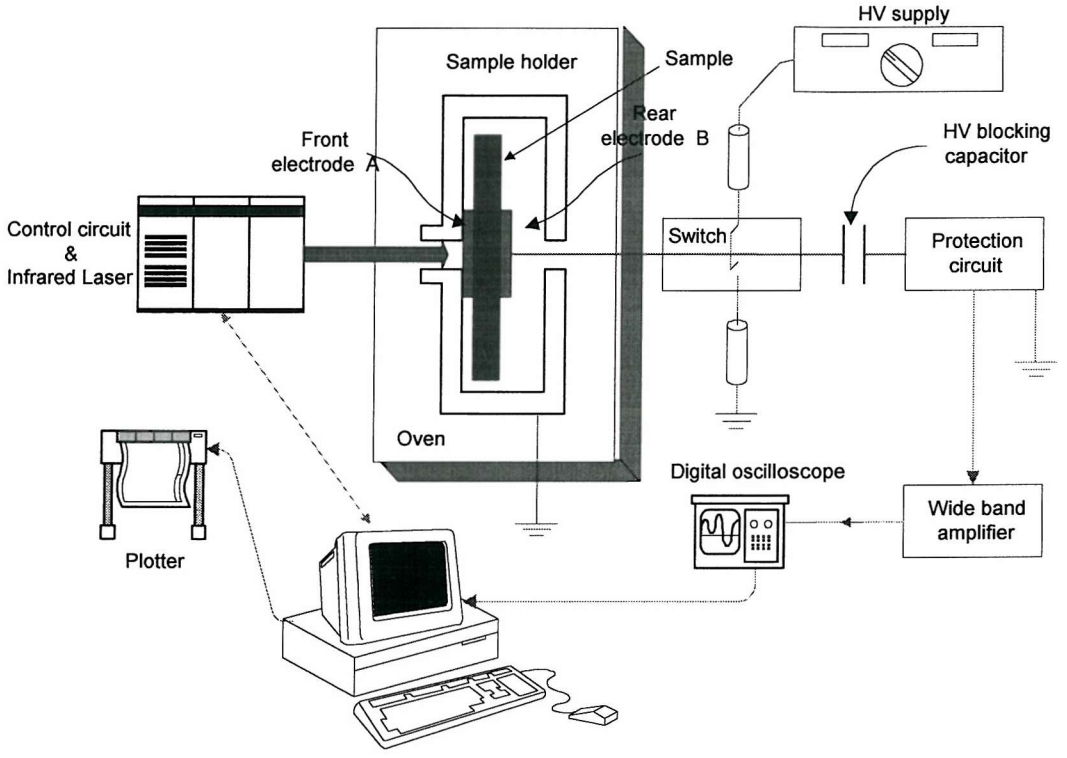

Figure 3.1. The existing dc LIPP system

A schematic diagram of the existing dc LIPP system is shown in figure 3.1, where a sample of homogeneous dielectric material is held in a screened chamber and electrically stressed between semicon electrodes 'A' and 'B'. A very short laser pulse (*~ns*) generated by a Q-switched 1.064 *μm* Nd/YAG laser system irradiates and heat the surface of the front electrode 'A'. This will cause the surface of the electrode 'A' to expand rapidly and relax as

it cools; thus an acoustic pressure wave as shown in trace (I) in figure 3.2 is produced and transverses through the sample at the velocity of sound u_{sa} [123-124].

As the dielectric sample is compressed by the leading edge of this pressure wave, then its atomic structure will be compressed and two effects are observed. A charge attached to the atomic structure will be slightly displaced and the relative permittivity of the sample modified due to the local variation in dipole and charge concentration as the pressure wave passes by.

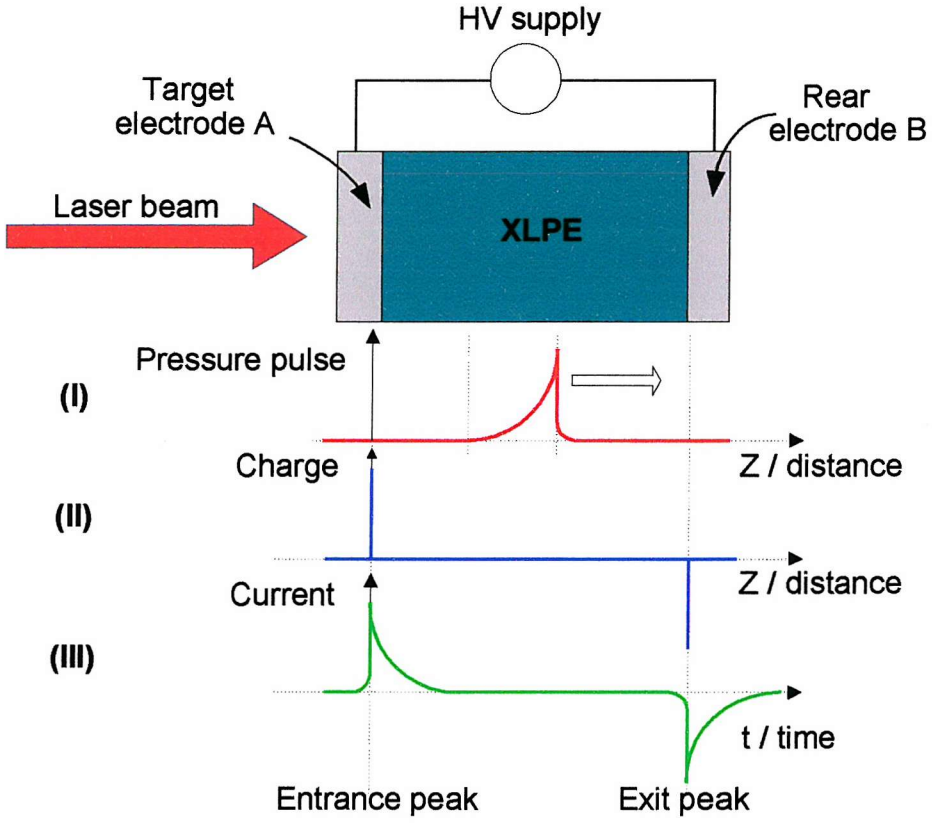

Figure 3.2. Schematic diagram of the LIPP technique

These two effects create a slight displacement of charge resulting in a simultaneous change in the induced charges on electrode 'A' and 'B'. Due to the 50 Ω-load impedance (input impedance of the amplifier) in the LIPP system, the change in the induced charges on the electrodes will produce a output current signal $I(t)$ in the external circuit, which can be defined in terms of pressure wave profile and stress distribution within the sample (Equation 3.1). The output current is directly related to the space charge within the sample and though the evolution of the current information on the space charge distribution under the applied

electric stress can be obtained. Further details of the equation 3.1 are given elsewhere [122, 125-129]. According to J. Lewiner [114], it was demonstrated that the existing dc LIPP system has a high spatially resolution ($10\mu m$) and the signal to noise ratio (SNR). However, the main disadvantage of this measurement system is that the capital cost of the Nd/YAG pulse laser in the system is high.

$$I(t) = \chi C_0 G(\varepsilon) \int_{z_f}^{d_0} E(z,t) \frac{d}{dt} p(z,t) dz \quad \text{or} \quad \text{where } C_0 = \frac{\varepsilon S}{d}$$

$$I(t) = -u_{sa} \chi C_0 G(\varepsilon) \int_{z_f}^{d_0} E(z,t) \frac{d}{dz} p(z,t) dz \text{ ---------- (3.1)}$$

where χ Compressibility of the sample,

C_o Capacitance of the non-compressed material,

$z_f(t)$ Position of the wave front at time t,

$E(z,t)$ Electric stress distribution,

$p(z,t)$ Pressure wave profile,

z Distance through the sample,

u_{sa} Speed of acoustic in the sample,

$G(\varepsilon)$ Coefficient that depends on the relationship between the permittivity and the pressure wave.

Trace (II) in figure 3.2 shows the charge distribution within the polymeric plaque sample, assuming the insulation is devoid of any space charge except for the surface charge on the sample/electrode interfaces due to the applied high voltage. As the pressure wave passes into the sample, it crosses the front sample/electrode interface; the charge on the surface of the electrode A is consequently moved and recorded as a current pulse. Assuming that there is no further charge throughout the bulk, then there will be no further current recorded until the pressure wave reaches the end of the sample. As the pressure wave pressure passes out of the sample, the surface charge on the rear sample/electrode interface (B) is displaced. This moving charge is also recorded as the second current pulse, which is of opposite polarity to that of the front electrode as the surface charge is equal but has opposite polarity to one another.

In practice the pressure wave is not an impulse but is in fact a compression wave with a fast leading edge followed by a gradual relaxation. As such, the surface charges through which the pressure wave passes will not be seen as a current impulse but will produce a current waveform as shown in trace (III) in figure 3.2. This waveform shows that the two equal but opposite surface charge produce two equal but opposite current peaks at the interface. However, in the practical case the typical output current signal as shown in figure 3.3 is not as simple as described. The amplitude and the profile of the pressure wave will be degraded (i.e. attenuated and dispersed) by the imperfect elastic properties of the polymeric material. As such, direct calculation of the charge distribution from the output current waveform is impossible and equation 3.1 must be solved by taking the pressure wave profile into account. In addition, the second peak of the current signal will also be interfered by the reflection wave (3rd peak of the current signal) from the metal electrode in the system, and some data processing method is required. Further discussion of these processing techniques will be given in a later chapter.

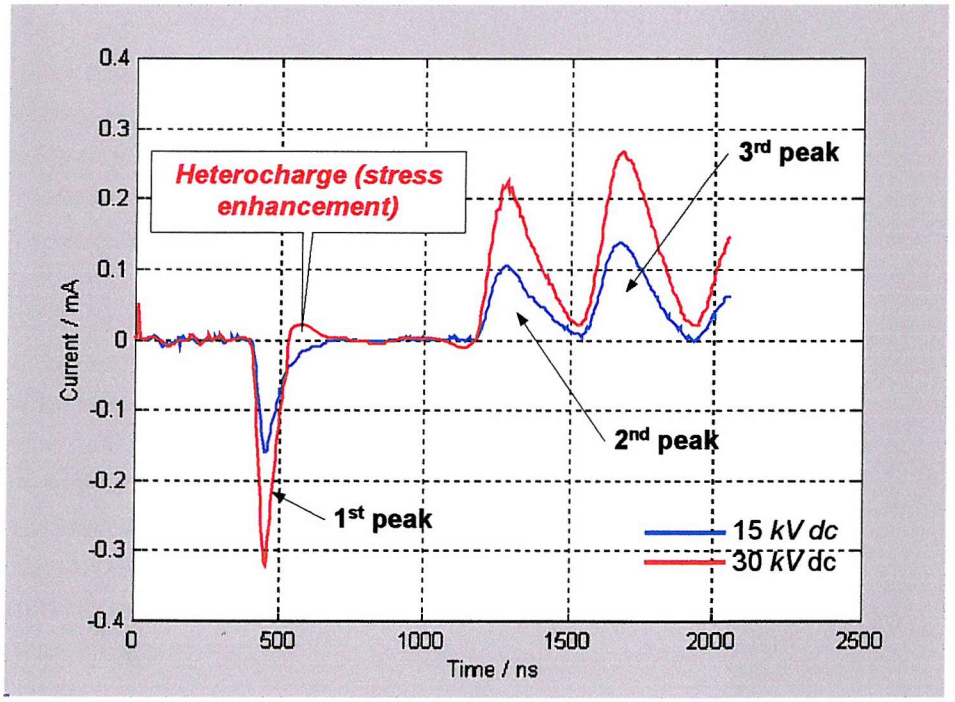

Figure 3.3 Typical LIPP current signal of the 1.5 *mm* XLPE sample at 15 and 30 *kV* dc

3.3 Difference between dc and ac LIPP system

For a dc LIPP system, the applied electric stress across the polymeric sample is constant throughout the ageing or measurement period; therefore a computer control data acquisition

system for the space charge measurement is not essential [130]. However, for an ac LIPP system, the applied electric stress is time dependent and the space charge distribution is complex due to the magnitude and polarity variations of the applied stress. It is impossible to perform the successive measurement at different precise points on wave manually. In addition, an electronic control system is required to perform automatic data acquisition as considerable amounts of data are generated for ac operating conditions in a short period of time.

In addition, as the LIPP utilises a high power Nd/Yag laser to generate the pressure wave, it will create excessive heating on the semicon target material; resulting in damage of the target and modification of its ultrasonic properties. For a dc space charge measurement, the semicon electrode (semicon target) on the test sample would need to withstand ~20 laser shots during an entire experiment (including ageing), and it transpires that the effect of target ablation to the signal calibration is insignificant. However, in the case of ac, the semicon target experiences "n" laser shots for each measurement ("n" is equal to number of point on wave measurement per cycle), therefore within the whole period of an ageing test, the target may be subjected to more than 60 laser shots. Under these conditions the effect of target ablation on the output current signal becomes significant and this would affect the measurements considerably [131]. To reduce the damage of the target, a target cooling system has been installed and controlled by electronics.

According to equation 3.1, the magnitude of the LIPP signal induced by the pressure wave depends on both the internal electric field distribution and the pressure shape (i.e. pulse magnitude and width). The pressure shape is directly related to the laser power; therefore any laser power variation from shot to shot during measurement can cause invalidation of the signal calibration. An online laser power monitor system has been installed in order to eliminate the effect of the laser power variation on the measurements.

3.4 Experimental principle of the ac LIPP system

Prior to the electrical, electronic and mechanical designs of the ac LIPP system, the establishment of its working principles is essential. For the space charge measurement under ac condition, considerable care must be exercised to ensure a direct correlation between the "instantaneously" applied electric stress and the measurement taken.

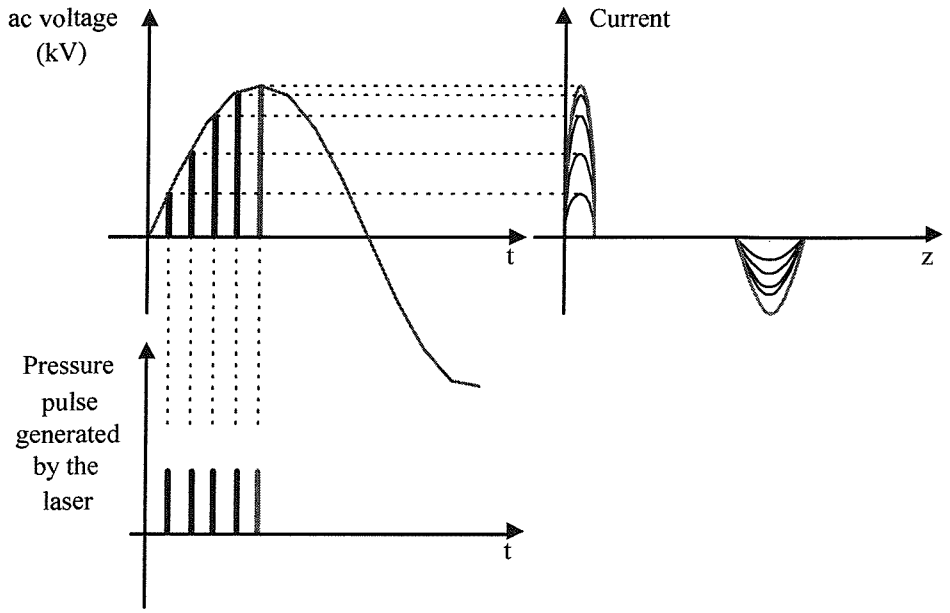

Figure 3.4 Measurement of space charge signal at successive point on wave of same cycle of applied ac voltage

This is best achieved with "point on wave" control of the applied voltage triggering the laser [76,130,132]. This control is made easier because the travel time for the propagation of the acoustic wave through a 2 *mm* XLPE sample (typical ~ 1 μsec) that is small compared to the period of one cycle of 50 *Hz* ac voltage (*20 ms*). Provided the laser is triggered on a specific point on the ac waveform, the applied stress can be considered constant during the period of a measurement. Therefore, it makes the ac LIPP system possible, where the space charge measurement at a number of different points on the voltage waveform is possible as shown in figure 3.4.

In order to overcome the problem of the damage of the semicon target changes in its ultrasonic properties, two measures have been utilised,

Measure 1: A liquid cooling system for the target has been installed. The principle of which is to inject silicon oil on to the surface of the semicon target material just before firing the laser pulse. (Silicon oil was used to eliminate the problem of oil absorption by the XLPE material, which could affect the measurement) This oil film not only assists in dissipating the majority of the laser energy and prevents the target being damaged but it also assists in increasing the efficiency of the conversion of the light energy into acoustic energy, hence helping to increase the output signal amplitude.

Measure 2: The space charge measurements are performed over successive ac cycles rather than a single cycle. Therefore, only one laser shot per ac cycle is used instead of firing many numbers of laser pulses on the target per ac cycle, hence the semicon target has enough time to cool down thus reducing the damage to its surface.

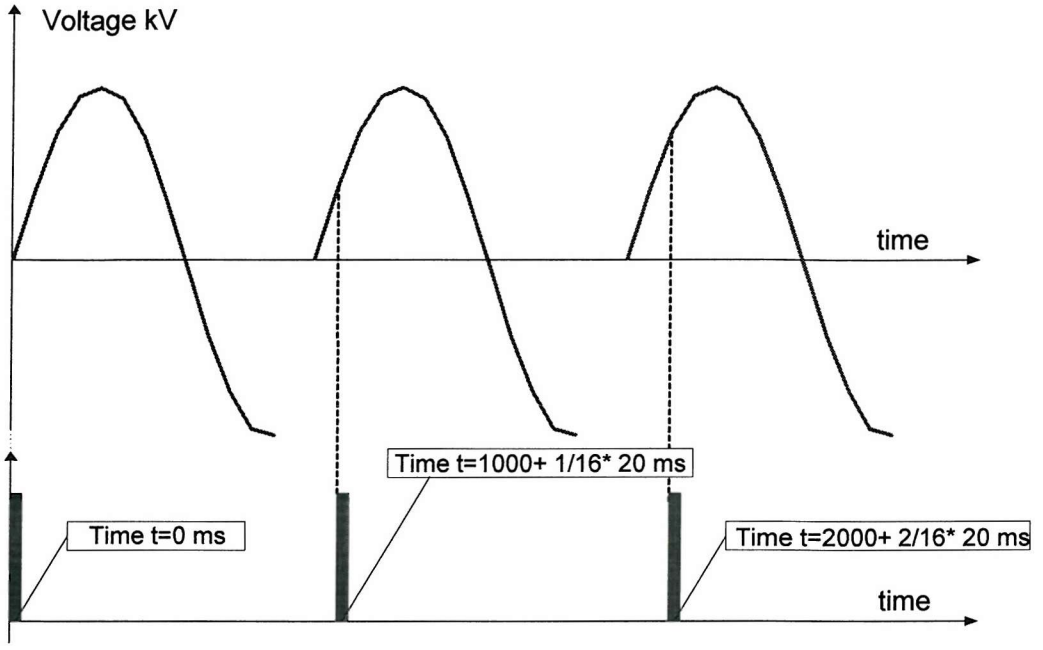

Figure 3.5. Measurement of space charge signal at successive phases of different cycles of applied ac voltage

For example, in order to achieve 17 measurements at different points on an ac wave, a time delay between two successive pulses is employed as shown in figure 3.5, which is equal to,

$$1000ms + \frac{1}{16} * 20ms \quad \text{-----(3.2)}$$

3.5 Newly designed LIPP experimental set-up

Figure 3.6 shows the block diagram of the newly designed LIPP arrangement. The polymeric sample placed in a holder is connected both to the high voltage power supply and the measurement system.

The laser is activated at a point on the ac wave using an electronic control system, which is controlled by the computer and synchronised with the ac high voltage. The instant voltage applied to the sample at a particular point during a measurement is stored on the computer.

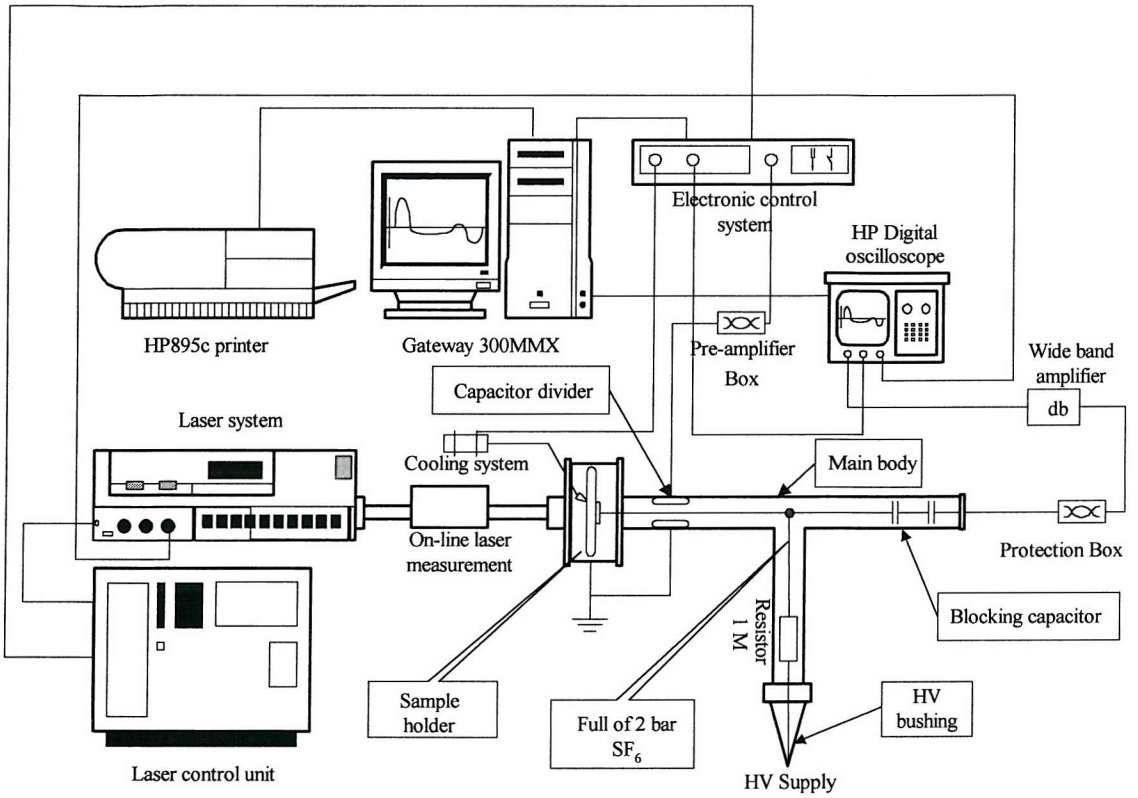

Figure 3.6. Block diagram of ac LIPP system (with plaque sample holder)

3.6 Electrical system design

In the newly designed LIPP system, there are three main electrical components, (1) the high voltage blocking capacitor, (2) the high voltage capacitor divider, and (3) the over-voltage pulse protection box.

3.6A The high voltage blocking capacitor

In order to de-couple the high voltage and the measurement system, two 140 *pF* HV blocking capacitors (in series with a total value of 70 *pF*) have been inserted between them. An equivalent circuit of the LIPP system including the blocking capacitor, sample capacitance and the amplifier is shown in figure 3.7.

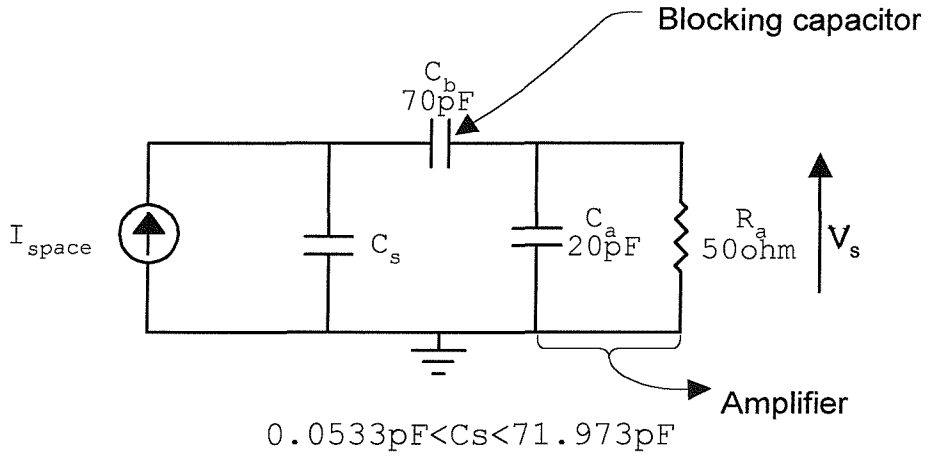

where

I_{space} Current output from the testing sample,

V_s Voltage measurement by the oscillscope,

C_s Sample capacitance,

C_b Capacitance of blocking capacitor,

C_a Capacitance of the measurement circuit,

R_a Resistance of the measurement circuit,

Figure 3.7. Equivalent circuit diagram of the LIPP system with the inclusion of the blocking capacitors

As the circuit design is based on the capacitance of the dielectric sample and some pre-chosen parameters (i.e. load impedance, etc) of the measurement circuit, it is important that with the inclusion of the blocking capacitor, all the frequency elements of the output current signal corresponding to the space charge distribution in the bulk should be below the cut off frequency of the circuit. The following four steps are used to ensure that the value of the capacitance is adequate.

Step 1: Pre-chosen values of the measurement circuit R_a=50 Ω

C_a=20 pF

C_b=70 pF

Step 2: Obtain the range of the electrode area of the samples

The system is capable of measuring space charge for samples with various sizes and the changes in electrode diameter and sample thickness are as follow:

Range of the electrode diameter: $0.01\ m \rightarrow 0.03\ m$

Range of sample thickness: $200\text{x}10^{-6}\ m \rightarrow 0.003\ m$

Area of the electrode with 10mm diameter

$$Area_1 = \pi \cdot r^2 = \pi \cdot \left(\frac{0.01}{2}\right)^2 = 78.540\times10^{-6}\,m^2$$

Area of the electrode with 30mm diameter

$$Area_2 = \pi \cdot r^2 = \pi \cdot \left(\frac{0.03}{2}\right)^2 = 706.858\times10^{-6}\,m^2$$

Therefore, the range of electrode area is $78.540\times10^{-6}\,m^2 \le A \le 706.858\times10^{-6}\,m^2$

Step 3: Calculate the range of the capacitance of the dielectric sample C_s

According to the dimensions of the sample with two extreme cases of electrode area A, the range of the sample capacitance C_s can be determined by equation 3.3 [133],

$$C_s = \frac{\varepsilon_r \cdot \varepsilon_0 \cdot A}{d}\ (F) \quad \text{---------- (3.3)}$$

where $\varepsilon_0 = 8.854\,pFm^{-1}$, $\varepsilon_r = 2.3$ and d is the thickness of the sample

For case 1:

$A = 78.540\times10^{-6}\,m^2$ and d=0.003 m

$$\therefore C_{s(Smallest)} = \frac{2.3 \times 8.854 \times 78.540 \times 10^{-6}}{0.03} = \underline{\underline{0.0533pF}}$$

For case 2:

$$A = 706.858 \times 10^{-6} m^2 \text{ and } d = 200 \times 10^{-6} m$$

$$\therefore C_{s(Largest)} = \frac{2.3 \times 8.854 \times 706.858 \times 10^{-6}}{200 \times 10^{-6}} = \underline{\underline{71.973pF}}$$

Step 4: Verification of the design

As mentioned earlier, the importance of the design is to ensure that all the frequency elements of the output current signal are below the cut off frequency after the blocking capacitor is inserted in the measurement circuit.

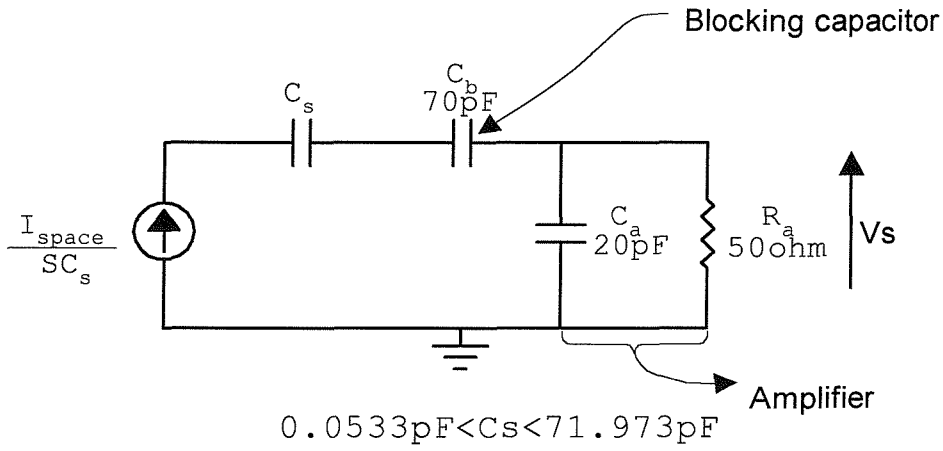

Figure 3.8. Equivalent circuit diagram of the LIPP system with the inclusion of the blocking capacitors (Simplify)

The equivalent circuit in figure 3.7 can be simplified and redrawn as shown in figure 3.8. The cut off frequency of the output signal can be expressed as follow (Figure 3.9),

$$V_s = \frac{\frac{R_a}{1+R_aC_aS}}{\frac{R_a}{1+R_aC_aS} + \frac{C_s+C_b}{C_sC_bS}} \cdot \frac{I_{space}}{C_sS} = \frac{R_a}{R_a + \frac{C_s+C_b}{C_sC_bS} \cdot (1+R_aC_aS)} \cdot \frac{I_{space}}{C_sS} \qquad \text{where } S = j\omega$$

$$= \frac{R_a}{R_a C_s S + \frac{C_s + C_b}{C_b}(1 + R_a C_a S)} \cdot I_{space} = \frac{R_a}{\frac{C_s + C_b}{C_b} + \left(\frac{R_a C_s C_b}{C_b} + \frac{C_s + C_b}{C_b} \cdot R_a C_a\right) S} \cdot I_{space}$$

$$\therefore \left|\frac{V_s}{I_{space}}\right| = \frac{R_a \cdot C_b}{C_s + C_b} \cdot \left[\frac{1}{1 + \left(\frac{R_a \cdot C_s \cdot C_b}{C_s + C_b} + R_a \cdot C_a\right) S}\right] \text{ ----- (3.4)}$$

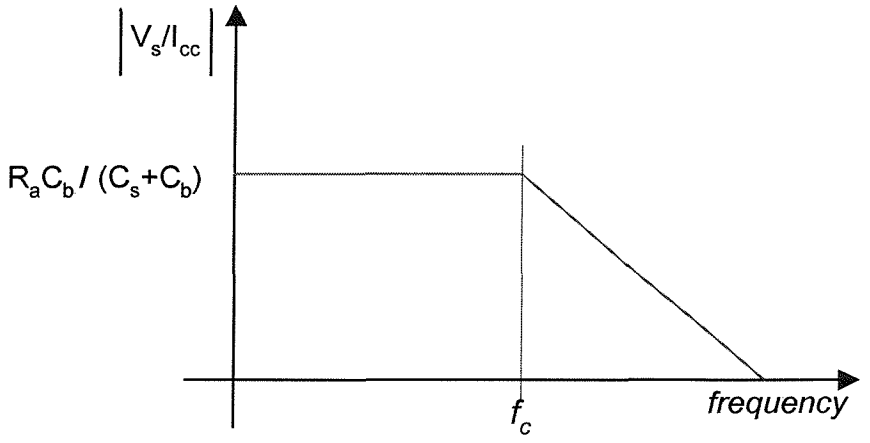

Figure 3.9 Frequency response of the quivalent circuit with the inclusion of the blocking capacitors (Cut off frequency)

And the cut off frequency is $f_c = \frac{1}{2 \cdot \pi \cdot R_a \left(C_a + \frac{C_s \cdot C_b}{C_s + C_b}\right)}$ ----- (3.5)

For case 1, the cut-off frequency corresponding to the system parameters and the sample capacitance is equal to,

$$f_c = \frac{1}{2 \cdot \pi \cdot 50 \cdot \left[20 \times 10^{-12} + \frac{0.0533 \times 10^{-12} \times 70 \times 10^{-12}}{0.0533 \times 10^{-12} + 70 \times 10^{-12}}\right]} = \underline{158.73 MHz}$$

which means that the output V_s is proportional to I_{space} if the signal frequency is below 158.73 *MHz* (i.e. the rise time (t_r) of the signal > 1.5 *ns*).

For case 2, the cut-off frequency corresponding to the system parameters and the sample capacitance is equal to,

$$f_c = \frac{1}{2\cdot\pi\cdot 50\cdot\left[20\times10^{-12} + \frac{71.973\times10^{-12}\times70\times10^{-12}}{71.973\times10^{-12}+70\times10^{-12}}\right]} = \underline{\underline{75.37MHz}}$$

which means that V_s is proportional to I_{space} if the signal frequency is below 75.37 *MHz* (i.e. the rise time (t_r) of the signal > 3.3 *ns*).

In the LIPP system, the rise time of the short circuit current signal produced by the pressure pulse on the semicon electrode is greater than 3.3 *ns* (i.e. Typically 20 *ns*) and its corresponding frequency is well below the cut off frequency determined above. This verifies that the value of the blocking capacitor is acceptable without affecting the frequency response of the measurement circuit.

3.6B The high voltage capacitor divider

In order to record the actual high voltage value and obtain the synchronised ac signal to activate the electronic board for the ac space charge measurement, a high voltage capacitor divider has been installed in the LIPP system. The circuit diagram for the high voltage measurement is shown in figure 3.10. To determine the values for capacitors, following steps are used.

Step 1: Obtaining the transfer function of the high voltage divider

For AC operation, if $R_1 >> \frac{1}{j\omega C_{bp}}$, then $i_R << i_{bp}$ and $i_{c_1} = i_R + i_{bp} \approx i_{c_{bp}}$

$$Z_1 = \frac{1}{j\omega C_1} \text{ and } Z_2 = \frac{1}{1/R_1 + j\omega C_{bp}}$$

$$\frac{V_2}{V_1} = \frac{\frac{1}{\left(1/R_1 + j\omega C_{bp}\right)}}{\left(\frac{1}{j\omega C_1} + \frac{1}{\frac{1}{R_1} + j\omega C_{bp}}\right)} \text{ -------- (3.6)}$$

$$= \frac{R_1(j\omega C_1)}{(1+j\omega C_{bp}R_1)+R_1(j\omega C_1)} = \frac{R_1C_1S}{1+R_1(C_1+C_{bp})S} \quad \text{where } S = j\omega$$

$$\approx \frac{R_1C_1S}{R_1(C_1+C_{bp})S} = \frac{C_1}{C_1+C_{bp}} \quad \because V_2 << V_1 \Rightarrow C_1 << C_1 + C_{bp}$$

$$\therefore \frac{V_2}{V_1} \approx \frac{C_1}{C_{bp}} \text{ or } \frac{V_1}{V_2} \approx \frac{C_{bp}}{C_1} \text{ ---------- (3.7)}$$

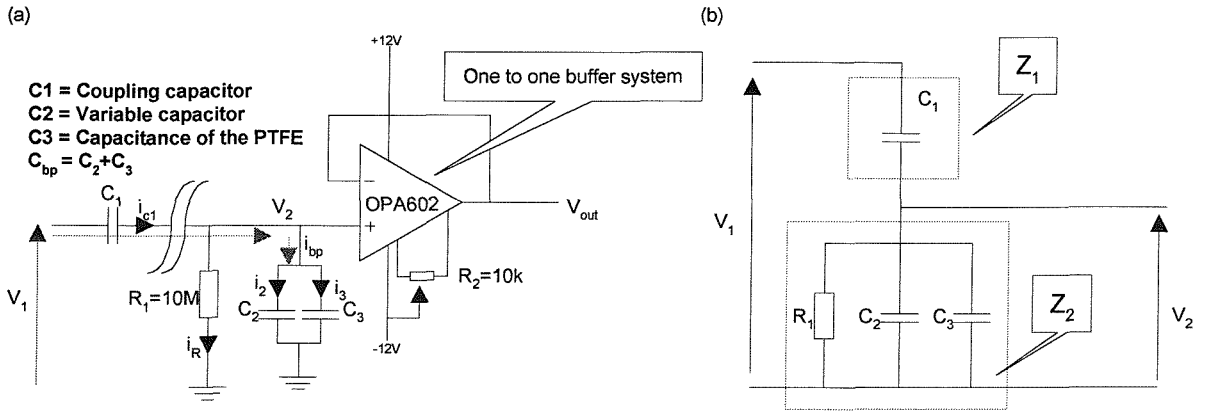

Figure 3.10. Circuit diagram and equivalent circuit for high voltage measurement

Step 2: Design of the high voltage capacitor divider

According to Gauss's law [133], $E \cdot \int_s ds = E \cdot 2\pi r = \frac{q}{\varepsilon}$ and $E = \frac{q}{2\pi\varepsilon r}$

where q is the charge per unit length of the capacitor, and
r is the radius of the capacitor

Let $a = \frac{d}{2}$ and $b = \frac{D}{2}$ as shown in figure 3.11,

$$V_b - V_a = -\int_a^b E dr \text{ --------- (3.8)}$$

As the outer surface of the main body is grounded, i.e. $V_b = 0$, the above equation becomes

$$0 - V_a = -\int_a^b \frac{q}{2\pi\varepsilon r} dr \Rightarrow \therefore V_a = \frac{q \cdot \ln\left(\frac{b}{a}\right)}{2\pi\varepsilon}$$

Since $C = \frac{q}{V_a} \Rightarrow C = \frac{2\pi\varepsilon}{\ln\left(\frac{b}{a}\right)}$ per unit length

And the value of capacitance of length L is $C = \frac{2\pi\varepsilon \cdot L}{\ln\left(\frac{b}{a}\right)}$ -------- (3.9)

It is clear that the high frequency noise created by corona discharges will affect the space charge signal and reduce the signal to noise ratio of the measurement. Therefore, in order to avoid discharges in the system, the entire free volume inside the sample holder and main body at the high voltage end has been filled with 2-bar pressurised SF_6 gas. (Dielectric constant = 1.0019)

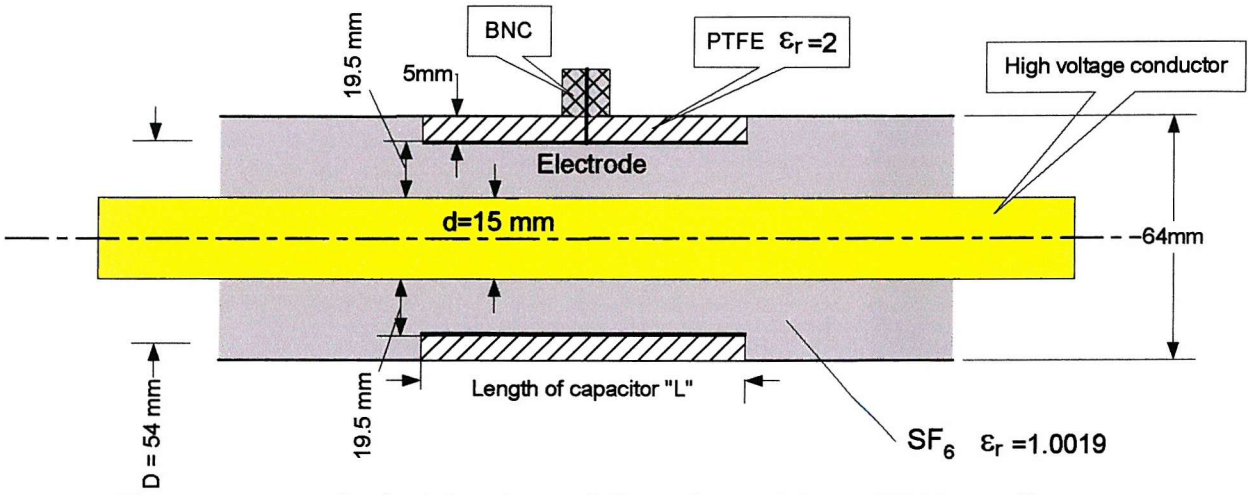

Figure 3.11. Mechanical drawing and dimensions of the ac LIPP coupling system

Table 3.1 below is the pre-chosen dimensions of the ac LIPP coupling system, and the length of the coupling capacitor is designed to be $L = 0.1m$.

Coupling capacitor	PTFE
$a = \frac{d}{2} = \frac{15}{2} = 7.5mm = 7.5 \times 10^{-3} m$	$a = \frac{54}{2} = 27mm = 0.027m$
$b = \frac{D}{2} = \frac{54}{2} = 27mm = 0.027m$	$b = \frac{64}{2} = 32mm = 0.032m$

Table 3.1 Pre-chosen dimensions of the ac LIPP coupling system

Substitute the above dimensions into equation 3.9; the capacitance of the coupling capacitor is,

$$C_1 = \frac{2\pi \cdot 1.0019 \cdot 8.85\times10^{-12} \times 0.1}{\ln\left(\frac{0.027}{7.5\times10^{-3}}\right)} = 4.349\times10^{-12} F = \underline{\underline{4.35pF}}$$

Substitute the above dimensions into equation 3.9; the capacitance of the PTFE is,

$$C_3 = \frac{2\pi \cdot 2 \cdot 8.85\times10^{-12} \times 0.1}{\ln\left(\frac{0.032}{0.027}\right)} = 65.5^{-12} F = \underline{\underline{65.5pF}}$$

By using the transfer function $\frac{V_2}{V_1} \approx \frac{C_1}{C_{bp}}$ from the step 1 and with a transform ratio of the capacitor divider $\frac{V_2}{V_1} = \frac{1}{10000}$, therefore the value of the $C_{bp} = 43.5\times10^{-9} = \underline{\underline{43.5nF}}$ and the value of the variable capacitor used in the pre-amplifier box should be equal to $C_2 = C_{bp} - C_3 = 43.4^{-9} F = \underline{\underline{43.4nF}}$. Also, in order to prevent high frequency noise entering the control and measurement systems, both circuits are placed in enclosed shielding boxes.

3.6C Protection circuit against the voltage pulse

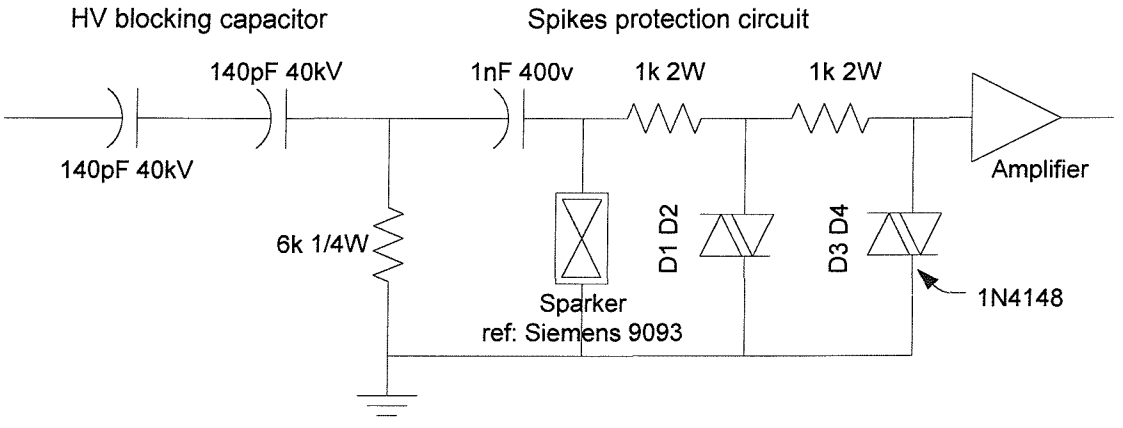

Figure 3.12 Circuit diagram of protection box

To avoid any damage caused by high voltage discharge 'spikes' to the costly components like the wide band amplifier and the computer system, a protection circuit with unity transfer function as shown in figure 3.12 has been inserted between the blocking capacitor and the wide band amplifier. The $1nF$ capacitor acts as a high-pass filter, which removes any dc offset from the output voltage signal. Any voltage spike ($> 0.6\ V$) within the output voltage signal will be shorted to the ground by the 'sparker' device and dissipated by the resistor ($6\ k\Omega$). Two sets of double diodes arrangement are acting as the final protections to ensure the output voltage is within $\pm 0.6\ V$ before entering to the amplifier.

3.7 Electronic system design

One of the technical difficulties of an ac LIPP system over a dc one lies in how to construct an automatic data acquisition system. It is because the space charge distribution in the sample alters correspondingly to the applied ac voltage in an order of "*msec*". Therefore, in order to perform the successive measurement at different precise points (or phase) on the ac wave and control the target cooling system, an electronic control system has been used, which was original designed by the "HLP technologies" and modified by Southampton University. The electronic control system makes the automatic data acquisition and target cooling possible. It synchronises the ac high voltage and triggers the laser firing at precise point on wave for the measurement. In addition, it controls the solenoid to inject silicon oil on to the surface of the semicon electrode just before firing the laser. Details of the circuit and the working principles of the electronic system can be referred to in Appendix 2.

3.8 Mechanical system design

Mechanical design is an essential part of the ac LIPP system to ensure reliable measurements. It includes high voltage insulation system, mechanism of cooling system and sample holder.

3.8A The compressed gas high voltage insulation system

If there are corona discharges in the HV system, the high frequency noise generated will superimpose on the measured signal and reduce the signal to noise ratio. Moreover, the ac

waveform obtained from the HV capacitor divider acts as an activation signal to the electronic system, if it contains any high frequency noise from the discharge, it may cause a mistrigger and affects the reliability of the measuring system. Therefore, it is important to eliminate any discharge activities.

In order to avoid discharge in the system, the entire free volume inside the sample holder and main body at the high voltage end has been filled with 2-bar pressurised sulphur hexafloride (SF_6) gas. "SF_6 " is universally used for high voltage equipment. It is non-poisonous, colourless and heavier than air and has a good insulating properties. However, one adverse characteristic of the SF_6 gas is that an extremely aggressive and poisonous byproduct will be produced if any discharge occurs [134]. Therefore, safety precaution must be taken; i.e. the pumping system for the exhaust gas must be filtering by the special chemical before it can be released. No discharge has been observed under 80 kV dc and ac up to 30 kV_{peak}.

3.8B The target cooling system

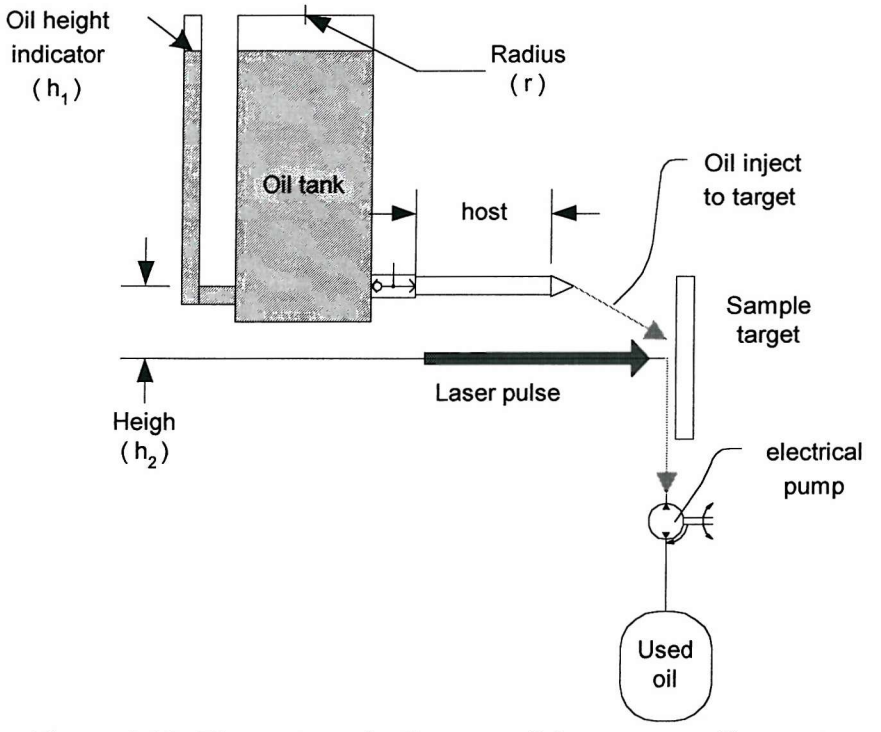

Figure 3.13. The systematic diagram of the target cooling system using gravitational force

In order to eliminate any inconsistent amount of silicon oil injected on the target surface for each measurement, a pressure pump has been installed. It was used to control the pressure and the amount of oil injected to the target surface. However, the main drawback of such an arrangement is the pump creates bubbles inside the oil, which can deposit on to the target. If the laser pulse lands on the oil film containing bubbles an unexpected loss of laser energy may arise. An alternative method using a header tank to create the liquid pressure as shown in figure 3.13 was then adopted. Since this method only relies on the gravitational force, no gas bubbles are created.

According to the Bernoulli's energy equation 3.10 [135], as the silicon oil tank with radius "*r*" is placed at height "h_2" above the outlet of the liquid system, then

$$\frac{P_1}{\rho g}+\frac{V_1}{2g}+h_2=\frac{P_2}{\rho g}+\frac{V_2}{2g}+\text{frictionalhead lost} \quad \text{---------- (3.10)}$$

$$A_1V_1=A_2V_2 \quad \text{--------- (3.11)}$$

where P_1 and V_1 are the pressure and velocity of the oil at the outlet of the water tank,

P_2 and V_2 are the pressure and velocity of the oil inject to the sample,

A_1 and A_2 are the cross-section area of the host,

ρ is the density of oil,

g is the pull of gravity,

Assuming that the cross-section area of the host liquid is constant and the energy by the frictional head loss is zero, then equation 3.10 can be rewritten as equation 3.12. It shows that the pressure P_2 of the oil at the injection point to the sample will only depend on the pressure and height of the oil tank.

$$\frac{P_1}{\rho g}+h_2=\frac{P_2}{\rho g} \quad \text{---------- (3.12)} \qquad \text{where } P_1=\frac{rh_1\rho g}{2}$$

As mentioned, any inconsistent amount of oil on the target surface will invalidate the signal calibration. Therefore, in order to avoid the accumulation of oil on the target surface from

shot to shot, an electrical pump has been installed as shown in figure 3.13 to remove the oil runoff from the target surface.

3.8C Construction of the plaque and cable sample holder

The newly designed LIPP system was further developed to include coaxial cable structures. The mechanical joins between both sample holders (i.e. plaque or cable) to the high voltage main body are the same, therefore depending on the geometry of the test sample it is only necessary to swap the sample holder to complete the measurement system. Sample holders for plaque and cable samples are constructed as shown in figure 3.14 and 3.15 respectively. (The details of mechanical drawing are shown in Appendix 3 and 4)

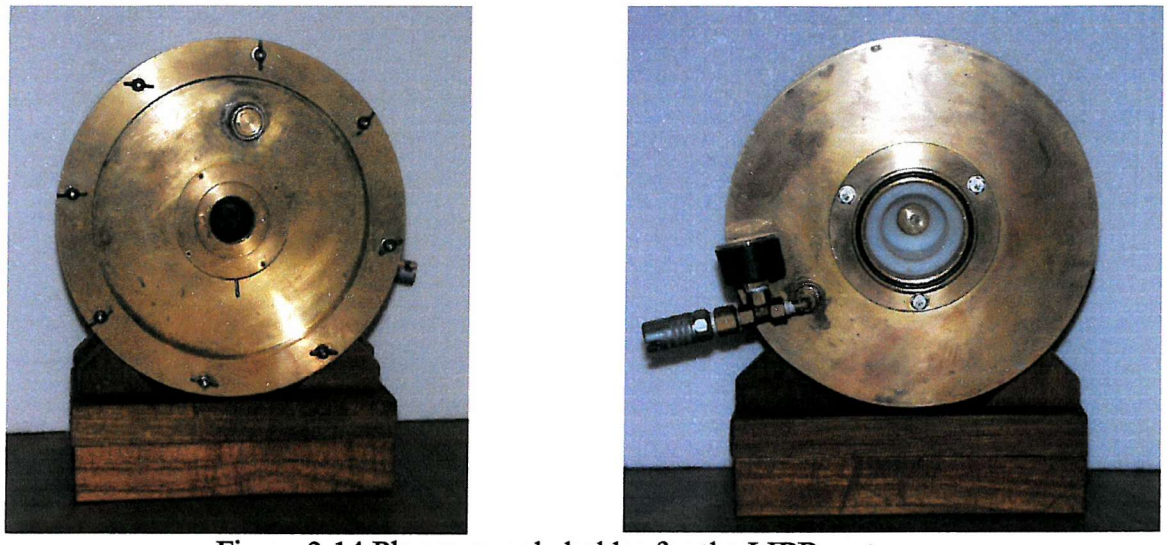

Figure 3.14 Plaque sample holder for the LIPP system

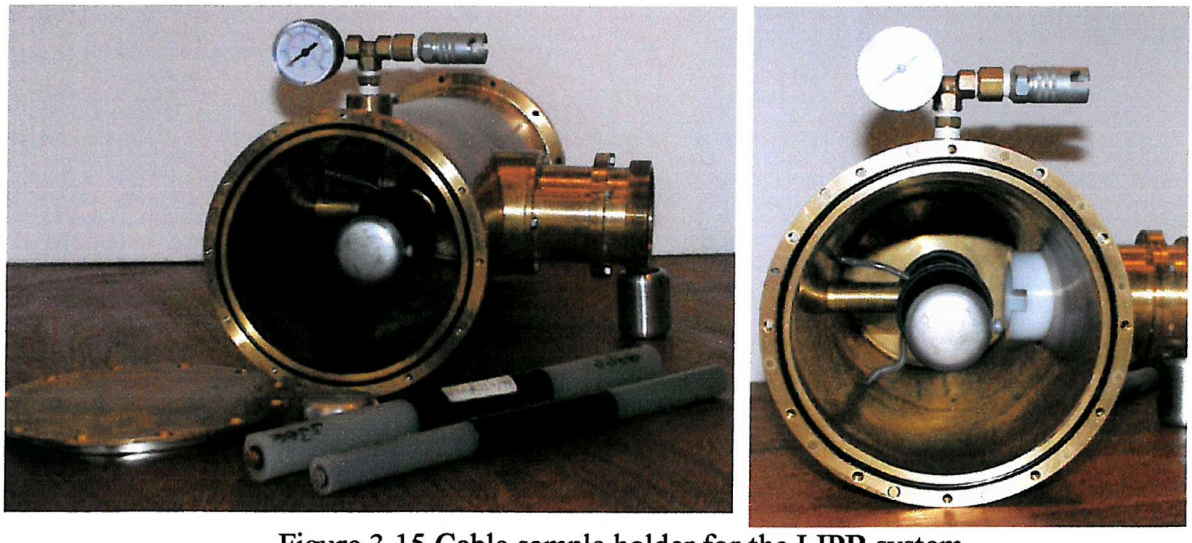

Figure 3.15 Cable sample holder for the LIPP system

3.9 Online laser power measurement and laser beam focusing system

Referred to equation 3.1, the magnitude of the LIPP signal induced by the pressure wave propagation through the sample depends on both the internal electrical field distribution $E(z,t)$ and its pressure shape $p(z,t)$. The pressure shape is directly related to the laser power. Any power variation during the measurement can cause a serious problem to the calibration and reproducibility of the space charge measurement. In order to eliminate the effect of the laser power variation on the space charge measurements, two solutions have been considered.

The first solution is to record a few signals and average them. This must be carried out for each measurement (calibration and ageing), and the effect of laser power variation becomes less important. In addition, this averaging method has a second beneficial effect. It can reduce the random noise level by a factor of $\sqrt{n}$ where n is the number of shots. However, target damage and the heating effect must also be taken into account, as each measurement "consumes" n shots of target. This method in fact can only apply to the sample stressed under dc condition.

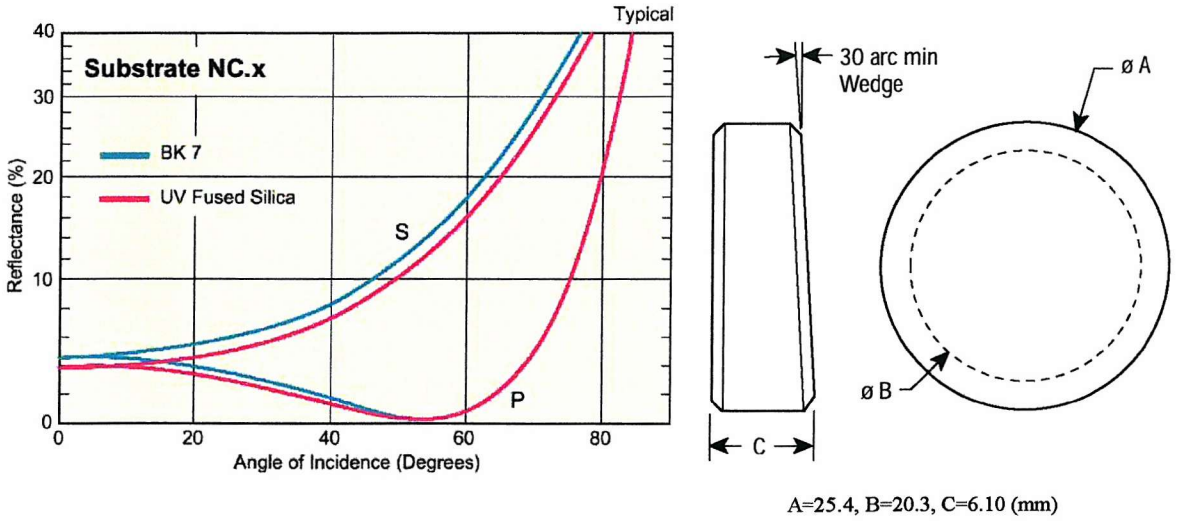

Figure 3.16. Characteristic and dimension of the laser splitter [136]

Another solution, which has been adopted in the LIPP system, is a "online laser power monitor". Since the magnitude of the space charge signal was directly proportional to the laser power, by measuring a small fraction (5 %) of laser power (Beam splitter), it is possible to normalise the output signals before any numerical treatment. The characteristic

of the laser beam splitter is shown in figure 3.16. If 5 % of laser power is reflected by a laser beam splitter to a laser power meter, the incident angle of the laser to the splitter should be 15 degree.

As mentioned earlier, space charge distribution in power cables is of great interest to the manufacturers and the end users, and one of the objectives is to use the LIPP system to investigate space charge formation and trapping characteristics in coaxial cable structures. However, due to the limited laser power, the pressure generated by the laser used for the 2 *mm* planar sample measurement was not powerful enough to obtain a signal with reasonable SNR for 4.5 *mm* or 6 *mm* thick cable.

In order to achieve higher laser power density (W/cm^2), one solution is to reduce the diameter of the laser beam.

Equation of laser power density: Power density $= \frac{P_{laser}}{\pi r^2}$ ---------- (3.13)

Since the original laser beam for the plaque samples was around 5 *mm* in diameter and the laser power density is equal to $\frac{P_{laser}}{0.0625\pi}$, by changing the optical lens 'A', the laser beam diameter in the LIPP system can be reduced to 2.5 *mm* or 1.5 *mm* and the density of the laser power will increase 4 times to $\frac{P_{laser}}{0.015625\pi}$ and 11 times to $\frac{P_{laser}}{0.005625\pi}$ respectively. In the system, an online laser power measurement and an optical system for the laser beam diameter reduction have been incorporated into a single unit with all the lens and power detecting sensor housed in an enclosed metal box as shown in figure 3.17.

As the time interval between 2 consecutive laser shot for ac space charge measurement is only "*1000+(1/N)*20 ms*", it is impossible to collect the laser power of each shot manually. A program that allows the communication between the laser power meter (FieldMaster GS) and the computer by using the serial port has been written under visual basic environment. This makes automatic data collection possible. The details of the technical parameters used in the visual basic program and the pin numbers assessment for the construction of the data collection cable are given in Appendix 5.

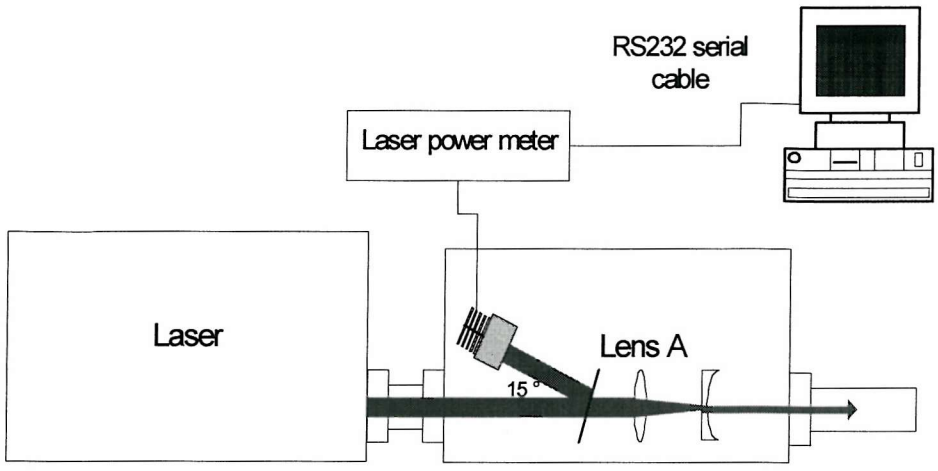

Figure 3.17 Block diagram of the online laser monitor system

3.10 Measurement resolution

In order to interpret the signal calibration correctly the measurement resolution of the LIPP system need to be considered. Broadly speaking, the spatial resolution can be determined at any position within the sample from the length of the leading edge of the pressure pulse [136]. This can be calaculated at the interfaces by measuring the rise time of the current pulse from the electrode/sample interface and multiplying the velocity of the sound for the material being tested. An example of such a measurement for a typical current pulse recorded from a front sample/electrode interface is shown in figure 3.18.

The typical rise time "τ_{rise}" of the current pulse in the newly designed LIPP system with target cooling system and semicon electrode is around 20 ns, hence giving a spatial resolution of $40\mu m$ as the velocity of sound in cross linked polyethylene is about $2000ms^{-1}$ [138]. Moreover, after the deconvolution of the current waveform the resolution can be increased by factor of 3 [137,139], which in this case the spatial resolution increases to about $13\mu m$. However, in the rear sample/electrode interface the measurement resolution will be slightly lower than that of the front sample/electrode interface due to the dispersion of the pressure wave through the sample. Therefore it will ultimately depend on the thickness of the sample. The resolution at any point within the sample can be determined by an interpolation between the spatial resolutions at the front and rear interfaces.

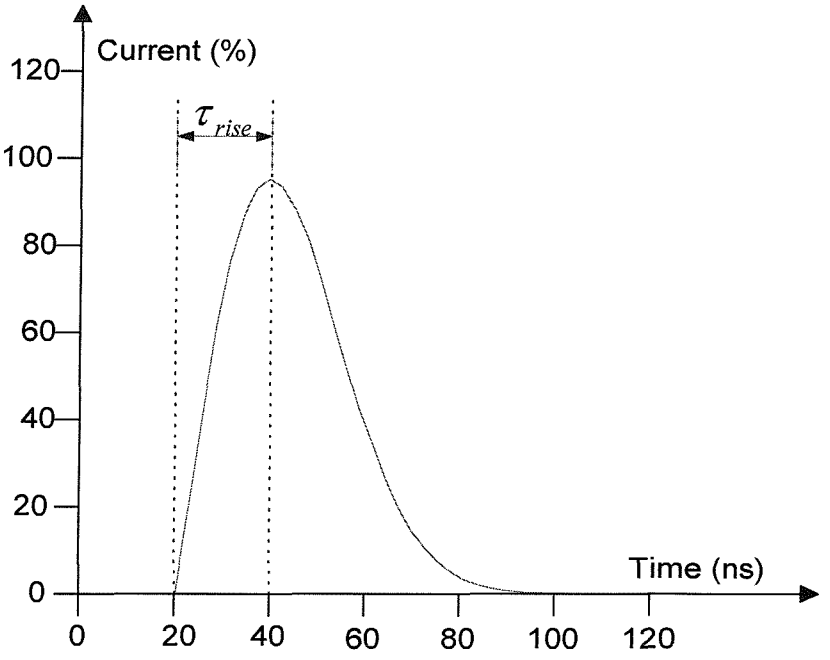

Figure 3.18 Illustrative diagram of the current pulse at the front sample/electrode interface (target) for the resolution calculation

The spatial resolution of the current signal of the LIPP system can also be affected by the bandwidth of the electronic elements and equipment used. In our LIPP system, the wide band amplifier and the 1 *GHz* digital oscilloscope have a bandwith of $400MHz$ and $250MHz$ respectively, therefore the electronic system resolution will be limited by the oscilloscope rather than the amplifier.

Capability of the digital oscilloscope

The "percentage error" of the typical current pulse with a 20 *ns*-rise time can be found by using the equation 3.14,

$$Error\% = \frac{\tau_{rise} - \tau_{measured}}{\tau_{rise}} \times 100\% \quad \text{--------- (3.14)}$$

where τ_{rise} is the signal rise time = 20 *ns*

$\tau_{measured}$ is the measured signal rise time

Also, with reference to [140] the "measured signal rise time" is defined as,

$$\tau_{measured} = \sqrt{\tau_{instrument}^{\ 2} + \tau_{rise}^{\ 2}} \quad \text{---------- (3.15)}$$

where $\tau_{instrument}$ is the "instrument rise time" equal to [140],

$$\tau_{instrument} = \frac{350}{\text{Bandwidth}\,(Hz)} \quad \text{--------- (3.16)}$$

For a 20 *ns* rise time current pulse the percentage error of the measurement signal will be around 0.24 %, which is within 5 % of the acceptable experimental error. In order to ensure the current signal does not suffer excessive quantisation noise during digitisation, the sample rate of the analogue to digital converter within the oscilloscope should also be considered. The oscilloscope used in our system samples at 1 *GHz*, which for accurate digitisation of the signal should be ten times the signal frequency. So that the maximum measurable frequency can be considered to be about 0.1 *GHz*, which is about twice of the highest frequency component of the typical current signal with a 20 *ns* rise time [139].

3.11 Conclusions

The basic principles of the LIPP technique and the existing dc LIPP arrangement are reviewed. The operational principles for ac LIPP system (i.e. point on wave measurement), technical design (i.e. electrical and electronic components) and construction (i.e. mechanical arrangement) of the newly designed LIPP system are given. In addition, as the space charge distribution of cable geometries is of great interest to the manufacturers and the end users, the newly designed LIPP system was modified, which allows space charge measurement in the coaxial cable sample.

In order to provide accuracy and consistency for space charge measurement, the effect of the "shot to shot laser power variation" in the magnitude of the output current signal is considered. To eliminate the measurement errors caused by this factor, an "online laser power monitor system" has been introduced. A correction factor has been taken into account during the stage of signal calibration and subsequent measurements to modify the output current signal before any numerical treatment.

Chapter 4

Data processing method for planar and cable sample

4.1 Introduction

The technique using for space charge measurement in this project was the LIPP method. In the present chapter some preliminary results and the details of the calibration and data processing method for planar sample are reported.

In addition, the relevant theoretical principles of space charge measurement in cable geometries using the LIPP technique is not well defined. Therefore, this chapter addresses this aspect and giving details of the analysis, calibration and data processing method used.

4.2 Quantitative space charge density calculation & calibration for the planar sample

With reference to section 3.2, the short circuit current obtained by the LIPP system using the short circuit measurement arrangement is shown as follow,

$$I(t) = -u_{sa}\chi C_0 G(\varepsilon)\int_{z_f}^{d_0} E(z,t)\frac{d}{dz}p(z,t)dz$$

If the duration of the pressure wave is very short in comparison to its transient time through the dielectric sample, it can be considered as a form of step input and the above equation can be simplified [139]. The instantaneous short circuit current will be dependent on the electric stress and is given by,

$$E(z,t) = \frac{-I(t)}{u_{sa}\chi C_0 G(\varepsilon)p(z,t)} \text{ ---------- (4.1)}$$

Assuming that the test sample is a homogenous dielectric, then the space charge density distribution can be determined by the differentiation of the electric stress (equation 4.1) with respect to the position "z" through the sample. Thus, the electric stress profile $E(z,t)$ and space charge density distribution $\rho(z,t)$ can be found.

$$\rho(z,t) = \varepsilon_0 \varepsilon_r \frac{\partial E(z,t)}{\partial z} \text{--------- (4.2)}$$

However, as there is no quantitative reference about electric stress and charge distribution, a scaling factor is required which can be derived from the calibration. In fact, a numerical solution of equation 3.1 is possible; however it is not stable because the small signal noise and numerical errors can produce large oscillations in the results [141]. Fortunately, there is another approach, which will give qualitative as well as quantitative information of the electric stress and charge distributions without recourse to any complex deconvolution process of equation 3.1.

Let the pressure wave start at the target electrode at "$t = 0\,sec$" and after period of "$t\,sec$" the leading edge of the pressure wave arrives at position $z = z_f(t)$, therefore the equation 3.1 can be rewritten as,

$$I(t) = -u_{sa}\chi C_0 G(\varepsilon) \int_0^{z_f(t)} E(z,t) \frac{d}{dz} p(z,t) dz \text{--------- (4.3)}$$

Assuming that the electric stress on the target electrode during measurement is equal to $E(0,t)$ and the front of the pressure wave $P(z_f,t) = 0$, then the short circuit current $I(t)$ corresponding to the target electrode/sample interface can then be simplified as equation 4.4, details can be referred to [138],

$$I(t) = -u_{sa}\chi C_0 G(\varepsilon) \cdot E(0,t) \int_0^{z_f} p(z,t) dz = -u_{sa}\chi C_0 G(\varepsilon) \cdot E(0,t)\left[p(z_f,t) - p(0,t)\right]$$

$$I(t) = u_{sa}\chi C_0 G(\varepsilon) \cdot E(0,t) \cdot p(0,t) \text{--------- (4.4)}$$

where $E(0,t)$ is the electrical field at the target electrode

With a similar approach, the electric stress on the rear electrode during measurement is equal to $E(d_0,t)$ and the tail of the pressure wave $P(z_t,t)=0$, the short circuit current $I(t)$ corresponding to the rear electrode/sample interface is [139],

$$I(t) = -u_{sa}\chi C_0 G(\varepsilon)\cdot E(0,t)\int_{z_t}^{d_0} p(z,t)dz = -u_{sa}\chi C_0 G(\varepsilon)\cdot E(d_0,t)\left[p(d_0,t)-p(z_t,t)\right]$$

$$I(t) = -u_{sa}\chi C_0 G(\varepsilon)\cdot E(d_0,t)\cdot p(d_0,t) \text{ --------- (4.5)}$$

where $E(d_0,t)$ is the electrical field at the rear electrode

4.2A Space charge signal calibration of plaque sample

It is clear that the space charges can easily be formed in the bulk by the application of an electric stress to the sample for a period of time, which will significantly alter the local electric field in the dielectric [143-144]. Therefore, in order to obtain the calibration data without space charge effect, the sample has to be stressed below a threshold voltage for a short period of time.

This calibration data obtained will only correspond to the surface charges $\rho(0,t)$ and $\rho(d_0,t)$ on both target and rear electrodes created by the applied voltage. Based on electromagnetic theory [145],

$$E_{anode} = \frac{V}{d_0} - \frac{1}{\varepsilon_0\varepsilon_r}\int_0^{d_0}\frac{d_0 - z}{d_0}\rho(z)dz \text{ ---------- (4.6)}$$

$$E_{cathode} = \frac{V}{d_0} - \frac{1}{\varepsilon_0\varepsilon_r}\int_0^{d_0}\frac{z}{d_0}\rho(z)dz \text{ ---------- (4.7)}$$

In the absent of space charge inside the bulk, the surface charge and the electric stress on both the anode and cathode should be the same (i.e. V/d_0) and hence $E(0,t)=E(d_0,t)=E_{cal}$. Assuming that the magnitudes of the pressure wave at the target and rear interfaces are equal to p_0 and p_{d_0}, then the calibration current at both target (equation 4.8) and rear (equation 4.9) electrodes are equal to,

$$I_{cal}(0,t) = u_{sa}\chi C_0 G(\varepsilon)\cdot E_{cal}\cdot p_0 \text{ ---------- (4.8)}$$

$$I_{cal}(d_0,t) = -u_{sa}\chi C_0 G(\varepsilon)\cdot E_{cal}\cdot p_{d_0} \text{ ---------- (4.9)}$$

By partial integration of equation 3.1 and $p(z_f,t)=0$ [114,139], the space charge current signal corresponding to position "z" within the bulk is,

$$I_{space}(t) = u_{sa}\chi C_0 G(\varepsilon)[E(0,0)\cdot p(0,t)] + u_{sa}\chi C_0 G(\varepsilon)\int_0^{z_f} \frac{d(E(z,t))}{dz} p(z,t)dz$$
$$= u_{sa}\chi C_0 G(\varepsilon)[E(0,0)\cdot p(0,t)] + \frac{u_{sa}\chi C_0 G(\varepsilon)}{\varepsilon_0\varepsilon_r}\int_0^{z_f} \rho(z)\cdot p(z,t)dz \text{ ---- (4.10)}$$

Assuming that, the position where the space charge current measurement performed is far away from the interface and the change in space charge density is slow and approximately constant over the region covered by the pressure wave. The current signal that contributes to the first term of equation 4.10 can be assumed zero. In order to perform the calculation, it assumes that the value of the pressure amplitude and dispersion at position "z" are p_z and $u_{sa}\tau$, hence the pressure wave can be expressed in the form of $\int_0^{z_f} p(z,t)dz = p_z\cdot u_{sa}\cdot\tau$, [139], and

$$I_{space}(t) = \frac{u_{sa}\chi C_0 G(\varepsilon)}{\varepsilon_0\varepsilon_r}\cdot\rho(z)\int_0^{z_f} p(z,t)dz$$
$$= \frac{u_{sa}\chi C_0 G(\varepsilon)}{\varepsilon_0\varepsilon_r}\cdot\rho(z)\cdot p_z\cdot u_{sa}\cdot\tau \text{ --------- (4.11)}$$

By equating the constant terms $u_{sa}\chi C_0 G(\varepsilon)$ at the equation 4.8 and 4.11, the space charge density distribution of the LIPP system at position "z" within the bulk is obtained [139,146],

$$\rho(z) = \frac{I_{space}(t)}{I_{cal}(0,t)}\cdot\frac{p_0}{p_z}\cdot\frac{\varepsilon_0\varepsilon_r E_{cal}}{u_{sa}\tau} \text{ --------- (4.12)}$$

where $\rho(z)$ is the charge density at location z,

$I_{space}(t)$ is the current recorded at location z,

$I_{cal}(0,t)$ is calibrated current at the target interface,

p_0 is the amplitude of the pressure wave at the target interface,

p_z is the amplitude of the pressure wave at location z,

ε_0 is the permittivity of free space,

ε_r is the relative permittivity,

E_{cal} is the electric stress for calibration,

u_{sa} is the velocity of acoustic wave in the sample,

τ is the width of the pressure wave at location z.

Referring to equation 4.12, it is noticed that some qualitative information should be gleaned for the determination of the charge density distribution $\rho(z)$,

- Threshold voltage $V_{cal} = E_{cal} \cdot d_0$,
- Calibrated peak current $I_{space}(t)$ at the target interface during the application of the threshold voltage,
- The pressure wave profile (i.e. magnitude and width) at location "z".

4.2B Threshold voltage and calibrated peak current for dc and ac measurements of plaque sample

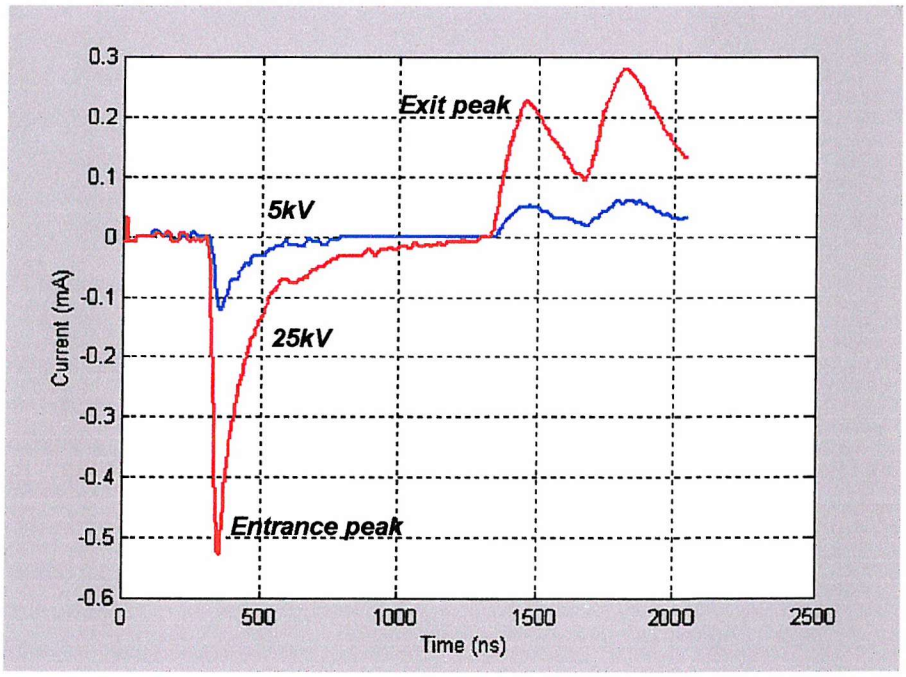

Figure 4.1 Typical plots of the LIPP current signal of the 2 *mm* degassed XLPE Sample at 5 *kV* and 25 *kV*

A low voltage, say "5 *kV*", is normally used for the calibration on 2 *mm* XLPE sample (Figure 4.1), based on the assumption that at this level of electric stress (2.5 *kV/mm*), no charge can be formed inside the bulk. Unfortunately, the "noise" is the main drawback at a low voltage calibration. The signal processing technique using high order wavelet filters can remove the noise, however it also reduces the signal peak amplitude and distorts the shape of the entrance and exit peak of the original signal. Hence, an error for the space charge density calculation could arise as a consequence.

Since space charge can be easily produced at a high electric stress, the calibration at high voltages should not be adopted without the information on the threshold voltage at which the space charge starts to accumulate and form inside the sample.

In order to determine the threshold voltage under dc stressing conditions, a "ramp rate test" is introduced which makes the higher voltage calibration possible. For a dielectric material without trapped charge in the bulk, the magnitudes of the current peaks and hence the interfacial stresses would be linearly dependent on the applied voltage. Once the space charge is formed in the bulk, the magnitudes of the current peaks will deviate from the linear relationship depending on the nature of the charge inside the material.

Referring to equations 4.6 and 4.7, if heterocharge is formed close to the interface, the interfacial stress becomes higher than the applied stress and the magnitude of the current peak will deviate negatively from the straight line. Conversely, if the magnitude of the current peak deviate positively from the extrapolated straight line, then it means that the interfacial stress is less than the applied stress, indicating the formation of homocharge close to the interface.

Figure 4.2 show a typical plot of the peak magnitudes of the output currents of the entrance and exit peaks against the applied dc voltage of a degassed sample. It can be seen that below 23 *kV* the entrance peak magnitude follows a straight line. However, when the applied dc voltage reaches 23 *kV*, the entrance peak against the applied voltage starts to deviate, showing that space charge is present in the bulk. Thus, the threshold voltage and the calibration peak current can be established.

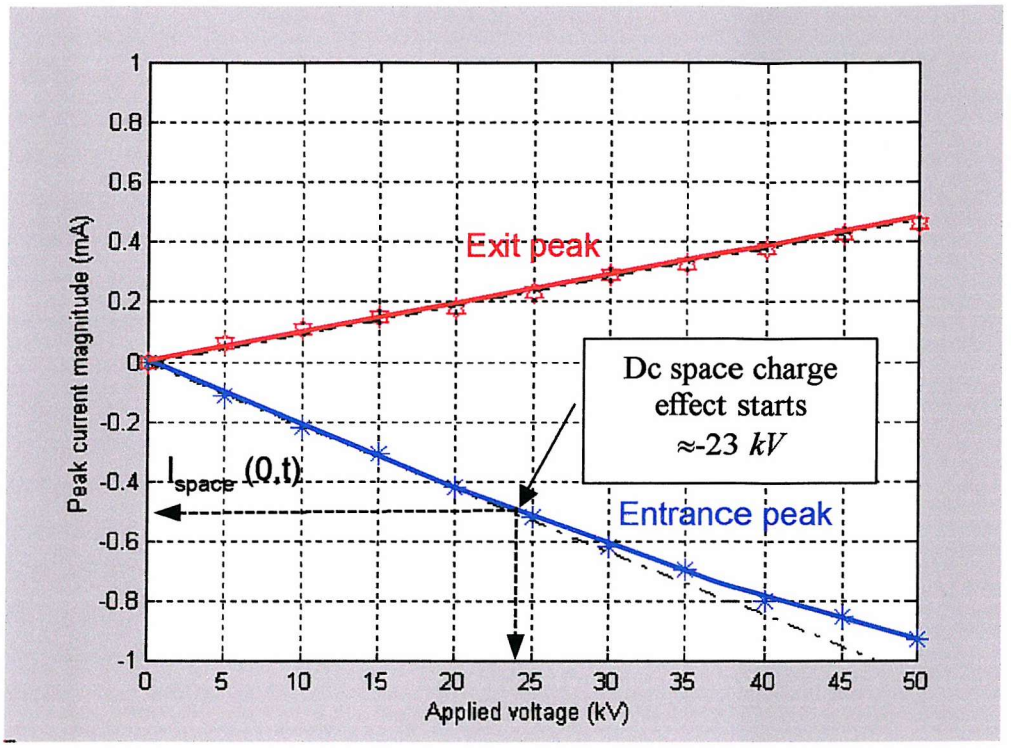

Figure 4.2 Typical plots of the peak magnitudes of short circuit current of the entrance and exit peaks against the HV dc applied voltage of the degassed sample

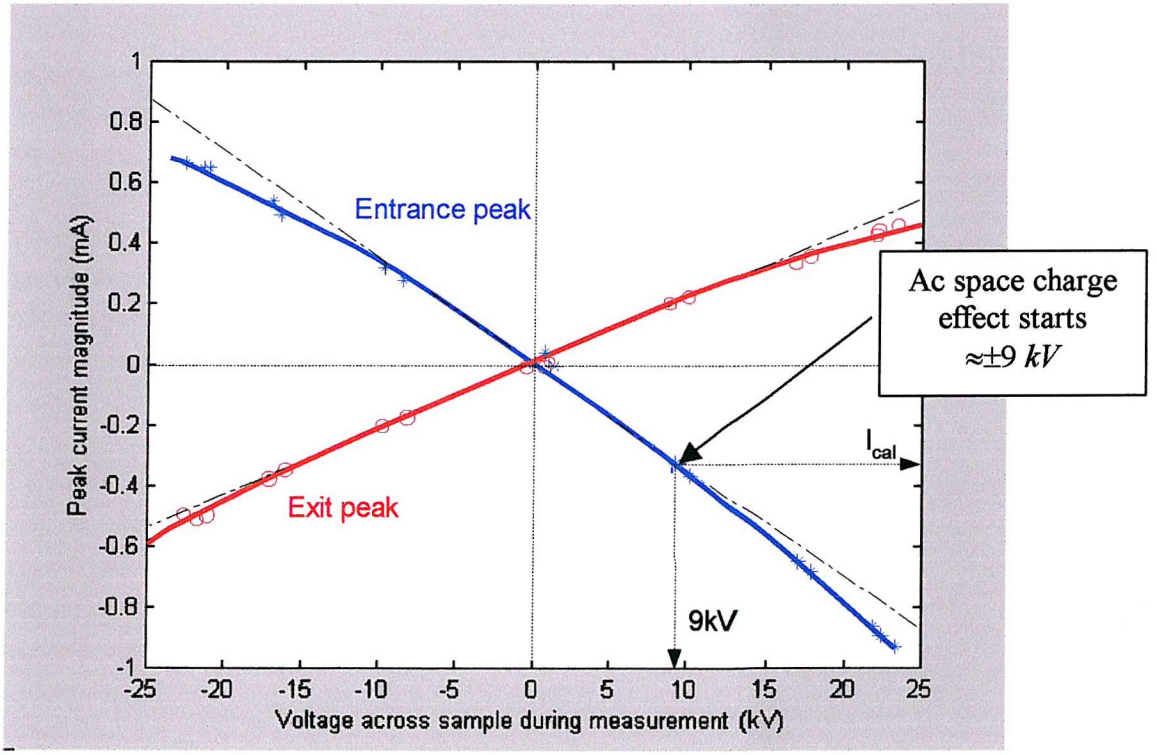

Figure 4.3. Example of the entrance and exit peak magnitudes of short circuit current against the HV ac applied voltage (X-plots)

However, in the ac case, the space charge distributions are measured at a number of different points on the wave for a complete ac cycle (i.e. 17 points on wave), hence no ramp rate test is needed. By using the same approach as the dc ramp rate test (i.e. magnitude of the signal peak against the applied voltage), the threshold voltage (i.e. $V_{cal} = \pm 9\ kV$) of a XLPE plaque with 0.8 *mm* bulk insulation for the calibration can be established as shown in figure 4.3.

Moreover, in order to perform the above calibration technique correctly, a limitation factor like the "measurement resolution" is needed to be considered. Practically, the leading edge of the pressure wave will not be instantaneous but be of a fixed duration (or distance), and the amplitude of the current pulse at the inteface will not simply be due to the stress across the interface but also dependent on the charge close to the electrode.

For example, if there is some positive charge extremely close to the anode, then the charge will produce a positive current close to the interface. If the surface charge on the electrode and the space charge in the bulk occur very close to one another, and the resolution is poor, then the output signal associated with the charges will be superimposed on each other increase the resulantant current pulse. Hence, in this case homocharge leads to an increse in the current signal amplitude. For this reason, before the current waveforms are used for the calibration correction, it should be examined carefully in order to determine what had actually caused the deviation in the current pulse amplitude at the interface.

4.3 Correction factor for the target ablation of plaque sample

Producing a well defined, consistent pressure wave is essential for accurate measurement of space charge. The efficiency of the laser absorption of the semicon surface will degrade after experiencing many laser shots. Consequently, the profile or shape of the pressure wave will change. Therefore, the effect of the target ablation of the semicon on the pressure shape must be taken into account especially for the ac space charge measurement.

For the dc space charge measurement, the semicon target on the test sample will only need to withstand less than 30 laser shots in total, therefore the effect of target ablation to the output current signal is insignificant. However, in the case of ac, the semicon experiences "n" laser shots in each measurement ("n" is equal to number of point on wave measurement

per cycle), therefore within the whole period of an ageing test, it may be subjected to more than 60 laser shots, thus the effect of target ablation to the output current signal becomes significant.

Figure 4.4 shows the variation of the entrance and exit peak magnitude against the number of laser shots for a 2 *mm* as-received sample stressed at 10 *kV* (5 *kV/mm*). It is assumed that no space charge can be formed inside the bulk at this stress and both the current peak heights (i.e. interfacial stress) against the number of laser shot should be constant. However, it is obvious that after ~50 laser shots on the semicon target, the magnitude of the entrance peak decreased significantly with the number of laser shots, indicating that the efficiency of the target material was degraded. In order to ensure that the magnitude variations of current signal or the deviations of the current peak heights against the applied voltages were caused purely by the space charge effect, a correction factor which according to the linear relationship shown in Figure 4.4 has been introduced to modify/normalise the raw current data before any data processing was performed.

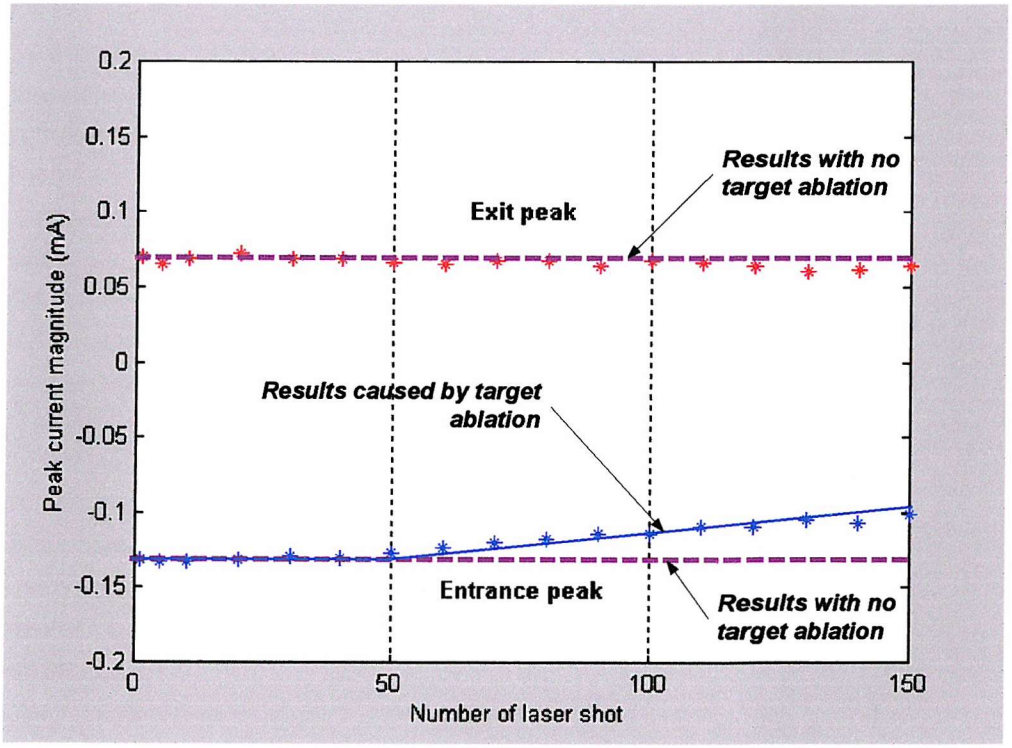

Figure 4.4 Variation of the current peak height against number of laser shot for an as-received sample

As the correction factor for semicon target degradation is dependent on both the semicon material and the sample thickness, it will vary from sample to sample. In order to obtain the

correction factor for an individual sample, a target ablation test needs to be performed on every new sample before any ac ageing experiment commences. After the target ablation test, the sample is then taken out of the sample holder and a new area on the semicon electrode selected before commencement of the ac-ageing test.

4.4 Recovery of the reflection current signal of plaque sample

The semicon electrodes placed on either side of the planar sample are an essential part of the test system, in that they allow the sample to be electrically stressed.

- ***For the target semicon electrode,***

  - The material must have a high absorption coefficient of light at wavelengths emitted by the laser, and acts as a target to absorb the laser radiation and initiate the pressure wave,
  - The thermal conductivity and vaporisation must be low to avoid damage by the high power laser,
  - It must have a good contact (i.e. no air-gap) with the insulating sample to allow the pressure wave to pass from the target electrode into sample efficiently, and
  - The mechanical and acoustic properties between the target semicon electrode and the insulating sample material must be matched. Otherwise, unexpected reflection or loss of energy may arise at the interface.

- ***For the rear semicon electrode,***

The basic material properties are the same as the target semicon electrode. However, after the pressure wave crossed the rear sample/electrode interface, it will traverse the semicon electrode until it reaches the high voltage electrode of the LIPP system (metal). Therefore, as the mechanical and acoustic properties between the semicon material and metal are not matched, the pressure wave will be reflected back through the sample electrode towards the insulating material. This produces a current signal superimposed on the exit peak as shown in figure 4.5.

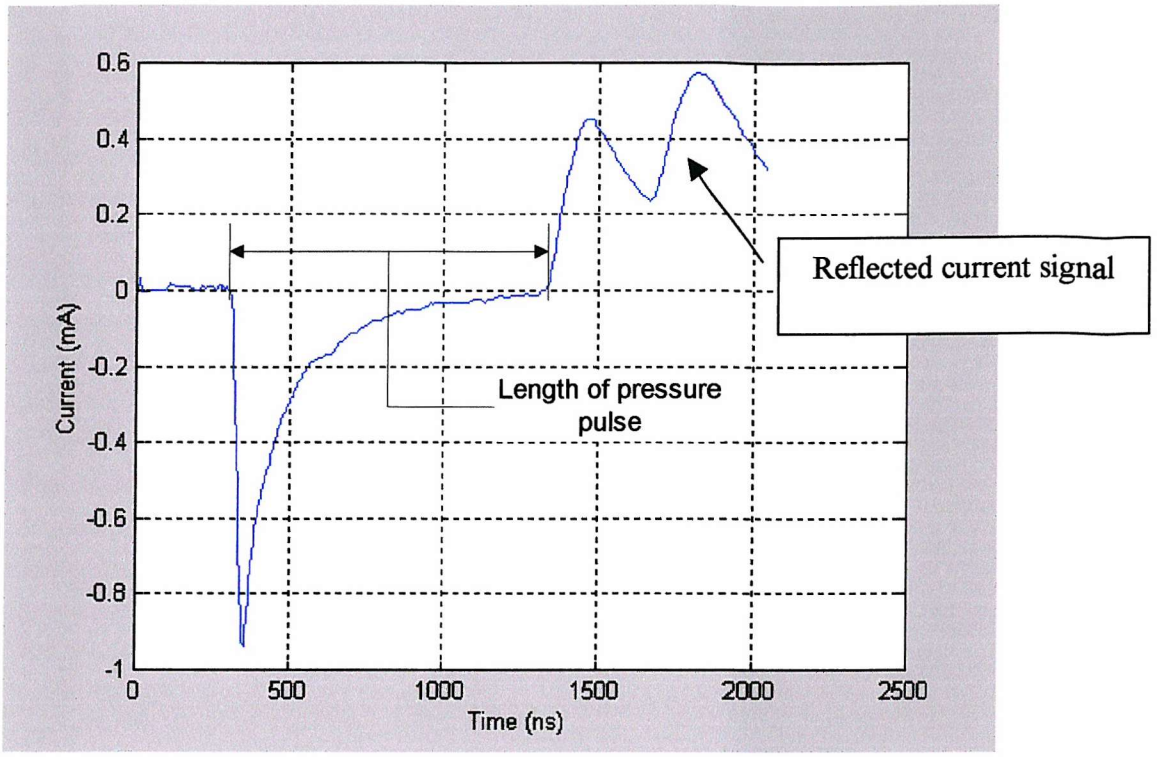

Figure 4.5 Typical LIPP current signal of 2 *mm* degassed sample at 50 *kV* dc

To avoid this reflected wave superimposing or interferring with the exit peak at the rear electrode, the thickness of the rear semicon electrode must be considerablely thick (~0.5 *mm*). However, in some cases, the rear semicon electrode may not be thick enough for the trailing edge of the pressure wave leaving the sample prior to the reflected leading edge re-entering the sample as shown in figure 4.5, hence a data processing for signal recovery is necessary.

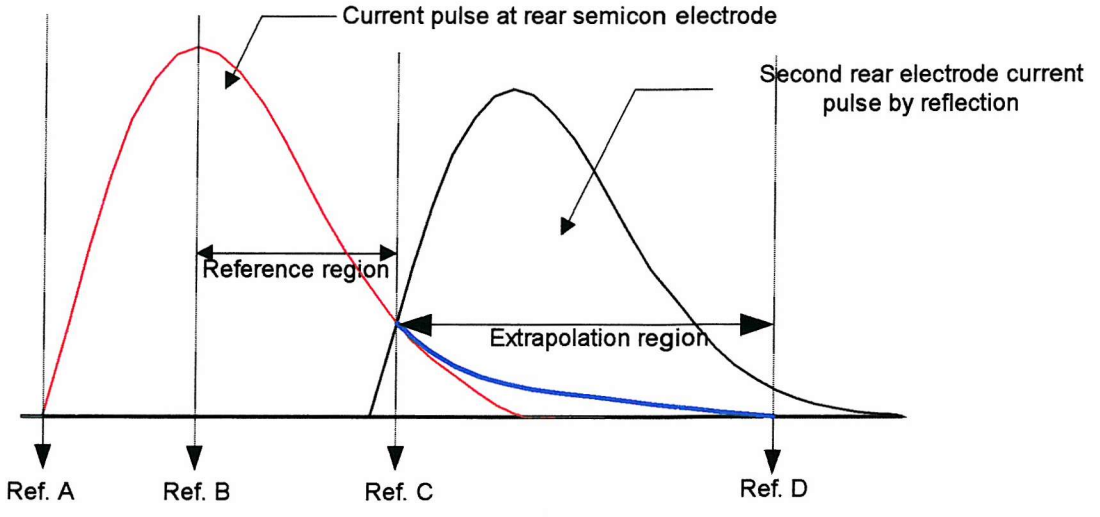

Figure 4.6 Systemic diagram of the recovery of the reflection wave at the rear electrode

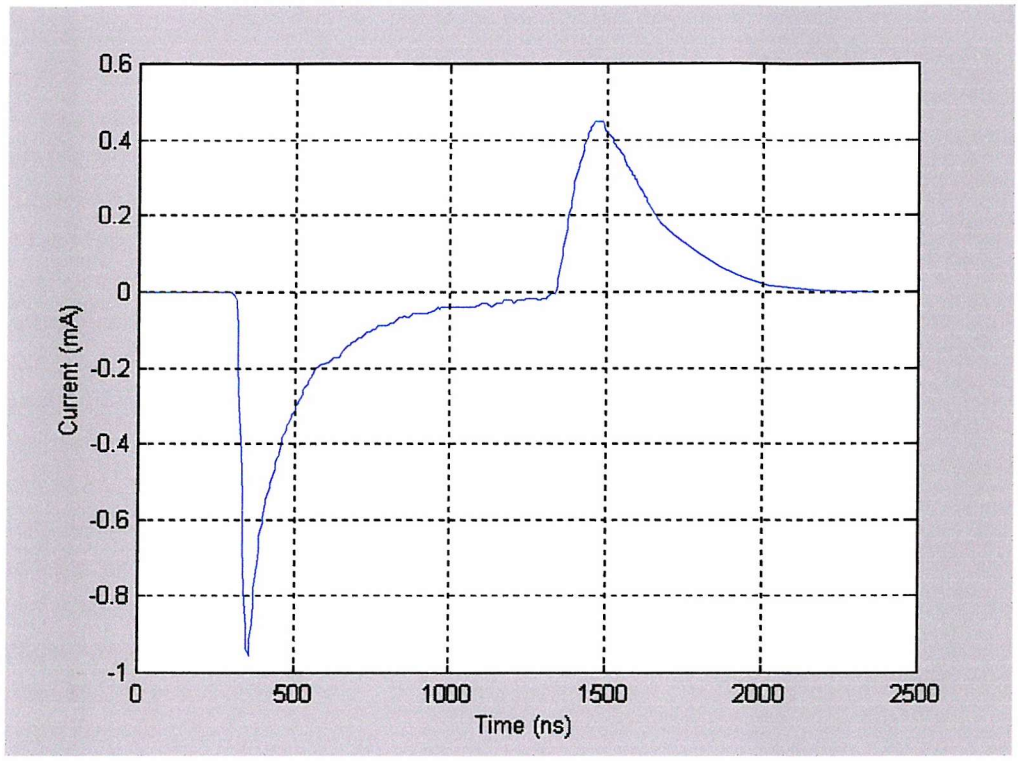

Figure 4.7. Typical LIPP current signal of 2 *mm* degassed sample after rear peak recovery process

The diagram in figure 4.6 illustrates a typical resulatant waveform of the current signal at the rear electode. The first current pulse at the rear electrode (red trace) is interferred by the reflected waves (black trace). In order to recover the trailing edge (blue trace) of the first current pulse at the rear electrode an approximate method that is based on the high order extrapolation technique has been adopted. Assuming that the distance between Ref. A to Ref. D is equal to length of pressure pulse shown in figure 4.5, therefore by extrapolating a line (blue trace) from the cross point at "Ref. C" to the termination point at "ref. D" using a higher order polynomial within the reference region ("Ref. B" to "Ref. C'), the whole waveform of the first current pulse can be mapped and the trailing edge of the first current pulse at the rear electrode recovered as shown in figure 4.7.

4.5 Pressure wave profile calculation of plaque sample

Referring to equation 4.12, apart from the threshold voltage and calibrated peak curent, the pressure wave profile is another factor, which affects the subsequent space charge density

distribution calculation. When the pressure wave $p(z,t)$ travels through the sample, a considerable degradation by the attenuation and dispersion will occur.

Figure 4.8 shows a typical pressure wave profile of the space charge calibration signal at the threshold voltage after the recovery of signals due to reflections. As there is no space charge accumulated inside the bulk, the amount of surface charges as well as electric stresses on both entrance and rear electrodes should be equal. In an ideal case, with no attenuation and dispersion during acoustic propagation, the shape of the pressure wave at both electrode/sample interfaces should be the same. However, it is obvious that the amplitude and the width of the rear (second) peak are significantly lower and broader than the entrance (first) peak, indicating that attenuation and dispersion of the pressure wave have occurred.

According to the basic principle of the LIPP technique for the planar geometry sample, the pressure wave created by the laser pulse can be expressed in terms of the frequency components [147],

$$p(z,t) = \frac{1}{2\pi} \int_{w_1}^{w_2} F(P)(z,\upsilon) \cdot \exp[i2\pi\upsilon t] dw \quad \text{---------- (4.13)}$$

where $F(P)(z,\upsilon) = \int_{w_1}^{w_2} p(z,t) \cdot \exp[-i2\pi\upsilon t] dt$ -------- (4.14), and

$F(P)(z,\upsilon)$ is the Fourier component of the pressure wave at the angular frequency υ and at abscissa z.

Assuming that all the frequency components of the pressure wave propagate at the velocity of sound $u_{sa}(\upsilon)$ with attenuation $\alpha(\upsilon)$ and dispersion $\frac{2\pi\upsilon}{u_{sa}(\upsilon)}$, the pressure wave at position "z" in term of the entrance pressure pulse and degradation factor is,

$$F(P)(z,\upsilon) = F(P)(0,\upsilon)\, e^{-\alpha(\upsilon)z} \cdot e^{-i2\pi\upsilon \frac{z}{u_{sa}(\upsilon)}} \quad \text{----------(4.15)}$$

where $e^{-\alpha(\upsilon)z}$ is the attenuation term,

$e^{-i2\pi\upsilon-\frac{z}{u_{sa}(\upsilon)}}$ is the dispersion term,

Given that $k(\upsilon)=\dfrac{2\pi\upsilon}{u_{sa}(\upsilon)}-i\alpha(\upsilon)$ and $A(\upsilon)=e^{-i\cdot k(\upsilon)}$,

$$F(P)(z,\upsilon)=F(P)(0,\upsilon)\cdot[A(\upsilon)]^{z} \text{ --------(4.16)}$$

By using the entrance and exit pressure wave at "$z=0$ and $z=d_0$", the degradation factor $A(\upsilon)$ can be obtained,

$$A(\upsilon)=\left(\frac{FFT[p(d_0,t)]}{FFT[p(0,t)]}\right)^{\frac{1}{d_0}}=\left(\frac{F(P)(d_0,\upsilon)}{F(P)(0,\upsilon)}\right)^{\frac{1}{d_0}} \text{ --------(4.17)}$$

The pressure wave profile at any position z within the bulk can be calculated using the inverse Fourier transform based on equation 4.18 and the results are shown in figure 4.8.

$$p(z,t)=FFT^{-1}\left[F(P)(0,\upsilon)\cdot[A(\upsilon)]^{z}\right] \text{ ----------(4.18)}$$

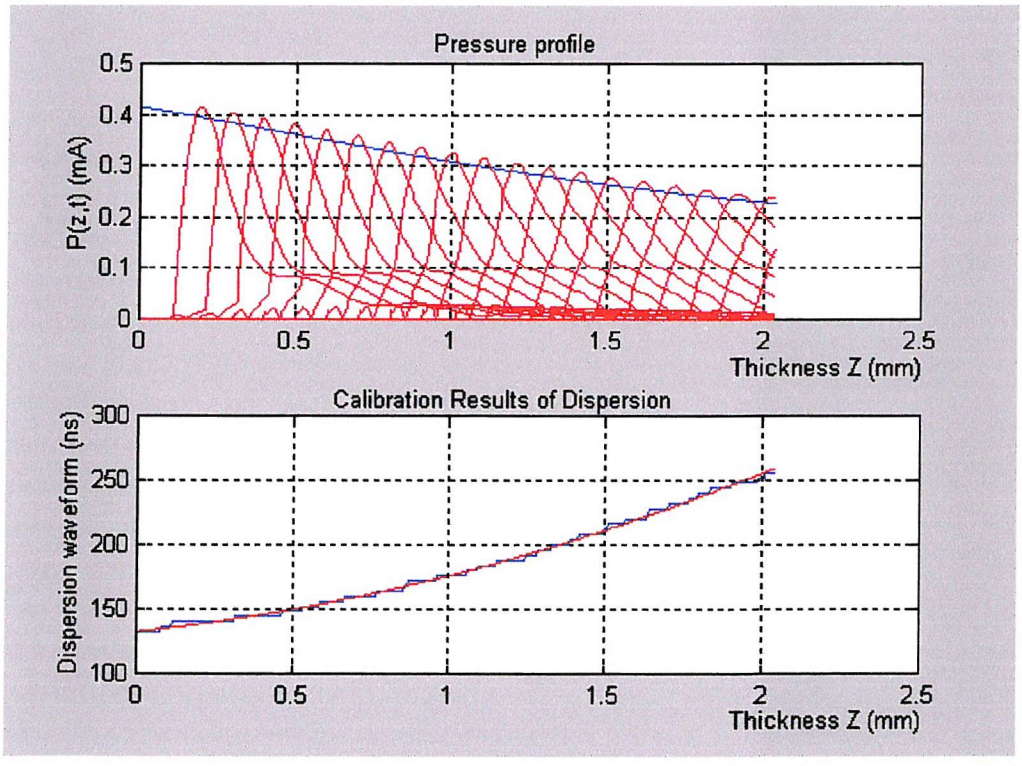

Figure 4.8 Example of the calculated attenuation & dispersion curve of a 2mm XLPE sample (20 *kV*)

4.6 Calculation of the electric stress distribution of plaque sample

As shown in figure 4.9, the semicon target limits the measurement resolution, therefore the pressure wave is no longer an impulse and its width will cause the magnitude of the charge density near the front and rear electrodes ($0 \sim z_f$) and ($z_r \sim d_0$) to be inaccurate. However, over the region ($z_f \sim z_r$) the current profile can be considered a good representation of the charge density distribution [141].

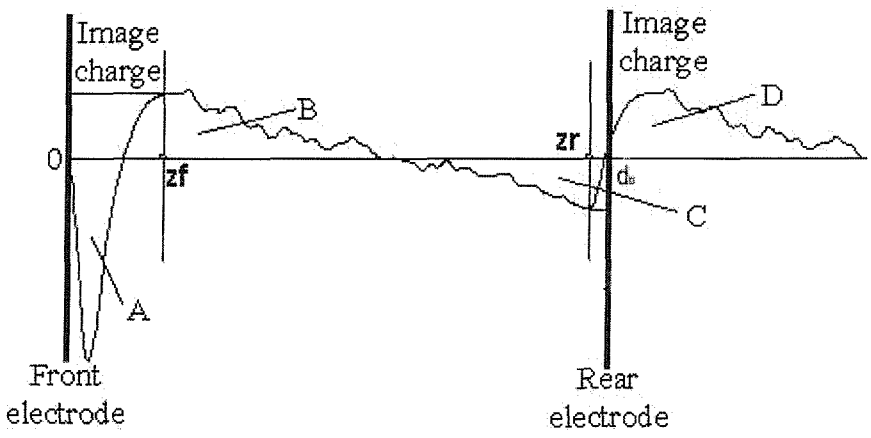

Figure 4.9 Charge density profile (with volts off) [141]

Assuming that the pressure waves during the entrance and exit of the sample are in the form of a step function, the electric stress E_{int} at the interface between the electrode and sample is given by,

$$E_{int} = \frac{I_{int}}{I_0'} E_0 \text{ --------- (4.19)}$$

where I_{int} is the peak current at interface,

I_0' is the calibrated peak current at either the input or output interface,

E_0 is the applied electric stress for the calibration.

In an ideal case, if the pressure wave is an impulse, the electric stress profile inside the bulk $(0 \rightarrow d_0)$ can be obtained theoretically by integrating the charge density,

$$E(z) = \int_0^z \frac{\rho(z)}{\varepsilon_0 \varepsilon_r} dz + C \quad , \quad 0 < z < d_0 \text{ --------- (4.20)}$$

The constant C can be determined from the "equal energy" principle,

$$\int_0^{d_0} E(z)dz = E_0 \cdot d_0 = V \text{ --------- (4.21)}$$

$$V = \int_0^{d_0}\left(\frac{1}{\varepsilon_0 \cdot \varepsilon_r}\cdot\int_0^{z}\rho(z)\cdot dz + C\right)dz$$

$$V = \frac{1}{\varepsilon_0 \cdot \varepsilon_r}\cdot\int_0^{d_0}\left(\int_0^{z}\rho(z)\cdot dz\right)\cdot dz + \int_0^{d_0} C\cdot dz$$

$$V = \frac{1}{\varepsilon_0 \cdot \varepsilon_r}\cdot\int_0^{d_0}\left(\int_0^{z}\rho(z)\cdot dz\right)\cdot dz + C\cdot d_0 \text{ --------- (4.21)}$$

Hence, the constant value of C can be obtained as:

$$C = \frac{V - \frac{1}{\varepsilon_0 \cdot \varepsilon_r}\int_0^{d_0}\left(\int_0^{z}\rho(z)\cdot dz\right)\cdot dz}{d_0} \text{ --------- (4.22)}$$

where d_0 is the thickness of the sample.

The electric field profile inside the bulk $(0 \rightarrow d_0)$is given,

$$E(z) = \frac{1}{\varepsilon_0 \cdot \varepsilon_r}\cdot\int_0^{z}\rho(z)\cdot dz + \frac{V - \frac{1}{\varepsilon_0 \cdot \varepsilon_r}\cdot\int_0^{d_0}\left(\int_0^{z}\rho(z)\cdot dz\right)\cdot dz}{d_0} \text{ --------- (4.23)}$$

Reiterating the point that the semi-conducting target limits the measurement resolution and the pressure wave is no longer an impulse equation 4.23 cannot be applied directly. The interfacial stress of the front and rear electrodes can be calculated using equation 4.19. Equation 4.24 is then used to obtain the preliminary shape of the electric profile within the region $(z_f \rightarrow z_r)$,

$$E(z) = \int_{z_f}^{z}\frac{\rho(z)}{\varepsilon_0\varepsilon_r}dz + C \quad , \quad z_f < z < z_r \text{ --------- (4.24)}$$

Either end of the 'electric stress profile' is joined to the interfacial stress at the front and rear electrode by a higher order polynomial extrapolation. Finally, the "equal energy" principle is employed to check the area under the applied electric stress E_0 and the area under the modified electric stress $E(z)$ due to the presence of space charge in the bulk of the sample, hence the areas of both are equal and the final electric profile $(0 \rightarrow d_0)$ obtained.

4.7 Electric field distribution in cable sample

The schematic diagram of the space charge measurement system for the coaxial cable using the LIPP method is shown in figure 4.10. Referring to equation 3.1, the current signal obtained by the LIPP technique is equal to the integration of the convolution of the electric profile and the change of the pressure wave.

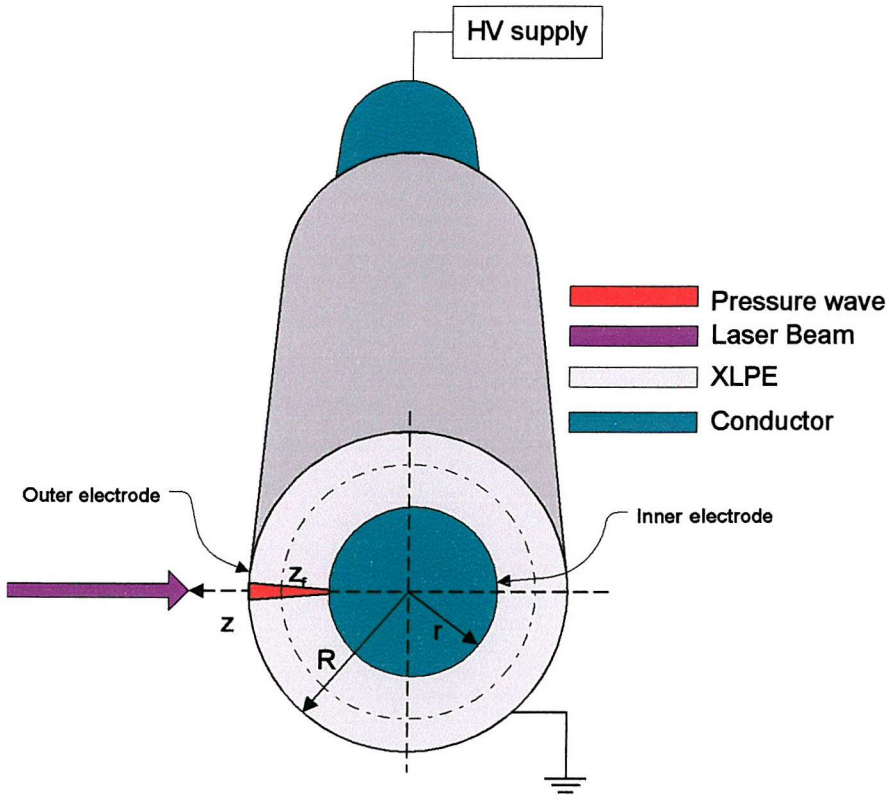

Cross-section of pressure wave propagating in a radial manner through the cable geometry

Figure 4.10. Schematic diagram of the LIPP measurement system for coaxial cable

$$I(t) = A\int_R^{z_f} E(z)\cdot\frac{d}{dz}p(z,t)dz \text{ ---------- (4.25)}$$

where $A = -u_{sa}\chi C_0 G(\varepsilon)$ and z_f is the radius reached by the wave front at time t (i.e. $z_f = R - u_{sa}t$)

Similar to the planar sample, the electric stress distribution $E(z)$ in the cable sample contains two components as shown in equation 4.26. However, in the case of the cable geometry the term $E_0(z)$ is position dependent [148].

$$E(z) = E_0(z) + E_{space}(z) \text{ --------- (4.26)}$$

where $E_0(z)$ and $E_{space}(z)$ are the electric stresses due to the applied voltage and space charge respectively.

4.7A Calculation of E_0

In the absence of space charge, the electric stress distribution within the cable [133] should only the related to the applied voltage V_0 and the position "z", the $E_{space}(z)$ contributed by the space charge should be equal to zero,

$$\therefore E(z) = E_0(z) = \frac{1}{z} \cdot \frac{V_0}{\ln\left(R/r\right)} \text{ ---------- (4.26)}$$

4.7B Calculation of E_{space}

However, if there is space charge formed or accumulated inside the bulk, the electric stress profile at different positions "z" within the cable sample will be distorted, resulting in local electric stress enhancement or reduction by a value of $E_{space}(z)$, which can relate to the charge density $\rho(z)$ at "z" abscissa.

According to the Poisson's equation and for a cylindrical geometry, the electric potential in the presence of space charge can be expressed as [149],

$$\frac{\partial^2 U}{\partial z^2} + \frac{1}{z}\frac{\partial U}{\partial z} + \frac{1}{z^2}\frac{\partial^2 U}{\partial \phi^2} + \frac{\partial^2 U}{\partial r^2} = -\frac{\rho(z,\phi,r)}{\varepsilon_0 \varepsilon_r} \text{ ---------- (4.27)}$$

where $\rho(z,\phi,r)$ represents charge density at any point,

ε_0 is the permittivity of free space,

ε_r is the relative permittivity of the material.

To simplify the above equation, it is assumed that the material is homogeneous; therefore the charge density $\rho(z)$ can be regarded as one dimension and only dependent on the "z" abscissa. Thus, Poisson 's equation 4.27 is reduced to [149],

$$\frac{\partial^2 U}{\partial z^2}+\frac{1}{z}\frac{\partial U}{\partial z}=-\frac{\rho(z)}{\varepsilon_0\varepsilon_r} \quad \text{---------- (4.28)}$$

By substituting $\frac{\partial U}{\partial z}=-E$ into equation 4.28, then

$$\frac{\partial E}{\partial z}+\frac{1}{z}E=\frac{\rho(z)}{\varepsilon_0\varepsilon_r} \quad \text{---------- (4.29)}$$

The equation 4.29 is a typical linear equation and its general equation can be found [150],

$$E(z_f)=\frac{1}{z_f\varepsilon_0\varepsilon_r}\int_R^{z_f} z\rho(z)dz+\frac{1}{z_f}C=E_{applied}+E_{space} \quad \text{---------- (4.30)}$$

where $C=$ constant, $z_f=R-u_{sa}t$, and $r<z_f<R$

Thus, $E_{space}(z_f)=\frac{1}{z_f}\left[\frac{1}{\varepsilon_0\varepsilon_r}\int_R^{z_f} z\rho(z)dz-\frac{V_0}{\ln\left(R/r\right)}+C\right]$

4.8 Geometric effect on the pressure wave in cable sample

Referring to equation 4.13 and 4.14, the pressure wave can be expressed as,

$$p(z,t)=\frac{1}{2\pi}\int_{w_1}^{w_2} F(P)(z,\upsilon)\cdot\exp[i2\pi\upsilon t]dw \quad \text{---------- (4.13)}$$

where $F(P)(z,\upsilon) = \int_{w_1}^{w_2} p(z,t)\cdot\exp[-i2\pi\upsilon t]dt$ -------- (4.14), and

$F(P)(z,\upsilon)$ is the Fourier component of the pressure wave at the angular frequency ω and at abscissa "z".

However, due to the cylindrical structure of the cable sample, the propagation of the pressure wave within the cable is different from that of the planar sample. The pressure wave will propagate radially inwards from the outer electrode, radius "R", towards the inner electrode, radius "r", at a velocity of u_{sa} (red trace, velocity u_{sa} for XLPE = 2000 ms^{-1}) and the Fourier transform of the pressure wave must satisfy the propagation equation 4.31 for the coaxial geometry [151, 152],

$$\partial F(P) + \frac{(2\pi\upsilon)^2}{u_{sa}^{\ 2}} F(P) = 0 \qquad \text{--------- (4.31)}$$

$$\text{i.e. } \frac{\partial^2 F(P)}{\partial z^2} + \frac{1}{z}\frac{\partial F(P)}{\partial z} + \frac{(2\pi\upsilon)^2}{u_{sa}^{\ 2}} F(P) = 0$$

Since $\frac{2\pi\upsilon}{u_{sa}} >> \frac{1}{z}$ [1], then the solution of the Fourier transform of the pressure wave at the frequency "υ" that propagates through the insulator for the coaxial geometry is given by [148, 151-153],

$$F(P)(z,\upsilon) = \sqrt{\frac{R}{z}}\cdot F(P)(R,\upsilon)\exp[-\alpha(\upsilon)\cdot(R-z)]\exp\left[-i\frac{2\pi\upsilon}{u_{sa}}(R-z)\right] \text{---------- (4.32)}$$

where u_{sa} Velocity of sound in the sample and opposite direction to z abscissa, the velocity frequency dependence,

$F(P)(z,\upsilon)$ Fourier transform of the pressure wave at the angular frequency υ and at z abscissa,

---

[1] Since $\upsilon \in [500kHz;100MHz]$; $u_{sa} = 2000ms^{-1}$; $z \in [5mm;50mm]$; so $\left(\frac{(2\pi\upsilon)}{u_{sa}} > 1500m^{-1}\right) >> \left(\frac{1}{z} < 200m^{-1}\right)$

$\sqrt{R/z}$ Geometric factor that indicates the strength of the acoustic wave varies with the square root of abscissa z.

4.9 Quantitative space charge density calculation and calibration of cable sample

In order to calculate the electric stress distribution within the cable bulk insulation, the charge density profile in equation 4.30 must be obtained. According to the basic principle of the LIPP technique, the short circuit current $I(t)$ obtained from the cable LIPP system shown in Figure 4.12 can be expressed as,

$$I(t) = A\int_R^{z_f} E(z)\cdot\frac{dp(z,t)}{dt}dz \qquad \text{where } z_f = R - u_{sa}t \text{ and } A = \chi C_0 G(\varepsilon)$$

$$= -Au_{sa}\int_R^{z_f} E(z)\cdot\frac{dp(z,t)}{dz}dz \qquad \text{where } \frac{dp(z,t)}{dt} = -u_{sa}\cdot\frac{dp(z,t)}{dz}$$

$$= B\int_R^{z_f} E(z)\cdot\frac{dp(z,t)}{dz}dz \text{ ---------- (4.33)} \qquad \text{where } B = -A\cdot u_{sa}$$

Applying partial integration to equation 4.33, then the current at any position "z" is equal to,

$$I(t) = B\left[E(z)\cdot p(z,t)\right]_R^{z_f} - B\int_R^{z_f}\frac{d(E(z,t))}{dz}\cdot p(z,t)dz$$

$$I(t) = B\left[E(z_f)\cdot p(z_f,t) - E(R)\cdot p(R,t)\right] - B\int_R^{z_f}\frac{d(E(z,t))}{dz}\cdot p(z,t)dz \text{ ---- (4.34)}$$

By using the argument that $p(z_f,t) = 0$ [139], then the space charge current signal can be rewritten as,

$$I(t) = B\left[-E(R)\cdot p(R,t)\right] - B\int_R^{z_f}\frac{d(E(z,t))}{dz}\cdot p(z,t)dz \text{ ---------- (4.35)}$$

Assuming that the change in space charge density at the position where the space charge measurement is performed is slow and the measurement position is far enough from the outer cable interface (R), the width of the pressure pulse does not cover the measurement

position and the electrode interface at the same time. Hence, the contributed to the current signal by the first term of equation 4.35 can be assumed zero.

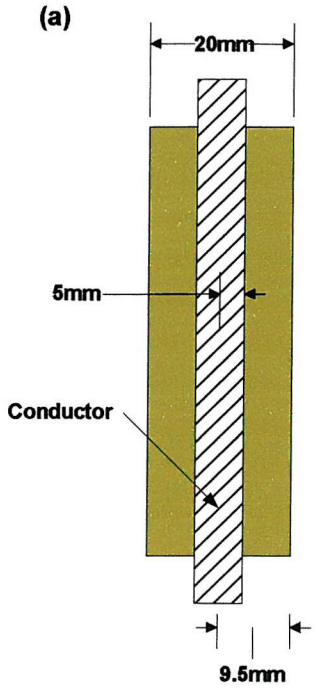

Figure 4.11 Cross section of cable sample with dimensions

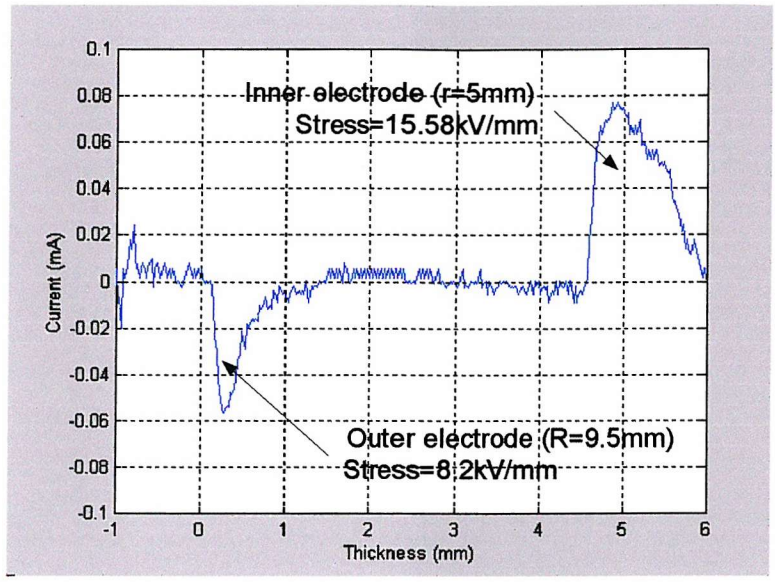

Figure 4.12 The output current signal obtained from a XLPE cable with 4.5 *mm* bulk insulation at 50 *kV* dc

In order to perform the calculation, it assumes that the value of the pressure amplitude and dispersion at position "*z*" are p_z and $u_{sa}\tau$. However, as the direction of pressure wave is opposite to the *z* abscissa the pressure wave at position "*z*" can be express in the form of $\int_R^{z_f} p(z,t)dz = -p_z \cdot u_{sa} \cdot \tau$. The current signal at any position "*z*" within the cable bulk insulation is,

$$I(t) = -B \cdot \rho(z,t) \int_R^{z_f} p(z,t)dz \qquad \text{where } z_f = R - u_{sa}t \text{ and } z_f \le z < R$$
$$= B \cdot \rho(z,t) \cdot p_z \cdot u_{sa} \cdot \tau \text{ --------- (4.36)}$$

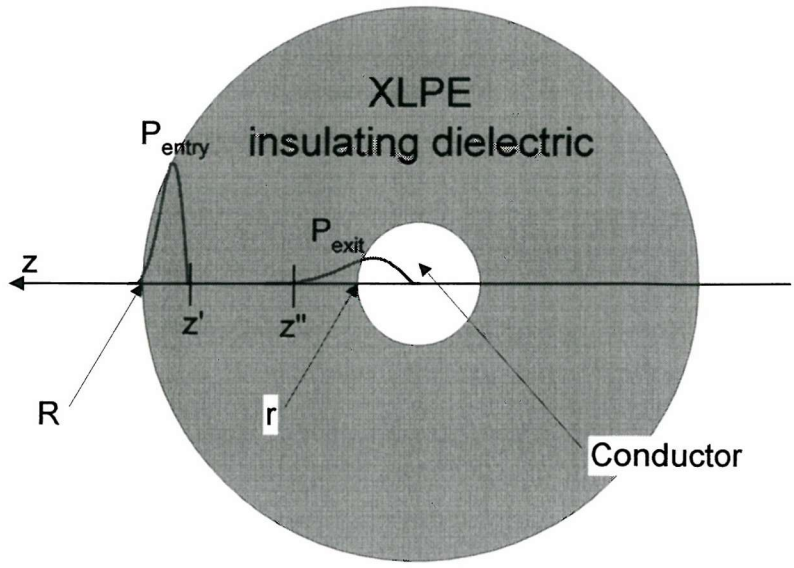

Figure 4.13 Example of the pressure pulse at the electrodes of the cable sample

Similar to the approaches used for the planar sample, the entrance and exit peaks of the output current signal below the threshold voltage will be used for signal calibration. The electric stresses at the outer (R) and inner electrode (r) are equal to $E_{cal}(R)$ and $E_{cal}(r)$. According to equation 4.35 and the figure 4.13, the current signals of the entry and exit peaks are equal to,

At the entry, $$I_{cal}(R,t) = -B \cdot E_{cal}(R) \int_{R}^{z'} \frac{dp(R,t)}{dz} dz \text{ ------- (4.37)}$$

At the exit, $$I_{cal}(r,t) = B \cdot E_{cal}(r) \int_{z''}^{r} \frac{dp(r,t)}{dz} \cdot dz \text{ -------- (4.38)}$$

In addition, assuming that the pressure wave magnitude at the enter and exit interfaces are equal to $P(R,t) = p_R$ and $p(r,t) = p_r$, hence the calibration currents at both target and rear electrodes are established,

At the entry, $$I_{cal}(R,t) = -B \cdot E_{cal}(R) \cdot [p(z',t) - p(R,t)]$$
$$= B \cdot E_{cal}(R) \cdot p_R \text{ ------- (4.39)}$$

At the exit, $$I_{cal}(r,t) = -B \cdot E_{cal}(r) \cdot [p(r,t) - p(z'',t)]$$
$$= -B \cdot E_{cal}(r) \cdot p_r \text{ -------- (4.40)}$$

where $E_{cal}(R) = \frac{V}{R\ln(R/r)}$ and $E_{cal}(r) = \frac{V}{r\ln(R/r)}$

By equating the constant terms "B in the equations 4.36 and 4.39, the space charge density distribution of the LIPP system at any position "z" within the cable bulk insulation is obtained,

$$\rho(z,t) = \frac{I(t)}{I_{cal}(R,t)} \cdot \frac{p_R}{p_z} \cdot \frac{\varepsilon_0 \varepsilon_r E_{cal}(R)}{u_{sa}\tau} \text{ --------- (4.41)}$$

4.10 Calculation of the pressure wave profile of cable sample

According to 4.41, the general equation for the space charge profile calculation in the cable sample is the same as the planar sample. The cable geometric effect is only reflected in the terms, corresponding to the pressure wave profile (i.e. p_R and τ).

When the pressure wave $p(z,t)$ travels through the cable sample, the acoustic properties of the dielectric material cause the pressure wave to be attenuated and dispersed. This effect on the pressure wave can be represented by a factor of $k(\upsilon)$.

By substituting $k(\upsilon) = \frac{\omega}{u_{sa}(\upsilon)} - i\alpha(\upsilon)$ into the equation 4.32, the following is obtained,

$$F(P)(z,\upsilon) = \sqrt{\frac{R}{z}} \cdot F(P)(R,\upsilon)\exp[-ik(\upsilon)\cdot(R-z)] \text{ --------(4.42)}$$

Given that $A(\upsilon) = \exp[-ik(\upsilon)]$, then

$$F(P)(z,\upsilon) = \sqrt{\frac{R}{z}} \cdot F(P)(R,\upsilon)\cdot[A(\upsilon)]^{R-z} \text{ --------- (4.43)}$$

Applying $z = r$, then

$$A(\upsilon) = \left[\sqrt{\frac{r}{R}}\frac{F(P)(r,\upsilon)}{F(P)(R,\upsilon)}\right]^{\frac{1}{R-r}} \text{ ---------- (4.44)}$$

The pressure wave profile at any abscissa z within the cable can be calculated using the inverse Fourier transform equation 4.45. An example of the pressure profile corresponding to the typical current signal obtained from a 4.5 *mm* XLPE cable at 50 *kV* dc is shown in figure 4.14.

$$p(z,t) = FFT^{-1}\left[\sqrt{\frac{R}{z}} \cdot F(P)(R,\upsilon) \cdot \left[\sqrt{\frac{r}{R}}\frac{F(P)(r,\upsilon)}{F(P)(R,\upsilon)}\right]^{\frac{R-z}{R-r}}\right] \text{----------(4.45)}$$

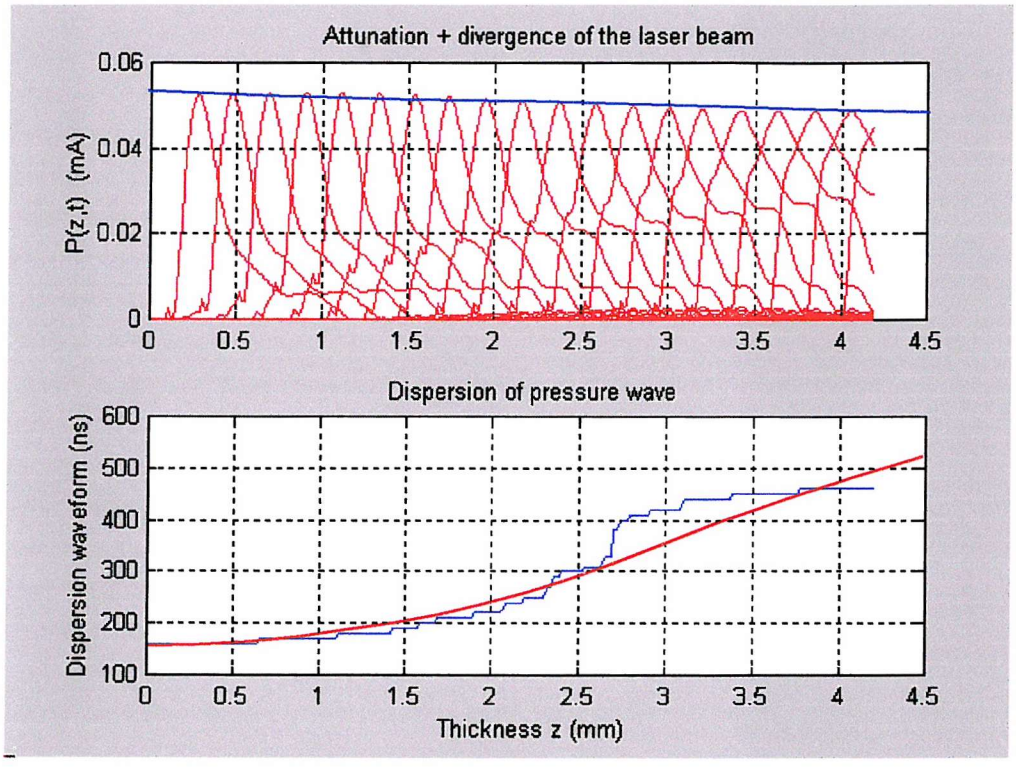

Figure 4.14 Typical profile of the pressure wave propagating a 4.5 *mm* XLPE cable sample

The trace of the dispersed waveform is similar to that for the planar sample. However, the resultant reduction (i.e. attenuation + laser beam divergence) of the pressure wave magnitude for the cable sample (<10 % in 4.5 *mm*) is smaller compared to the planar sample (40 % in 2 *mm* shown in Figure 4.9). This is because the dependence of the geometric term "$\sqrt{\frac{R}{z}}$" corresponding to the laser beam divergence in equation 4.32 is partially compensating the attenuation of the pressure wave [148].

4.11 Calculation of electric stress distribution of cable sample

Similar to the planar sample, it is assumed that the pressure wave at the entrance of the electrode/sample interface is in the form of a step function. Therefore, the electric stress E_{int} at the interface between the electrode and cable insulation can be given by,

$$E_{\text{int}} = \frac{I_m}{I_{cal}} \cdot E_{cal}(z,t) \text{--------} (4.46)$$

where

I_m is the peak current magnitude of the measured signal at the outer (R) or inner (r) interface,

I_{cal} is the calibrated peak current magnitude at the outer (R) or inner (r) interface

E_{int} is the electric stress at the outer (R) or inner (r) interface.

$E_{cal}(z = R \text{ or } r) = \frac{V}{z \ln(R/r)}$ is the electric stress at the interface between the outer (R) or inner (r) electrodes of cable during calibration.

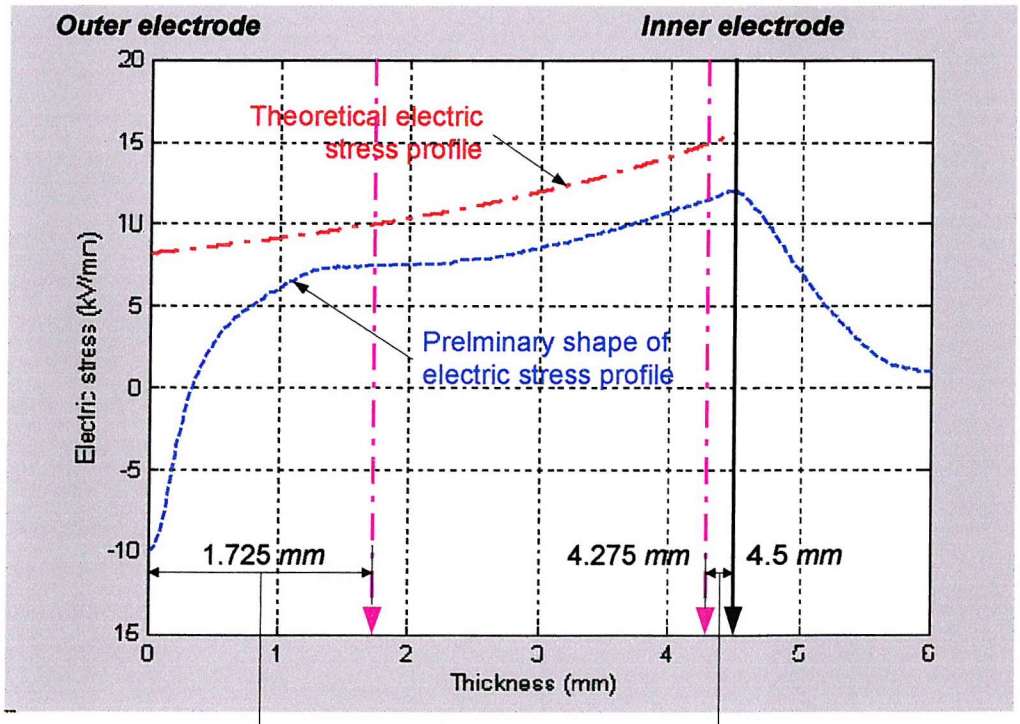

Figure 4.15 Preliminary shape of electric stress profile of the cable sample (50kV dc)

After the interfacial stress at the outer and inner electrodes is calculated using equation 4.46, then equation 4.30 will be used to obtain the preliminary shape of the electric stress profile within the cable bulk insulation as shown in figure 4.15 (Blue dotted line). Finally, either end of the 'preliminary electric stress profile is mapped to the interfacial stress at the outer and inner electrode by a higher order polynomial extrapolation (i.e. 5^{th} order). The "equal energy" principle is employed to check that the area under the applied electric stress E_0 and that under the modified electric stress $E(z)$ due to the presence of space charge in the bulk are equal [141].

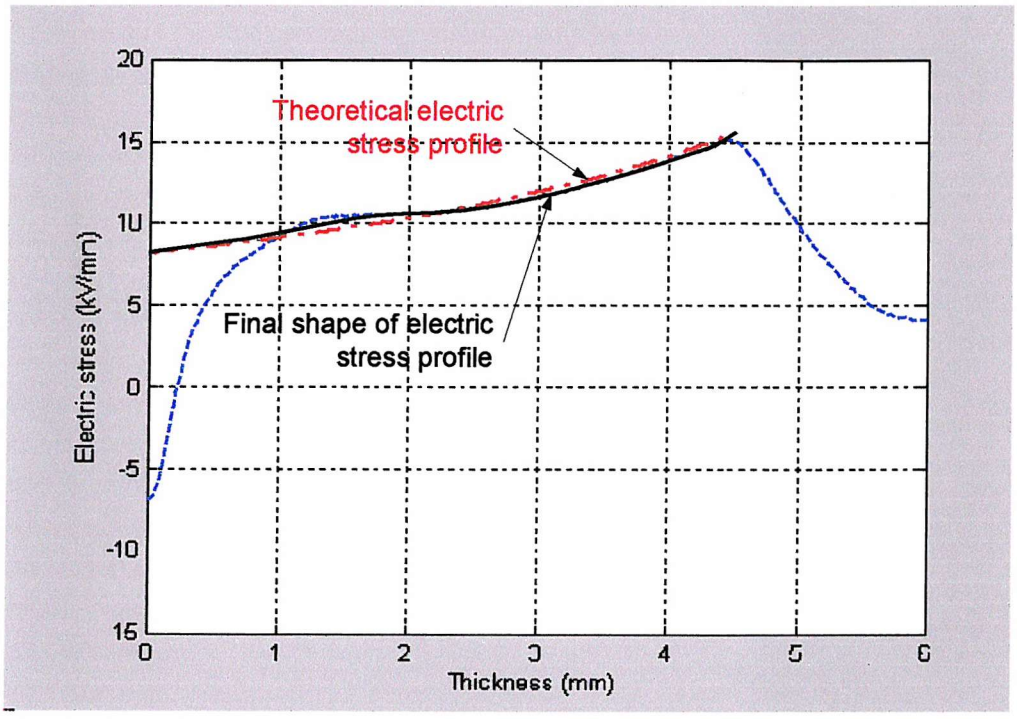

Figure 4.16 Final shape of electric stress profile of the cable sample

Figure 4.16 shows the final electric stress distribution (black solid line) in the cable sample corresponding to the typical current signal in figure 4.12b. Since the trace of the final electric stress distribution is in a very good agreement with the trace of the theoretical one (red dashed line), therefore it was believed that the newly designed LIPP system and the data processing method for the coaxial cable sample has been successfully set-up. This clearly demonstrates that the cable LIPP system is capable of studying space charge characteristics under dc conditions.

4.12 Current signal from the cable sample under ac condition

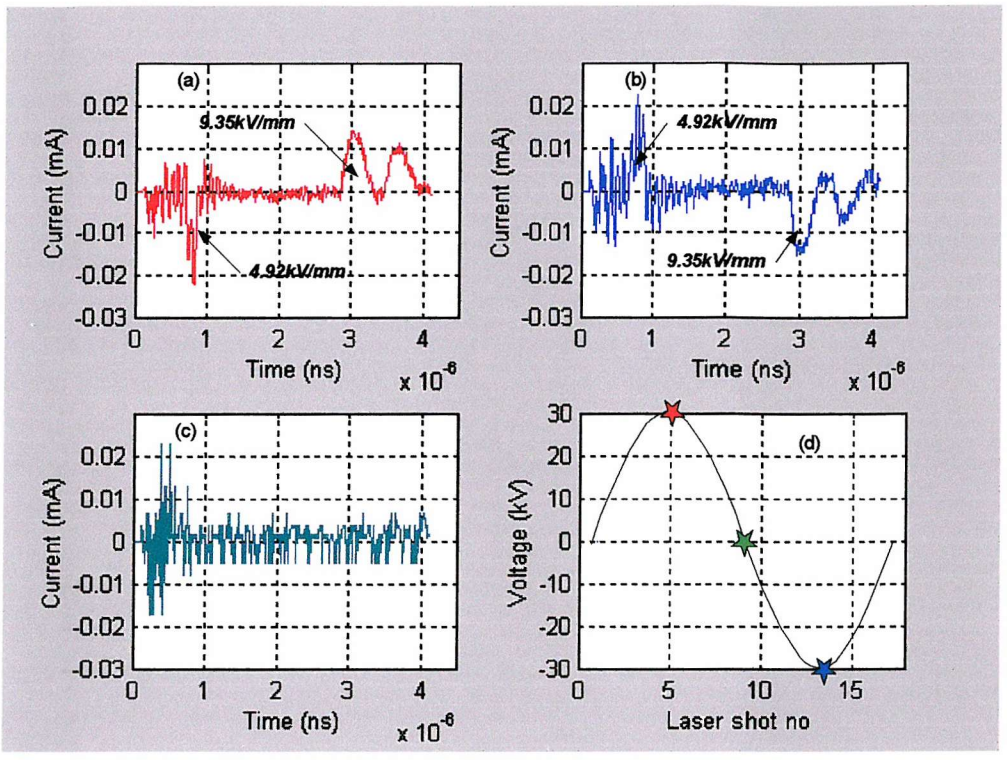

Figure 4.17a to 4.17c. The current signal in the cable sample under *30* kV_{peak} ac conditions

Figure 4.17d The corresponding point on wave voltage during the ac space charge measurement

Figure 4.17a to 4.17c show the three-selected output current signals obtained from a XLPE cable (4.5 *mm* bulk insulation) under 30 kV_{peak} ac conditions using the newly designed LIPP system. The corresponding points on wave voltage can be referred to 4.17d. It can be seen that due to the limitation of the maximum voltage of the HV transformer (i.e. 30 kV_{peak}), the SNR of the output signal is lower compared to the dc measurement (Figure 5.2b) and the maximum applied electric stress that can be achieved for the ac space charge measurement of the cable is 9.35 *kV/mm* at the inner electrode. The value is lower than the threshold voltage 11.5 *kV/mm* required to initialise the space charge effect in XLPE insulation.

4.13 Conclusion

In this chapter, the theoretical principles and preliminary results of the LIPP measurement in the planar and cable samples are reported. It is evident that the newly designed LIPP system has been successfully set-up, and it is capable of measuring the space charge distribution of

the planar and cable geometry sample under both dc and 50 *Hz* ac conditions. In addition, the signal calibration and data processing method to recover the reflected current signal and determinate space charge density as well as electric stress distribution in the planar and coaxial cable sample have also been developed.

However, due to the limitation imposed by the HV dc power supply and ac transformer in the current system, the applied electric stress is low. Consequently the SNR of the measurement signals in the cable sample is low and the space charge effect was not significant. Therefore, in this project our interests are to study space charge under both dc and ac conditions in the planar sample, the space charge measurement in the cable sample will be left as further work.

Chapter 5

Technical notes and validation of the newly designed LIPP system

5.1 Introduction

One of the main objectives of this research project is devoted to the technical design and construction of the LIPP system, which is able to determine the space charge and electric stress distribution of the planar and coaxial cable sample under both dc and 50 *Hz* ac stressing conditions. Therefore, prior to the application of the newly designed LIPP system to investigate the space charge evolution in the polymeric insulation, it is important to validate the system performance and reliability.

5.2 Plaque sample

Figure 5.1a shows a schematic diagram of a plaque sample, which was used for dc measurements. However, samples with this sharp edge profile on the semicon, are prone to electric failure under ac electric stress ageing within a short period of time. Figure 5.2 illustrates the break down site of a 1.5 *mm* XLPE plaque sample after 50 *mins* of 24 *kV* ac ageing. It was noticed that the path of the break down was initialised at the sharp corner of the HV semicon. Therefore, in order avoid the sample break down within the ac aging period, a curve profile has been introduced at the edge of the semicon to relief the electric stress at the edge of the semicon as shown in figure 5.1b.

All the plaque samples used for system validation and experiments in this project were cable quality as-received and degassed cross-linked polyethylene (XLPE) or LDPE plaques samples. The degassing process was to remove cross-linking byproducts, which was carried out by taking the sample up to 60 ^{O}C for 48 hours. Both the front and rear semicon electrodes with a thickness of ~0.5 *mm* were hot pressed into the insulation plate. The electrodes were made of the same grade of XLPE or LDPE material with a large amount of carbon black. The front electrode also acted as a target for the laser pulse.

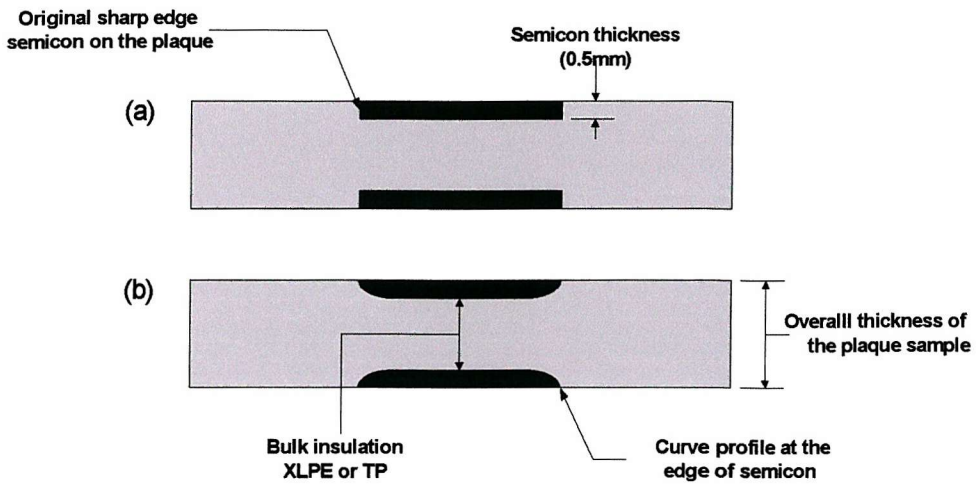

Figure 5.1a and 5.1b Plaque sample with sharp and curved profile semicon electrode

The advantage of such a sample structure is that the electrode/insulator interface is that encountered in practice. The target is robust and able to sustain more laser impacts without any noticeable reduction in thickness. However, the main disadvantage of this plaque design is the target can only be placed on relatively thicker samples and this will place an upper limit on the electric stress that can be applied.

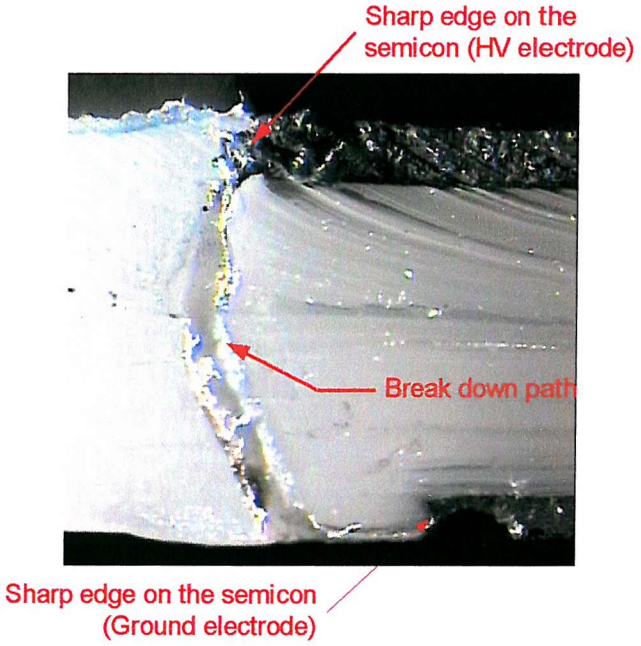

Figure 5.2 The broken down photo of plaque sample with sharp semicon profile

5.3 Cable sample and experimental arrangement

All the cable samples used for system validation and experiments in this project were 11 *kV* cross-linked polyethylene (XLPE) cables with a 4.5 *mm* thick of insulation, which was

obtained from BICCGeneral cable. Figure 5.3a shows the cross section of the prepared cable sample. The arrangement inside the screened cable sample holder is shown in figure 5.3b.

In order to obtain a compact measurement system with a small-screened sample holder (figure 5.3b), a long high voltage termination on the cable sample cannot be used. To eliminate the discharge and corona effect, 100 *mm* of the semicon layers at the two ends have been stripped off and two stress relief cones placed on the either side of the cable sample.

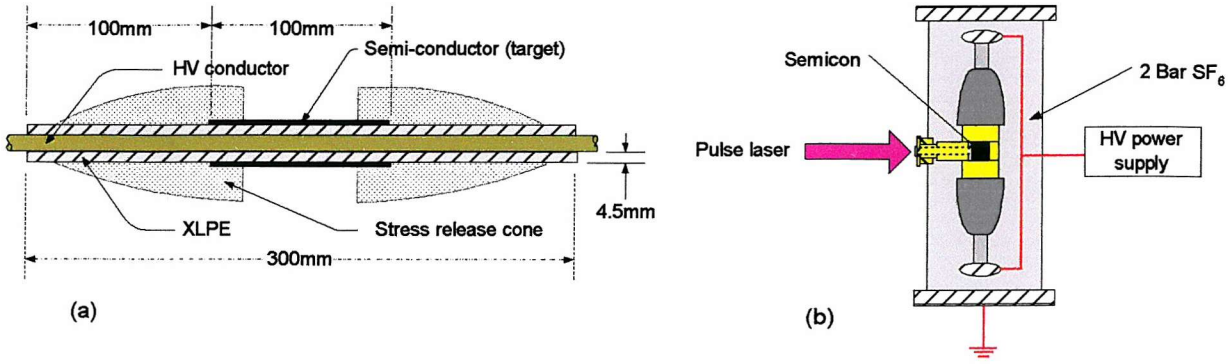

Figure 5.3a and 5.3b Cross-section diagram of the prepared cable sample and the arrangement of the sample inside the screened test holder

5.4 High frequency noise under ac high voltage

As stated in design section 3.4B, in order to avoid high frequency (HF) noise created by corona discharges superimposed on the output current signal, the entire free volume inside the sample holder and main body at the high voltage end have been filled with 2-bar pressurised SF_6 gas. It is expected a clear and high SNR current signal should be obtained.

However, when 30 *kV* ac voltage was applied to a 2 *mm* plaque sample, an unexpected HF noise was found superimposed on the output current waveforms as shown in figure 5.4a to 5.4c and the corresponding points on wave voltage can be referred to 5.4d. The characteristics of the HF noise were,

- The noise could only be observed under high voltage ac not dc,
- The noise extended well beyond the input electrode/sample interface, and
- The noise also increased with the applied ac voltage.

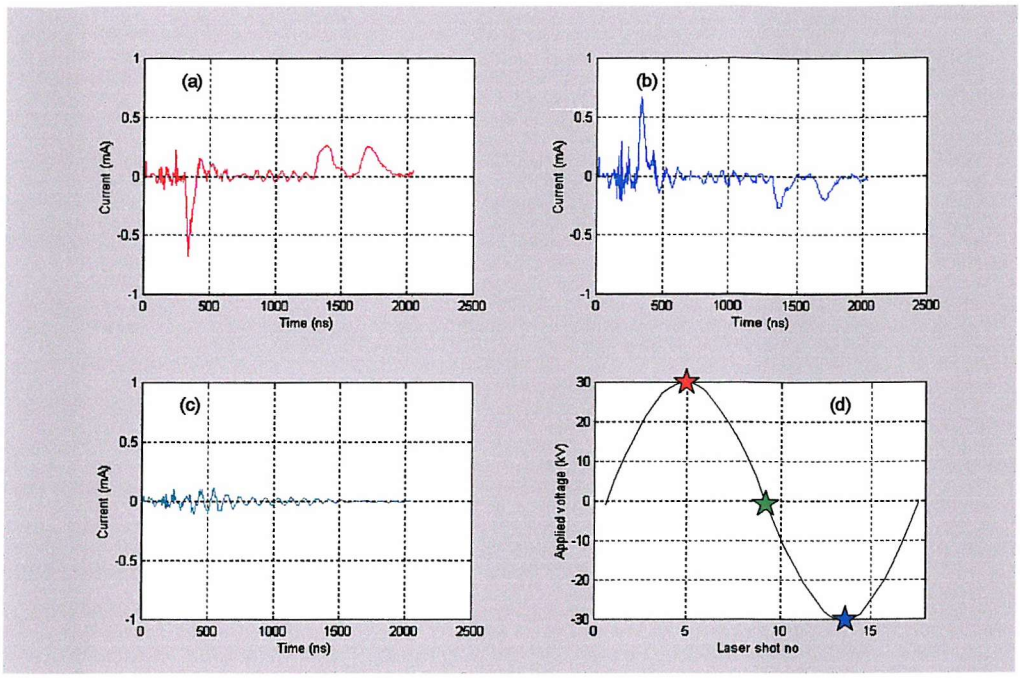

Figure 5.4a to 5.4c The current signal with the high frequency system noise
Figure 5.4d The corresponding point on wave voltage during measurement

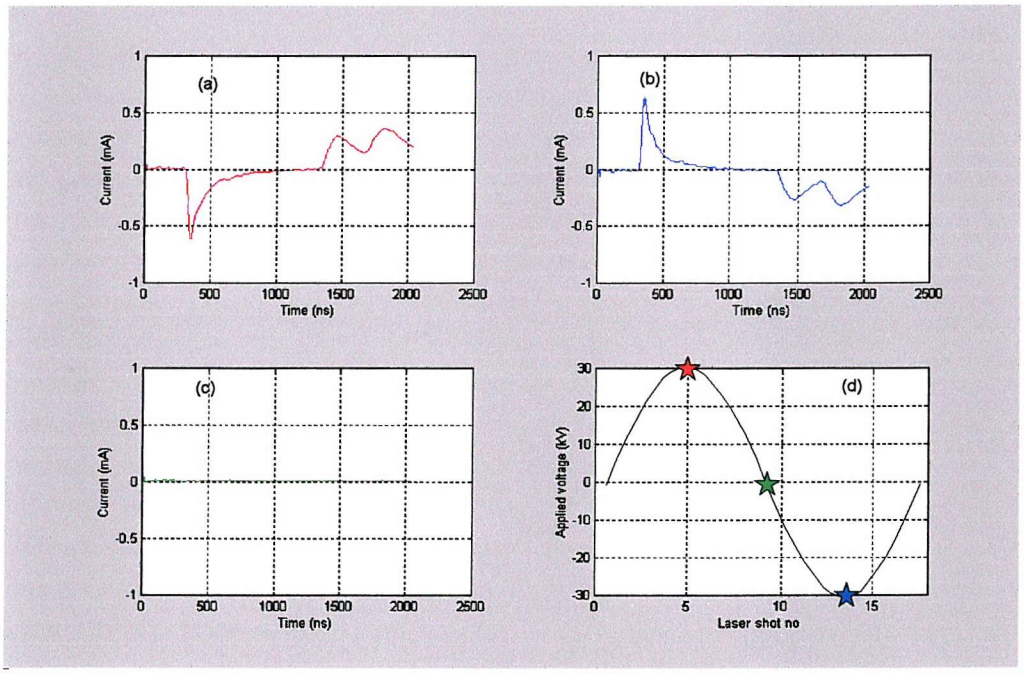

Figure 5.5a to 5.5c. The current signal after the installation of the coupled capacitors (DN441047) and figure 5.5d the corresponding point on wave voltage during measurement

According to the above characteristics, the initial thought was that the HF noise was not from the laser or caused by some form of component failure in the system, but it might came from the power supply or the transformer (i.e. live or ground). Eventually, it was found that the HF noise was entering into the LIPP system via the lead of the power supply on the

screened pre-amplifier box (referred to figure 3.3). Therefore, two coupled capacitors (DN441047) were installed between the power supply and the shielding box and the HF noise problem was solved. The current signals after the installation of the coupled capacitors are shown in figure 5.5a to 5.5c and the corresponding point on wave voltage can be referred to 5.5d.

5.5 Validation of the electronic system

In order to create an activation signal to the electronic system and record the actual high voltage value at the point on wave where a measurement is carried out, a high voltage capacitor divider has been installed in the LIPP system (Details can be found in section 3.6B). According to the design and the timing sequence of the electronic control board (figure A2-1 and A2-2), by changing the pre-set value at the switch-U11, the period of time delay between two consecutive laser shots as well as number of shot per cycle can be altered (Table A2-1).

Figure 5.6 shows two typical ac HV waveforms recorded during space charge measurements of a 2 *mm* planar sample stressed at 24 *kV* ac with 17 shots per cycle. It can be seen that the electronic control board gives repeatable results. However, the ac waveform is not symmetrical as it should be, there exists a 1 *kV* offset and this can lead to a serious problem for comparing the space charge effect between positive and negative cycles.

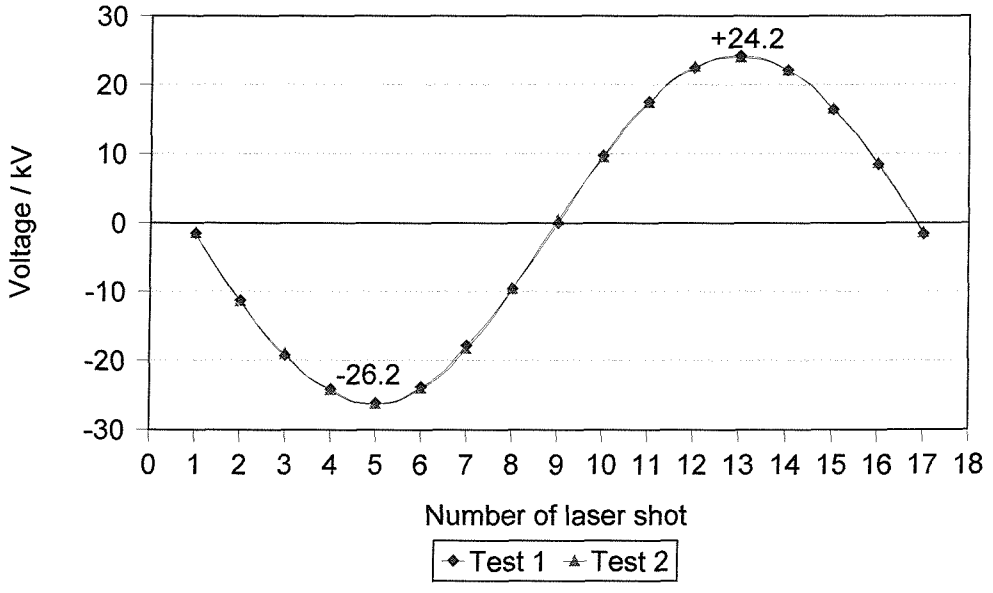

Figure 5.6. The point on wave voltage by using the operational amplifier AD711J

Any dc offset from the main power supply should be removed by the HV transformer, so this problem was believed to be due to the poor response of the electronic circuit. In order to solve this offset problem, an operational amplifier with high input impedance, high speed and offset adjustment null should be used. There are not many operational amplifiers, which have extremely high input impedance, say 10^{14} Ω (*Typical* 10^{12} Ω) with offset null function, which can replace AD711J. Therefore, a great deal of time and considerable effort was spent to find a suitable device to replace this operational amplifier.

Finally, a high-speed precision Difet operational amplifier OPA602 from BURR-BROWN was found which is suitable for the ac LIPP system. Since OPA602 has a high input impedance, 10^{14} Ω, as well as an offset null, hence less than 1 % offset was finally achieved as shown in Figure 5.7.

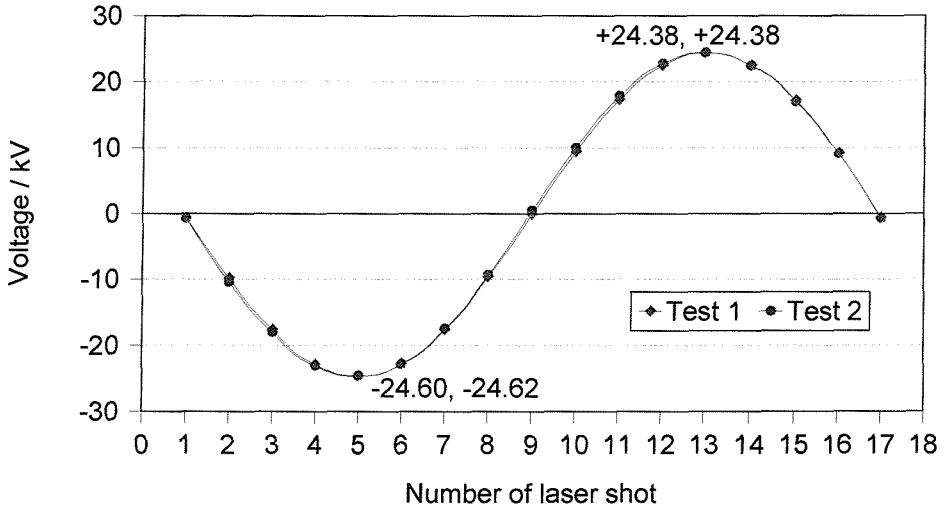

Figure 5.7 The point on wave voltage by using the operational amplifier OPA602

5.6 Validation of the online laser power monitor system

As mentioned previously, the entrance and exit peaks of the current signal is directly proportional to the magnitude of the interfacial stresses and it is expected that both entrance and exit peaks should increase linearly with the applied voltage in the absence of space charge in the bulk. However, when the space charge is generated in the bulk, the slope of the peaks height against the applied voltage will deviate from the linear response.

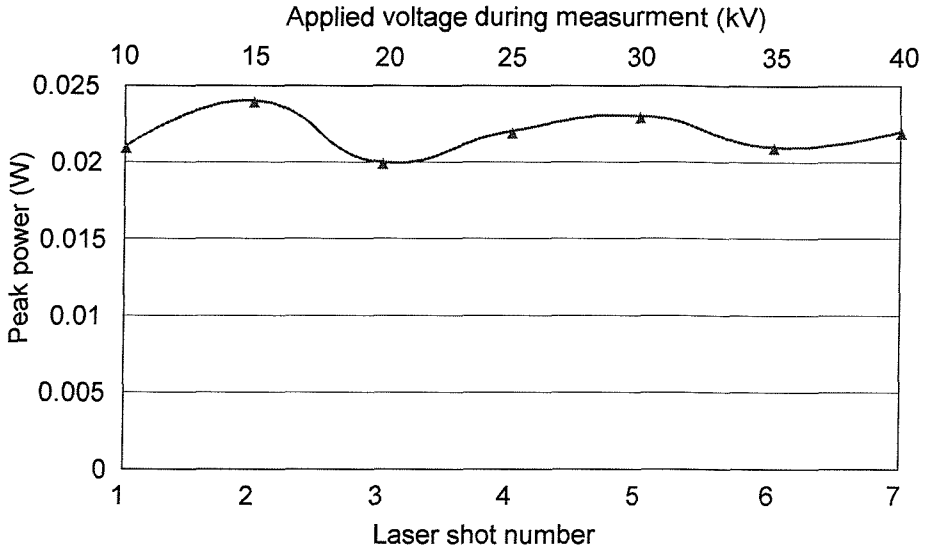

Figure 5.8 Variation of the laser power at different measurement

However, if there is a variation in laser power from shot to shot during the measurement, the deviation of the peak heights against the applied voltage will be affected and no longer reflect the true stress value at the electrode. An online laser power monitor system has been installed and a test on a 2 *mm* pure LDPE plaque sample has been carried out. As it is not expected that any significant charge is formed at the maximum stress applied, both the entrance and exit peaks should be directly proportional to the applied voltage under the dc ramp rate test. (the applied voltage increased from 10 *kV* up to 40 *kV* with step size of 5 *kV*)

The laser power collected by the laser power meter during the dc ramp rate test of the LDPE sample is shown in figure 5.8, which illustrates the high percentage variation ($\approx\pm 10$ %) in laser power from shot to shot.

Both linear regression lines of the entrance peak height against the applied voltage before and after taking laser power variation into consideration have been plotted in figures 5.9 and 5.10 respectively. By comparing the coefficient of determination (R-square) between these two linear regression lines, it can be seen that the R-square term for the entrance peak height against the applied voltage after removing laser power variation is nearly unity. This demonstrates that the peak height after removing the laser power variation fits a linear model and verifies the usefulness of the online laser power monitor system.

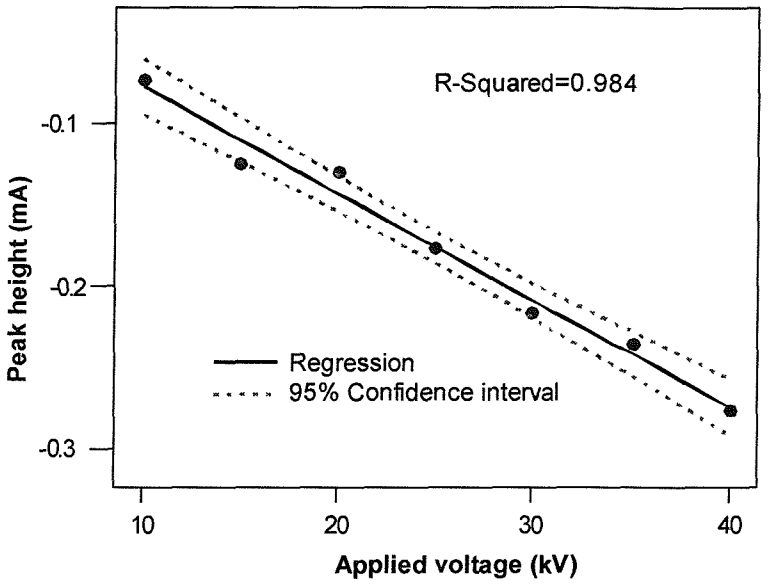

Model	R	R Square
Linear	.992	.984

Figure 5.9 Regression plot of peak height against the applied voltage

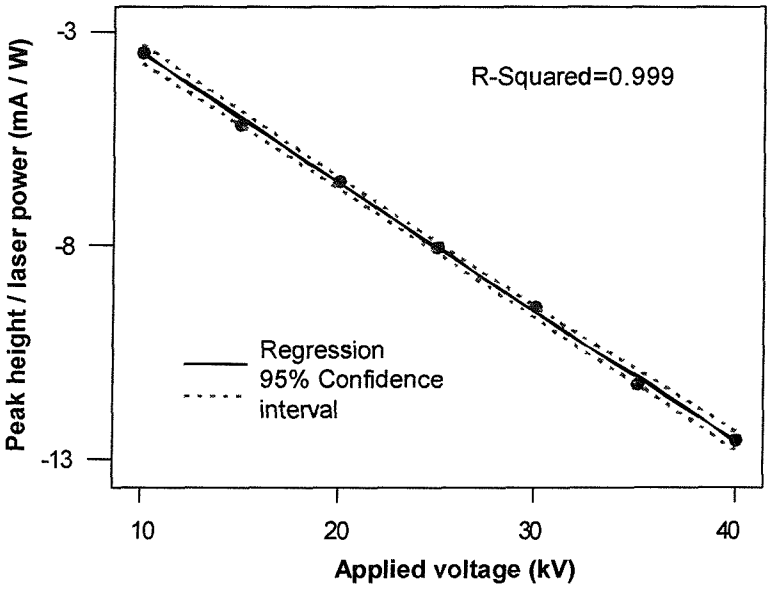

Model	R	R Square
Linear	.999	.999

Figure 5.10 Regression plot of peak height/laser power against the applied voltage after removing laser power variation

5.7 Effect of semicon target thickness on the measurement resolution

As mentioned in section 4.4, the thickness of the rear electrode should be at least 0.5 *mm* to reduce the possible superimposition on the output signal due to pressure wave reflection

from the HV metal electrode. However, in order to ensure a consistent measurement resolution and avoid the pressure wave reflection at the target electrode, the thickness of the semicon target electrode on the test sample is also need to be considered.

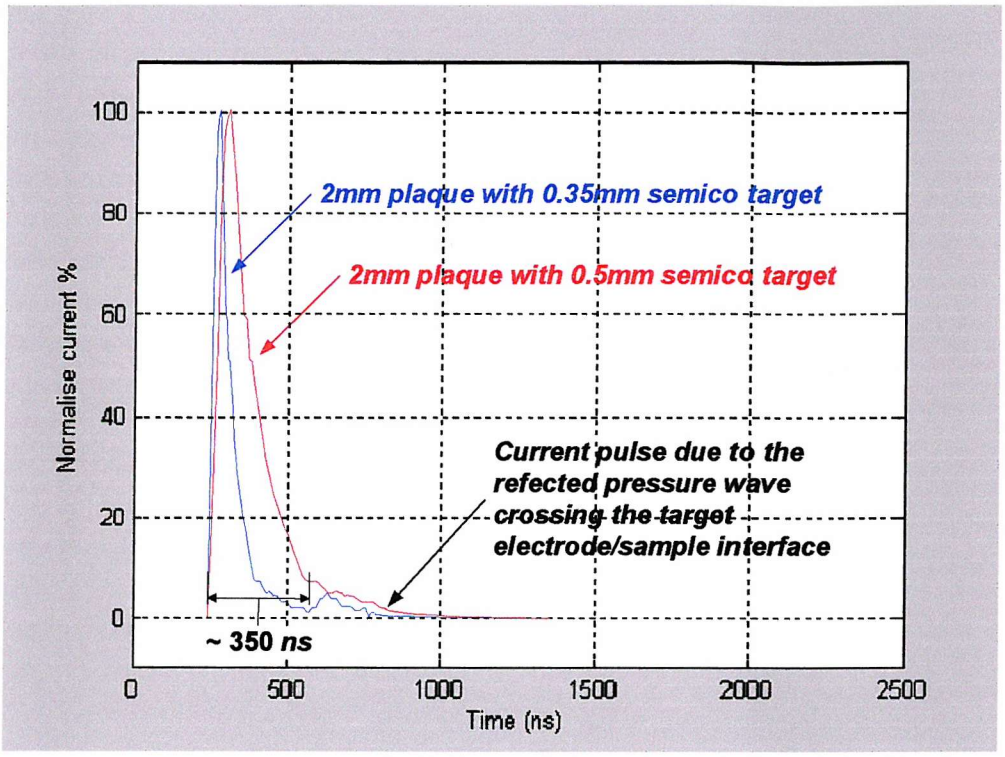

Figure 5.11 Effect of the semicon target thickness to the measurement resolution

Figure 5.11 show two normalised entrance peaks from two identical 2 *mm* XLPE plaque samples with 0.35 *mm* (blue trace) and 0.5 *mm* (red trace) semicon target respectively. It can be seen that the spatial resolution using the thinner (0.35 *mm*) semicon is about 2 times higher than the thicker (0.5 *mm*) semicon. Although the material used for the target electrode was made of the same grade of XLPE material loaded with carbon black, the acoustic properties are slightly different from XLPE without carbon black. Therefore, if the target semicon is too thin (like 0.35 *mm*), then the reflected pressure wave will be created at the front electrode/sample interface which bounces back through the target and is then reflected from the front of the target semicon back towards the sample [5,40]. This pressure wave will then pass through the sample/electrode interfaces a short time 350 *ns* (i.e. $350ns * 2000ms^{-1} * 1000 = 0.7mm \approx 2 *$ semicon thickness) after the original pressure wave and create a second electrode/sample current peak as shown in figure 5.11. This could be interpreted as a layer of charge within the sample.

Therefore, in order to get a reasonable resolution, avoid the reflection at both electrodes and provide a thick semicon electrode which can withstand many laser shots for the ac space charge measurement, the semicon electrodes using on the plaque samples for system validation and experiments in this project are ~0.5 *mm* in thickness.

5.8 Effect of sample thickness on the target relaxation

The rate of relaxation of the target, as it cools, is also an important factor. If the cooling period of the target is long, then the target may still be relaxing (i.e. residual pressure) when the leading edge of the pressure wave reached the rear interface. In some cases the leading edge of the current pulse at the rear interface will interact with the tail of the current pulse from the front interface, causing an incorrect space charge distribution indicated as a "signal offset" towards the rear of the sample as shown as the red trace in figure 5.12.

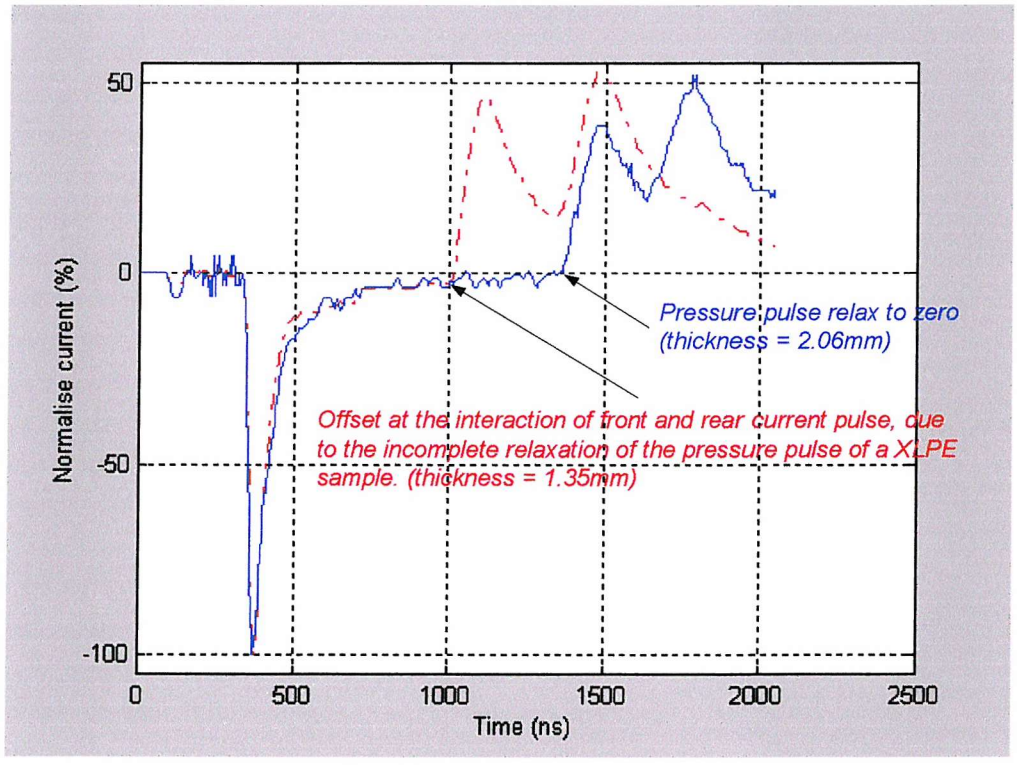

Figure 5.12 Effect of the incomplete relaxation of the pressure wave

In order to ensure the pressure wave has been completely relaxed before it reaches the rear electrode, the bulk insulation inside the sample should be considerably thicker, say 2 *mm* (blue trace). However, as the maximum ac voltage of the HV transformer is 30 *kV*, therefore

it limits the maximum electric stress that can be applied for the space charge measurement. To achieve higher ac stresses for the space charge measurement the thickness of the plaque samples was reduced to 0.8 ~ 1.6 *mm*. Consequently, the current signal close to the rear electrode may be not accurate due to a reduction in resolution, therefore a simple method has been developed in Chapter 8, which enables a comparison of space charge effects due to different treatments and ageing to be made.

5.9 Effect of the laser degradation on the space charge measurement

As far as the LIPP system design is concerned, the high power laser is only used as an external source to produce an acoustic pressure wave for the space charge measurements. Therefore, the initial considerations only concentrated on the effect of laser power variation to the signal calibration and the usefulness of the online laser power monitor system to the signal calibration.

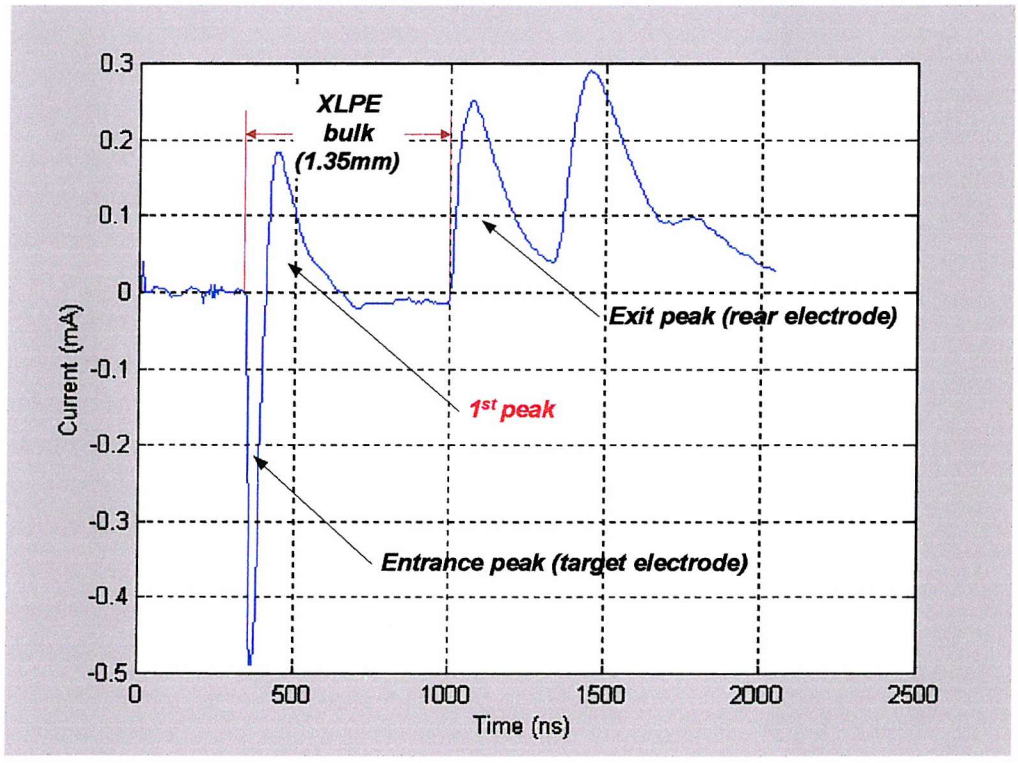

Figure 5.13 Unexplainable current signal due to the laser degradation

However, during one of the plaque sample ageing experiment, incorrect and unexplainable current signals, which are similar to figure 5.13, has been obtained using the newly designed LIPP system. A great deal of time and considerable effort has been spent to identify the

cause of the 1st peak. The entire system has been stripped down and checked, it was concluded that the 1st peak was not caused by the component failure in the system. It was then suspected that the ionisation from the semicon electrode may be responsible for the 1st peak. However, referred to equations 4.6 and 4.7, if there were heterocharge formation close to the entrance peak (cathode), the magnitude of the entrance peak height, which corresponding to the interfacial stress at the cathode would be much higher than the result obtained.

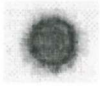

Figure 5.14a Original shape and size of the laser beam

Figure 5.14b Shape and size of laser beam after flash lamp degradation

Eventually, and almost purely by chance, it was found that the output laser beam reduced in size compared to the original beam (Figure 5.14). After the service engineer checked the laser system, it was noticed that the flash lamp, which is used to produce the laser had degraded. After the replacement of the flash lamp, perfect and clear current signals were obtained.

Chapter 6

Space charge accumulation in the plaque samples under dc electric stress

6.1 Introduction

Generally speaking, several processes can take place when an insulation material is subjected to a dc electric stress. Referring to [113], heterocharge and homocharge can be accumulated within the bulk insulation of the as-received and degassed cross-linked polyethylene (XLPE) during the period of dc ageing. The heterocharges in the as-received sample are due to the bulk process, which may be caused by the ionisation of the cross-linking byproducts and the impurities inside the sample and the homocharges formation in the degassed sample was believed to be injected from the electrode.

As stated in Chapter 1, LDPE is another material, which has been used for the cable insulation. However, as the insulation is not cross-linked it is generally believed that there is no significant space charge formed inside the bulk under HV dc electric stress. Consequently, a lot of effort have been made on the space charge measurements in XLPE materials over the last decade, works on the dynamics and the roles of space charge inside LDPE has received limited attention [157-161] and has not been conclusive.

The primarily aim of this chapter was to use the newly designed LIPP system to investigate and compare the space charge evolution of the cross-linked polyethylene (XLPE) and LDPE plaque samples under dc electric stressing. Space charge results taken during voltage ramp and electric ageing of cable quality as-received and degassed cross-linked polyethylene (XLPE) and LDPE plaques with both cross-linked polyethylene (XLPE) and LDPE semicon electrodes are presented.

It was understood from the sample supplier (BICCGeneral cable) that the materials being tested in this project were for newly designed HV dc power cables. Therefore, the space

charge level under HV dc electric ageing was expected to be lower than the conventional XLPE insulation. To verify this expectation, comparisons have been made between the tested sample (Sample A to E) and the conventional insulation (P153). In addition, the entrance and exit current peak of the LIPP signal are correlated to the interfacial stresses at the electrodes. Therefore, in order to compare the electric ageing effect on different materials without resorting to a complex mathematical treatise, a simple method, which based on the percentage deviation of the entrance peak, has been introduced.

6.2 DC experimental procotols

6.2A Ramp rate test (Calibration)

In order to correlate the output current to the charge density and determine the threshold voltage, at which the space charge starts to appear inside the bulk material, ramp rate experiments were performed on the plaque samples. The applied voltage started from 0 kV up to 30 kV with voltage step size of 5 kV.

6.2B DC ageing test

The plaque samples after the ramp rate experiment were subsequently stressed at a dc voltage (30 kV) for a period of 24 hours at 25 ^{o}C. The space charge distributions were measured at various times with and without voltage application within the period of dc ageing.

6.3 Sample details

The samples used to investigate the time dependence of space charge accumulation were as-received and degassed (i.e. heating the sample up to 60^{o}C for 48 hours to remove the volatile byproducts within the bulk insulation), cross-linked polyethylene and LDPE plaques with a bulk thickness of between 1.3 mm to 1.6 mm. Semicon electrodes were made of the same grade polyethylene loaded with carbon black. The sample details are shown in Table 6.1.

Sample no	Polymer	Semicon	Treatment	Bulk thickness (*mm*)	Applied Stress (*kv/mm*)
A	XLPE (XL1046)	XLPE	1	1.30	23.10
B	XLPE (XL1046)	XLPE	2	1.40	21.43
C	LDPE (P285)	XLPE	1	1.29	23.26
D	LDPE (P285)	XLPE	2	1.24	24.19
E	LDPE (P285)	LDPE (P285)	Nil	1.56	19.20

Table 6.1 Plaque sample details (Treatment 1: as-received, Treatment 2: degassed)

6.4 Experimental results and discussion

6.4A Results and discussion of the ramp rate experiment

The results of the ramp rate measurements on "Sample A" to "Sample E" are summarised in Figure 6.1a to Figure 6.1e. It illustrates that the magnitude of the entrance peak against the applied stress for all the samples with XLPE semicons deviates, positively, from the "extrapolated straight line". This line is obtained from the region over which the entrance peak height of the current signal is linearly dependent on the applied stress. This implies that above the threshold stress, the interfacial stress at the cathode is less than the applied stress, indicating that homocharge has been formed close to the XLPE/semicon interface (cathode).

In order to establish the effect of the sample degassing on the threshold stress, comparisons have been made between the ramp rate results of the as-received and degassed samples (Sample A to B and Sample E to F). The results show that the degassing process reduced the threshold stress in the samples with XLPE semicons by approximately 30 %. This suggests that after the degassing process, which removed the cross-linking byproducts, the effect of ionisation process in the bulk was minimal and the space charge was mainly due to charge injection from the semicon electrodes. However, in the case of LDPE samples with XLPE semicons, the threshold stress between the as-received and degassed samples showed only a 4 % difference. Since the LDPE samples have no cross-linking byproducts present within the bulk insulation, therefore degassing would not have any significant effect on the

threshold stress. The homocharge present is mainly due to the charge injection from the semicon electrodes.

To examine the influence of the semicon material on the space charge, a ramp rate measurement on LDPE samples with LDPE semicons (Sample E) has been performed. It illustrates that the entrance peak against the applied dc stress followed the extrapolated straight line up to a significantly high stress (~19.2 kV/mm), indicating that no homocharge has been formed close to the cathode. By comparing the results between "Samples C and E", it is resonable to assume that the source of the negative charge close to the cathode during the ramp rate measurement in the samples with XLPE semicons was prossiblely due to the homocharge injection from the XLPE electrode (cathode) rather that the ionisation process of the byproducts inside the bulk, which is strongly dependent on the semicon material.

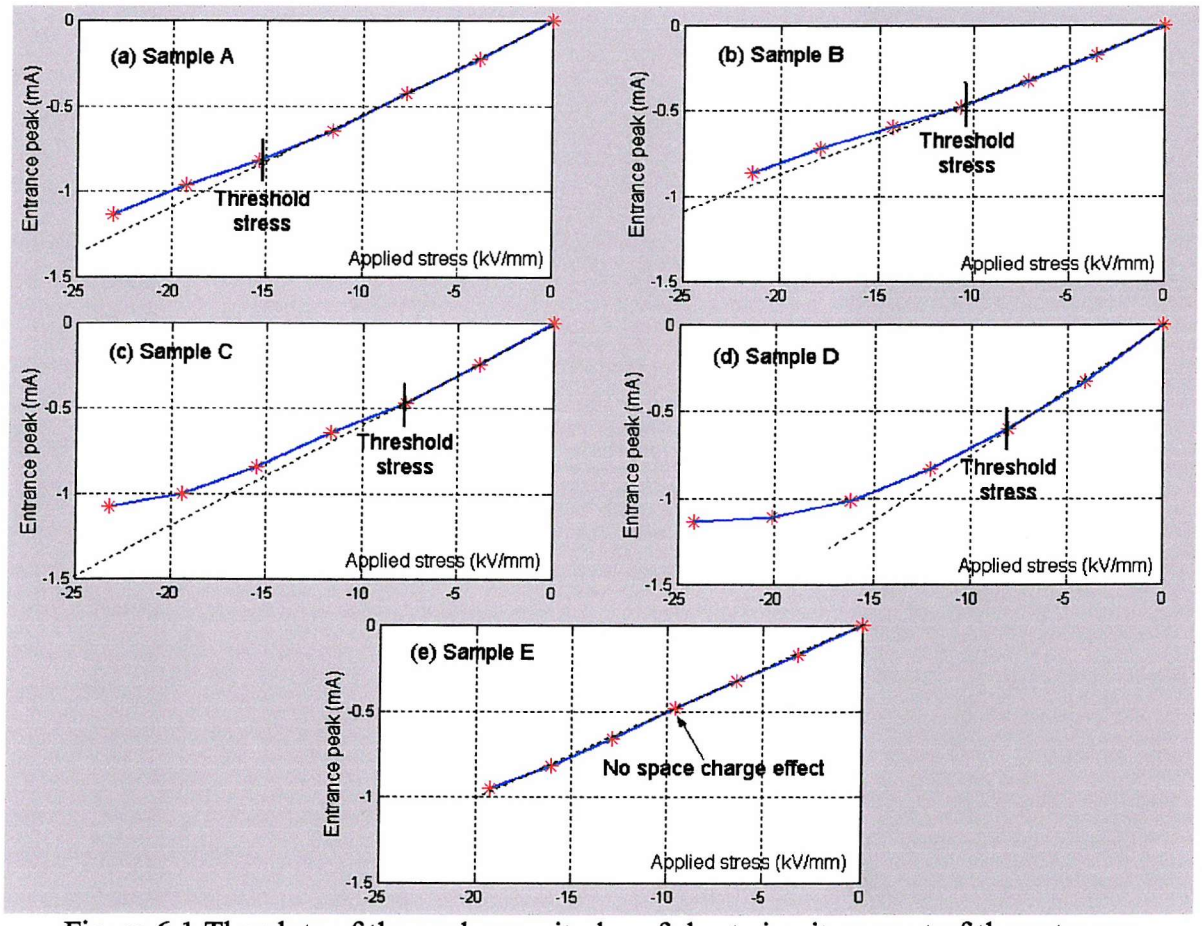

Figure 6.1 The plots of the peak magnitudes of short circuit current of the entrance peaks against the applied stress on the samples A to F

6.4B Results and discussion of charge evolution during 24 hours dc ageing

❖ *As-received XLPE with XLPE semicon plaque (Sample A)*

Figure 6.2 shows the space charge evolution of "Sample A" with 24 hours of dc ageing (23.1 *kV/mm*) at room temperature (25 ^{O}C). During the first hour of aging, there was clear evidence of heterocharge accumulation close to both electrodes (i.e. positive charge accumulation near the cathode and negative charge near the anode). This phenomenon is believed to be associated with the electric field assisted ionisation process of the cross-linking byproducts and impurities inside the bulk. Beyond 8 hours, the positive charge near the cathode reduced gradually and may be due to the negative charge injected from the cathode, which then recombine with the positive charge created from the ionisation process. However, throughout the 24 hour ageing period, the variation of the negative charge accumulated close to the anode was insignificant whilst there was a marked change at the cathode side after the first hour.

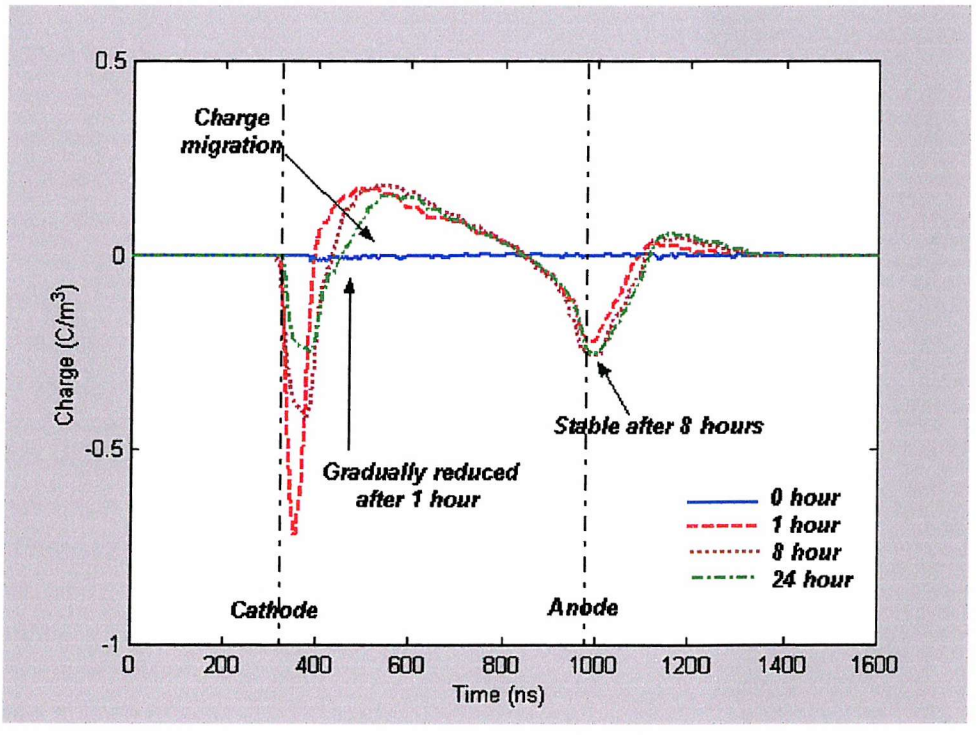

Figure 6.2 The evolution of the space charge formation of the "Sample A" during 24 hours ageing process (Volts off)

Since the breakdown of high voltage cable is normally initiated at the interfaces, therefore the interfacial stresses at the electrode/insulator interfaces is of a greater

interest to the cable manufacturer and end user. For this reason, emphasis was placed on the effect of space charge on the electrode/insulator interface stress rather than relevant charge density distributions with "voltage on". The effect of space charge evolution on the interfacial stresses is shown in Figure 6.3. It can be seen that over the first 8 hours ageing the stress at the cathode was increased by 9 % compared to the value at 0 hour (-19.2 *kV/mm* ➔-21.0 *kV/mm*); the increased stress at the interface coincident with the heterocharge accumulation in the vicinity of the cathode shown in Figure 6.2. However, from 8 to 24 hours, the interfacial stress at the cathode decreased from –21.0 to –16.2 *kV/mm* (-15 % compared to the 0 hour). One possible cause of this is that the stress enhancement caused by the heterocharge (positive charge) close to the cathode initiated the negative charge injection, which recombined some of the ionised dissociable cross-linking byproducts (positive charge) close to the electrode and lower the electric stress at the electrode/XLPE interface. This is supported by the diminish of the positive charge close to cathode from 8 to 24 hours as shown in Figure 6.2.

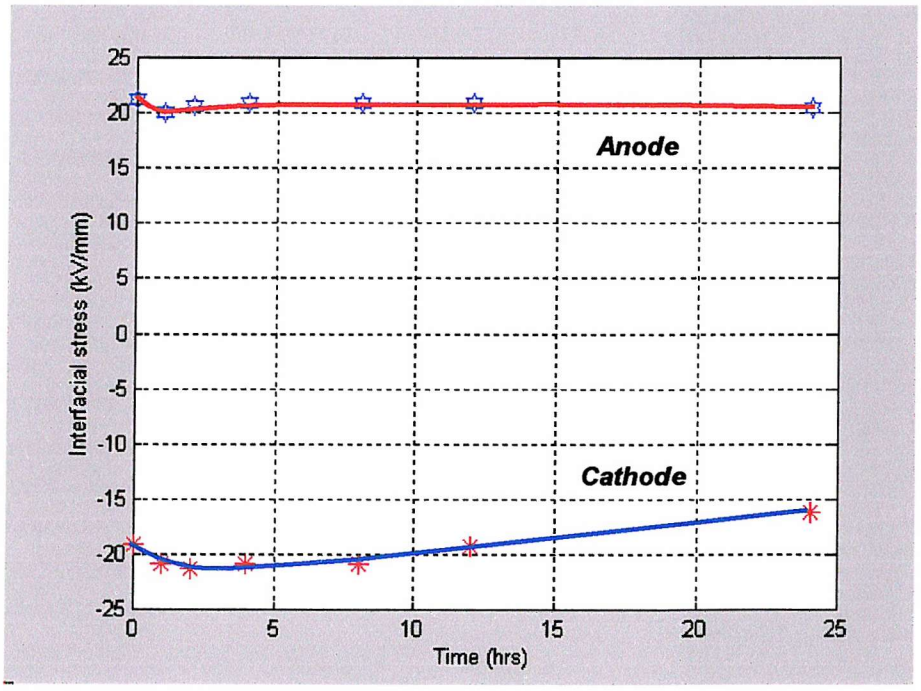

Figure 6.3 The interfacial stress of the "Sample A" during 24 hours ageing process (Volt on)

In the vicinity of the anode, there was an obvious heterocharge accumulation (Figure 6.2) after the first hour of dc ageing. However, the interfacial stress reduced by approx 5 % comparing to the stress at 0 hours (Figure 6.3). This phenomenon may probably be

attributed to the relatively large amount of positive charge rather than negative charge accumulated inside the bulk insulation after the first hour of ageing. In addition, as the position of the positive charge is far away from the anode, the effect of the space charge on the anode (5 % stress reduction) should be smaller than that at the cathode (up to 12 % stress enhancement). As the amount of positive charge inside the bulk insulation decreased with the ageing period, the stress reduction at the anode was reduced from 5 % to 2 % after 24 hours.

❖ ***Degassed XLPE with XLPE semicon plaque (Sample B)***

In order to study the degassing effect, space charge measurements on the degassed XLPE plaques with XLPE semicons has been performed. Figure 6.4 shows the space charge evolution of "Sample B" versus ageing time up to 24 hours (21.43 *kV/mm*) at room temperature (25 ^{O}C).

Referring to Figure 6.4, although there has already been clear evidence of negative charge injection at the cathode during the ramp rate measurement (i.e. the magnitude of the entrance peak against the applied dc stress of Sample B deviates positively from the "extrapolated straight line" shown in Figure 6.1b), after the first hour of dc aging there was still no appearance of charge accumulation within the bulk insulation when the dc voltage was removed. After 8 hours, it noticed that there was a small amount of negative charge (i.e. homocharge) starting to accumulate within the bulk with no indication of any positive charge formation. Judging from the results, it was believed that after the removal of the cross-linked byproducts (via degassing process), the injection process governed the space charge dynamics and the source of these negative charges was possibly due to the injection from the cathode. After 24 hours, the amount of negative charge increased significantly and became widely distributed within the bulk insulation.

In order to verify the above explanation of the space charge evolution, the interfacial stress at the cathode and anode during the 24 hours ageing period has been plotted in Figure 6.5. Over 0 to 8 hours ageing, in contrast to the results of the as-received XLPE sample (i.e. stress enhancement of 12 %), it has been noticed that the stress at the cathode reduced from -16.8 *kV/mm* to –14.0 *kV/mm* (approximately 16.7 % reduction).

The decrease in stress at the interface was believed to be associated with the homocharge (i.e. negative) injection at the cathode.

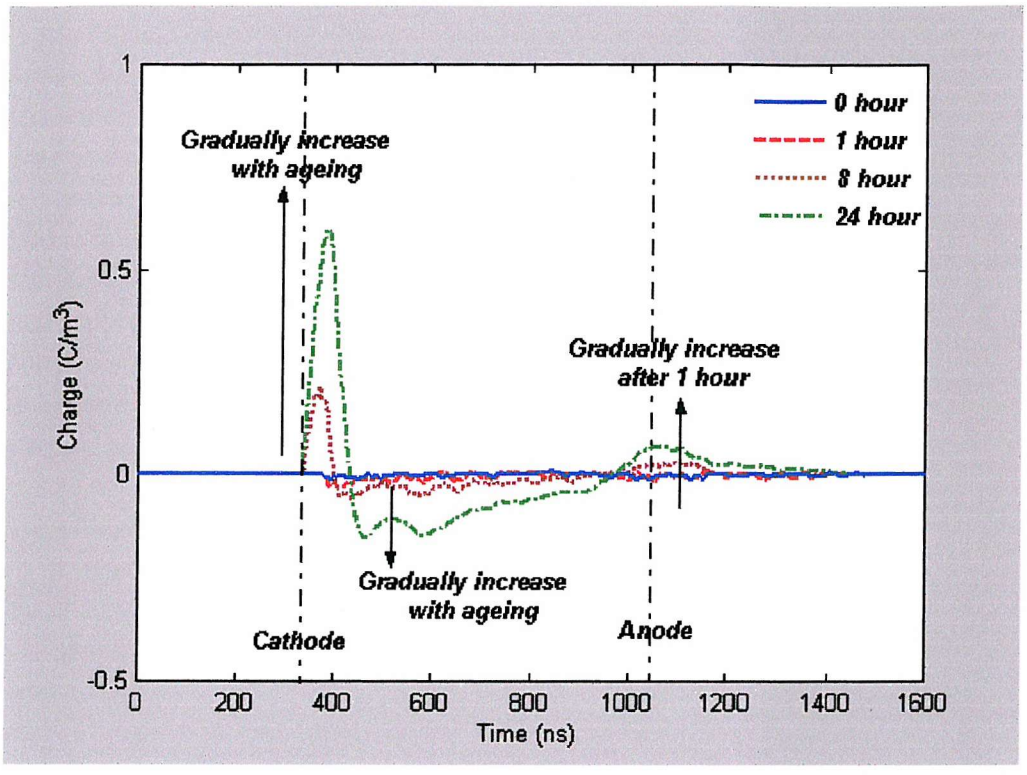

Figure 6.4 The evolution of the space charge formation of the "Sample B" during 24 hours ageing process (Volt off)

However, similar to what was observed in the as-received "Sample A", during the first 8 hours, the interfacial stress at the anode was approx 5 % reduced with respect to 0 hour and remained constant over the next 16 hours of dc ageing. It was believed that although the amount of negative charge accumulated inside the bulk increased with ageing time, the trapping position is far away from the anode, and the effect of the space charge on the interfacial stress at the anode was insignificant.

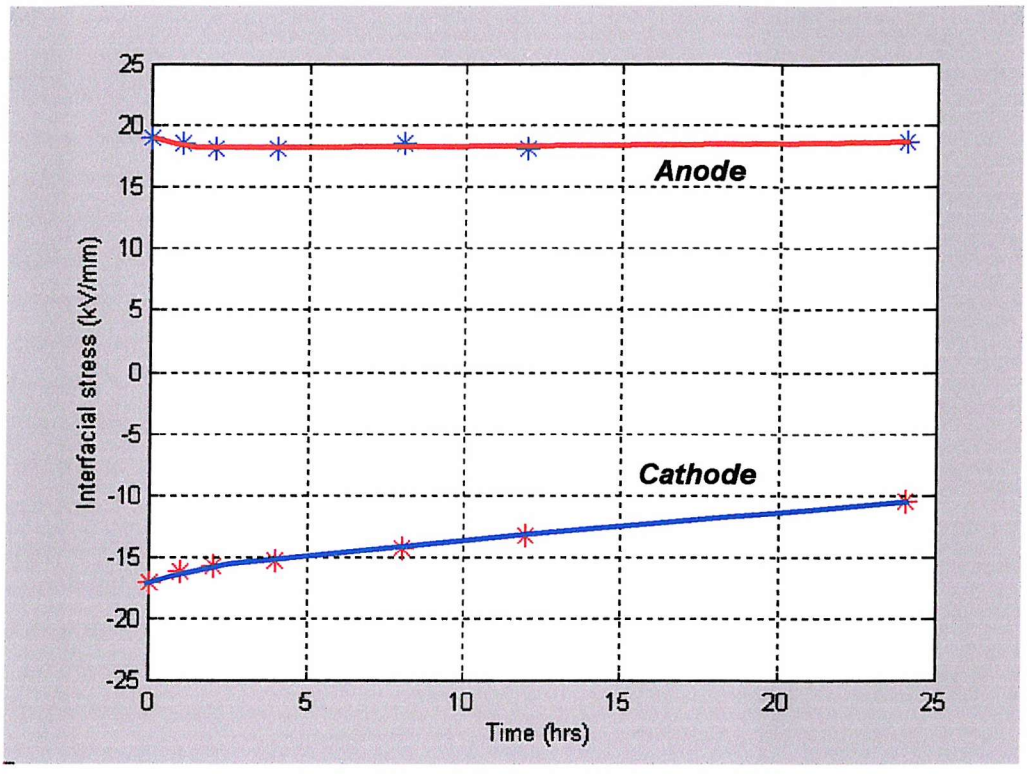

Figure 6.5 The interfacial stress of the "Sample B" during 24 hours ageing process (Volts on)

❖ ***As-received LDPE with XLPE semicon plaque (Sample C)***

Based upon the test results of "Sample A" and "Sample B", the space charge dynamics in the XLPE materials were significantly affected by the degassing process. In order to examine the effect of semicon on the space charge formation in the different insulation, LDPE samples with XLPE semicons have been tested. This may give useful information about how to select semicon screens for the cable manufacturers to control the space charge within the bulk. Also, as there are no cross-linking byproducts present within the LDPE insulation, the space charge dynamics is expected to be similar to the degassed XLPE sample, which is mainly controlled by the charge injection process.

To investigate the effect of the sample degassing process on the space charge dynamics of the LDPE insulation, two plaque samples (Sample C and D) with LDPE bulk with XLPE semicon electrodes have been manufactured. "Sample C" tested at the as-received condition and "Sample D" tested after degassing.

Figure 6.6 illustrates the space charge evolution of "Sample C" within 24 hours dc ageing (23.26 *kV/mm*) at room temperature (25 ^{O}C). Over 24 hours of the ageing period, there was clear evidence of negative charge accumulation within the bulk insulation. However, as there were no cross-linking byproducts within the LDPE insulation, the accumulated negative charge is believed to be supplied by the electron injection from the cathode.

In the vicinity of the cathode, it was noticed that a small amount of positive charge accumulated after one hour, which became more pronounced after 8 hours of ageing. However, from 8 to 24 hours this small amount of positive charge was gradually reduced and eventually was masked by the positive image charge at the cathode. Considering the above phenomena, a possible explanation, which relates to the sample manufacturing process, is suggested. The semicon electrodes were made from the XLPE material, and during the sample manufacturing process the cross-linking byproducts within the semicon diffused into the LDPE bulk and caused the field assisted byproduct ionisation close to the interface region to occur.

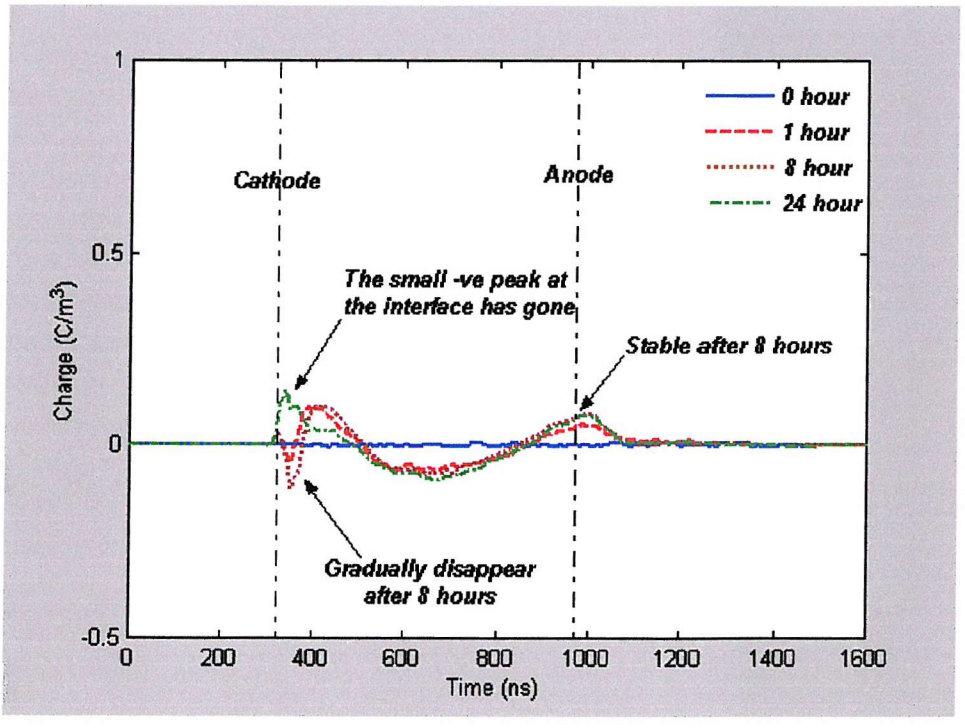

Figure 6.6 The evolution of the space charge formation of the "Sample C" during 24 hours ageing process (Volts off)

Figure 6.7 illustrates the evolution of the interfacial stress at the cathode and anode of the "Sample C" within 24 hours ageing. Over the first 8 hours aging, it was noticed that the stress at the cathode and anode increased by +25 % (-15 to -18.8 *kV/mm*) and +11 % (18 to 20 *kV/mm*) corresponded to that at to 0 hours. This was consistence to the previous observations of heterocharge accumulation (i.e. ionisation) close to the interface. However, from 8 to 24 hours, the interfacial stress at the cathode decreased from -18.8 to -16 *kV/mm* (+25 % to +6.7 %). One possible cause was that the stress enhancement due to the heterocharge close to the cathode initiated the negative charge injection and lowered the electric stress at the electrode/LDPE interface.

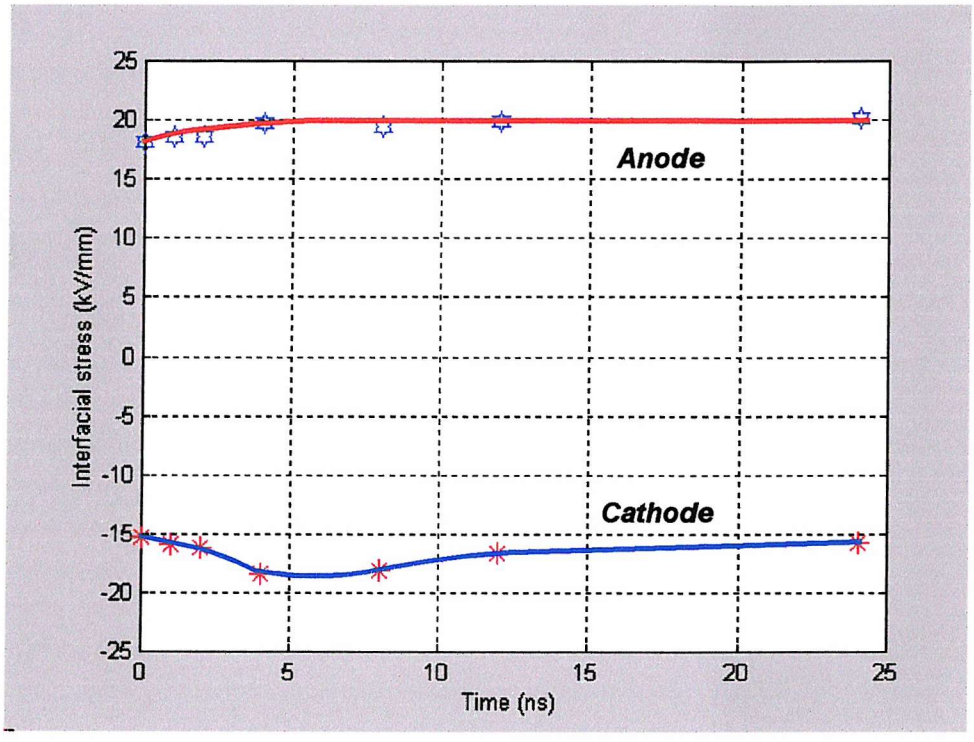

Figure 6.7 The interfacial stress of the "Sample C" during 24 hours ageing process (Volts on)

❖ ***Degassed LDPE with XLPE semicon plaque (Sample D)***

In order to examine the effect of the degassing process on the space charge dynamics in the LDPE sample with XLPE semicons and to verify that the source of the small amount of positive charge accumulated in the vicinity of the cathode was due to the byproducts diffusion, a degassed LDPE plaque with XLPE semicons (Sample D) has been tested. Figure 6.8 and 6.9 illustrate the space charge and interfacial stress evolution of "Sample D" within 24 hours ageing (24.19 *kV/mm*) at room temperature (25 ^{O}C).

It can be seen from Figure 6.8 that in the degassed "Sample D" there was only negative charge accumulation throughout the 24 hours ageing period. In addition, the evolution of the space charge accumulation inside the bulk was similar to what was encountered in the as-received "Sample C". However, in contrast to what was observed in the as-received LDPE sample with XLPE semicons, there was no indication of the small amount of positive charge accumulated in the vicinity of the cathode. By comparing the results of "Sample C and D", the degassing process is responsible for the difference in the observed results. The origin of the small negative peak at the interface region in sample C over the first 8 hours of dc ageing is possibly due to the image positive charge close to the electrode, which is created by the ionisation of the cross-linking byproducts diffused from the XLPE semicons into the LDPE bulk during the sample manufacturing process.

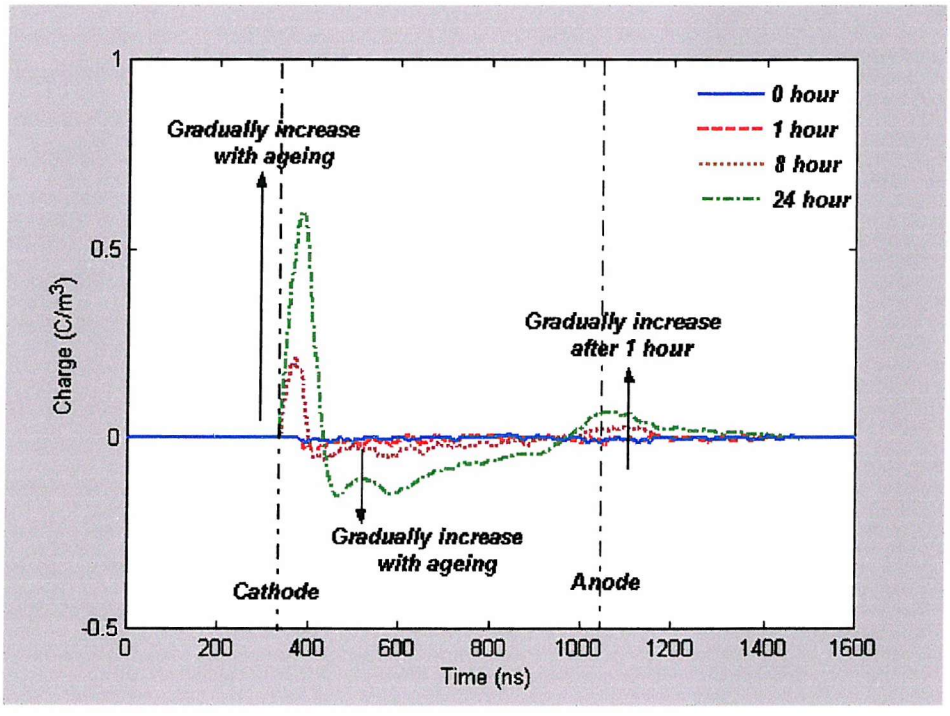

Figure 6.8 The evolution of the space charge formation of the "Sample D" during 24 hours ageing process (Volts off)

Referring to Figure 6.9, similarly to what was observed for the degassed "Sample B", it has been noticed that after 24 hours of ageing the stress at the cathode was reduced approximately by 40 % compared to that at 0 hours. The decreased stress at the cathode agreed with the suggestion that the homocharge (i.e. negative) injection from the

cathode and the removal of the byproducts via the degassing process from the bulk of LDPE sample with XLPE semicon was the cause of this effect.

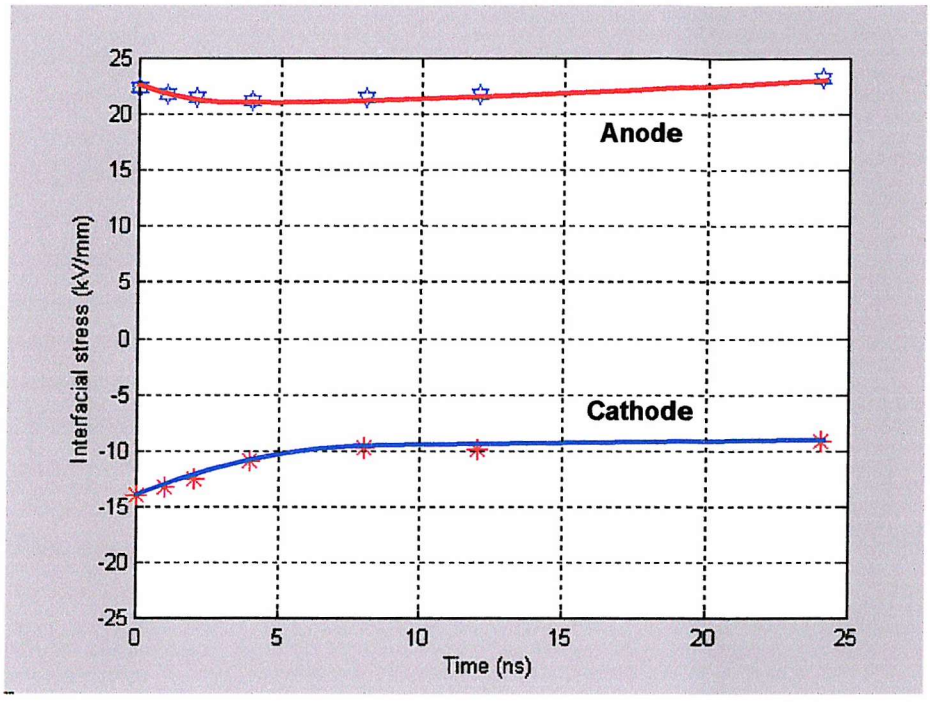

Figure 6.9 The interfacial stress of the "Sample D" during 24 hours ageing process (Volts on)

❖ ***LDPE with LDPE semicon plaque (Sample E)***

To correlate the semicon material selection to that of the space charge dynamics within the bulk insulation, a LDPE plaque with LDPE semicons has been tested. Figure 6.10 and 6.11 show the space charge distribution and interfacial stress evolution of "Sample E" within 24 hours of ageing (24.19 kV/mm) at room temperature (25 ^{O}C).

It was noticed that there was no significant trapped charge accumulation within the LDPE bulk insulation (Figure 6.10) and electric stresses at both of the electrodes were constant (Figure 6.11) throughout the whole period of 24 hours dc ageing. By comparing the ageing results between samples with XLPE semicons and LDPE semicons, it is confirmed that the negative charge injection from the cathode only takes place in the samples with XLPE semicon electrodes, not with LDPE semicon electrodes.

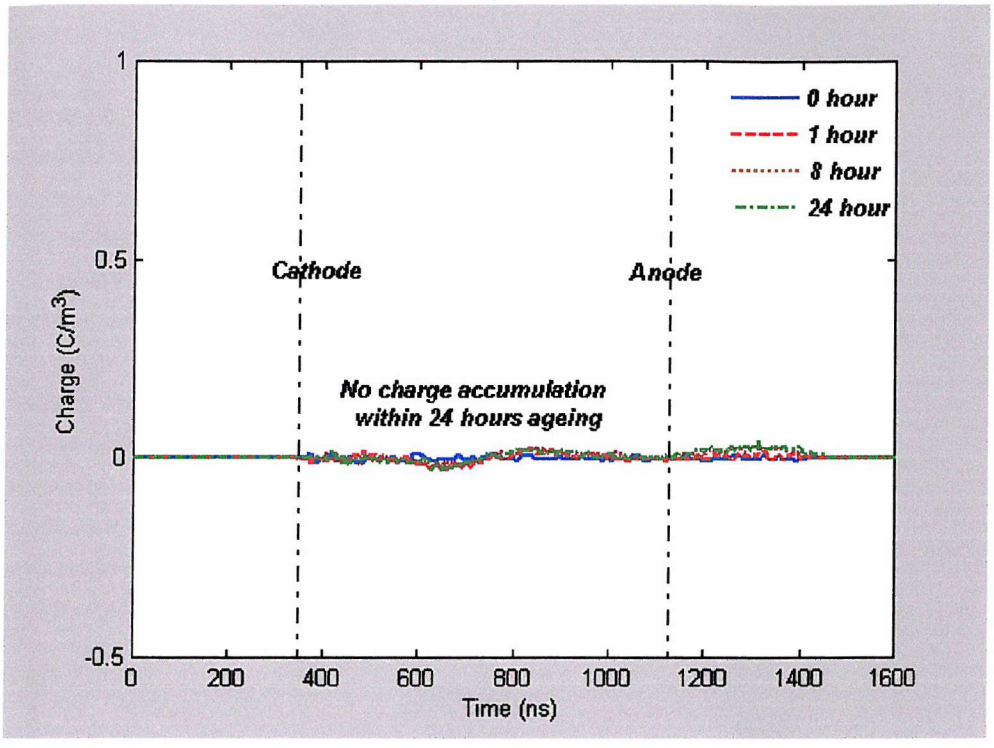

Figure 6.10 The evolution of the space charge formation of the "Sample E" during 24 hours ageing process (Volts off)

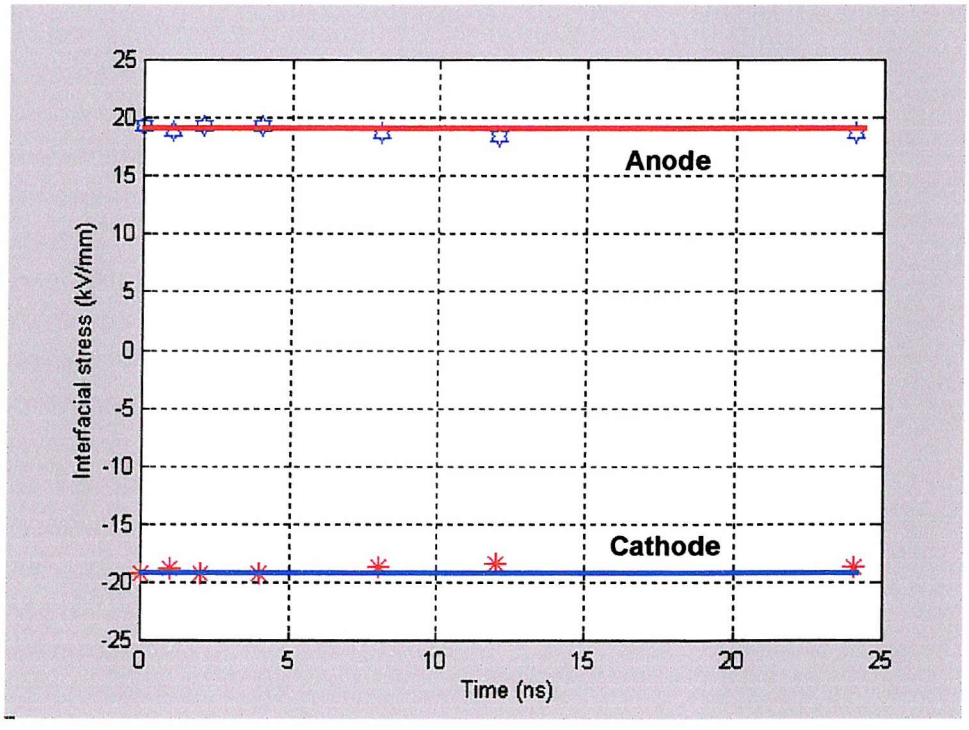

Figure 6.11 The interfacial stress of the "Sample E" during 24 hours ageing process (Volts on)

6.5 Sample comparison

According to the sample supplier (BICCGeneral cable), "XL1046 (XLPE) and P285 (LDPE)" being tested in the project are newly designed material for use in HV dc power cables. Therefore, the space charge level under HV dc electric stress was expected to be lower than the conventional XLPE insulation material (P153), which has been extensively tested by another researcher in the previous project. In order to verify the above information, this section summaries the dc ageing results (shown in section 6.4) and makes a comparison with the conventional insulation material (P153).

In the previous section, we have already demonstrated that the entrance and exit peak magnitudes (i.e. interfacial stresses) of the LIPP signal are correlated to the space charge evolution within the bulk insulation and the results have shown that the space charge effect within the tested samples were more pronounced at the cathode (i.e. entrance peak) than anode (i.e. exit peak). Therefore, in order to analyse and compare different materials during the electric ageing period without resorting to a complex mathematical treatise, a simple method, which based on the percentage deviation of the entrance peaks, has been used.

6.5A Method of analysis

The procedure used for analysing the *ageing data* was:

I. To calculate the entrance peak current per unit stress at each ageing time,

$$\frac{mA}{kV/mm} = \frac{\text{Peak current}}{\text{Applied stress}} \text{ --------- (6.1)}$$

II. To calculate the average value of the entrance peak current per unit stress at different ageing times for each material, (more than one sample of each material had been tested)

III. Since the samples (P153) have been tested three years ago using the old LIPP system (without the on line laser power monitor measurement), and in order to remove the effect of the variation in the laser power and system setting on the output current level, the average entrance peak current per unit stress at different ageing times was

normalised with respect to the average entrance peak current per unit stress at 0 hours for each material.

IV. To plot the percentage changes in the normalised entrance peak currents per unit stress obtained in step III, which represents the variation of the space charge level during the ageing period versus the insulation material, semicon effect and the sample treatment (Figure 6.12 and 6.13).

6.5B Results of the sample comparison

The percentage changes in the entrance peak for different samples during 24 hours dc ageing are shown in Figure 6.12 and Figure 6.13. These results effectively indicate the percentage change in the level of space charge, where 100 % indicates no space charge effect at the cathode. Any value below 100 % represents homocharge formation and any value above 100 % represents heterocharge formation close to the electrode/ insulation interface (i.e. cathode).

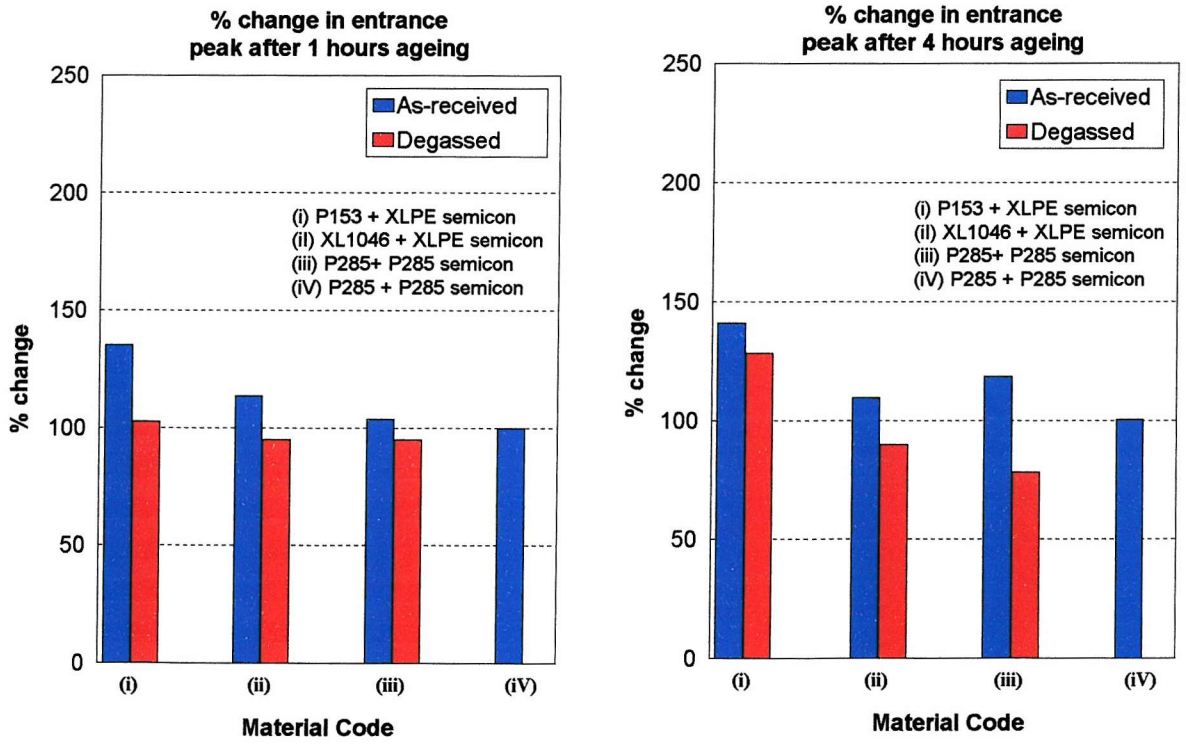

Figure 6.12 Percentage variation in entrance peak magnitude after 1 and 4 hours

According to the above results, the as-received and degassed P153 samples (i) gave a positive percentage deviation (i.e. interfacial stress enhancement) of the entrance peak within the whole period of dc ageing. The deviations became approximately 10 times higher than that measured in samples (ii) and (iii) after 24 hours. These results clearly indicate the improvement of the dc space charge performance in the newly designed material XL1046 and P285.

By comparing the results between the newly designed as-received and degassed XLPE samples (ii), it was also noticed that over the 4 hours to 8 hours of dc ageing, the as-received XLPE samples give a positive percentage deviation (i.e. interfacial stress enhancement) and the degassed XLPE samples give a negative percentage deviation (i.e. interfacial stress reduction). The differences in the results clearly illustrate the effect of sample treatment (degassing). It indicates that the space charge dynamics in the as-received sample is governed by the ionisation process (i.e. heterocharge formation) and while in the degassed sample it is governed by the injection process (homocharge injection) within the first 8 hours of dc ageing.

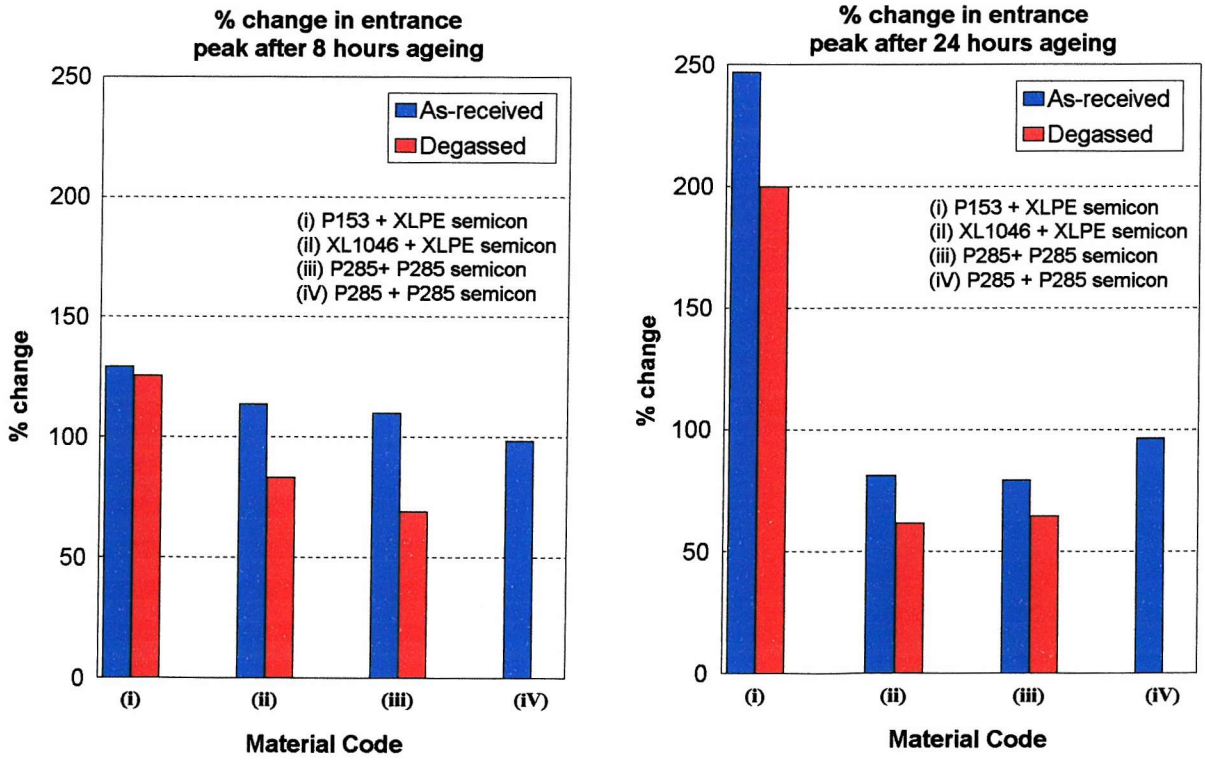

Figure 6.13 Percentage variation in entrance peak magnitude after 8 and 24 hours

After 24 hours, it can be seen that the percentage deviation of the entrance peak in the as-received XLPE sample (XL1046) gave a negative value (i.e. stress reduction at the cathode). However, the conventional XLPE sample P153 still shows a relatively high positive percentage deviation (i.e. interfacial stress enhancement). A few possible causes for the phenomena observed above are listed below:

- As the recipe for P153 is quite different from samples tested even after the degassing process, there might be more cross-linking byproducts left in P153 than that of as-received XL1046.
- In addition, after 24 hours most of the dissociable byproducts in the as-received XL1046 have been ionised, leading to formation of heterocharge close to the cathode. The stress enhancement caused by the heterocharge formation (i.e. ionisation) close to the cathode initiates the negative charge injection and reduces the interfacial stress of the as-received XL1046.

In order to get a better idea for material and semicon selection and to investigate the effect of XLPE semicons on the space charge formation in the LDPE insulation, LDPE samples with XLPE semicons have been tested. According to the results shown in Figures 6.12 and 6.13, it is interesting to notice that the trend of the interfacial stress at the cathode of (ii) and (iii) was similar during the dc ageing. Since both of the samples have the same semicons, this suggests that the space charge is dominated by the semicon effect rather than bulk insulation.

Finally, in the case of the LDPE with LDPE semicons, the samples showed a significant lower level of space charge than the as-received LDPE with XLPE semicons. There was only a <3 % reduction in the interfacial stress after 24 hours ageing. Compare this value to the as-received LDPE with XLPE semicons (-20.5 %), it is believed that the difference may be attributed to the LDPE semicon electrodes that were used with this sample. Consequently the level of space charge in the tested samples A to D have been significantly affected and increased by the XLPE semicons.

6.6 Conclusions

In this chapter, the ramp rate (space charge threshold) and dc ageing results (space charge evolution) on the as-received and degassed XLPE (XL1046) and LDPE (P285) samples with different semicon electrodes (Sample A to E) are presented. The repeatable results have proved that the newly designed LIPP measurement system is fit for the purpose, and is suitable for the determination of the space charge distribution of the plaque sample under dc stressing conditions.

In addition, in order to verify the space charge performance of the newly designed dc insulation materials from BICCGenernal Cable, comparisons on the space charge level between the tested samples (A to E) and the conventional insulation material (P153) are also reported.

DC ramp and ageing test

- ***Ramp rate test***

1. The ramp rate results demonstrated that by using XLPE semicon electrodes the homocharge formation is significant during ramp rate measurement.

2. The results showed that the after the removal of the cross-linking byproducts within the XLPE bulk insulations via the degassing process the threshold stress within XLPE sample with XLPE semicon electrodes reduced approximately by 30.0 %.

3. Since there were no cross-linking byproducts in the LDPE bulk insulation, the effect of degassing process on the threshold stress was found insignificant during the ramp measurements.

4. The LDPE samples with LDPE semicon electrodes indicated that there was no significant space charge formation even at high electric stresses (~19.2 *kV/mm*) during the ramp test. Therefore, it can be concluded that the source of the negative charge close to the cathode (i.e. Sample A to D) during the ramp rate measurement was due to the homocharge injection from the XLPE semicon electrodes.

- ***Dc ageing test***

The dc ageing results presented in this chapter have shown that the space charge accumulation in the as-received XLPE samples with XLPE semicon electrodes mainly resulted in heterocharge formation. These observations were consistent with the results published by other researchers, where the charge formation was explained by field assisted ionisation of cross-linking byproducts within the bulk insulation. However, as the positive charge close to the cathode diminish gradually over the ageing period, it is believed that after all the available cross-linking byproducts within the bulk insulation have been ionised, the charge injection dominated the charge dynamics and the negative charge injected from the cathode recombined with the positive charge, leading to a reduction in positive charge.

For the degassed XLPE samples with XLPE semicon electrodes, there was no positive charge formation inside the bulk insulation throughout the 24 hours dc ageing period. However, the amount of negative charge within the bulk increased significantly during ageing. This indicated that the injection process governed the charge dynamic in the degassed XLPE sample and the negative charges are originated from the homocharge injection from the cathode.

In the case of the as-received and degassed LDPE samples with XLPE semicon electrodes, both of the resulting space charge distributions were similar to what was encountered in the degassed XLPE sample, with the exception of a small amount of accumulated positive charge at the interface of the as-received sample during the first 8 hours of dc ageing. It concluded that by applying XLPE semicons to LDPE bulk insulation, the cross-linking byproducts from the semicons might diffuse across the XLPE/LDPE interface, which affects the space charge performance.

For the LDPE samples with LDPE semicon electrodes, there was no significant charge accumulation within the bulk insulation and electric stresses at both of the electrodes were constant throughout the period of dc ageing. By comparing the ageing results between samples with XLPE semicons and LDPE semicons, it can be deduced that the negative charge injection from the cathode is only occurring in the samples with XLPE semicons, not with LDPE semicons.

Samples comparison

A great improvement in the dc space charge performance in the newly designed material has been achieved. The interfacial stress of the conventional material (P153) is approximately a 150 % than the newly designed materials (XL1046 and P285) after 24 hours dc ageing.

The difference in the interfacial stress between the as-received and degassed sample in the newly designed materials is small (<15 %) compared to the conventional insulation material P153 (~50 %) after 24 hours of dc ageing. This indicates that the effect of the sample degassing process on the conventional insulation is more significant than on the newly designed material for a given applied voltage.

The LDPE samples with LDPE semicon electrodes only shows a <3 % reduction in the interfacial stress after 24 hours ageing, which is insignificant comparing with the value of the as-received LDPE with XLPE semicon electrodes (-20.5 %). Therefore, from the point of view of space charge performance, the LDPE samples with LDPE semicons is better than the XLPE samples with XLPE semicons and the LDPE samples with XLPE semicons under HV dc application.

Chapter 7

Space charge accumulation in the plaque samples under ac electric stress

7.1 Introduction

Work on the dynamics and the role of space charge on electrical breakdown under 50 *Hz* ac conditions has only received limited attention. However, there is an increasing body of opinion that space charge build up can be a contributing factor to electric tree initiation in high voltage insulation. The majority of XLPE cables will be operating under ac conditions in the immediate future, therefore it is important to investigate the charge trapping and mobility under such conditions.

This chapter reports the results of space charge and electric stress distribution under 50 *Hz* ac stresses by using the newly designed LIPP system. Samples used are the as-received and degassed cross-linked polyethylene (XLPE) and LDPE plaque samples with two different kinds of semicon electrodes. The samples were electrically aged at room temperature at stresses in the region of 20 to 30 kV/mm_{peak} for a period of 24-hours. Measurements were taken at various times. Emphasis has been placed on establishing a simple method, termed "X-plots" for analysing the vast amounts of ac space charge data without resorting to a complex mathematical treatise. A comparison of the ac space charge characteristics between these two insulation systems with the different semicon electrodes has been made. In addition, the effects of sample treatment (i.e. degassing) on the space charge dynamics under the ac electric stresses are also presented.

7.2 AC experimental procotols and sample details

7.2A Experimental protocols

According to Fanjeau et al [162], the effect of fast charge (charge with high mobility) is expected to be more significant than the slow charge (charge with low mobility) under

50 *Hz* ac ageing conditions. Consequently, all the measurements were taken with the ac voltage applied across the sample (volts on). The as-received and degassed samples were aged at ac stresses in the region of ≤30 kV/mm_{peak} for a period of 24-hours at room temperature (25 °C). The charge distribution was measured at various times using the protocols shown in Table 1.

Data	*Time (hrs)*	*Data point*	
		<25 kV/mm	30 *kV/mm*
1 cycle of data points	0	1-9	1-17
1 cycle of data points	1	10-18	18-34
1 cycle of data points	8	19-27	35-51
1 cycle of data points	24	28-36	52-68

Table 7.1 Ac experimental protocols

7.2B Sample details

Sample no	**Polymer**	**Semicon**	**Treatment**	**Bulk thickness (*mm*)**	**Applied Stress (*kv/mm*)**
F	XLPE (XL1046)	XLPE	1	1.30	23.10
G	XLPE (XL1046)	XLPE	2	1.40	21.43
H	LDPE (P285)	XLPE	1	1.29	23.26
I	LDPE (P285)	XLPE	2	1.24	24.19
J	LDPE (P285)	LDPE	Nil	1.56	19.20
K	XLPE (XL1046)	XLPE	1	0.8	30
L	XLPE (XL1046)	XLPE	2	0.8	30

Table 7.2 Plaque sample details (Treatment 1: as-received, Treatment 2: degassed)

The samples used in the study were as-received and degassed cross-linked polyethylene (XLPE) and LDPE plaques. Both the front and the rear semicon electrodes were hot pressed on to the sample. The semicon electrodes were made of the either XLPE or LDPE material, but were loaded with carbon black to increase its conductivity. The resultant thickness of the bulk insulation was between 0.7 *mm* to 1.6 *mm*. The degassing was carried out by heating

the samples to 60°C for 48 hours to remove cross-linking byproducts. The samples details are shown in Table 7.2.

7.3 AC data presentation --- "X-plots"

It is known from previous dc studies that without the presence of trapped charge in the bulk, the magnitudes of the entrance and exit peaks (positions of both peaks are shown in figure 7.1) and hence the interfacial stresses are linearly dependent on the instantaneously applied voltage. With space charge present, the magnitudes of the current peaks deviate from this linear relationship depending on the nature of the charge formation inside the bulk.

Figure 7.1a shows a typical output current signals at 3 different selected points on the ac waveform for a 0.8 *mm* XLPE plaque subjected to 24 kV_{peak} ac voltage. The corresponding voltages across the sample during the space charge measurements are shown in Figure 7.1b. By plotting the magnitudes of the entrance and exit peaks against the instantaneous applied ac voltages, a diagram which summaries the information of the ac space charge effect is produced, this kind of data presentation is termed "X-plot" within this thesis.

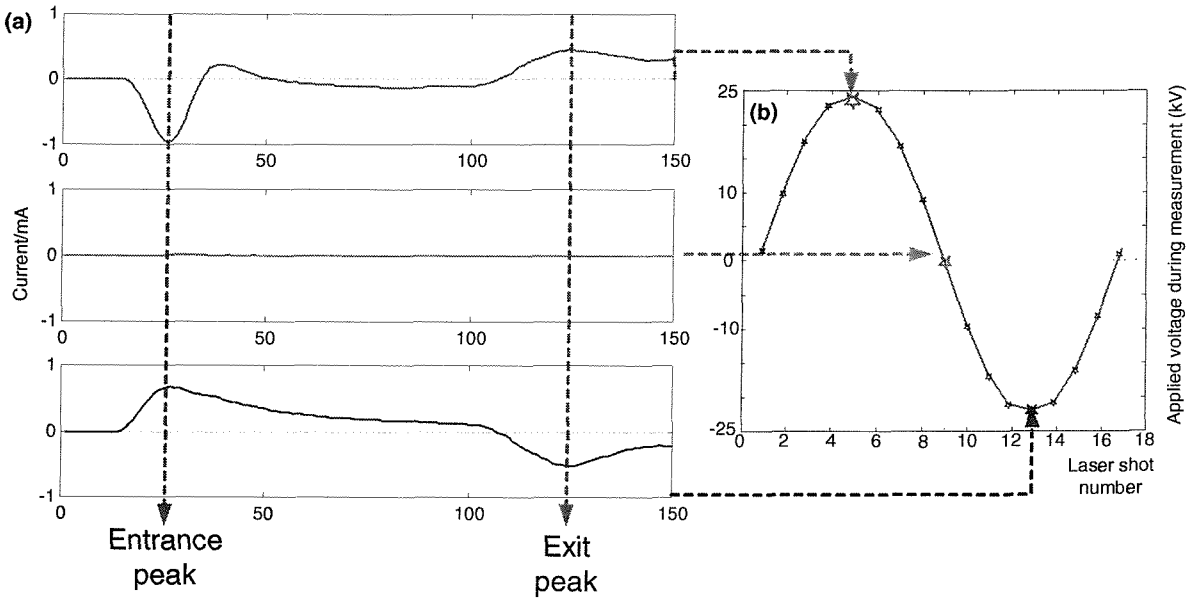

Figure 7.1 Typical results of XLPE sample at 30 kV/mm_{peak} ac electric stress (Sample L at 0 hours)

Figure 7.2 shows an example of the X-plot of a XLPE sample, illustrating that both entrance and exit peaks vary linearly when the magnitude of the instantaneous voltage is below

9 kV_{peak}. However, when the instantaneous voltage magnitude is above 9 kV, the amount of space charge in the bulk is sufficient to modify the interfacial stresses at both electrodes and affect the linear dependence of the current peak height with the applied voltage. In this case, 9 kV is defined as the "threshold voltage" above which space charge can be formed within the bulk insulation. Therefore, calibration should only carried out below the threshold voltage.

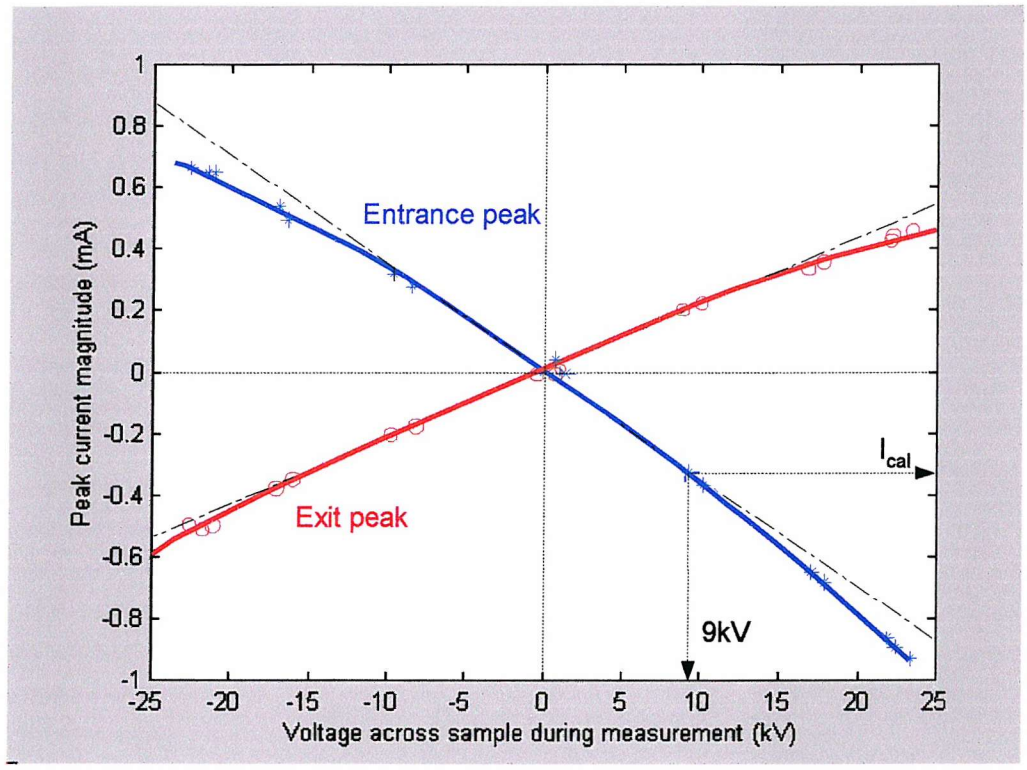

Figure 7.2 Example of calibration X-plot (Sample L at 0 hours)

7.4 AC experimental results and discussion

7.4A Results of ac ageing in the region of 25kV/mm$_{peak}$

- ***XLPE with XLPE semicons (Sample F and G)***

The X-plots of Sample F and G at 0 and 24 hours ac ageing are shown in Figure 7.3. The results show that during the positive half ac cycle at 0 hour (Figure 7.3a and 7.3c), the magnitude of the entrance peak (cathode) of the as-received and degassed XLPE with XLPE semicons both deviate positively from the extrapolated straight line by 30 % at

+30 *kV*. It can be concluded that above the threshold voltage (+17 *kV* or +11.3 *kV/mm*), the interfacial stress at the cathode is less than the applied stress, indicating homocharge (injection) has been formed close to the semicon/XLPE interface (cathode).

For the negative half ac cycle at 0 hour, the magnitude of the entrance current peak (anode) follows the extrapolated straight line and the exit peak (cathode) deviates positively from the extrapolated straight line by 15 % at -30 *kV* (i.e. the interfacial stress at the cathode has decreased by around 15 %). The change in the stress is believed to be similar to the phenomena encounter in the positive half cycle in that negative charge (homocharge) developed close to the cathode.

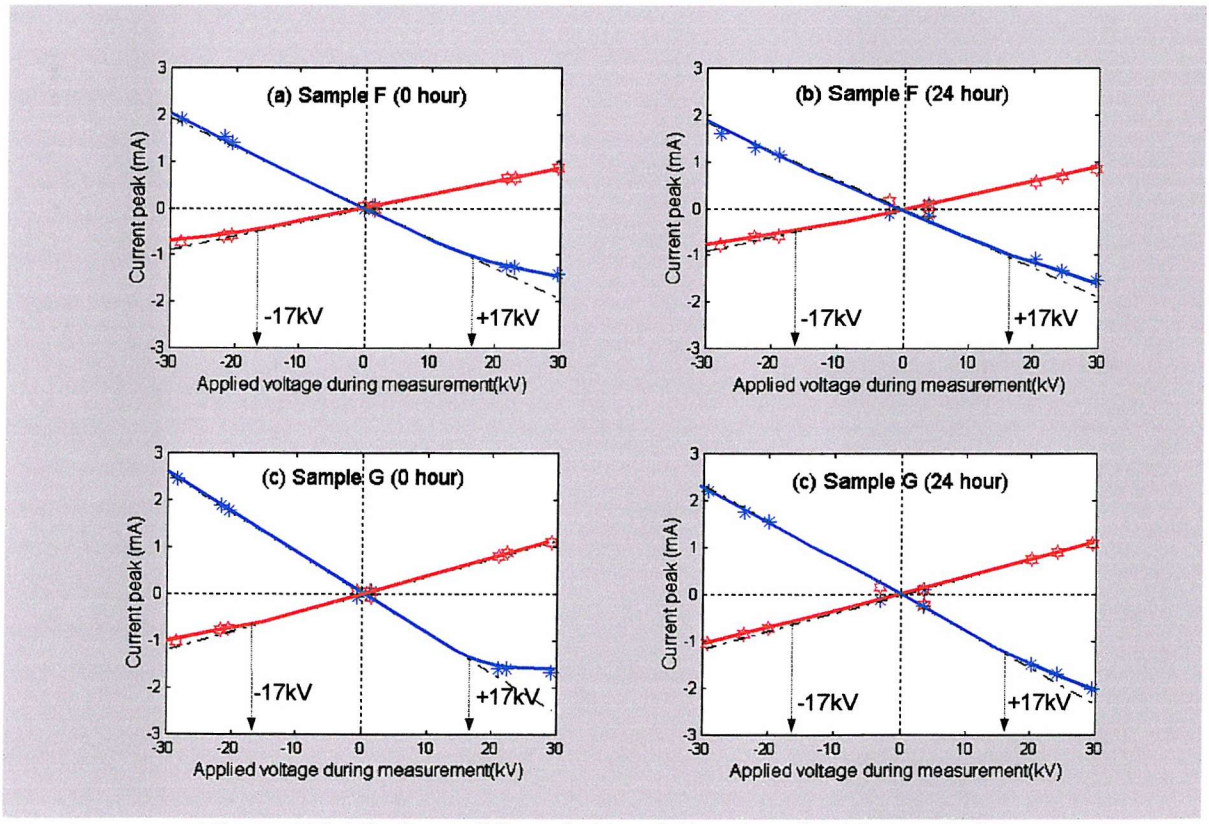

Figure 7.3. X-plots of Sample F and G at 0 and 24 hours (ac)
(Entrance peak-blue, Exit peak-red)

After 24 hours of ac ageing, it was found that the deviation (from the extrapolated straight line) of the entrance peak on the positive half ac cycle was reduced for both samples. The difference between samples with treatment 1 and 2 was insignificant. Therefore, it may concluded that the space charge dynamics for the XLPE with XLPE

semicon electrodes, subjected to 50 Hz ac electric stress depends on the ac ageing period and may be unaffected by the sample degassing process.

- ***LDPE with XLPE semicons (Sample H and I)***

The X-plots of Sample H and I at 0 and 24 hours of ac ageing are shown in Figure 7.4. Similar to the results encountered in sample F and G, the magnitude of the entrance peak (cathode) deviates positively from the extrapolated straight line by 30 % at +30 kV during the positive half ac cycle (at 0 hour). It means that above the threshold voltage (+13 *kV* or +8.7 *kV/mm*), the interfacial stress at the cathode is less than the applied stress, indicating that homocharge (injection) has been formed close to the semicon/LDPE interface (cathode).

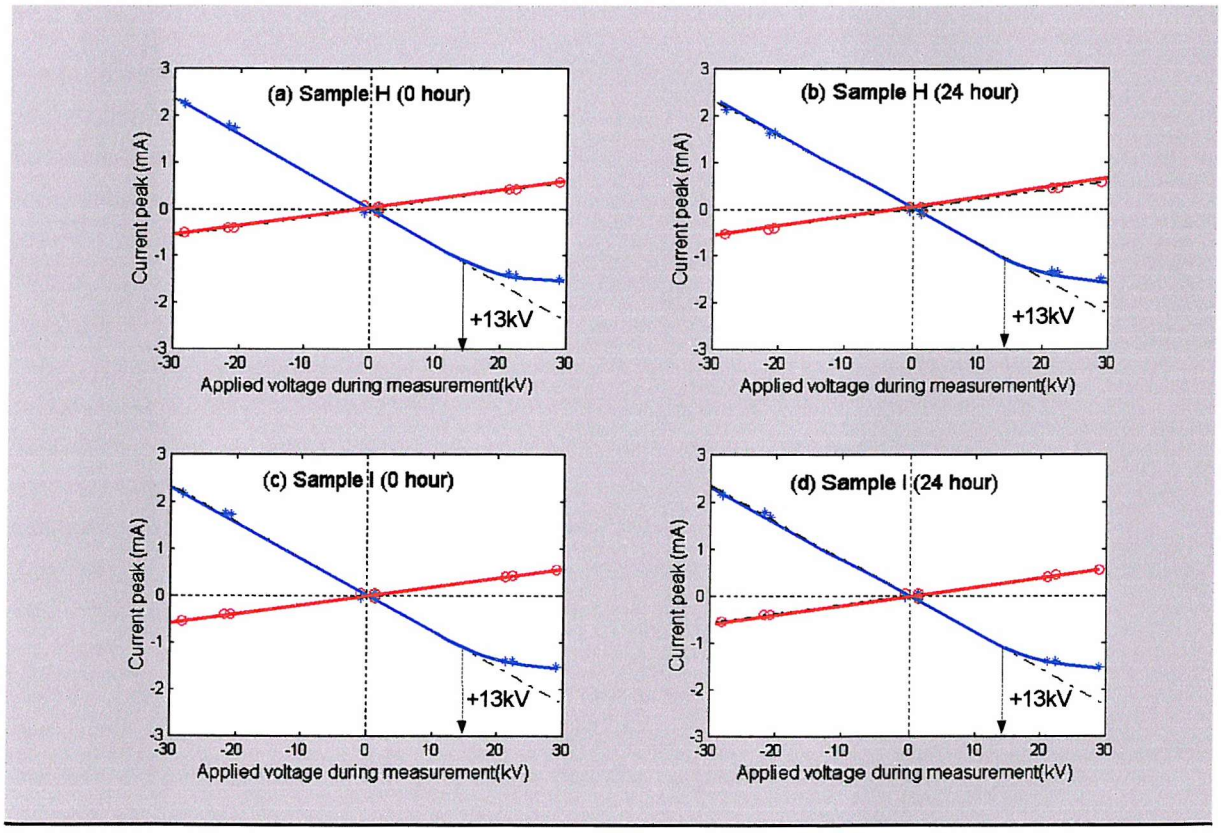

Figure 7.4. X-plots of Sample H and I at 0 and 24 hours (ac)
(Entrance peak-blue, Exit peak-red)

However, comparing with what was observed in the XLPE samples F and G, there was no deviation (from the extrapolated straight line) of the exit peak (cathode) on the negative half ac cycle. This may be due to the reduction of the measurement resolution

at the exit peak because of the high attenuation of the signal through the LDPE sample or the loss of acoustic energy due to the mismatch of the acoustic characteristic of the LDPE bulk insulation and the XLPE semicons.

There is no significant difference between the X-plots at 0 and 24 hours for both samples H and I (Figure 7.4b and 7.4d). It can be deduced that the space charge effects in the LDPE with XLPE semicons may be independent on the ac ageing period (in the region of 25 kV/mm$_{peak}$) and also is unaffected by the sample degassing process.

- ***LDPE with LDPE semicons (Sample J)***

Figure 7.5 shows the X-plots of Sample J at 0 and 24 hours ac ageing. It is observed that there is no peak deviation from the straight line either during positive or negative half ac cycle at 0 and 24 hours (Figure 7.5a and 7.5b). These features indicate that there are no space charge effects in the LDPE sample with LDPE semicon electrodes under 50 *Hz* ac electric stresses. The interfacial stress at the cathode and anode is proportional to the applied stress.

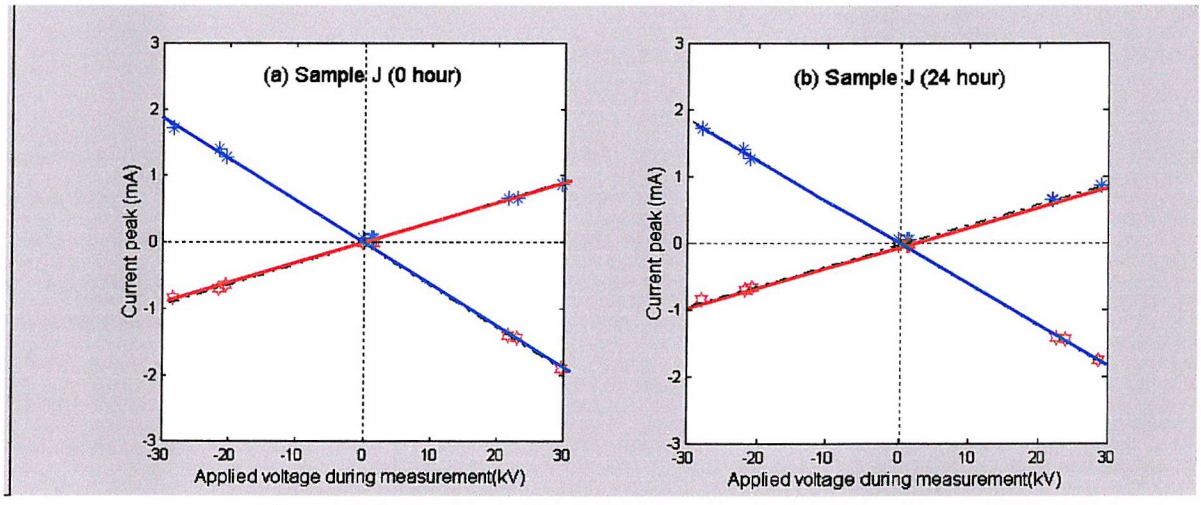

Figure 7.5 X-plots of Sample J at 0 and 24 hours (ac)

(Entrance peak-blue, Exit peak-red)

7.4B Results of ac ageing of XLPE sample with XLPE semicon at 30kV/mm$_{peak}$

Referring to the ac ageing results reported in the previous section, it has been shown that the effect of sample treatment (degassing) on the space charge threshold under ac conditions is

not as significant as under dc. The results also showed that the effect of ac ageing on space charge in the XLPE samples with XLPE semicons (i.e. Sample F and G) is evident, but not in LDPE samples with XLPE or LDPE semicons (i.e. Sample H, I and J).

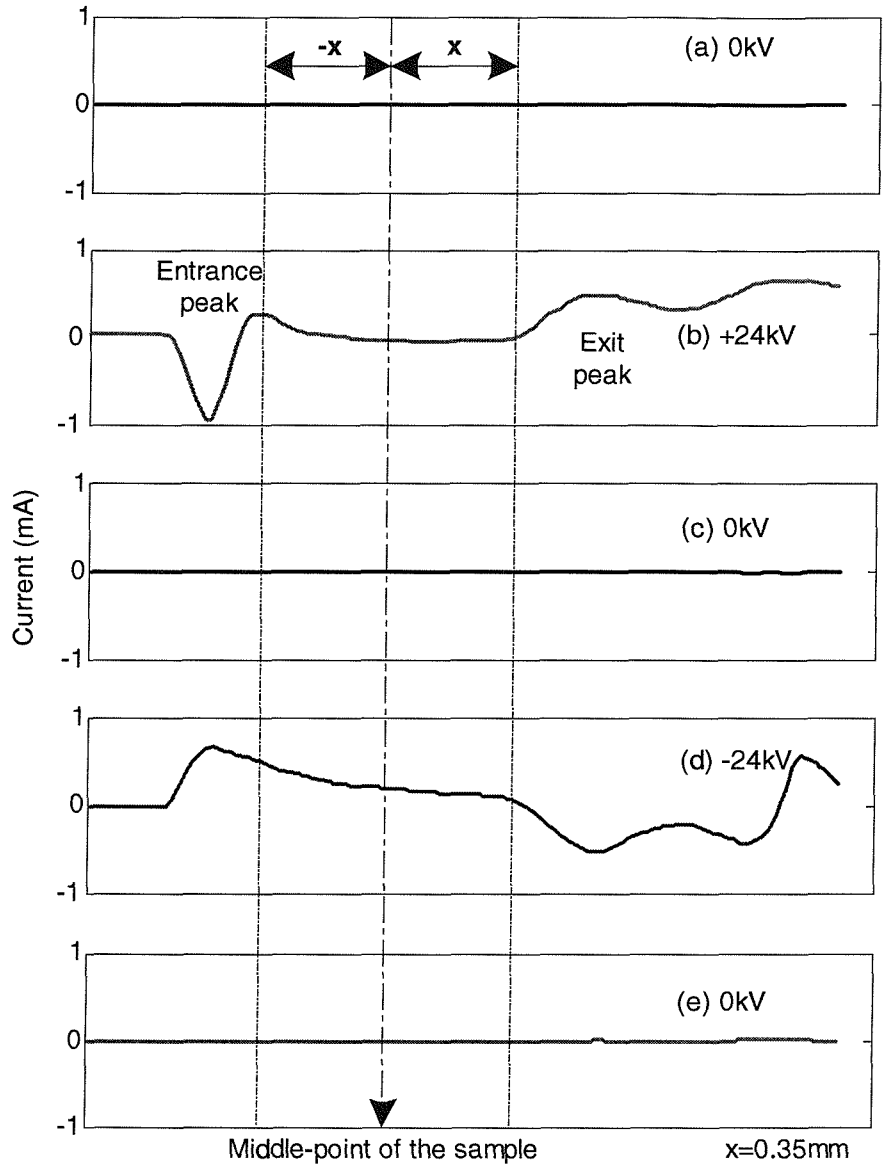

Figure 7.6 (a) to (e). Space charge distribution signal at phase angle of (a) 0^{o},(b) 90^{o},(c) 180^{o},(d) 270^{o} and (e) 360^{o} (Degassed sample L at 0 hours)

In order to explore further the ac ageing effect in the XLPE insulation, two 0.8 *mm* thick XLPE samples with XLPE semicons (Sample K and L) have been tested at the higher ac electric stress level ($30\ kV/mm_{peak}$).

Figure 7.6 shows the output current signals at five different selected points on the ac waveform for a degassed XLPE sample (Sample L). The corresponding voltage and stress across the sample during the space charge measurements are shown in Figure 7.7. By plotting the magnitudes of the entrance and exit peaks against the instantaneous applied ac voltage (X-plots), the threshold stress and the corresponding calibrated peak current I_{cal} can be established.

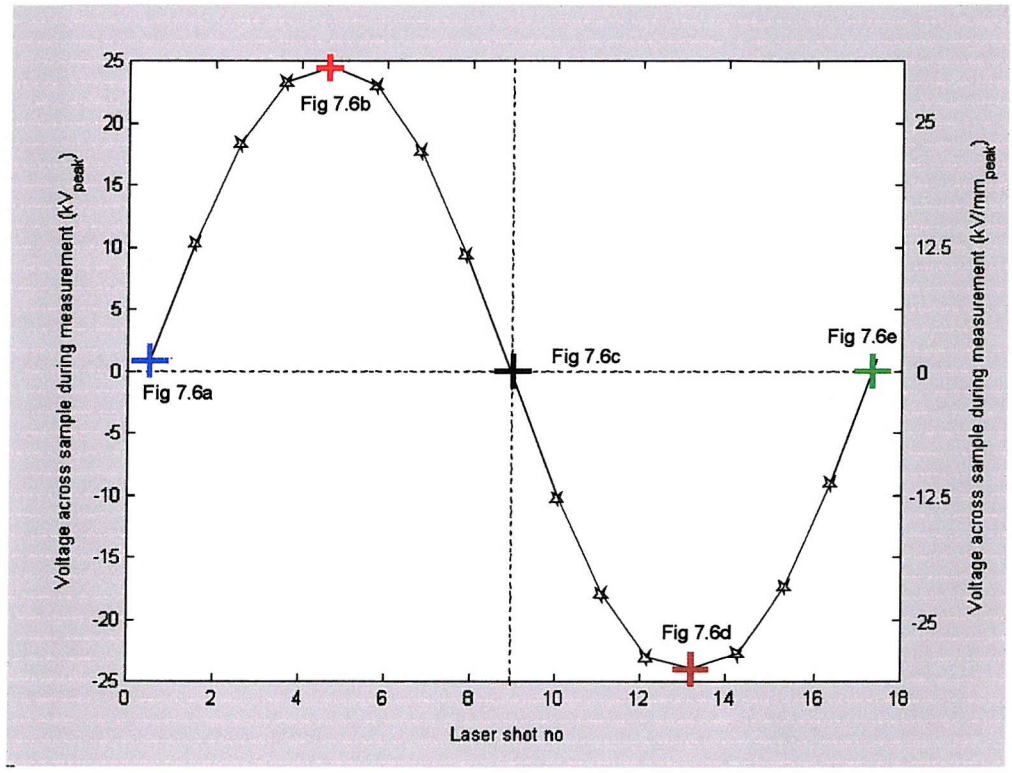

Figure 7.7. Five selected points on voltage wave during measurement (Degassed sample L at 0 hours)

Figure 7.8 shows the X-plot of the degassed XLPE sample (Sample L) at the beginning of the ac electrical ageing (0-hour). The threshold voltage is 9 kV_{peak} (i.e 11.25 kV/mm_{peak}). In order to achieve high accuracy, the calibration should be carried out at the voltage just below the threshold voltage.

Figure 7.9 shows the calculated space charge density distribution of Sample L at +24 kV_{peak} and -24 kV_{peak}, and the corresponding electric stress distributions by using the data processing technique described in *Section 4.5* are shown in Figure 7.10.

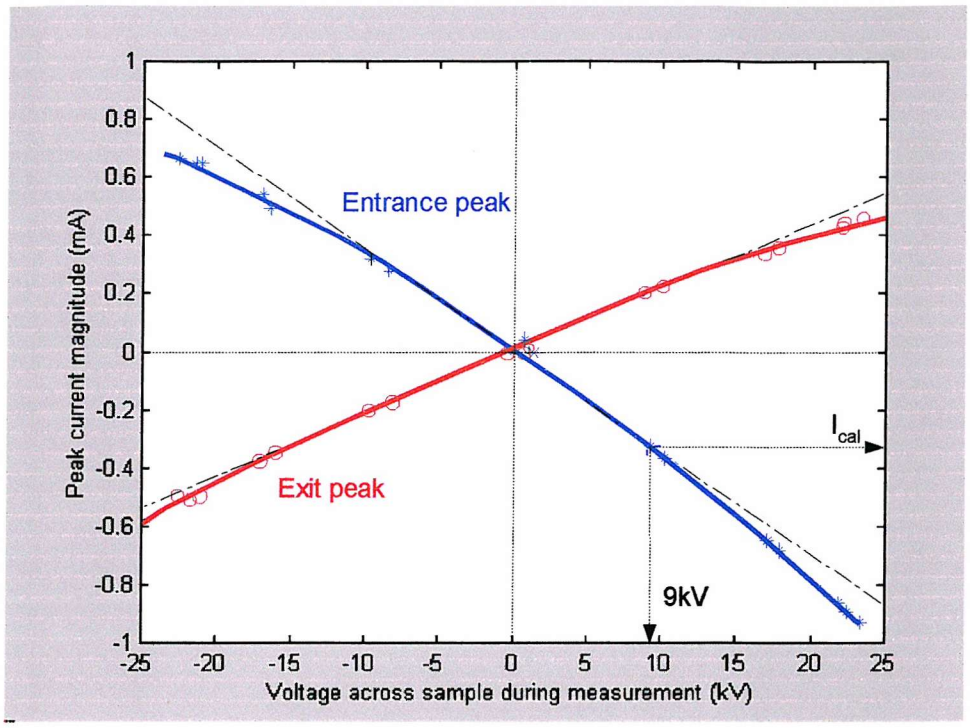

Figure 7.8. Entrance and exit peak heights of current signals
(Degassed sample L at 0 hours)

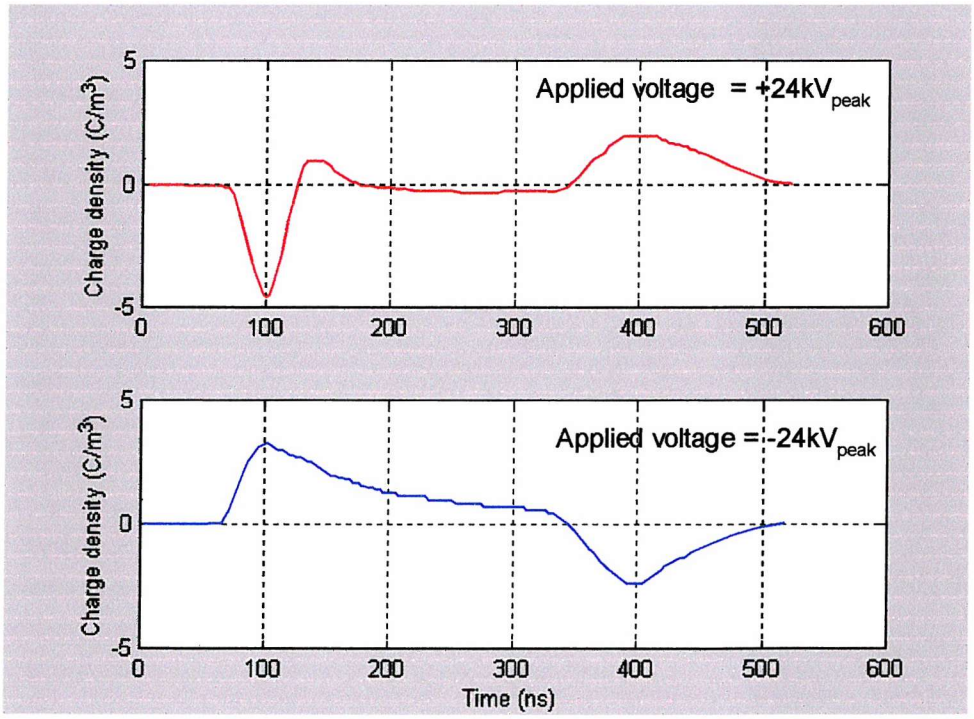

Figure 7.9. Space charge density distribution of degassed sample L at ±24 kV_{peak} (0-hour)

As electrical trees and breakdown in high voltage ac XLPE cable are normally initiated at the interfaces, the emphasis has been placed on the effect of space charge on the stresses at

the electrode/insulator interface (using the X-plot) rather than the stress distribution within the bulk insulation as shown in Figure 7.10.

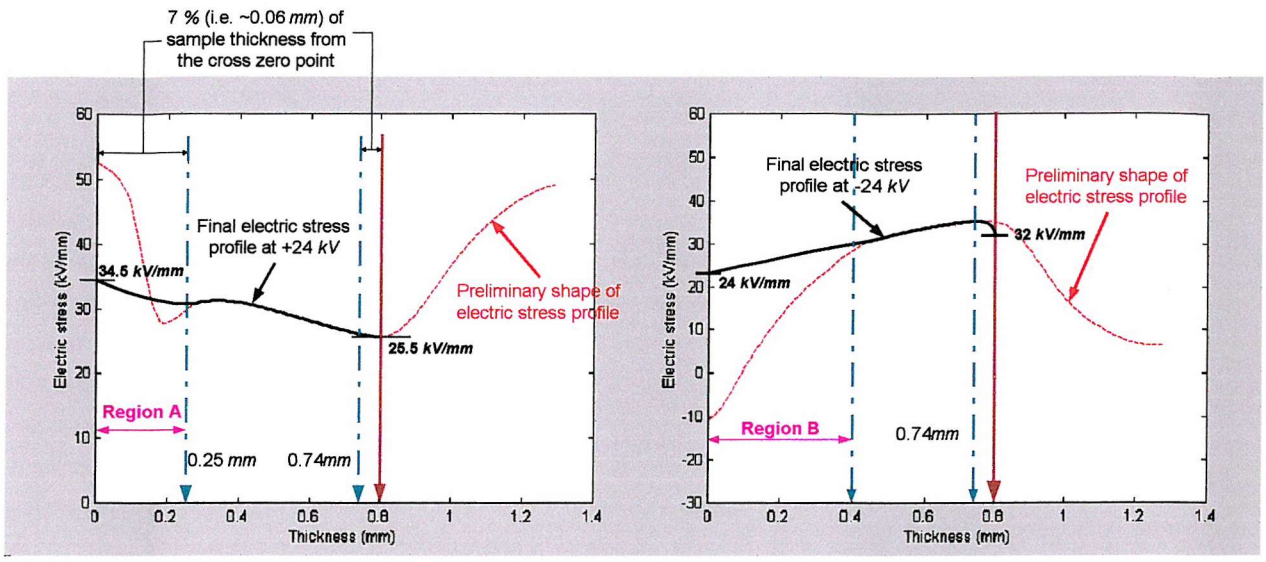

Figure 7.10. Electric stress distribution of degassed sample L at ±24 kV_{peak} at 0-hour (±30 kV/mm_{peak})

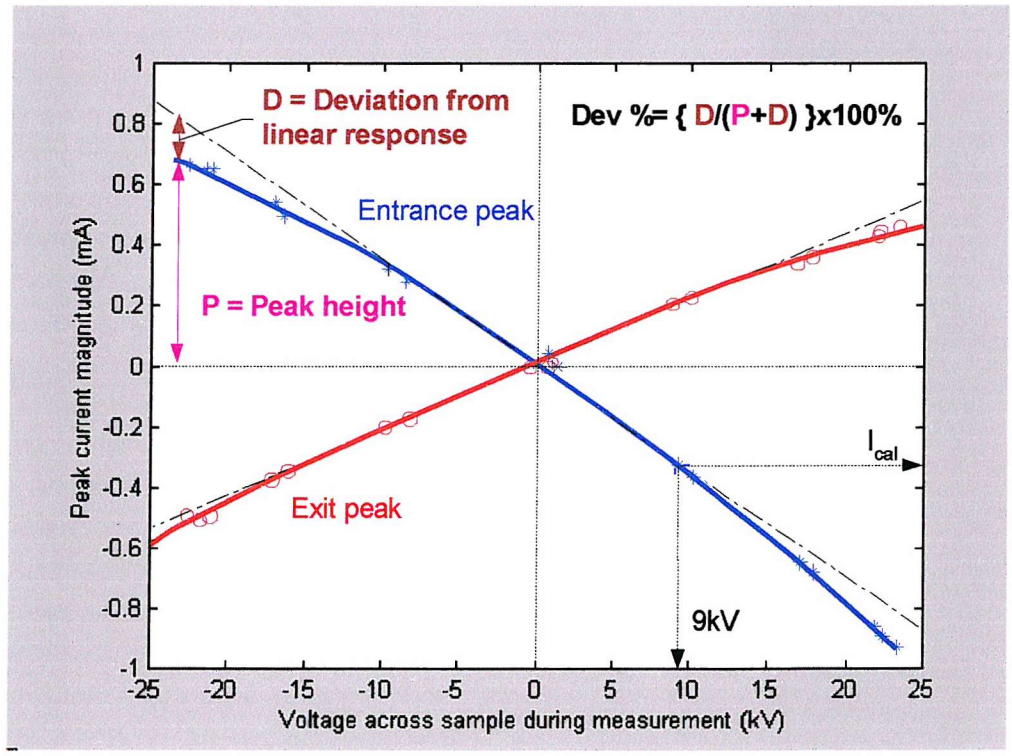

Figure 7.11 Calculation approach of the "Dev%"

In order to summarise the X-plots results and compare the space charge effect at the positive and negative part of the cycle more clearly, the percentage peak deviations (i.e. *Dev%*) away from the linear response are calculated by using the approach shown in Figure 7.11.

Figure 7.12 shows the change in the percentage peak deviations (i.e. *Dev%*) of the degassed XLPE sample (Sample L) at the beginning of the ac ageing (0-hour). The zero deviation between ± 9 kV_{peak} confirms that no space charge is present within the bulk of the sample below the threshold voltage. The interface stresses at both electrodes show a linear dependence on the applied ac voltage. Above the threshold voltage, the deviation becomes non-zero and this shows that there is sufficient space charge within the bulk to modify the interfacial stresses as well as the electric stress distribution within the bulk insulation (Figure 7.10).

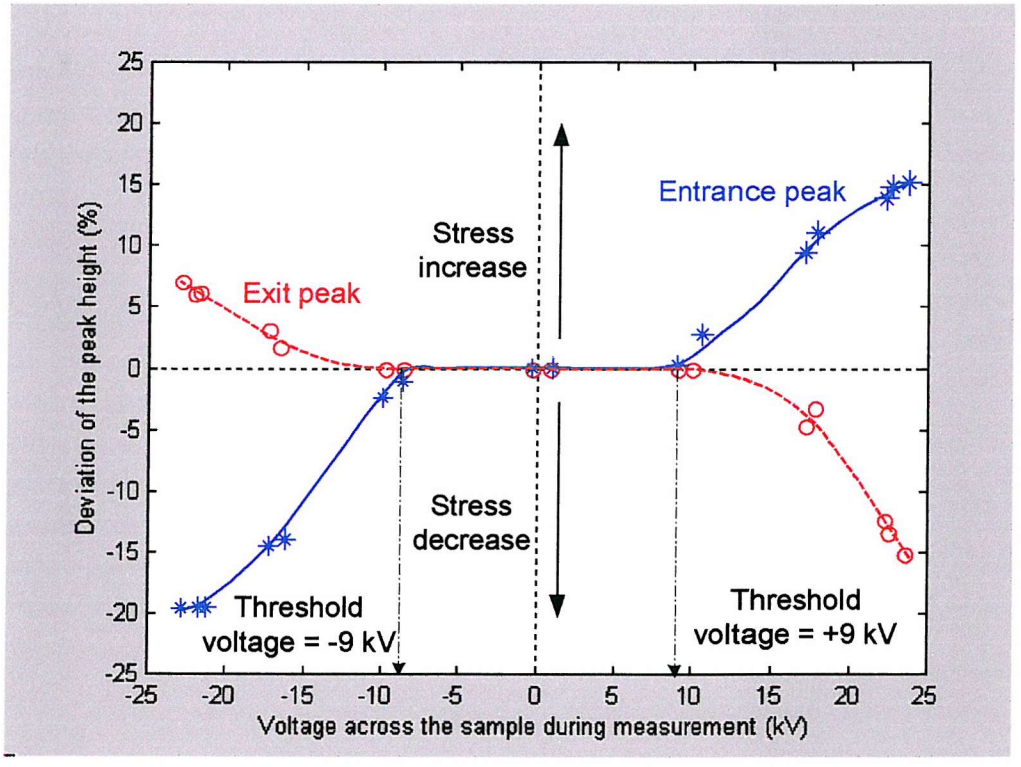

Figure 7.12 Percentage of the deviation of the entrance and exit peak heights (Degassed sample L at 0 hour)

During the positive half ac cycle, the magnitude of the entrance current peak (cathode) increases and the exit peak (anode) decreases with the applied voltage. At an instantaneous applied voltage of 24 kV_{peak} (30 kV/mm_{peak}) the current peak corresponds to the interfacial stress has increased by 15 % at the cathode and decreased by 15 % at the anode. This change in stress may be due to positive charge (heterocharge) developed near the cathode and

positive charge (homocharge) developed near the anode. This suggestion agreed with the output current signal (Figure 7.6b) by the positive peak close to the entrance peak and the broadening of the exit peak.

Referring to Figure 7.6c, at the cross over point of the ac cycle (i.e. 180 degrees), there was no space charge remaining from the previous negative half cycle. This shows space charge can be appear and disappear very quickly under an ac voltage. This supports the assertion in the ac experimental protocol that fast charge formation is more significant than slow charge formation under ac ageing.

For the negative half cycle, different features have been observed at the entrance (anode) and exit peaks (cathode). Figure 7.12 shows that the magnitude of the entrance peak current decreases and the exit peak current increases with the applied ac voltage when the instantaneous voltage across the sample is above -9 kV_{peak} (i.e. -11.25 kV/mm_{peak}). The interfacial stress at the anode with the instantaneous voltage of -24 kV_{peak} (i.e. -30 kV/mm_{peak}) decreases by 20 % and that at the cathode increases by 7 %. This suggests that homocharge (positive charge) is developed near the anode and heterocharge (positive charge) accumulates at the cathode. This agrees with the result shown in Figure 7.6d. The entrance peak of the space charge signal (anode) becomes broader which is associated with the positive charge formation near the anode and some positive current near the exit peak (cathode) suggests heterocharge.

The technique used to produce Figure 7.12 can be applied to any point in the bulk of the insulation. Figure 7.13 shows the magnitude of the current signal at a position ±0.35 *mm* from the middle (Figure 7.6) of the degassed sample (Sample L). If there was no space charge present inside the bulk, the current magnitudes at these two points would show a linear relationship with the applied voltage. In the present case, however, the magnitude of the current signal at -0.35 *mm* starts to deviate significantly from a linear response at an instantaneous voltage of +13 kV_{peak} (+16.25 kV/mm_{peak}). This suggests that substantial positive charge (heterocharge) has developed near the cathode during the negative half ac cycle.

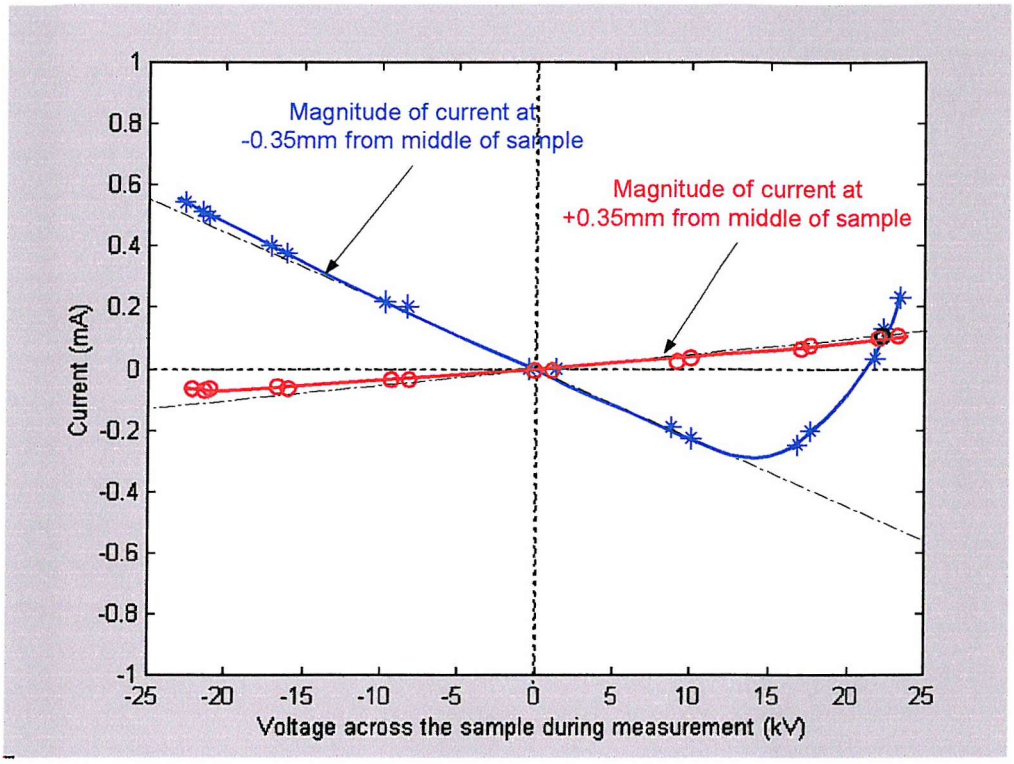

Figure 7.13 Magnitude of current signal at ±0.35 ***mm*** away from the middle of the sample (Degassed sample L at 0 hour)

Similar analysis was carried out on the as-received samples (Sample K), which were electrically aged for up to 24-hours. It has been found that space charge build up showed different features at the entrance and exit peaks during the 24 hours ac ageing period. In particular, it was noted that the variation of exit current peak magnitude was insignificant whilst there was a marked change in the entrance peaks over the period of ageing.

Figure 7.14 shows the percentage deviation of the entrance current peaks for the as-received XLPE sample (Sample K) at 0, 4, 8 and 24 hours of ageing. Over the first 4 hours, the results show similar characteristics to those for the degassed samples (Sample L shown in Figure 7.12). However, after 8 hours ageing, the deviation of the entrance peak height at the positive cycle changes from positive to negative and becomes more significant after 24 hours of ageing. The electric stress close to the cathode increases by approximately 8 % over the first 4 hours and then decreases to –21 % over the next 16 hours. This suggests that the initial accumulation of heterocharge is replaced by homocharge. One possible cause of this is that the stress enhancement caused by the heterocharge close to the interface initiates charge injection from the electrode.

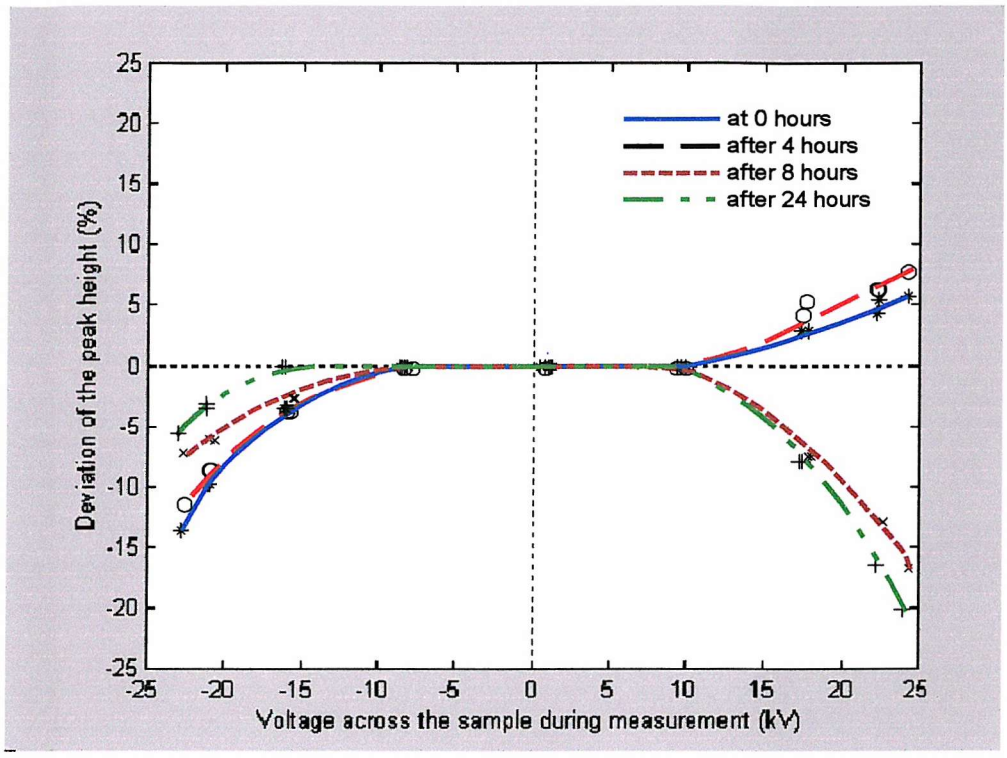

Figure 7.14 Percentage deviation of the entrance peak heights for the as-received XLPE sample K at the 0, 4, 8 and 24 hours within a 24 hour ageing period

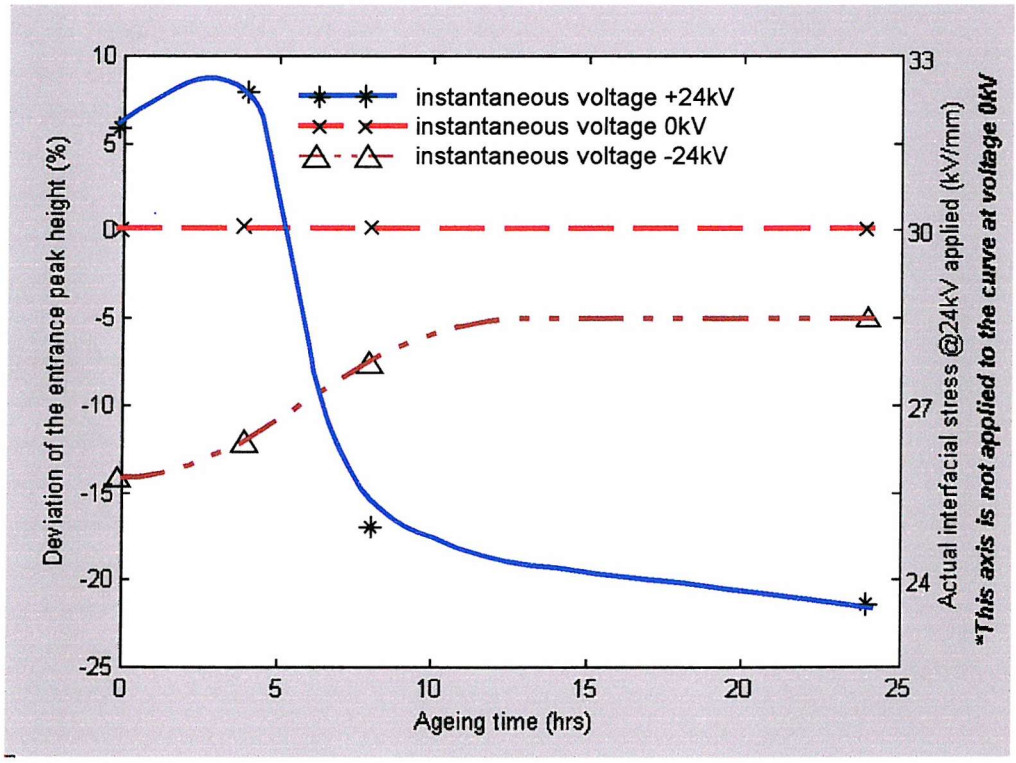

Figure 7.15. Percentage deviation of the entrance peak heights for the as-received XLPE sample K within a 24 hour ageing period at the instantaneous voltages 0, -24 and +24 kV.

Figure 7.15 shows the percentage deviation of the entrance peak heights for the as-received XLPE sample (Sample K) at three selected instantaneous voltages over a 24-hour ageing period (i.e. 0 kV_{peak}, +24 kV_{peak} and -24 kV_{peak}). It was found that at an instantaneous voltage 0 kV_{peak} (i.e. 0 kV/mm_{peak}) the percentage deviation at the entrance peak remained 'zero'; this verifies that fast charge is more pronounced than slow charge over the 24 hour ageing period. However, at an instantaneous applied voltage of -24 kV_{peak} (i.e. -30 kV/mm_{peak}), the deviation of the entrance peak decreases from –14 % to –7 % over the first 8 hours and then gradually decreases to approximately –5 % over the next 16 hours. It implies the amount of homocharge close to the anode at the instantaneous voltage of -24 kV_{peak} (i.e. -30 kV/mm_{peak}) is reduced over the ac ageing period. At an instantaneous applied voltage of +24 kV_{peak} (i.e. +30 kV/mm_{peak}), the entrance peak height increased over the first 4 hours and then decreased over the next 16 hours. This suggests that initially heterocharge is accumulated and then replaced by homocharge.

7.5 Conclusions

In this chapter, ac ageing results for the as-received and degassed XLPE and LDPE samples with different semicon electrodes (Sample F to L) are presented. The newly designed laser induced pressure propagation (LIPP) system has been successfully used to study the space charge dynamics of XLPE insulation subjected to 50 *Hz* ac electric stresses. In addition, a simple quantitative appraisal of the stress and charge profiles at the electrode interfaces (i.e. X-plots and *Dev%*) are presented and validated. It can process a vast amount of ac raw data without resorting to a complex mathematical treatise.

The results from the X-plots have demonstrated and confirmed the existence of space charge in the insulation material under 50 *Hz* ac conditions. It has been showed that space charge effects in XLPE and LDPE with XLPE semicon electrodes are significant when the applied ac stress is above a threshold value, say "11.3 kV/mm_{peak}". It also illustrated that the fast charge formation (charge injection) is more pronounced than the slow charge under the 50 *Hz* ac electric stresses. Moreover, the presence of the fast charge inside the bulk will modify the ac electric stress distribution as well as the electrode/insulation interfacial stress by a maximum of 30 % in some cases.

According to the ageing results (Samples F to J) in the region of 25 kV/mm_{peak}, it was noticed that the effect of sample treatment (degassing) on the space charge threshold of both XLPE and LDPE under an ac electric stress is not significant comparing to the dc condition. Moreover, the effect of the ac ageing can only be found in the XLPE samples with XLPE semicons (Sample F & G), but not LDPE samples with XLPE semicons (Sample H & I). These features ascertained that the space charge dynamics in the LDPE with XLPE semicons samples might be independent of the ac ageing period in the region of 25 kV/mm_{peak}.

Comparing the results of XLPE samples (Samples F & G) to the LDPE samples (Samples H & I), it indicated that the deviation of the exit peak (cathode) of the LDPE samples with XLPE semicons is insignificant compared to XLPE samples with XLPE semicons in the negative half ac cycle. This phenomena may be due to the reduction of the measurement resolution at the exit peak because of the high attenuation of the signal through the LDPE sample or the lost of acoustic energy due to the mismatch of the acoustic characteristic of the LDPE bulk insulation and the XLPE semicons.

However, in the case of the LDPE samples with LDPE semicon electrodes, both entrance and exit peaks have followed the approximate straight line for the positive and negative half ac cycle throughout the 24 hours ageing period. These features illustrated that there are no significant space charge effects in the LDPE samples with LDPE semicon electrodes under 50 *Hz* ac electric stress condition (in the region of 25 kV/mm_{peak}).

According to the limiting high stress ageing results (*30* kV/mm_{peak}) of two 0.8 *mm* thick XLPE samples with XLPE semicon electrode (samples K and L), the space charge dynamic of XLPE insulation under 50 *Hz* ac electric stress showed a strong dependence on the applied ac stress level, polarity and the ageing period. The deviations in the interfacial stress at 30 kV/mm_{peak} vary between 5 % and 20 % during ageing, which is lower than the maximum 30 % deviation observed in the region of 25 kV/mm_{peak}.

However, as there were only one as-received and one degassed XLPE sample with XLPE semicons (0.8 *mm* thick) obtained from BICCGeneral Cable, the discussions included in the section *7.4B* are not conclusive but a possible explaination. The certain reasons for the charge formation and the relationship between the applied voltage polarity and the space

charge dynamic at 30 kV/mm_{peak} during ac ageing are not fully understood. In order to check the validity of the ac ageing results at $30\ kV/mm_{peak}$, and to obtain a complete picture of space charge dynamics under ac ageing condition, further study is required.

Chapter 8

Conclusions and further work

The efforts and the technological achievements, which includes electrical, mechanical and electronic design of the newly designed LIPP has been reported. Based on the "point on wave" measurement technique, a new version of the LIPP system has been successfully designed and constructed. The new LIPP system is capable of measuring space charge and its evolution within polymeric materials with different sample treatments under either dc or 50 *Hz* ac ageing conditions for both plaque and cable samples.

Prior to the application of the newly designed LIPP system to investigate the space charge evolution in the polymeric insulation, the system performance and reliability have been carefully considered, and the newly designed LIPP system is adequate, gives repeatable results and fully meets all the requirements initially set.

For the LIPP technique the accurate and consistence of the space charge measurements rely on the assumption that a constant magnitude pressure pulse is produced each time. However, in practice there are several factors, which may cause variations in the magnitude of the output current signal between measurements. These include "shot to shot laser power variation" and "laser target efficiency and target ablation". In order to eliminate the measurement errors caused by these factors, i.e. effects of the laser power variation (i.e. online laser power monitor system) and target efficiency (i.e. target ablation test) have been considered and verified. Two correction factors have been taken into account during the stage of signal calibration and subsequent measurements to modify the output current signal before any numerical treatment.

Data processing constitutes an important part of the result analysis, therefore, in order to simplify the data processing process, labour intensive programs based on MATLAB environment have been written, which can calculate the pressure wave profile as well as the space charge and electric stress distribution within the bulk insulation. In addition, a high order extrapolation technique has been adopted in the MATLAB program to recover the exit

current peak due to the reflection caused by the acoustic mismatch between semicon and the HV metal electrodes.

The space charge measurement for cable geometries using the LIPP technique are not well defined; therefore the corresponding data processing methods have been developed in this project. From the preliminary results obtained from the 4.5 *mm* cable samples, it is evident that the newly designed LIPP system is capable of measurement of space charge distributions in cable geometry samples under both dc and 50 *Hz* ac conditions. Moreover, the calculated electric stress distribution derived from experimental results shows a very good agreement with the theoretical distribution, indicating that the data processing method has been successfully developed. However, limitations of HV dc power supply and ac transformer produced poor SNR of the measurement signals from the cable sample and the space charge effect was not as significant as that in the planar sample.

Solutions to some of the technical problems such as, unexpected sample breakdown within the ageing period, the high frequency noise, offset of the point on wave voltage, effect of the semicon thickness to measurement resolution etc have been successfully achieved.

Dc Results

In this project, the ramp rate and dc ageing results on the as-received and degassed XLPE and LDPE plaque samples with different semicon electrodes are reported.

- ***DC ramp test***

  From the dc ramp rate results, it demonstrated that there is homocharge formation in the XLPE and LDPE samples with XLPE semicon electrodes above the threshold stress. Comparing the ramp rate results between as-received and degassed XLPE samples, it is evident that the degassing process reduced the value of the dc threshold stress in the samples with XLPE semicons by approximately 30 %. This suggests that with the removal of the majority of cross-linking byproducts in the degassing process, the effects of ionisation in the bulk was minimal and the space charge was mainly due to charge injection from the semicon electrodes. For the LDPE samples with XLPE semicons, the dc threshold stress between the as-received and degassed samples showed only about

4 % difference. Since the LDPE samples have no cross-linking byproducts present within the bulk insulation, degassing would not have any significant effect on the threshold stress.

However, with the results of LDPE samples with LDPE semicon electrodes, it has shown that there is no indication of space charge formation in the material at a significant high stress (~19.2 *kV/mm*) during the voltage ramp measurements. By comparing the result with the LDPE samples with XLPE semicon electrodes, it is reasonable to assume that the source of the negative charge close to the cathode was due to the homocharge injection, which is strongly dependent on the semicon material.

- ***DC ageing test***

Dc ageing results showed that space charge accumulation in the as-received XLPE samples with XLPE semicon electrodes was heterocharge initially, which is believed to be associated with the electric stress assisted ionisation of cross-linking byproducts within the bulk insulation. However, after a few hours of ageing, the positive charge close to the cathode reduces. A possible cause of this reduction is the recombination of some of the ionised cross-linking byproducts within the bulk insulation with the charges injected from the cathode. By contrast, for the degassed XLPE samples with XLPE semicon electrodes, there was no positive charge formation inside the bulk insulation throughout the 24 hours dc ageing. However, negative charge within the bulk increased significantly during the ageing period. It is believed that after the removal of the cross-linking byproducts (via degassing process), the semicon electrodes dominated the charge dynamics in the sample and the negative charges were originated from the injection process.

In the case of the as-received and degassed LDPE samples with XLPE semicon electrodes, the resulting space charge distributions were similar with the exception of a small amount of negative charge accumulated at the interface of the as-received samples. Comparing the results, it is suggested that these negative charges adjacent to the interface were possibly due to the ionisation of the cross-linking byproducts from the XLPE semicons, which had been diffused into the LDPE bulk during the sample manufacturing process.

No significant trapped charge accumulation is observed in the LDPE sample with LDPE semicon electrodes after 24 hours of dc ageing. In summary, both the insulation and semicon materials have a significant effect on the space charge characteristics.

- ***Samples comparison***

The purpose designed HV dc materials from BICCGeneral cables (i.e. XL4931, XL1046 and LDPE) show around 5 ~ 25 % stress reduction at the electrode/polymer interface after 24 hours dc ageing. However, the conventional material (P153) shows approximately 150 % enhancement in the interfacial stress after 24 hours dc ageing. By comparing these results, it evident a significant improvement in the dc space charge performance of the purpose designed materials have been achieved. In addition, it is noticed that the difference of the interfacial stress between the as-received and degassed sample of the purpose designed materials (<15 %) is smaller compared to the conventional insulation material (~50 %) after 24 hours of dc ageing. It is deduced that the effect of the sample degassing process on the space charge in the conventional insulation is more significant than the purpose designed material.

The LDPE samples with LDPE semicon electrodes only shows a <3 % reduction in the interfacial stress after 24 hours dc ageing, which is insignificant comparing with that of the LDPE samples with XLPE semicon electrodes (-20.5 %). This suggests that the space chrge performance in the LDPE sample with LDPE semicon electrodes is better than both XLPE sample with XLPE semicon electrode and LDPE sample with XLPE semicon electrode under HV dc application.

AC results

In this project, 24 hours ac ageing on the as-received and degassed XLPE and LDPE samples with different semicon electrodes are performed. The results illustrated that the newly designed LIPP system is capable of studying the space charge dynamics of XLPE insulations subjected to 50 *Hz* ac electric stresses. In addition, a qualitative and simple quantitative appraisal of the stress and charge profiles at the electrode interfaces (i.e. X-plots

and *Dev%*) are introduced and validated. It is able to process a vast amount of ac raw data without resorting to a complex mathematical treatise. The results from X-plots demonstrated the existence of space charge in the insulation material subjected to 50 *Hz* ac stresses. They showed that space charge effects in XLPE and LDPE with XLPE semicon electrodes are significant when the applied ac stress is above 11.3 $kV/mm_{peak.}$ Also illustrated is that the fast charge formation (charge injection) is more pronounced than the slow charge under 50 *Hz* ac electric stresses. Moreover, the presence of the fast charge inside the bulk modified the ac electric stress distribution as well as the electrode/insulation interfacial stress by a maximum of 30 % in some cases.

- ***AC ageing results (25 kV/mm_{peak})***

  The effect of sample degassing on the space charge threshold of both XLPE and LDPE under an ac electric stress is not significant compared to dc. In addition, within the period of ageing and specified ageing stress the effect of the ac ageing can only be observed in the XLPE samples with XLPE semicon electrodes but not in LDPE samples with XLPE semicon electrodes.

  There are no significant space charge effects in the LDPE samples with LDPE semicon electrodes under 50 *Hz* ac electric stresses conditions in the region of 25 kV/mm_{peak}.

- ***AC ageing results (30 kV/mm_{peak})***

  According to the limited high stress ageing results (*30* kV/mm_{peak}) from two 0.8 *mm* thick XLPE samples with XLPE semicon electrodes (samples K and L), the space charge dynamic of XLPE insulation under 50 *Hz* ac electric stress showed a strong dependence on the applied ac stress level, polarity and ageing period. Further study is still required.

Recommendation of further work

According to the recent studies by different researchers, the temperature during the electrical ageing has a significant influence on the space charge dynamic in planar samples under dc and ac conditions. In practice, power cables experience elevates temperatures in normal operation; therefore all the dc and ac ageing experiments reported in this thesis can be repeated at different temperatures. It will provide valuable information for both cable manufactures and the end users.

Polarity reversal is a quite common operation in dc transmission systems. When a dc cable is stressed with one polarity of a dc high voltage, formation space charge begins either by charge injection or byproduct ionisation. It reaches its steady state distribution after a certain period of time. If such space charge cannot move in response to the sudden change in voltage polarity, there will be a danger of insulation failure. So the space charge behaviour in materials designed for dc power cable applications under voltage polarity reversal would be another area for the further study.

The investigation into space charge in cables was limited by the HV dc power supply and ac transformer in this project in that the stresses applied are not sufficient to generate space charge in cables. However, as the space charge distribution in power cables is of a great interest to the manufacturers and the end users, it is highly desirable to extend the current work to high stresses under both dc and ac ageing at different temperatures and different sample treatments.

Finally, in order to produce a complete picture of space charge dynamic within the dielectric material, another technique such as Thermally stimulated current (TSC) and conduction current measurement should be used in future work. For example, the TSC measurements can give information about the depth of charge traps within the bulk material where as the conduction current measurement is capable of distinguishing the Ohmic conduction and other high field phenomena. Combining the results of these techniques should produce more information about the charge trapping/transport processes within the dielectric.

References

[1] W.G. Meese, "Underground transmission assert or liability", IEEE Conf. on: Underground transmission, Pittsburgh, USA, 1972, pp.7-14.

[2] B.M. Weedy, "Underground transmission of electric power", J. Wiley & Sons, 1980, ISBN 0-471-27700-2.

[3] D. McAllister, "Electric cables handbook", Granada, 1983, ISBN 0-246-11467-3. pp.408-429.

[4] D. McAllister, "Electric cables handbook", Granada, 1983, ISBN 0-246-11467-3. pp.561-564.

[5] G. A. Cartwright, PhD thesis, "The measurement of space charge and its effect on the breakdown strength of solid polymeric insulation, 1994, University of Southampton.

[6] D. McAllister, "Electric cables handbook", Granada, 1983, ISBN 0-246-11467-3. pp.318-319.

[7] D. McAllister, "Electric cables handbook", Granada, 1983, ISBN 0-246-11467-3. pp.513-533.

[8] D. McAllister, "Electric cables handbook", Granada, 1983, ISBN 0-246-11467-3. pp.51.

[9] G. Mazzanti and G. C. Montanari, "A Comparison Between XLPE and EPR as Insulating Materials for HV Cables", IEEE Transactions on Power Delivery, Vol. 12, No. 1, January 1997, pp. 15-28.

[10] G. Mazzanti, G. C. Montanari, A. Motori and P. Anelli, "Comparison of Electrical aging Tests on EPR-insulated Minicables and Ribbons from Full-sized EPR Cable", IEEE Transactions on Dielectrics and Electrical Insulation Vol. 2 No. 6, December 1995, pp. 1095-1098.

[11] G. C. Montanari, G. Pattini, "Electrical aging of EPR cables", Material Engineering 1989, Vol. 1, NO. 2, pp.605-613.

[12] G. Marchesini and P. Gazzana-Priaroggia, "Ethylene-propylene copolymers for insulating and Sheathing Electric Cables", 4th Rubber Technology Conf., London, 1962, pp.162-72.

[13] M. Brown, "Performance of Ethylene-Propylene Rubber Insulation in Medium and High Voltage Power Cable", IEEE Transactions on Power Apparatus and Systems, Vol. PAS-102, No. 2, February 1983, pp. 373-381.

[14] Electrical World, "EPR Insulation Shows Endurance in Test", Nos.: 1988, Vol. 202 (Jan), HL-15043, pp. 41.

[15] Electrical World, "Cable Polymer XLPE & EPR Battle for the T & D Market", Nos.: 1998, Vol. 203 (Mar), HL-15044, pp. S-18-S-22.

[16] P. L. Cinquemani, F. L. Kuchta, M. M. Rahman, F. Ruffinazzi and A. Zaopo, "105°C/ 140°C Rated EPR Insulated Power cables", IEEE Transactions on Electrical Insulation, Vol. 11 No. 1, January 1996, pp. 31-42.

[17] A-M. Jeffery and D. H. Damon, "Dielectric relaxation Properties of Filled Ethylene Propylene Rubber", IEEE Transactions on Dielectrics and Electrical Insulation Vol. 2 No. 3, June 1995, pp. 394-408.

[18] E. Occhini, P. Metra, G. Portinari and B. Vecellio, "Thermal, Mechanical and Electrical Properties of EPR Insulations in Power Cables" IEEE Transactions on Power Apparatus and Systems, Vol. PAS-102, No. 7, July 1983, pp. 1942-1953.

[19] B. S. Bernstein and J. Marks, "EPRI Report on Research Results Point Toward Improved Cable life", IEEE Electrical Insulation Magazine, September/ October 1990-Vol. 6, No. 5, pp. 49-50.

[20] J. Xu and A. Garton, "The Chemical Composition of Water Trees in EPR Cable Insulation" IEEE Transactions on Dielectrics and Electrical Insulation Vol. 1 No. 1, February 1994, pp. 18-24.

[21] G.M. Lanfranconi, B. Vecellio, "EPR high voltage cables", JICABLE'87 Int. Conf. of polymer insulated power cables, Paper A.8.1 1987, pp.390-393.

[22] S. Grzybowski, A. Rakowska and J. E. Thompson, "Relation Between Structure and Dielectric Properties of Polypropylene", 1984 Annual Report of the Conference on Electrical Insulation and Dielectric Phenomena, Claymont, DE, USA, 21-25 October 1984, pp. 169-174.

[23] S. G. Swingler, "Factors Controlling the Electric Strength of Extruded Polyethylene Cable – A Review", Central Electricity Research Laboratories, Lab. Note No. RD/ L/2104N81, August 1981, pp. 1-16.

[24] S. R. Barnes, "Polymer Communications, Morphology of Cross-linked Polyethylene", Polymer, 1980, Vol. 21, July, pp. 723-725.

[25] J. Muccigrosso and P. J. Philips, 'The Morphology of Cross-linked Polyethylene Insulation", IEEE Transactions on Electrical Insulation Vol. EI-13 No. 3, June 1978, pp. 172-178.

[26] B. Yoda and K. Muraki, "Development of EHV Cross-linked Polyethylene Insulated Power Cables", IEEE PES Conference on Underground Transmission, 21-24 May 1972, Paper 72 CHO 608-0-PWR, Insulated Conductors Committee of the IEEE Power Engineering Society Publication, pp. 506-513.

[27] Z. Lin, Y. Zou and C Tang, "The Research on Cross-linked Polyethylene for Electric Cable", Proceedings Second International Conference on Properties and Applications of Dielectric Materials, 12-16 September 1988, Vol. 1, IEEE, pp. 372-375.

[28] Y. D. Lee and P. J. Philips, "The Electrically Ruptured Area of Cross-linked Polyethylene", IEEE Transactions on Electrical Insulation Vol. 26 No. 1, February 1991, pp. 171-177.

[29] C. Robertson, M. R. Wertheimer, D. Fournier and L. Lamarre, "Study on the Morphology of XLPE Power Cable by Means of Atomic Force Microscopy", IEEE Transactions on Dielectrics and Electrical Insulation Vol. 3 No. 2, April 1996, pp. 283-288.

[30] F. Rodriguez, "Principles of polymer systems", McGraw-Hill, ISBN 0-07-053382-2, pp.1-16.

[31] B.M. Weedy, "Thermal design of underground systems", J. Wiley & Sons, 1980, ISBN 0-471-91673-0.

[32] L. A. Dissado and J. C. Fothergill, "Electrical degradation and breakdown in polymers, IEE material and devices series 9, ISBN 0-86341-196-7, pp204

[33] M. Ieda, "Electrical Conduction and Carrier Traps in Polymeric Materials", IEEE Transactions on Electrical Insulation Vol. EI-19 No. 3, June 1984, pp. 162-178.

[34] T. Fukuda, S. Irie, Y. Asada, M. Maeda, H. Nakagawa and N. Yamada, "The Effect of Morphology on the Impulse Voltage", IEEE Transactions on Electrical Insulation Vol. EI-17 No. 5, October 1982, pp. 386-391.

[35] B Brijs, J Becker, G Geerts, X Delfree, "150kV Underground links in Belgium: A new technical stage got XLPE insulated cables", CIGRE 21-101, 2000.

[36] I Evans, MSc Thesis "A comparison of the environmental impacts of crosslinked polyethylene and oil-filled paper insulation for extra high voltage cables", The Open University, 2000.

[37] F. Chapeau, C. Alquié and J. Lewiner, "Influence of the Manufacturing Process of LDPE on the Build up of a Space Charge Distribution under electric Stress", Annual report Conference on Electrical Insulation and Dielectric Phenomena, 1986, IEEE Dielectrics and Electrical Insulation Society, pp. 180-185.

[38] T. Tabata, T. Fukuda and Z. Iwata, "Investigations of Water Effects on Degradation of Cross-linked Polyethylene Insulated Conductors", IEEE Transactions on Power Apparatus and Systems, Vol. PAS-91, pp. 1361-1370.

[39] D. W. Auckland, S. M. F. Kabir and B. R. Varlow, "Space-charge and Breakdown in Artificial Tree Channels", International Conference on: "Dielectric Materials, Measurements and Applications 1992, IEE Pub. No. 363, pp. 197-200.

[40] Y. Zhang, J. Lewiner, C. Alquié and N. Hampton, "Evidence of Strong Correlation Between Space-charge Build up and Breakdown in Cable Insulation", IEEE Transactions on Dielectrics and Electrical Insulation Vol. 3 No. 6, December 1996, pp. 778-783.

[41] Z. Liu, R. Liu, H. Wang and W. Liu, "Space Charges and Initiation of Electrical Trees" IEEE Transactions on Electrical Insulation Vol. 24 No. 1, February 1989, pp. 83-87.

[42] M. Cacciari, G. C. Montanari, L. Simoni, A. Cavallini and A. Motori, "Long-term Electrical Performance and Life Model Fitting of XLPE and EPR Insulated Cables", IEEE Transactions on Power Delivery, Vol. 7, No. 2, April 1992, pp. 634-641.

[43] G. C. Montanari, G. Mazzanti, F. Palmieri, G. Perego and S. Serra, "Dependence of space charge trapping threshold on te,perature in polymeric DC cable, 7th international conference on solid dielectrics, June 2001, pp.81-84.

[44] L. Dissado, G. Mazzanti and G. C. Montanari, "The Incorporation of Space Charge Degradation in the Life Model for Electrical Insulating Materials", IEEE Transactions on Dielectrics and Electrical Insulation, Vol. 2 No. 6, December 1995, pp. 1147-1158.

[45] G. Damamme, C. Le Gressus and A. S. De Reggi, "Space Charge Characterization for the 21st Century", IEEE Transactions on Dielectrics and Electrical Insulation, Vol. 4 No. 5, October 1997, pp. 558-584.

[46] L. A. Dissado, G. Mazzanti and G. C. Montanari, "The Role of Trapped Space Charges in the Electrical Aging of Insulating Materials", IEEE Transactions on Dielectrics and Electrical Insulation, Vol. 4 No. 5, October 1997, pp. 496-506.

[47] A. E. Davies and D. A. Hodgson, " Electrical Ageing Effects in Polyethylene", 1988, 5th International Conference on: "Dielectric Materials, Measurements and Applications", IEE publication No. 289, pp. 254-257.

[48] G. Dreyfus and J. Lewiner, "Electric fields and Currents due to Excess Charges and Dipoles in Insulators", Physical Review B, Volume 8, Number 6, 15 September 1973, pp. 3032-3036.

[49] D. K. Das-Gupta and S. B. Lang, "Spatial Distributions of Polarization and Space Charges in Polymers", Antec 86, pp. 246-249.

[50] N. Hozumi, H. Suzuki, T. Okamoto, K. Watanabe and A. Watanabe, "Direct Observation of Time-dependent Space Charge Profiles in XLPE Cable under High Electric Fields", ", IEEE Transactions on Dielectrics and Electrical Insulation Vol. 1 No. 6, December 1994, pp. 1068-1075.

[51] M. Ieda, "Dielectric Breakdown Process of Polymers", IEEE Transactions on Electrical Insulation Vol. EI-15 No. 3, June 1980, pp. 206-224.

[52] M. Ieda, "Carrier Injection, Space Charge and Electrical Breakdown in Insulating Polymers", Conference Record of the 1985 International Conference on Properties and Applications of Dielectric Materials, 24-29 June 1985, Vol.1, IEEE, pp. 17-22.

[53] M. Ieda and M. Nawata, "DC Treeing Breakdown Associated with Space Charge Formation in Polyethylene", IEEE Transactions on Dielectrics and Electrical Insulation, December 1994, pp. 201-204.

[54] Q. Lei and T. Xie, "Effect of Injected Space Charges on Breakdown Strength in LDPE Films", Proceedings 2nd International Conference on Conduction and Breakdown in Solid Dielectrics, 7-10 July 1986, IEEE/ Electrical Insulation Society, pp. 155-159.

[55] C. Laurent, C. Mayoux and S. Noel, "Space Charge and Electroluminescene in Polyethylene Under Highly Divergent Field", Conference Record of 1984 IEEE International Symposium on Electrical Insulation, 11-13 June 1984, pp. 76-79.

[56] T. Mizutani, "Space Charge Measurement Techniques and Space Charges in Polyethylene", IEEE Transactions on Dielectrics and Electrical Insulation Vol. 1 No. 5, October 1994, pp. 923-933.

[57] P. K. Watson, F. W. Schmidlin and R. V. Ladonna, "The trapping electrons in polyethylene", IEEE Transactions on Electrical Insulation Vol. 27 No. 4, August 1992, pp. 680-686.

[58] Y. Suzuoki, H. Muto, T. Mizutani and M. Ieda, "Effects of Space Charge on Electrical Conduction in High-density Polyethylene", J. Phys. D: Appl. Phys. Vol. 18(1985), pp. 2293-2302.

[59] H. Schädlich and J. Klaβ, "Influence of DC and Impulse Voltage Prestressing on the AC Breakdown Strength of Aged (XL) PE 20 kV Cables", Cired 1989, pp. 274-277.

[60] K. Yamashita, H. Nakamura and T. Hino, "Effect of Ionic Space Charges on Dielectric Breakdown of Polyethylene Terephthalate", Electrical Engineering in Japan, Vol. 101, No. 3, 1981, pp. 25-30.

[61] K. Yoshino, J. Kyokane, T. Nishitani and Y. Inuishi, "Charge Transport and Breakdown in Polyethylene", 1976 Annual Report Conference on Electrical Insulation and Dielectric Phenomena, (CEIDP), National Academy of Sciences, pp. 65-73.

[62] K. R. Bambery and R. J. Fleming, "Space Charge Accumulation in Two Power Cable Grades of XLPE", IEEE Transactions on Dielectrics and Electrical Insulation, Vol. 5 No. 1, February 1998, pp. 103-109.

[63] M. Mammeri, C. Laurent and J. Salon, "Influence of Space Charge Build up on the Transition to Electrical Treeing in PE under ac Voltage", IEEE Transactions on Dielectrics and Electrical Insulation Vol. 2 No. 1, February 1995, pp. 27-35.

[64] T. Takeda, N. Hozumi, H. Suzuki, K. Fujii, K. Terashima, M. Hara, Y. Murata, K. Watanabe and M. Yoshida, "Space Charge Behaviour in Full-size 250 kV DC XLPE Cables", IEEE Transactions on Power Delivery, Vol. 13, No. 1, January 1998, pp. 28-39.

[65] T. Sun, J. Li, Q. Ying and Z. Fan, "Space Charge in Extruded Insulation under D.C. Divergent Field", Proceedings Second International Conference on Properties and Applications of Dielectric Materials, 12-16 September 1988, IEEE Publication, pp. 678-681.

[66] R. Patsch, "Space Charge Phenomena in Polyethylene at High Electric Fields", J. Phys. D: Appl. Phys. Vol. 23 (1990), pp. 1497-1505.

[67] S. Mahdavi, Y. Zhang, C. Alquié, J. Lewiner and B. Dalle, "Determination of Space Charge Distributions in Polyethylene Samples Submitted to 120 kV DC Voltage", 1990 annual Report: Conference on Electrical Insulation and dielectric Phenomena 1990, pp. 520-526.

[68] S. Mahdavi, Y. Zhang, C. Alquié and J. Lewiner, "Determination of Space Charge Distribution in Polyethylene Samples Submitted to 120 kV dc Voltage", IEEE Transactions on Electrical Insulation Vol. 26 No. 1, February 1991, pp. 57-62.

[69] S. Hole, C. Alquié and J. Lewiner, "Measurement of Space-charge Distributions in Insulators under Very rapidly Varying Voltage", ", IEEE Transactions on Dielectrics and Electrical Insulation Vol. 4 No. 6, December 1997, pp. 719-724.

[70] Rongsheng Liu, Tatsuo Takada, Tsuyoshi Uozumi and Yuichi Yamada, "Measurement of space charge distribution in solid dielectrics under AC electrical fields", National convention record IEE Japan 1992, Volume 3, pp. 3-51.

[71] R. Liu, T. Takada and N. Takasu, "Pulsed electro-acoustic method for measurement of space charge distribution in power cables under both DC and AC electric fields", J. Phys. D: Appl. Phys. 1993, Vol. 26, pp.986-993.

[72] T. Tanaka, "Charge Transfer and tree Initiation in Polyethylene Subjected to ac Voltage Stress", IEEE Transactions on Electrical Insulation Vol. 27 No. 3, June 1992, pp. 424-431.

[73] E. Wasilenko, "Electrical ageing of Polyethylene at Impulse and A. C. Test Voltages", 5th International Conference on: "Dielectric Materials, Measurements and Applications", IEE publication No. 289, 1988, pp. 387-390.

[74] M. Mammeri, C. Laurent and J. Salon, "Influence of space charge build up on the transition to electrical treeing in PE under ac voltage", IEEE Transactions on Dielectrics and Electrical Insulation, Vol. 2, No. 1, Feb 1995, pp27-35.

[75] T. Tanaka, "Charge transfer and tree initiation in polyethylene subjected to ac voltage stress", IEEE Transactions on Electrical Insulation, Vol. 27, No. 3, June 1992, pp424-431

[76] Y. F. F. Ho, G. Chen, A. E. Davies, R. N. Hampton, S.G. Swingler, S. J Sutton, "Do semicons affect space charge?, 7th international conference on solid dielectric, 2001, pp105-108.

[77] International union of pure and applied chemistry, "Report on nomenclature in the field of macromolecules", J. polymer science, Vol. 8, No. 3, pp. 257-277.

[78] E,W, Billmeijer, "Textbook of polymer science", Wiley & Sons, New York, 1984

[79] F. H. Kreuger, Industrial high voltage, Volume 3, Delft university press.

[80] R. W. Dyson, "Polymerisation", in specialty polymers, ed: R. W. Dyson and Blakie, Chapter 2, pp. 20-37

[81] J. D. Hoffman, "Mechanical and electrical properties of polymers: An elementary molecular approach", IEEE Transactions on component parts, pp. 42-69.

[82] D. McAllister, "Electric cables handbook", Granada, 1983, ISBN 0-246-11467-3.

[83] P. J. Phillips, "Morphology-electrical property relations in polymers", IEEE Transactions on Electrical Insulation, Vol. EI-13 No. 2, 1978, pp. 69-81

[84] G. A. Cartwright, PhD thesis, "The measurement of space charge and its effect on the breakdown strength of solid polymeric insulation, 1994, university of Southampton, pp.36

[85] D. McAllister, "Electric cables handbook", Granada, 1983, ISBN 0-246-11467-3, pp., 52-54.

[86] D. McAllister, "Electric cables handbook", Granada, 1983, ISBN 0-246-11467-3, pp.54-55.

[87] T. Fukuda, S. Irie, Y. Asada, M. Maeda, H. Nakagawa and N. Yamada, "The Effect of Morphology on the Impulse Voltage breakdown in XLPE cable insulation", IEEE Transactions on Electrical Insulation Vol. EI-17 No. 5, October 1982, pp. 386-391.

[88] R. M. Eichhorn, "Organic Residues in Polyethylene Insulation Cross-linked with Dicumylperoxide", IEEE Underground Transmission Conference, 22-24 May 1972, pp. 282-285.

[89] A. Garton, J. H. Groeger and J. L. Henry, "Ionic Impurities in Cross-linked Polyethylene Cable insulation", IEEE Transactions on Electrical Insulation Vol. 25 No. 2, April 1990, pp. 427-434.

[90] Y. Miyashita and H. Kato, "Cross-linking Reaction of LDPE and the Behaviour of Decomposition Products from Cross-linking Agents", Symposium on Electrical Insulating Materials (1988), pp. 259-262.

[91] D. McAllister, "Electric cables handbook", Granada, 1983, ISBN 0-246-11467-3, pp.332-333.

[92] N.F. Mott and R.W. Gurney, "The contact between a metal and an insulator", in: "Electronic processes in ionic crystals", 2nd edition, Clarendon press, Oxford, pp.168-173.

[93] L. I. Maissel, "Handbook of thin film tech", McGraw-Hill, New York, pp.14.25-14.27

[94] W. Schottky, "Űber den einfluß von strukturwirkungen, besonder der thomsonschen bildkraft, auf die elecktronenemission der metalle", Z. Phys, 1914, Vol. 15, pp.872-878

[95] L. I. Maissel, "Handbook of thin film tech", McGraw-Hill, New York, pp.14.14-14.15

[96] R.H. Fowler and L.W. Nordheim, "Electron emission in intense electric fields", Proc. Roy. Soc. A, Vol. 119, pp.173-181.

[97] M. Ieda, "Carrier Injection, Space Charge and Electrical Breakdown in Insulating Polymers", Conference Record of the 1985 International Conference on Properties and Applications of Dielectric Materials, 24-29 June 1985, Vol.1, IEEE, pp. 17-22.

[98] M. Ieda, T. Mizutani and Y. Suzuoki, "TSC and TL studies of carrier trapping in insulating polymers", Memoirs of Faculty of engineering, Nagoya university, Vol. 32, No. 2, pp. 173-219.

[99] P. J. Flory, "On the morphology of the crystalline state in polymers", J. Amer. Chem. Soc., Vol. 84, pp.2857-2867

[100] T.J. Lewis, "Electrical effects at interfaces and surfaces", Proc. 5th Int. Symp. On: Electrets, IEEE, New York, pp. 75-87.

[101] M. Ieda, "Electrical Conduction and Carrier Traps in Polymeric Materials", IEEE Transactions on Electrical Insulation Vol. EI-19 No. 3, June 1984, pp. 162-178.

[102] P. J. Phillips, "Morphology- electrical property relations in polymers", IEEE Transactions on Electrical Insulation, Vol. EI-13 No. 2, 1978, pp. 69-81.

[103] T. Mizutani and M. Ieda, "Carrier transport in high density polyethylene", J. Phys. D: Appl. Phys., Vol. 12, pp.291-296.

[104] Y. Takai, K. Mori, T. Mizutani and M. Ieda, "Investigation of traps in γ-irradiated polyethylene by photo stimulated detrapping current analysis", Japan. J. Appl. Phys., Vol. 15, pp2341-2347.

[105] Y. Suzuoki, K. Yasuda, T.Mizutani and M. Ieda, "The influence of oxidation on thermally stimulated current from trapped carriers in high density polyethylene", Japan. J. Appl. Phys., Vol. 10, pp1985-1990.

[106] Y. Tanaka, S. Tanaka and Y. Ohki, "Effects of Additives on Space Charge Formation in Polyethylene", International Conference on: "Dielectric Materials, Measurements and Applications 1992, IEE Pub. No. 363, pp. 135-137.

[107] J. L. Gil-Zambrano and C. Juhasz, "Space charge polarisation in Bylon films", J. Phys. D: Appl. Phys., Vol. 15, pp.119-128.

[108] M. Ieda, T. Mizutani and Y. Suzuoki, "TSC and TL studies of carrier trapping in insulating polymers", Memoirs of Faculty of engineering, Nagoya university, Vol. 32, No. 2, pp. 173-219.

[109] L. I. Maissel, "Handbook of thin film tech", McGraw-Hill, New York, Chapter 16.

[110] H. J. Wintle, " Conduction process in polymers", Engineering dielectrics Vol. IIA

[111] J. G. Simmons, "DC conduction in thin films", Mills & Boon Ltd London, ISBN 263-51786

[112] L. I. Maissel, "Handbook of thin film tech", McGraw-Hill, New York, pp.14.28-14.29

[113] B. Sanden, "XLPE cable insulation subjected to HVDC stress:- space charge conduction and breakdown strength", PhD thesis of Norwegian university of science and technology, 1996

[114] P. Laurenceau, G. Dreyfus and J. Lewiner, "New Principle for the Determination of Potential Distributions in Dielectrics", Physical Review Letters, Volume 38, Number 1, 3 January 1977, pp. 46-49.

[115] F. Chapeau, C. Alquié and J. Lewiner, "The Pressure Wave Propagation method for the Analysis of Insulating Materials: Application to LDPE used in HV Cables", IEEE Transactions on Electrical Insulation, Vol. EI-21 No. 3, June 1986, pp. 405-410.

[116] F. Chapeau, C. Alquié and J. Lewiner, "Application of the Pressure Wave Propagation Method for the Analysis of Insulating Materials", 5th International Symposium on Electrets (ISE 5), Heidelberg 1985 (Avail. From IEEE, NY), pp. 559-565.

[117] M. P. Cals, J. P. Marque and C. Alquié, "Application of the Pressure Wave Propagation Method to the Study of Interfacial Effects in e-Irradiated Polymer Films", Journal of Applied Physics, 72 (5), 1 September 1992, pp. 1940-1951.

[118] T. Ditchi, C. Alquié, J. Lewiner, R. Favrie and J. Jocteur, "Electrical Properties of Electrode-polyethylene-electrode Structures", 6th International Symposium on Electrets (ISE 6), 1-3 September 1988, IEEE Electrical Insulation Society, pp. 7-13.

[119] T. Ditchi, C. Alquié, J. Lewiner, R. Favrie and J. Jocteur, " Electrical Properties of Electrode/ polyethylene/ electrode Structures", IEEE Transactions on Electrical Insulation, Vol. 24 No. 3, June 1989, pp. 403-408.

[120] J. Lewiner, "New Experiment Techniques", 5th International Symposium on Electrets (ISE 5), 4-6 September 1985, IEEE Electrical Insulation Society, pp. 429-443.

[121] J. Lewiner, "Direct Determination of Space Charge Distributions in Dielectrics: The Pressure WAVE Propagation Method", Proceedings 3rd International Conference on Conduction and Breakdown in Solid Dielectrics, 3-6 July 1989, IEEE/ Electrical Insulation Society, pp. 548-555.

[122] J. Lewiner, "Evolution of Experimental Techniques for the Study of the Electrical Properties of Insulating Materials", IEEE Transactions on Electrical Insulation Vol. EI-21 No. 3, June 1986, pp. 351-360.

[123] A.C. Tam, "Pulsed laser generation of ultra short acoustic pulses: Application for thin film ultrasonic measurements", Applied Physics letter, Vol. 45, No.5, pp.510-512.

[124] G. M. Sessler, R. Gerhard- Multhaupt, J.E. West and H. Von Seggern, "Optoacoustic generation and electrical detection of sub-nanosecond acoustic pulses", Applied Physics letter, Vol. 58, No.1, pp.119-121.

[125] C. Alquié, J. Lewiner and G. Dreyfus, "Analysis of Laser Induced Acoustic Pulse Probing of Charge Distributions in Dielectrics", J. Physique – Letters 44 (1983), pp.171–178.

[126] C. Alquié, T. Ditchi and J. Lewiner, "Measurement of Charge Distribution in Insulating Materials for High Voltage Cables", Proc. 2nd Conf. on: properties and applications of dielectric materials, IEEE, New York, 1988, pp.434-437.

[127] C. Alquié, G. Dreyfus and J. Lewiner, "Pulsed Laser Determination of Surface Electric Charge Distributions", J. Physique – Letters 43 (1982), pp.687–693.

[128] C. Alquié, F. Chapeau, J. Lewiner, "Evolution of charge distributions in F.E.P. films analysed by the laser induced acoustic pulse method", Annual report conference on electrical insulation and dielectric phenomena, 1984, pp. 488-494.

[129] C. Alquié, C. Laburthe Tolra, J. Lewiner and Sidney B. Lang, "Comparison of polarization distribution measurement by the LIMM and PWP methods", IEEE Transactions on Electrical Insulation, Vol. 27, No.4, August 1992, pp. 751-757.

[130] C. Bert, C. Heninion, J. Lewiner, C. Alquié, N. Hampton, J. Freestone and S. Verne, "Measurement of Space Charge Distribution under 50 Hz AC Stress", Jicable 95, pp. 195-199.

[131] D. Malec, "Design Note Technical problems encountered with laser induced pressure pulse method in studies of high voltage cable insulators", Meas. Sci Technol. 11 (2000), N76-N80.

[132] Y. F. F. Ho, G. Chen, A. E. Davies, R. N. Hampton, S. Hobdell, S.G. Swingler, S. J Sutton, "Space charge measurements in XLPE insulation under 50Hz A.C. electric stress", International Conference on: "Dielectric Materials, Measurements and Applications 2000, pp.68-73

[133] J. D. Kraus, "Electromagnetic", McGraw-Hill international edition, 1992, ISBN 0-07-035621-1

[134] F. H. Kreuger, Industrial high voltage, Volume 3, Delft university press.

[135] B. S. Massey, Mechanics of fluids, Chapman & Hall, 1989.

[136] Newport optics catalogue 1997/98, pp.5-4 to 5-5

[137] G. Bouillier, "Etude d'une Methode de mesure des distributions de charges electriques dans les structures metal-isolant-semiconducteur", Thesis de Doctorat de L' Universite Paris VI, 1987.

[138] R.S. Moore, "Sound absorption", in "Encyclopaedia of polymer science and technology", Vol. 12. pp 700-725, J. Wiley, New York.

[139] T. Ditchi, "perfectionnement de la methode de L'Onde de Pression. Application a L' Etude de structures isolantes a base de polyethylene", Thesis de Doctorat de L' Universite Paris VI, 1990.

[140] Hewelett Packard HP54510A, Digital oscilloscope instruction manual.

[141] A.E. Davies, G. Chen, X. Wu, R.N. Hampton, S. J. Sutton, S. G. Swingler, "Calculation of space charge density and electric stress in XLPE compounds", Jicable 1999, pp. 728-732.

[142] R. Hare and C. Budd, "Modelling Space Charge and field in Solid Dielectrics", International Conference on: "Dielectric Materials, Measurements and Applications 1992, IEE Pub No. 363, pp. 81-84.

[143] G. M. sessler, "Electrets", Springer-Verlag Berlin Heidelberg, New York, 1980.

[144] G. M. Sessler, "Electric fields and Forces due to Charged Dielectrics", J. Appl. Phys. Vol. 43, No. 2, February 1972, pp. 405-408.

[145] Y. Suzuoki, H. Muto, T. Mizutani and M. Ieda, "Effects of Space Charge on Electrical Conduction in High-density Polyethylene", J. Phys. D: Appl. Phys. Vol. 18(1985), pp. 2293-2302.

[146] Y. Zhang, J. Lewiner, C. Alquié and N. Hampton, "Space Charges of Different Mobilities: A Novel Data Processing Method", Journal of Applied Physics, Vol. 77, No. 10, 15 May 1995, pp. 5195-5200.

[147] Manual of the "Pressure wave propagation software V 3.2"2 HLP technologies, Paris.

[148] S. Mahdavi, C. Alquié, J. Lewiner, "Direct measurement of space charge in synthetic cables by the pressure wave method", Proc. Int. Conf. Polymer insulated power cable, Versaille, July 1991, pp. 534-41.

[149] M. Fu, G. Chen, A. E. Davies and J. G. Head, "Space charge measurements in power cables using a modified PEA system", International Conference on: "Dielectric Materials, Measurements and Applications 2000, pp. 74-79.

[150] A. E. Davies, G. Chen and A. Vazquez, "Space charge measurement in dispersive dielectrics", Versailles, JICABLE 99, pp.733-738

[151] T. Ditchi, C. Alquie, J. Lewiner, "Broadband determination of ultrasonic attenuation and phase velocity in insulating material", J. Acoustic. Soc. Am., 94, pp.3061-3066.

[152] T. Ditchi, "Deconvolution in coaxial geometry", (internal report)

[153] Morse and Ingard, "Theoretical Acoustics", New York, McGraw-Hill, 1968.

[154] S. Mahdavi, C. Alquié and J. Lewiner, "Measurement of Charge Distributions in Coaxial Structures. Application to High Voltage Cables", IEEE 1989 Annual Report, Conference on Electrical Insulation and Dielectric Phenomena, 29 October-1 November 1989, pp. 296-302.

[155] M. S. Khalil and A. A. Zaky, "The Effect of Cable Structure on Space Charge Formation", IEEE Transactions on Electrical Insulation Vol. 23 No. 6, December 1988, pp. 1043-1046.

[156] J. R. Hanscomb and E. P. George, "Space Charge and Short-circuit Discharge in High-density Polythene", J. Phys. D: Appl. Phys. Vol. 14 (1981), pp. 2285-2294.

[157] H. Kon, Y. Suzuoki, T. Mizutani, M. Ieda and N. Yoshifuji, "Packet-like Space Charges and Conduction Current in Polyethylene Cable Insulation", IEEE Transactions on Dielectrics and Electrical Insulation Vol. 3 No. 3, June 1996, pp. 380-385.

[158] M. S. Khalil and B. S. Hansen, "Investigation of Space Charge in Low-density Polyethylene Using a Filed Probe Technique", IEEE Transactions on Electrical Insulation Vol. 23 No. 3, June 1988, pp. 441-445.

[159] R.J. Fleming, M.M. Henriksen, M. Henriksen, J. T. Hoboll, "LIPP and PEA space charge measurement on LDPE", International conference on conduction and breakdown in solid dielectrics, Leicester, England, 1995, pp. 234-238

[160] J. M. Alison and L. A. Dissado, "Electric field enhancement within moulded samples of low density polyethylene – a mean of failure characterised by voltage ramp tests and space charge measurement", IEE Conf. Pub. Vol. 430, 1996, pp. 4-7.

[161] M. A. Brown, G. Chen, B. F. Rogers, A. E. Davies, C. Rochester, "Dc electrical accelerated ageing tests on polyethylene insulation". IEE Conf. Pub. Vol. 430, 1996, pp 281-284.

[162] O. Fanjeau, D. Mary and D. Malec, "A note on charge recombination in low density polyethylene under a moderate ac 50 Hz field", Journal of Applied Physics 33, L61-64, 2000

[163] T. Maeno, T. Futami, H. Kushibe, T. Takada and C. M. Cooke, "Measurement of Spatial Charge Distribution In Thick Dielectrics Using the Pulsed Electroacoustic Method", IEEE Transactions on Electrical Insulation Vol. 23 No. 3, June 1988, pp. 433-439.

[164] P. Morshuis and M. Jeroense, "Space Charge Measurements on Impregnated Paper: A Review of the PEA Method and a Discussion of Results", IEEE Electrical Insulation Magazine, 1997, pp. 26-35.

[165] T. Maeno, T. Hoshino, T. Futami and T. Takada, "Application of Ultrasonic Techniques to the Measurement of Spatial Charge and Electric Field Distributions in Solid Dielectric Materials", Electrical Engineering in Japan, Vol. 109, No. 5, 1989, pp.58-64.

[166] K. Fukunga and T. Maeo, "Measurement of the Internal Space Charge Distribution of an Anti-electrostatic Discharge Polymer", IEEE Transactions on Dielectrics and Electrical Insulation Vol. 2 No. 1, February 1995, pp. 36-39.

[167] P. Morshuis and M. Jeroense, "Space Charge Measurements on Impregnated Paper: A Review of the PEA Method and a Discussion of Results", IEEE Electrical Insulation Magazine, 1997, pp. 26-35.

[168] T. Takada, T. Mizutani, T. Tanaka and N. Hozumi, "New direct observation technique for electric charge behaviour in insulating materials and its application to power cables, Cigre 1998, 15-303.

[169] G. Chen, A.E. Davies, H.M Banford, N. Adachi, Y. Tanaka and T. Takada, "The role of oxidation in the formation of space charge in Gamma-irradiated Low-density polyethylene, 11th International symposium on high voltage engineering, 1999, pp4.75-4.78.

[170] Y. Li, M. Yakada, "Pulsed electroacoustic method for measurement of charge accumulation in solid dielectrics", IEEE Transactions on Dielectrics and Electrical Insulation Vol. 1 No. 2, 1994, pp. 188-195.

[171] S. B. Lang and D.K. Das-Gupta, "A technique for determination the polarisation distribution in thin polymer electrets using periodic heating ferroelectrics, Vol. 39, 1981, pp. 1249-1252.

[172] S. B. Lang and D.K. Das-Gupta, "Complex polarisation distributions in PVDE samples", Ferroelectrics, Vol. 55, 1984, pp. 151-154.

[173] S. B. Lang and D.K. Das-Gupta, "A new technique for determination the spatial distributions of polarisation in polymer electrets", Ferroelectrics, Vol. 60, 1984, pp. 23-36.

[174] S. B. Lang and D.K. Das-Gupta, "Laser intensity modulation method: A technique for determination of spatial distributions of polarisation and space charge in polymer electrets", Proc. 5th Intern, Symp. On electrets, Heidelberg, 1985, pp. 444-449.

[175] D. K. Das-Gupta and A. W. Pattullo, "A Method for Space Charge Distribution Determining in Thick Dielectric Samples", 6th International Symposium on Electrets (ISE 6), 1-3 September 1988, IEEE Electrical Insulation Society, pp. 435-439.

[176] D. K. Das-Gupta and J. S. Hornsby, "A Non-destructive Technique for the Determination of Spatial Charge and Polarization Distributions in Insulating Polymers", J. Phys. D: Appl. Phys. Vol. 23 (1990), pp. 1485-1490.

[177] G. Dreyfus and J. Lewiner, "Electric fields and Currents due to Excess Charges and Dipoles in Insulators", Physical Review B, Volume 8, Number 6, 15 September 1973, pp. 3032-3036.

[178] D. K. Das-Gupta and S. B. Lang, "Spatial Distributions of Polarization and Space Charges in Polymers", Antec 86, pp. 246-249.

[179] C. Alquié, C. Laburthe Tolra, J. Lewiner and Sidney B. Lang, "Comparison of polarization distribution measurement by the LIMM and PWP methods", IEEE Transactions on Electrical Insulation, Vol. 27, No.4, August 1992, pp. 751-757.

[180] N. H. Ahmed and N. N. Srinivas, "Review of Space Charge Measurements in Dielectrics", IEEE Transactions on Dielectrics and Electrical Insulation, Vol. 4 No.5, October 1997, pp. 644-656.

[181] R. E. Collins, "Practical Application of the Thermal Pulsing Technique to the Study of Electrets", J. Appl. Phys. 51(6), June 1980, pp. 2973-2986.

[182] R. E. Collins, "Analysis of Spatial Distribution of Charges and Dipoles in Electrets by a Transient Heating Technique", Journal of Applied Physics, Vol. 47, No. 11, November 1976, pp. 4804-4808.

[183] R. E. Collins, "Distribution of charge in Electrets", Applied Physics Letters, Vol. 26, No. 12, 15 June 1975, pp. 675-677.

[184] Y. Suzuoki, H. Muto, T. Mizutani and M. Ieda, "Effects of Space Charge on Electrical Conduction in High-density Polyethylene", J. Phys. D: Appl. Phys. Vol. 18(1985), pp. 2293-2302.

[185] A. Toureille and J. P. Reboul, "The Thermal-step-technique Applied to the Study of Charge Decay in Polyethylene Thermoelectrets", 6th International Symposium on Electrets (ISE 6), 1-3 September 1988, IEEE Electrical Insulation Society, pp. 23-27.

[186] R. Grehard-Multhaup, G. M. Sessler, J. E. West, K. Holdik, M. Haardt and W. Eisenmenger, "Investigation of Piezoelectricity Distributions in Poly (vinylinylidene fluoride) by means of Quartz- or Laser-generated Pressure Pulses", J. Appl. Phys. 55 (1984), pp. 2769-2775.

[187] R. A. Anderson and S. R. Kurtz, "Direct Observation of Field-injected Space Charge in a Metal-insulator-metal structure", J. Appl. Phys. 56 (10), 15 November 1984, pp. 2856-2863.

[188] R. A. Anderson and S. R. Kurtz, "Properties of Metal-polymer-metal Structures Observed with Space Charge Mapping Techniques – I. High Field Stressing Experiments", 1986 Annual report Conference on Electrical Insulation and Dielectrics phenomena, 2-6 November 1986, IEEE Dielectrics and Electrical Insulation Society, pp. 104-111.

[189] R. A. Anderson and S. R. Kurtz, "Radiation induced space charge in polymer film capacitor", Applied physics letter, Vol. 49, 1986, pp. 1484-1486

[190] A. Migliori and J. D. Thompson, "A Non-destructive Acoustic Electric Field Probe", J. Appl. Phys. Vol. 51 (1), January 1980, pp. 479-485.

[191] A. Migliori and T. Hofler, "Use of Laser-generated Acoustic Pulses to measure the Electric Field Inside a Solid Dielectric", Rev. Sci. Instrum. 53 (5), May 1982, American Institute of Physics Publication, pp. 662-666.

Appendix 1 Review of space charge measurement technique for solid dielectrics

A1.1 Pulsed Electroacoustic method (PEA)

"Pulsed electroacoustic method" shown in Figure A1-1 has developed by Prof. T. Takada (Japan) in close cooperation with Prof. C.M. Cooke (USA) in 1983 [163-167].

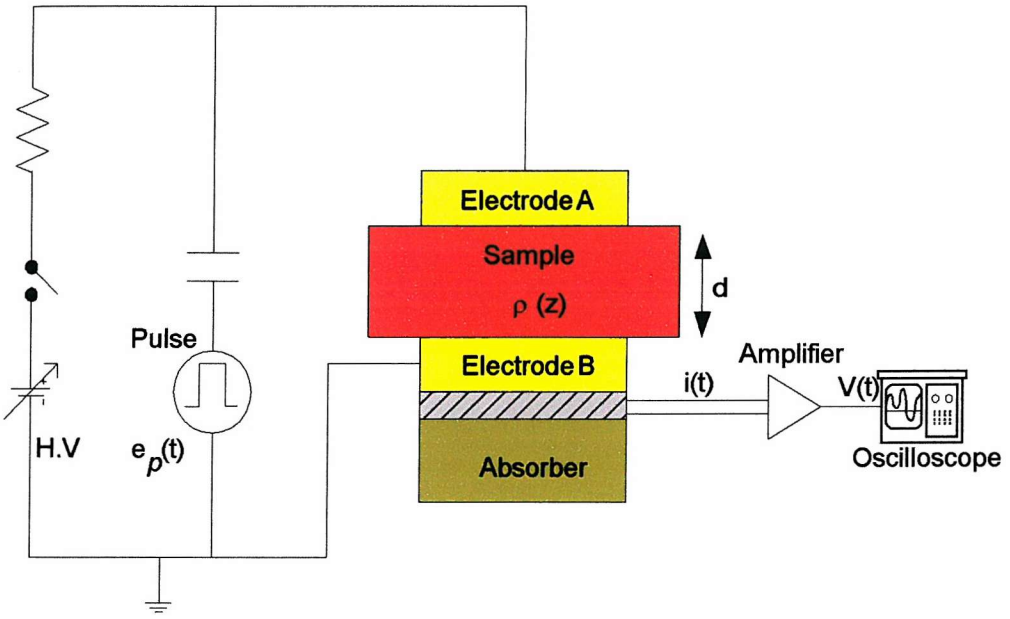

Figure A1-1 Block diagram of the pulsed electro-acoustic method

Consider a planar dielectric sample with thickness d containing space charge $\rho(z)$ trapped in the sample. In order to measure the space charge distribution inside the bulk, a high-voltage narrow electric pulse $e_p(t)$ of duration ΔT ($5ns$) with a short rise and fall time is applied to the sample between its electrodes A and B. As a result, spaces charge inside the bulk is stimulated by the electric pulsed applied and experience a pulsed force that travels as acoustic waves through the sample. By detecting the resultant pressure pulse $p(t)$ arriving at the piezoelectric transducer (PVDF foil) in intimate contact with the electrode B, the space charge distribution in the dielectric sample can be obtained from the evolution of the output voltage $V(t)$ of the transducer as given by [168].

$$p(t) = k\int_0^t \rho(z)e_p(t-t')d\tau \quad \text{---------- (A1)}$$

$$V(t) = k\int_0 h(\tau)p(t-t')d\tau \text{ ---------- (A2)}$$

where $\rho(z)$ is charge density distribution,

$p(t)$ is total acoustic density (N/m^2),

k is a constant,

$e_p(t)$ is the electric pulse (V/m),

$h(\tau)$ is the transfer function of the transducer (V/m)/(N/m^2), and

$V(t)$ is the output voltage.

The resolution of the PEA system depends on the duration of the electric pulse and the speed of the acoustic wave in the sample. A spatial resolution of 15 μm in PE and XLPE has been demonstrated with the application of a 350 ns pulse [169].

The main advantage of the PEA system is the cost of the instruments that is relatively low compared with the other measurement system like "LIPP". For the past limitation of this method comes from the difficulty of detecting complex charge profiles. However, according to a recent study by Li Ying [170], the use of a thin piezoelectric transducer with an extremely wide frequency range, low acoustic impedance, and a very short duration applied electric pulse makes it possible to avoid the deconvolution technique required to obtain the space charge profile. However, as the measured voltage signal from the PEA system is small, SNR is poor. An averaging approach is necessary for the PEA technique to reduce the random noise level by a factor of $\sqrt{n}$ where n is the number of measurements signal for averaging and is normally >200.

A1.2 Laser intensity modulation method (LIMM)

The "Laser intensity modulation method" was developed by Lang and Das-Gupta in 1984 [171-178]. This method utilises a sinusoidal-modulated surface heating of dielectric samples to produce spatially non-uniform temperature distributions through the thickness. In the LIMM system, the test sample is mounted in an evacuated ($<10^{-5}$ $torr$) sample chamber containing optical windows through which radiant energy can be admitted. Each surface of the sample coated with an opaque electrode is exposed to a laser beam which is intensity

modulated in a sinusoidal fashion by an acousto-optic modulator or a light chopper as shown in figure A1-2.

As the laser beam is absorbed by the front of the electrode of the sample, the sinusoidal modulation of the laser beam will cause a sinusoidal fluctuation in the temperature of the electrode on which it impinges resulting in the propagation of temperature waves into the sample. These temperature waves are both attenuated and retarded in phase as they progress through the sample. The amount of attenuation and phase retardation is a function of the depth in the sample and its thermal diffusivity. Thus, a non-uniformly distributed and time-varying thermal force acts on the sample [179].

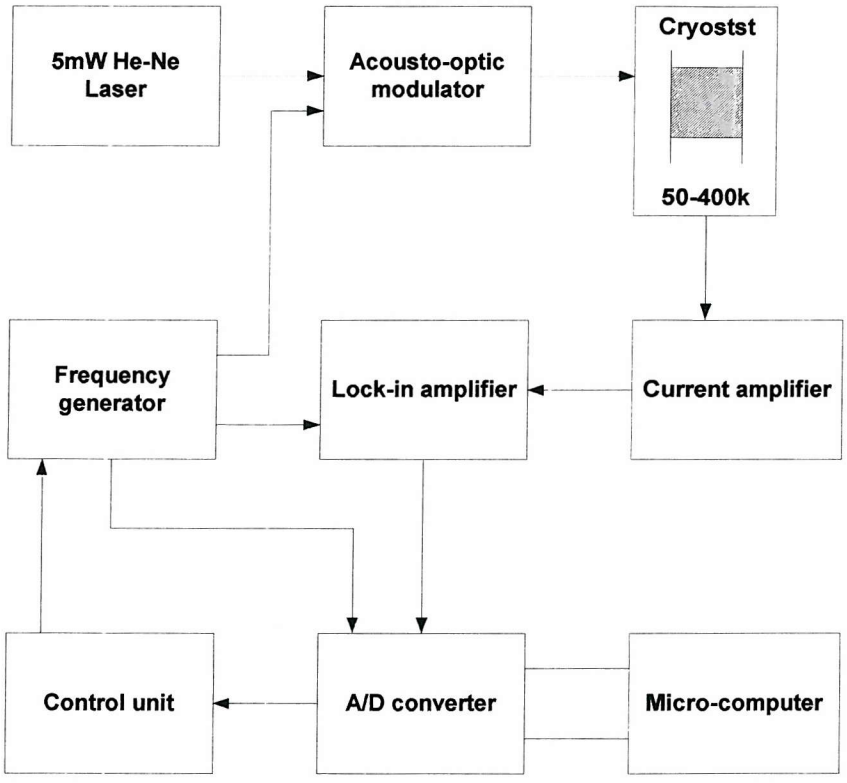

Figure A1-2 Block diagram of the laser intensity modulation method [179]

Under short circuit conditions, the interaction of the fluctuating temperature, the spatially distributed polarisation and space charge produces a sinusoidal pyroelectric current I. The amplitude and phase of this current I *is* in respect to the phase of the modulated frequency with a lock-in-amplifier. Since the pyroelectric measurements are made for a number of different temperature distributions, then the produced current should be a unique function of

the modulation frequency, which can provide sufficient information to analysis the charge distributions of polarisation as given below [176],

$$\frac{I_L}{I_0} = 1 + C_1 \int_0^1 P^*(y)\left(\frac{\upsilon \cosh \upsilon y}{\sinh \upsilon}\right)dy + C_2 \int_0^1 \rho(y)\left(\frac{\sinh \upsilon y}{\sinh \upsilon} - y\right)dy \quad \text{--------- (A-3)}$$

$$\frac{I_Z}{I_0} = 1 + C_1 \int_0^1 P^*(y)\left(\frac{\upsilon \cosh[\upsilon(1-y)]}{\sinh \upsilon}\right)dy + C_2 \int_0^1 \rho(y)\left(\frac{\sinh[\upsilon(1-y)]}{\sinh \upsilon} - (1-y)\right)dy \quad \text{--- (A-4)}$$

where $\upsilon = \left(\frac{\omega}{2K}\right)^{\frac{1}{2}} \cdot L(1+i)$, $C_1 = \frac{\alpha_p + \alpha_x - \alpha_\varepsilon}{p}$ and $C_2 = \frac{\alpha_x - \alpha_\varepsilon}{p} L$

i is the imaginary operator, I_0 the current I at zero frequency, L the thickness of the sample, K the thermal diffusivity, I_L the pyroelectric current when the laser beam impinges on the surface $x = L$, I_z the current when the laser beam incident on the surface $x = 0$, p the pyroelectric coefficient, ω the angular frequency and α_p, α_x and α_ε are the relative temperature dependence of the polarisation, thermal expansion coefficient and permittivity respectively. By using a coordinate x to represent the distance inside the thickness from surface $x = 0$ to $x = L$ and with $y = x/L$, the unknown distributions of the polarisation $P^*(y)$ and space charge $\rho(y)$ can be found [173,176].

However, the disadvantage of the LIMM technique is that a mathematical complex deconvolution technique is required to compute the polarisation and space-charge distributions from the current-frequency data. The measurement resolution $\sim 2\mu m$ on the polarisation and space charge distributions has been reported [180].

A1.3 Thermal pulse or Step method (TPM or TSM)

"Thermal pulse method" for probing space charge in dielectric was firstly proposed by Collins in 1977 [181-183] and later modified by Suzuoki *et al* in 1985 [184]. The basic principle in the latter system was the same as that described by Collin. However, the Collin's TPM system measures the open circuit voltage while the Suzuoki's TSM system measures the current response and utilises a longer, step like heat pulse.

Basically, the thermal technique consists of applying a thermal pulse to one surface of the dielectric by means of a light flash and measuring the electrical response generated by the sample as a function of time while the thermal transient diffuse across the sample. Moreover, this time dependence electric response carries the information about the trapped charge and polarisation distribution inside the bulk.

However, as the TPM technique requires a complex mathematical deconvolution process (Collins' and Dereggi's model) to compute the space-charge distributions, it limits the usefulness of this technique (resolution $\geq 2\mu m$). In addition, as the principle interest lies in the behaviour of space charge in a specimen under voltage application or short circuit condition [184], it is more appropriate to measure the current response than the open circuit voltage, which was utilised by Collins. The details of TPM technique will not be included here and the full mathematical models and deconvolution methods can be found in [180-181].

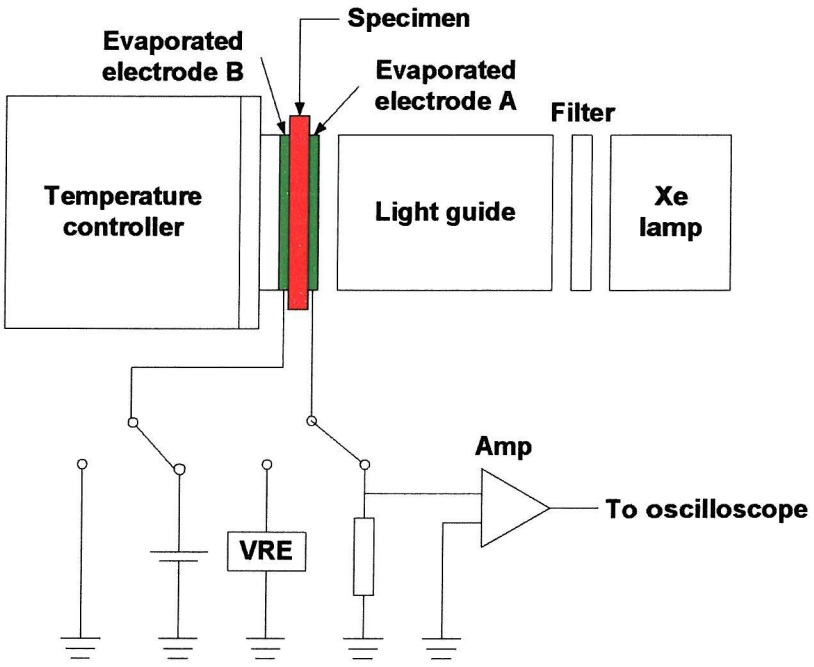

Figure A-3. Schematic diagram of TSM experimental set-up [184]

Figures A-3 and A-4 show the schematic experimental set-up and representation of the Suzuoki's TSM system. It considers a planar dielectric specimen which containing an arbitrary distribution of space charge $\rho(x)$ under short circuit condition (Figure 2.5).

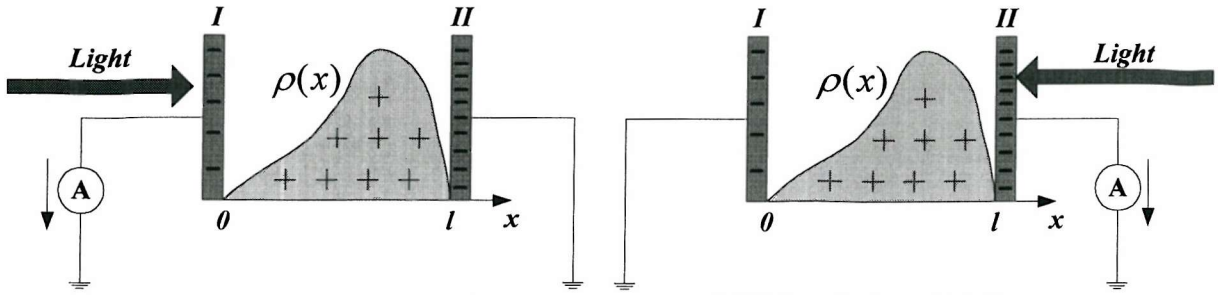

Figure A-4. Schematic representation of TSM technique [184]

When a step-like heat pulse is applied to one side, the dielectric specimen starts to expand non-uniformly. This non-uniform thermal expansion will produce a variation of image charges induced on adjacent electrodes and resulting a thermal pulse current in the external circuit that is reflecting the space charge distribution inside the bulk.

In the TSM system, it assumes that the thermal pulse current (TPC) at the initiation of the heat pulse is proportional to the electric stress at the electrode as given in equations A5 and A6 [184].

$$J_I = -A\int_0^t \frac{l-x}{l}\cdot\frac{\rho(x)}{\varepsilon_0\varepsilon}dx \text{ --------- (A5)}$$

$$J_{II} = -A\int_0^t \frac{x}{l}\cdot\frac{\rho(x)}{\varepsilon_0\varepsilon}dx \text{ --------- (A6)}$$

where *I* and *II* represent the cases in which electrode *I* and *II* are heated respectively, A is a constant, which can be determined experimentally, and $\varepsilon\varepsilon_0$ is the permittivity of the specimen.

The total space charge amount Q_t and the position of charge centroid x_c are given by equation A7 and A8, details can be found elsewhere [184],

$$Q_t = -\left(\frac{\varepsilon\varepsilon_0}{A}\right)\left(J_I(0)+J_{II}(0)\right) \text{ --------- (A7)}$$

$$\frac{x_c}{l} = \frac{J_{II}(0)}{J_I(0)+J_{II}(0)} \text{ --------- (A8)}$$

where l is the specimen thickness.

When the heat pulse is applied to the specimen under an applied voltage V, equations A5 and A6 of the resultant thermal pulse current can be rewritten as A9 and A10. Through the evolution of this current, information on the space charge distribution inside the sample can be obtained.

$$J_I = -A\left(\int_0^l \frac{l-x}{l}\cdot\frac{\rho(x)}{\varepsilon_0\varepsilon}dx - \frac{V}{l}\right) = -AE_I \text{ --------- (A9)}$$

$$J_{II} = -A\left(\int_0^l \frac{x}{l}\cdot\frac{\rho(x)}{\varepsilon_0\varepsilon}dx + \frac{V}{l}\right) = -AE_{II} \text{ -------- (A10)}$$

where the additional terms represent the TPC due to the change in the capacitance of the specimen with thermal expansion, V is the potential of electrode I with respect to electrode II and E_I & E_{II} are the internal electric stresses at electrodes I and II respectively.

A1.4 Piezoelectically generated pressure step method (PPS)

The schematic set-up of the "piezoelectically generated pressure step method" which was used by Gerhard-Multhaupt [186] is shown in Figure A1-5. This space charge measurement method is based on the propagation of an acoustic step wave generated by the electrical excitation of a piezoelectric quartz plate.

A 100 *ns* long square pulse with amplitude of 400 V to 600 V generated by the relay-triggered discharge of a coaxial cable is used to drive a piezoelectric X-quartz plate. The resulting pair of alternating pressure steps will be coupled by the silicon oil layer and passing into the dielectric sample. Considering a charged sample under a short-circuited condition, the electric fields between the charge layers in the bulk will accompany the induced charges on the electrodes. As a pressure step created from the piezoelectric X-quartz transverses through the bulk then an inhomogeneous compression will create a temporary rearrangement of the induced charges, which manifests a current $I(t)$ response between the rubber electrodes and grounded quartz. Hence, a direct image of the space charge of the dielectric sample is provided. Further details of the mathematical descriptions can be found in [186].

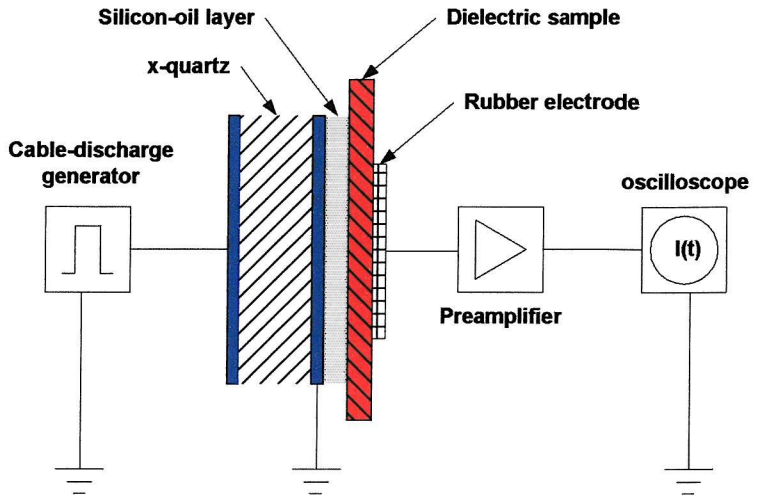

Figure A1-5. Schematic set-up of the PPS method [186]

$$I(t) = -\frac{A}{s}\upsilon e_{33}^{*}(ct) = -\frac{A}{s}\cdot\frac{p}{\rho_0 c}e_{33}^{*}(ct) \text{--------- (A11)}$$

where A is the area,

e_{33}^{*} is the apparent piezoelectric coefficient in the thickness direction,

s is the thickness of the sample,

υ is the particle velocity of the step wave in the dielectric sample,

c is the velocity of sound,

p is the pressure amplitude of the step wave,

ρ_0 is the density of the sample, and

t is the given time after the step wave entered the sample.

The disadvantage of the PPS method is that the electrical excitation of the piezoelectric quartz permits variation of the acoustic pulse duration, which will degrade the measurement. The resolution of the space charge distributions measurement by using the PPS method can be $1.5\mu m$ [186].

A1.5 Thermoelectrically generated LIPP method

Figures A1-6 and A1-7 show the schematic experimental arrangement and representation of the "thermoelastically-generated LIPP method" which was developed by R.A. Anderson and S.R. Kurtz for measuring space charge in dielectric materials [180, 187-189].

In the experimental arrangement shown in Figure A1-6, a laser pulse with negligible duration enters a transparent solid and encounters a buried optical absorbing layer. At the instant energy is absorbed, the solid is constrained against the thermal expansion and a compressive stress, which is proportional to the local temperature increment, which generated and propagating across the dielectric sample.

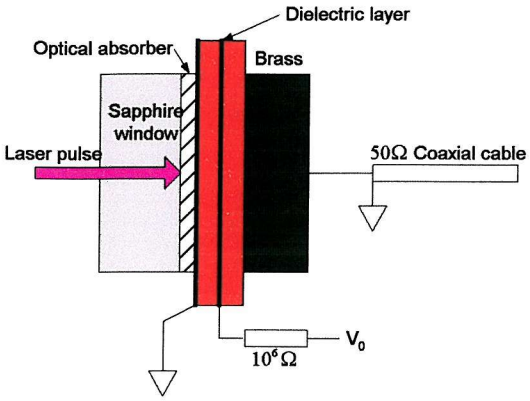

Figure A1-6 Schematic experimental arrangement of the thermoelastically generated LIPP method

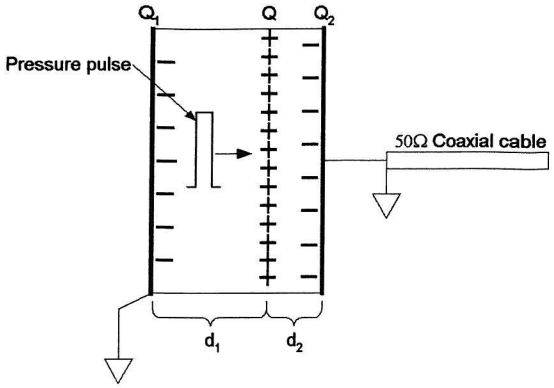

Figure A1-7 Schematic representation of the thermoelastically generated LIPP method

Consider a dielectric sample, which contains a plane of space charge (total amount of charge Q) shown in Figure A1-7. The sample is imagined to be a pair of dielectric layers enclosing the charge. The amounts of charge induced on the electrodes are found equating the potential difference between the electrodes to ground. With zero net charge, the charge on the right-hand electrode is given by [187],

$$Q_2 = -\frac{QC_2}{C_1 + C_2} \text{ ---------- (A12)}$$

where C_1 and C_2 are the capacitances of the dielectric layers

d_1 and d_2 represent the respective electrodes and plane of space charge

As the pressure pulse depicted in the left-hand portion of the dielectric, approaching to the embedded charge, then the capacitance C_1 increases and C_2 retains its unperturbed value

[187]. At the moment the pressure pulse enters the right-hand portion of the dielectric, C_1 assumes its unperturbed value while C_2 increases. By comparing the value of Q_2 (equation A12) before and after the passage if the pressure pulse through the plane of space charge, the amount of charge, which is transferred via the external circuit at the moment of passage may be calculated.

$$\Delta Q = Q\left(\frac{\delta}{d}\right)(1+\gamma_3) \text{ --------- (A13)}$$

where d is the overall thickness of the sample,

δ is the amount of mechanical displacement carried by the pressure pulse,

γ_3 is the uniaxial electrostriction coefficient.

Since each layer of space charge can yield a pulse of induced current in the external circuit upon arrival of the pressure pulse, thus the induced current response provides a direct probe of the space charge distribution in the bulk. Referring to [180, 187], a spatially resolution of $1\mu m$ has been achieved by a numerical deconvolution. Anderson and Kurtz [187-189] have used this method to resolve the distribution of field-injected charge in polymer film capacitors electrically stressed at room temperature.

A1.6 Non-structured acoustic pulse method

This method was developed by A. Migliiori and J.D. Thompson in 1979 [180, 190], which utilised a non-structured broadband acoustic pulse to compress locally a homogeneous dielectric, in which space charge is present. By comparing the voltage signal output V_m (Figure A1-8) at the points distant (position z) from the compressed region, the space charge distribution within the bulk can be determined by using equation A14, which relates the voltage across the parallel plate capacitor to the local internal electric stress during the acoustic pulse propagation. The full mathematical deviations can be found in [190].

$$V_m(t) = \left(2 - \frac{1}{K}\right)\chi \int_{-\infty}^{\infty} P(ct - z)E(z)dz \text{ --------- (A14)}$$

where $V_m(t)$ is the change in voltage across the capacitor,

χ is the pressure independent compressibility,

K is equal to the $\varepsilon/\varepsilon_0$, and

$P(z)$ and $E(z)$ are pressure pulse and electric stress amplitude in position z.

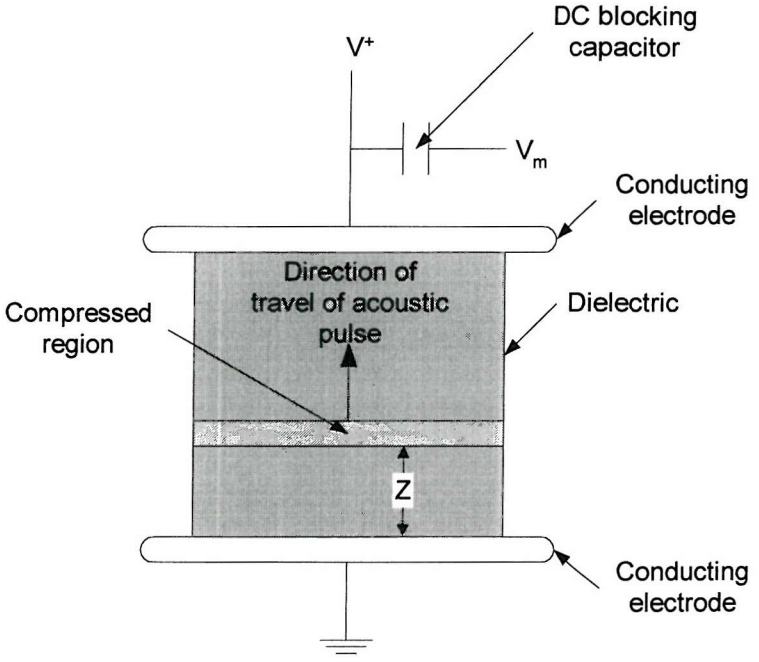

Figure A1-8 Parallel plate capacitor geometry used for the derivation of the response of an insulating system to a sharp, single acoustic pressure pulse [190]

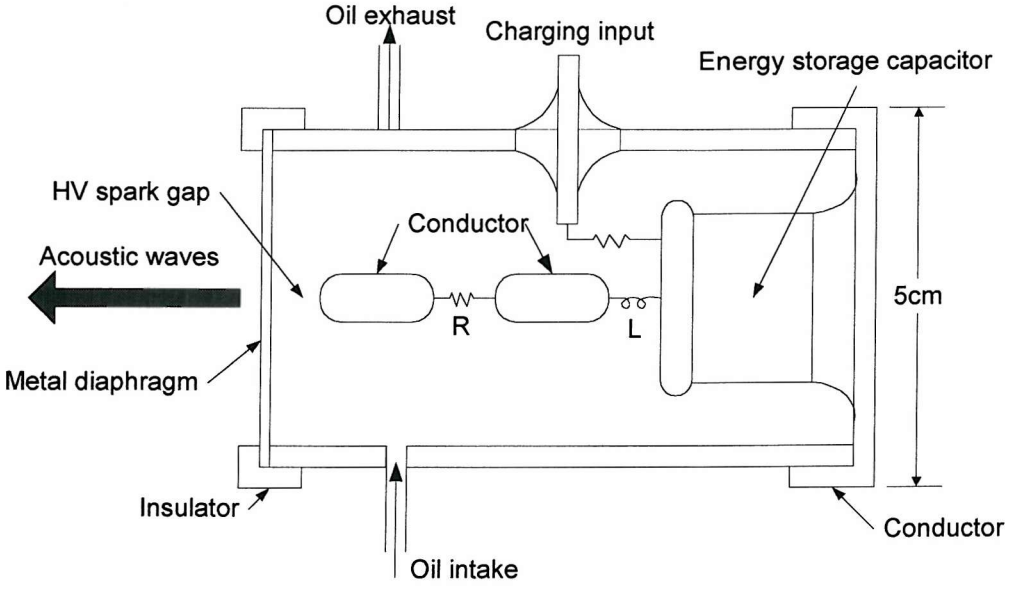

Figure A1-9 Diaphragm-type acoustic pulse generator used in the non-structured acoustic pulse method to generate non-structured acoustic pulse [190]

Figure A1-9 shows the diaphragm-type acoustic pulse generator used by A. Migliiori and J.D. Thompson. To generate the non-structured acoustic pulse, the tube is filled with transformer oil and the energy storage capacitor is charged gradually until breakdown (i.e. HV spark) occurs between the electrode and diaphragm. This non-structured acoustic pulse method has been used to study the electric stress and space charge distribution inside solid and liquid dielectrics. A resolution of 1 *mm*, a sensitivity of 10 *V/mm* for a range of sample thickness (up to 10 *cm*) have been demonstrated for the dielectric materials such as oil and polymethyl-methacrylate [180,190]. However, the disadvantage of this method is that the non-structured acoustic pulse has insufficient bandwidth and has a very high ratio of low-frequency energy to high frequency noise. As the acoustic pulse has a poor reproducibility, the consistence, sensitivity and spatial resolution of the measurement are degraded.

A1.7 Laser generated acoustic pulse method

In order to improve the resolution of the non-structured acoustic pulse measurement technique, A. Migliiori and T. Hofler introduced another measurement technique in 1982 [180,191], which is called "laser generated acoustic pulse method". The basic principles of this method are the same as the non-structured acoustic pulse method described in section A1.6, the only difference is the use of a laser as a power source for the acoustic pulse instead of a diaphragm-type acoustic pulse generator. Equation A15 describes the relationship of the time-dependent voltage across the parallel plate capacitor to the electric stress during the acoustic pulse propagation. The full mathematical deviations can be found in [191].

$$V(t) = \frac{\chi}{3}\left[\varepsilon + 4 - \frac{2}{\varepsilon}\right]\int_0^{z=ct} P\left(\frac{z}{c} - t\right)E(z)dz \quad \text{-------- (A-15)}$$

The schematic set-up of the laser generated acoustic method for space charge measurement is shown in figure A1-10. An Apollo ruby laser [191] was used to produce 15 *ns*, 1.5 *J* laser pulses. The laser beam is directed through a plate-glass window into an aluminium tank filled with liquid $C_2F_3Cl_3$ (Freon). The aluminium tank contains a laser-beam absorber (convert radiation to pressure), pressure transducer, the sample under test and a pre-amplifier. The laser beam absorber consists of a sheet of *NU-KOTE* carbon paper with the

carbon side toward the beam. Acoustic pulses are produced when the laser beam is absorbed by the carbon paper, heating the paper and the $C_2F_3Cl_3$ trapped between the paper fibres.

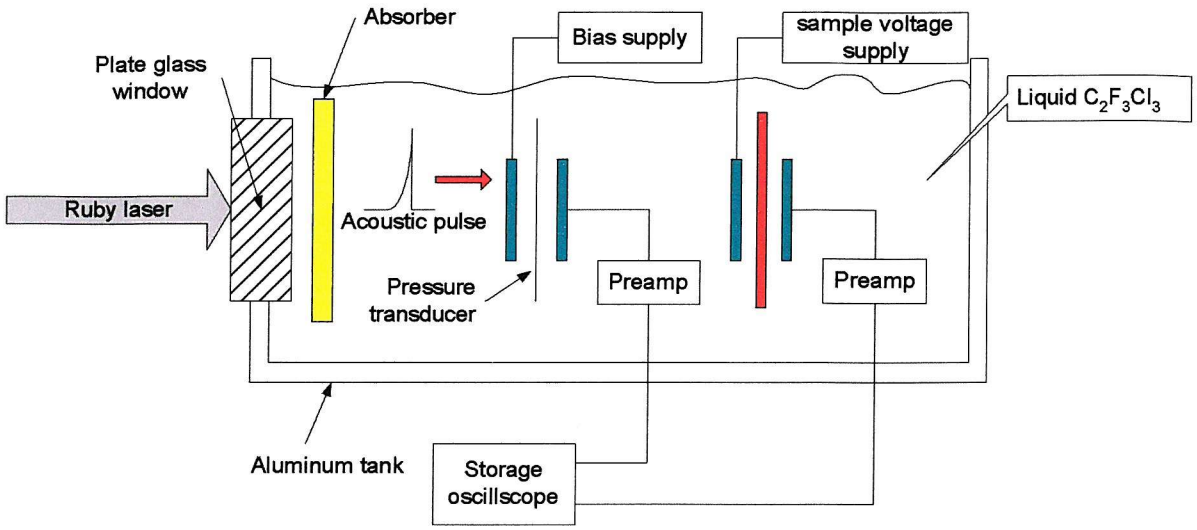

Figure A1-10 Schematic set-up of the laser generated acoustic method

Referencing to [180,191], the "laser generated acoustic pulse method" for space charge measurement method has achieved 50 μm spatial resolution in 3 mm thick PMMA samples with the aid of a numerical deconvolution. This is shows a significant improvement compared to a resolution of 1 mm obtained by the non-structured acoustic pulse method. In addition, the sensitivity of the laser-generated acoustic pulse method has reported to be as good as 5×10^4 V/m by using a pressure pulse with peak amplitude of about 5×10^5 Pa.

Appendix 2 Circuit details and working principles of the electronic system

The following is the circuit details and the working principles of the electronic system. It can be seen that the designed circuit has three main parts,

- ❖ The high voltage ac voltage synchronise system (Blue-box),
- ❖ The timing control system (Red-box), and
- ❖ The shot pre-set and phase control system (Green-box).

- ***The high voltage ac synchronise system***

Based on Chapter 3, a low voltage ac waveform corresponding to the magnitude of high voltage ac applied to the sample will be obtained at the output of the pre-amplifier box. This waveform is in phase with the HV ac voltage and will act as an activation signal to the electronic system for the ac space charge measurement.

Referring to the circuit enclosed by the blue dash line in figure A2-1, the 50 *Hz* ac waveform from the pre-amplifier box is firstly converted to the 5 *Volt* 50 *Hz* square waves. Then by using the phase lock loop circuit, this 50 *Hz* square wave will be locked and a 3.2 *kHz* square wave output is generated, which is the clock signal for the following "timing control system".

- ***The timing control system***

In order to incorporate the "data acquisition" with the "target cooling system" and ensure the space charge measurement starts at the same point (or phase) on wave. A timing control system, which is enclosed by the red dash line in figure A2-1, has been included. It initialises the measurement and triggers the target cooling system. The timing sequence and the block diagram of the electronic circuit are shown in figure A2-2 and A2-3 respectively.

➢ The "Dual D-type positive edge-triggered flip-flop (74HC74D)" ensure the counter starting with a "no load" condition, therefore the first laser shot will be triggered at Phase=0^{o} after the counter is reset for 1280 *ms* (16x16x16 = 4096 clock signal), and

- The "4-bit synchronous binary counters U14, U15 and U16" are used to trigger the cooling liquid device then fires the laser 40 *ms* later. The counter is then reset and the above procedure repeats for any point on wave measurement.

- ***The shot pre-set and phase control system***

The timing sequence in figure A2-2 illustrates that by changing the pre-set value at the switch-U11 on the electronic board to different configurations, the period of time delay between two consecutive laser shots as well as number of shot per period can be altered as shown in table A2-1

In addition, referred to the equation 3.1, the time delay between two consecutive laser shots are given by,

$$1000ms + \frac{1}{N-1} * 20ms \qquad \text{where } N = number\ of\ shot\ per\ cycle$$

By changing the switch setting on U12 and U13 on the circuit, this delay time constant "1000 *ms*" in the equation can be changed.

No of shots per period	Pre-set value of switch U-11	Time delay between two consecutive laser shots (*ms*)
9	1000	1002.5
17	1100	1001.25
33	1110	1000.625
65	1111	1000.3125

Table A2-1

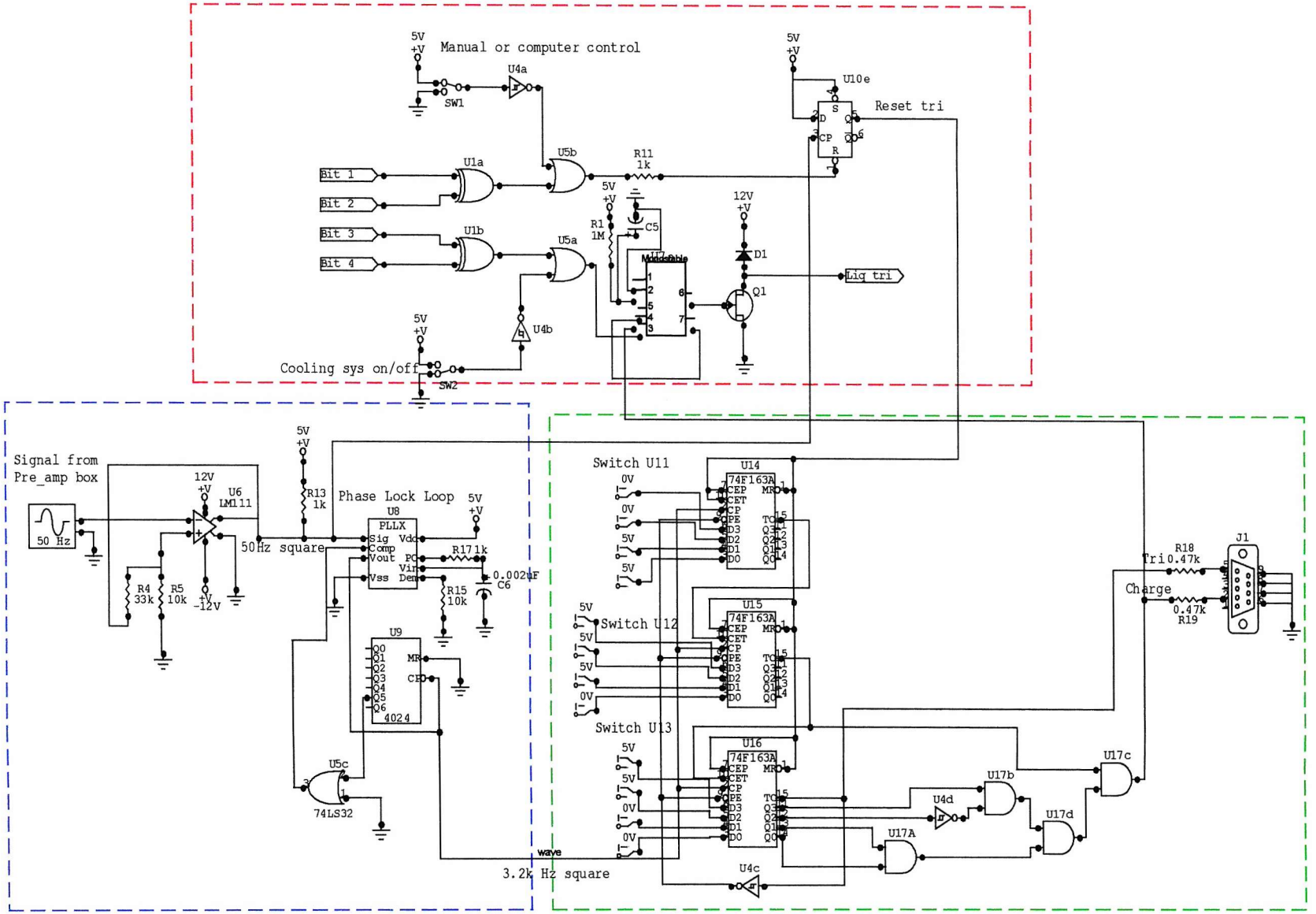

Figure A2-1. The electronic board of the ac LIPP system

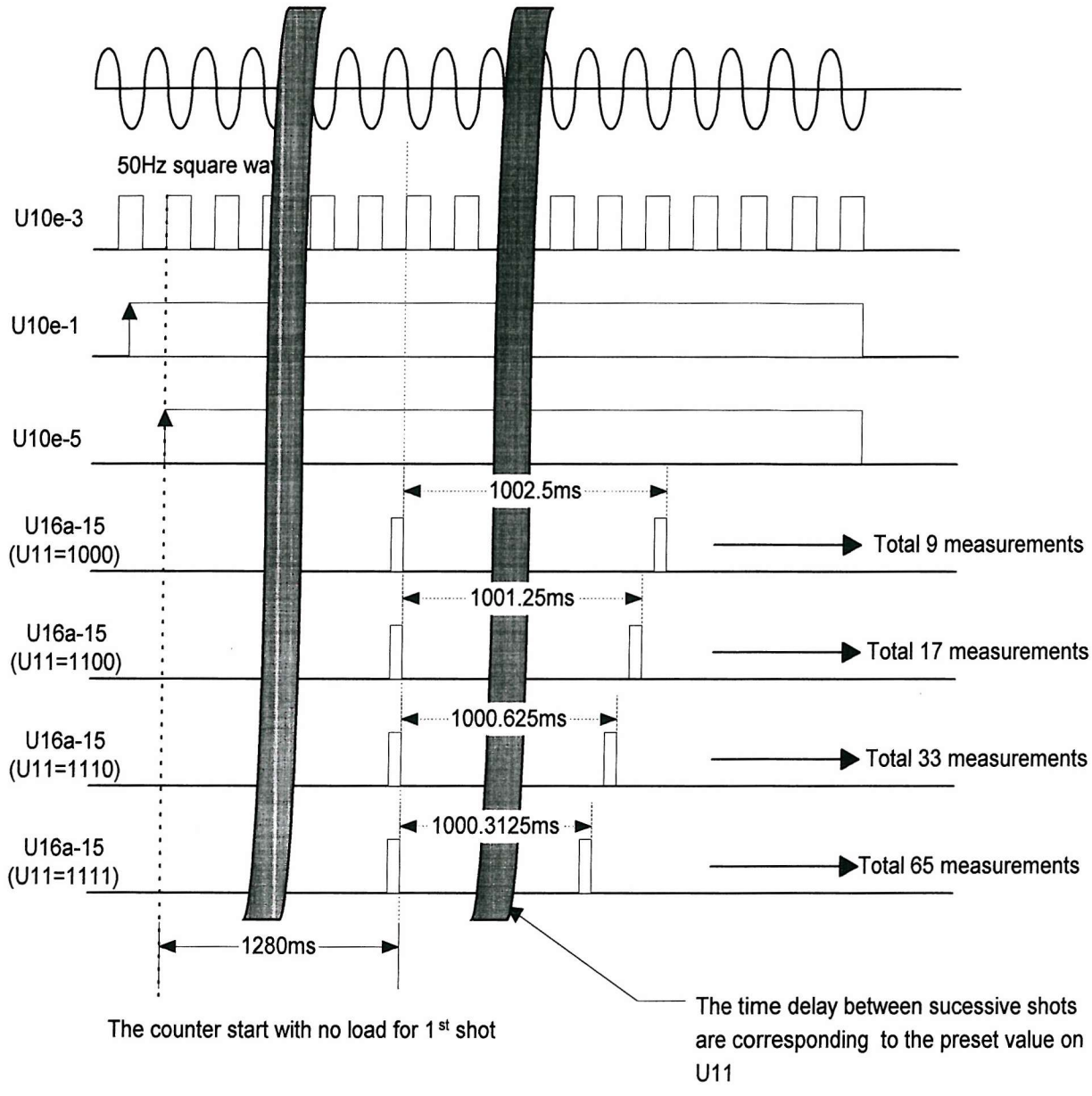

Figure A2-2. The timing sequence of the electronic board

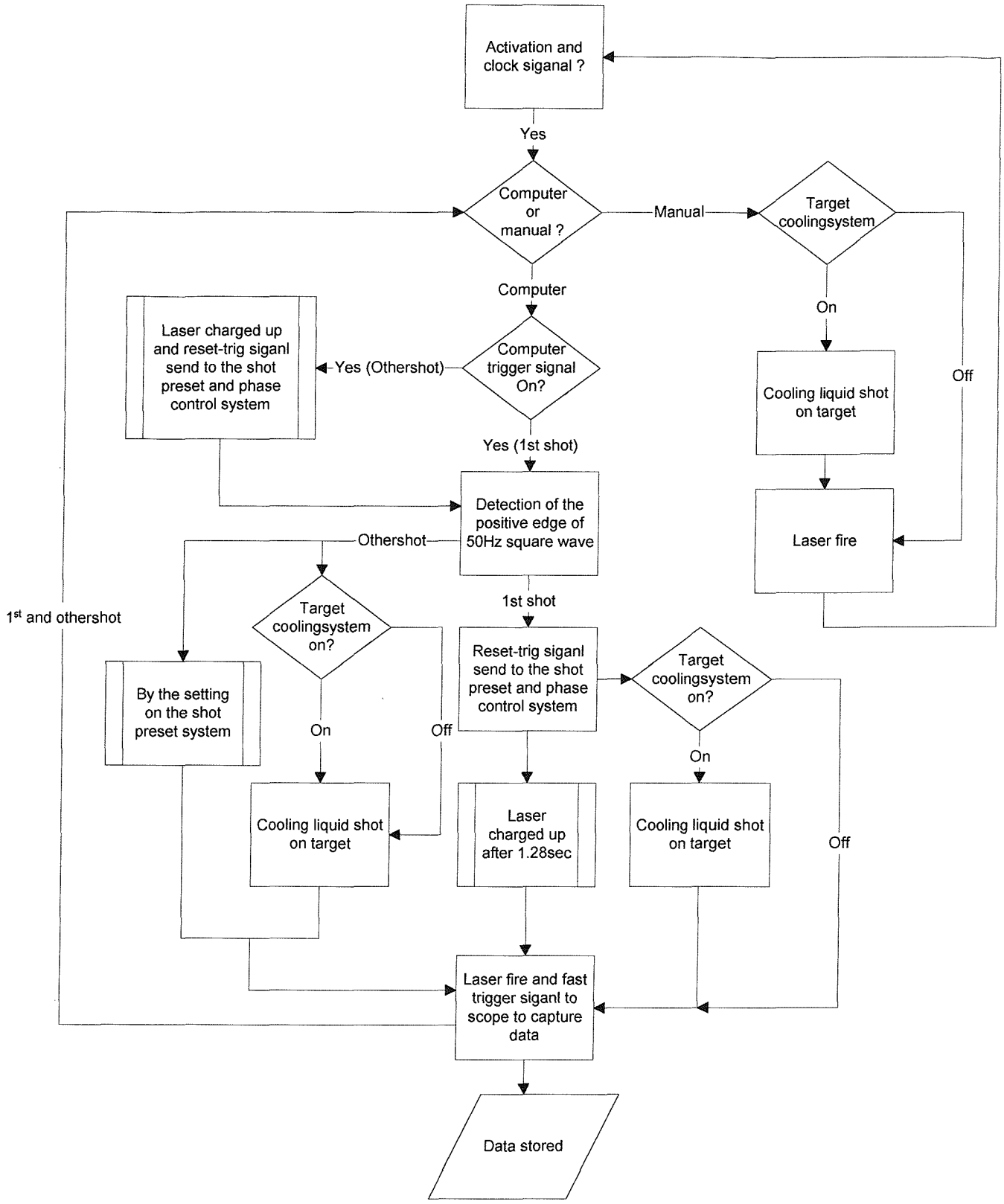

Figure A2-3 The block diagram of the electronic board

Appendix 3 Mechanical drawing of the plaque sample holder

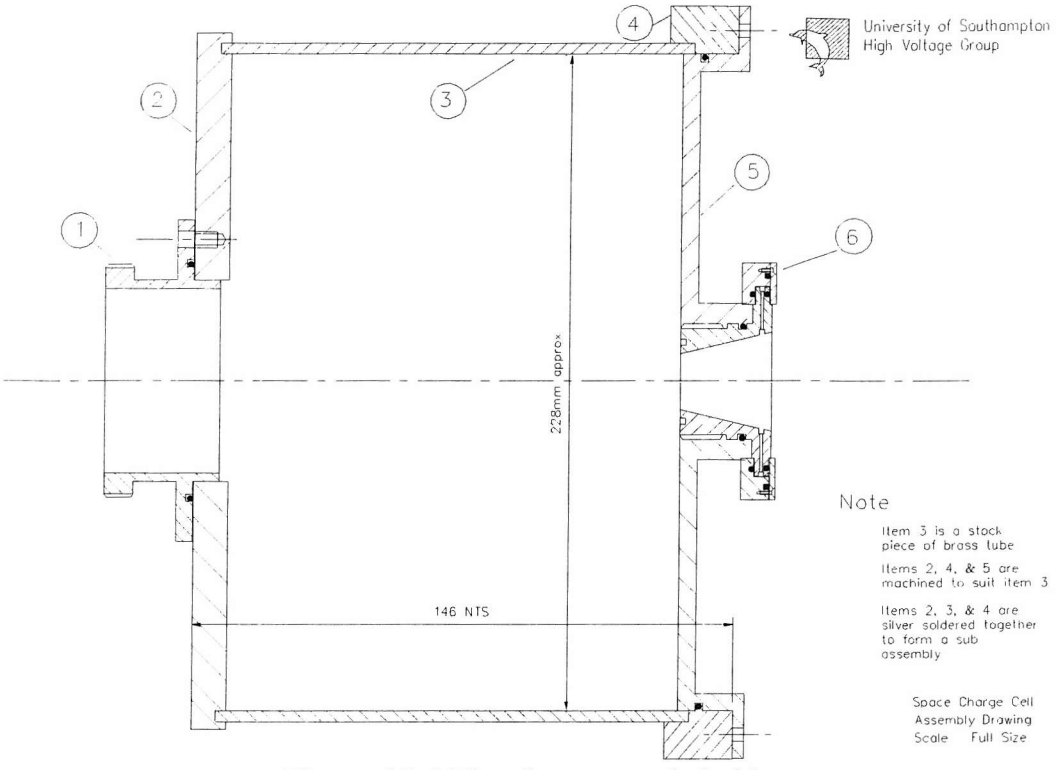

Figure A3-1 The plaque sample holder

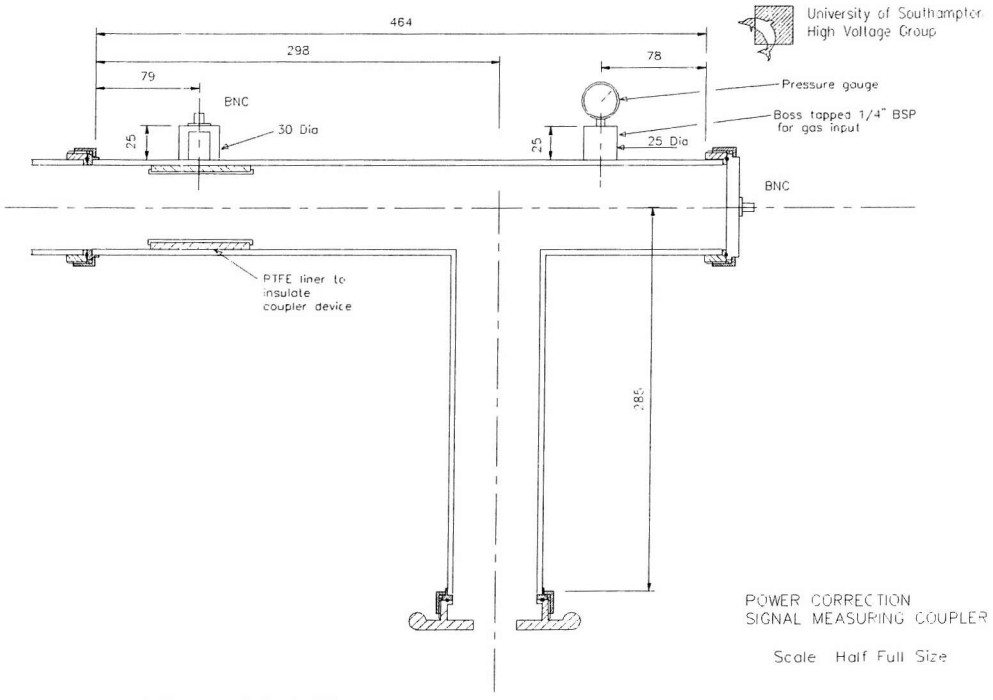

Figure A3-2 The HV main body of LIPP system

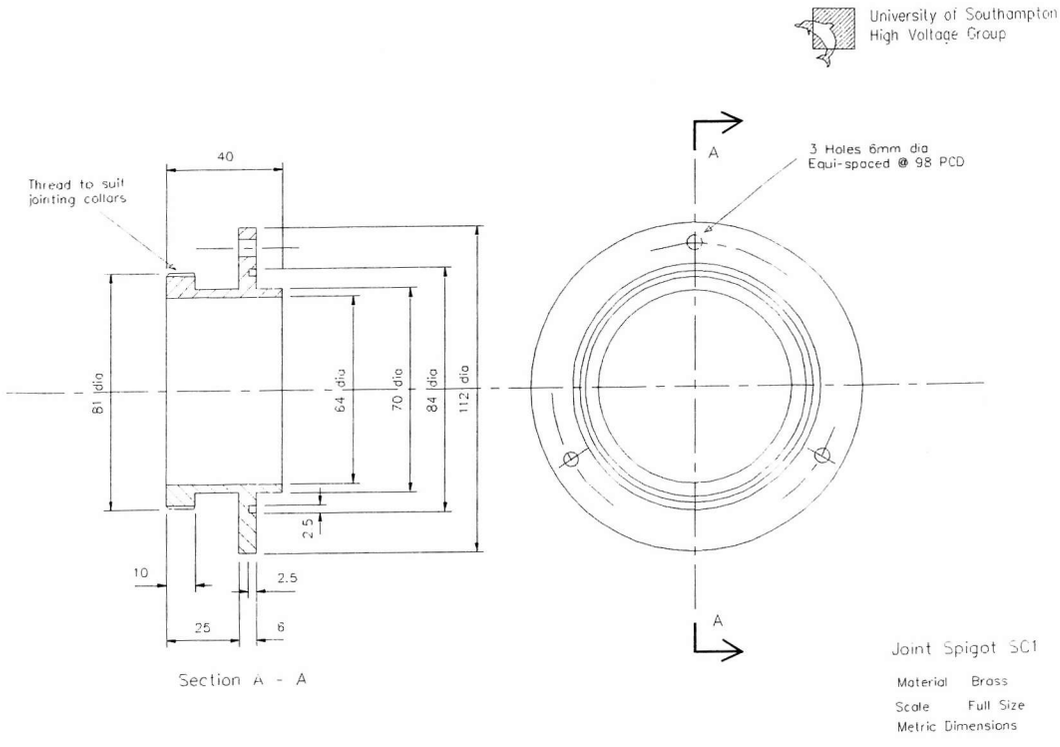

Figure A3-3 Joint Spigot SC1

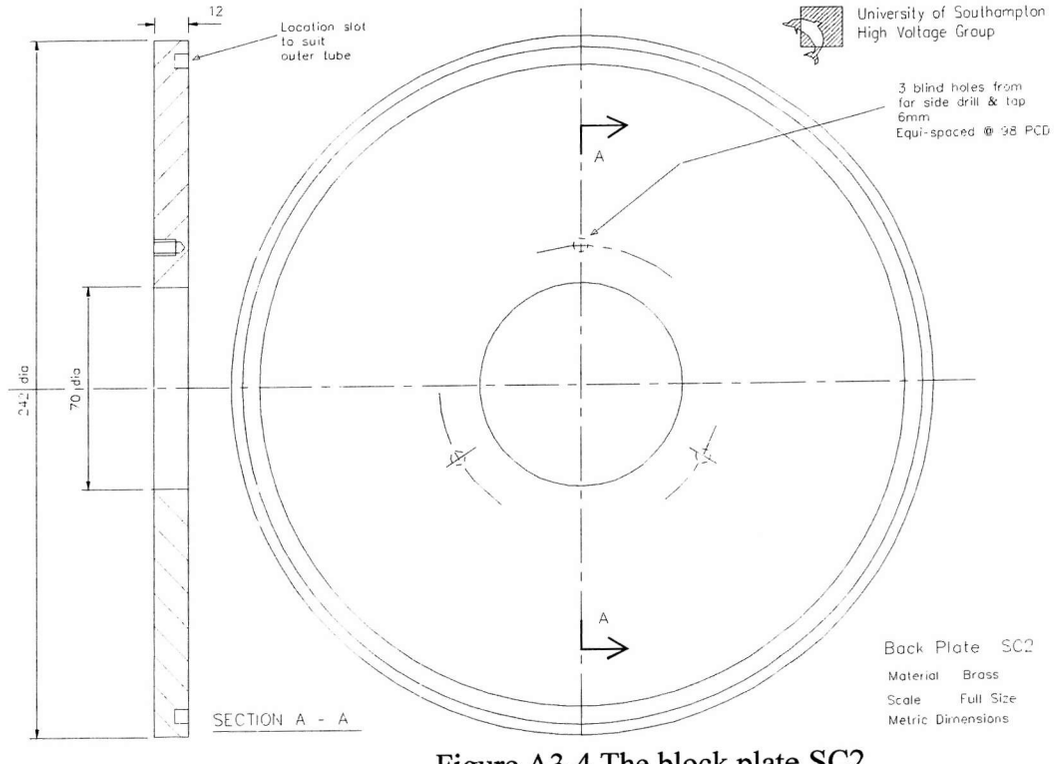

Figure A3-4 The block plate SC2

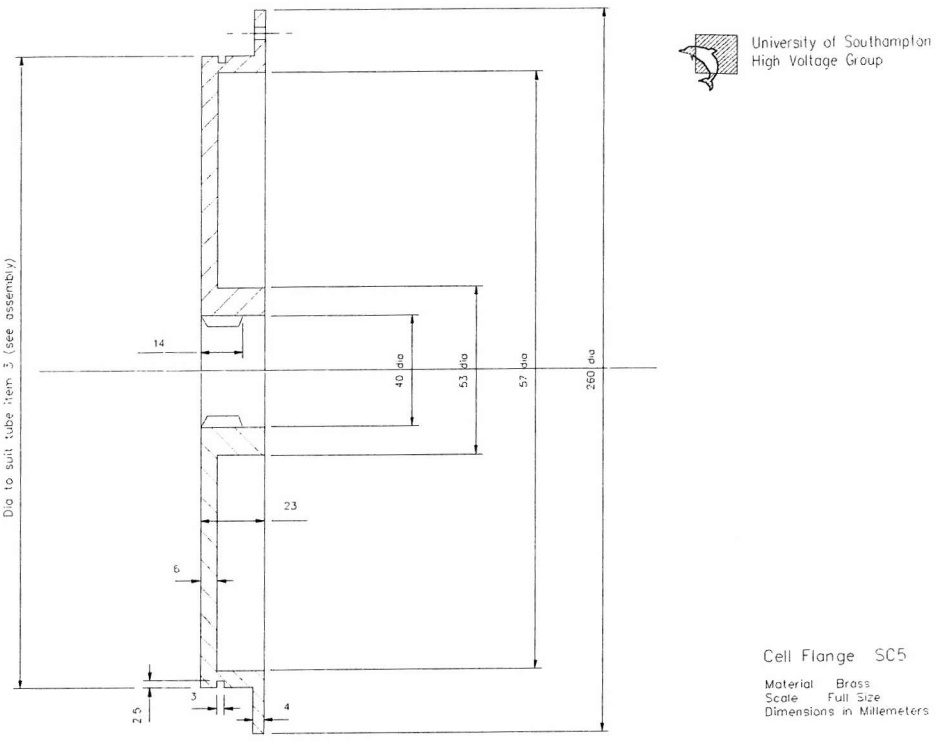

Figure A3-5 The cell flange SC5

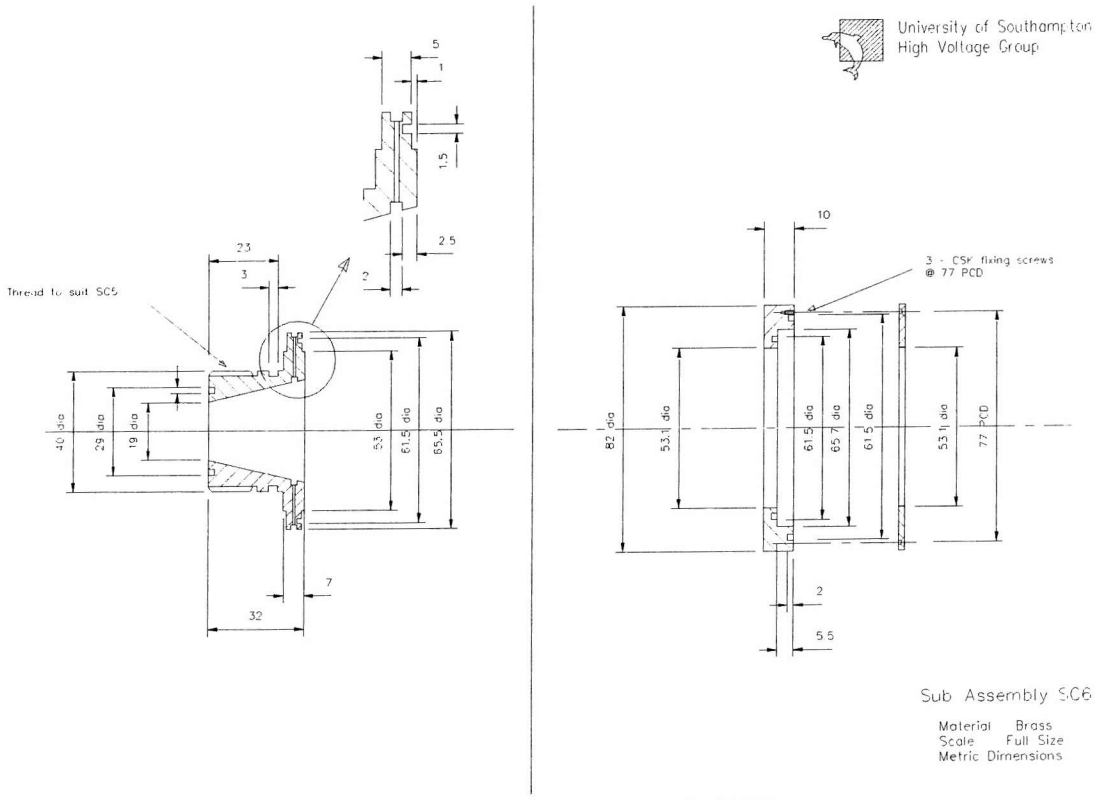

Figure A3-6 The Sub assembly SC6

Appendix 4 Mechanical drawing of the cable sample holder

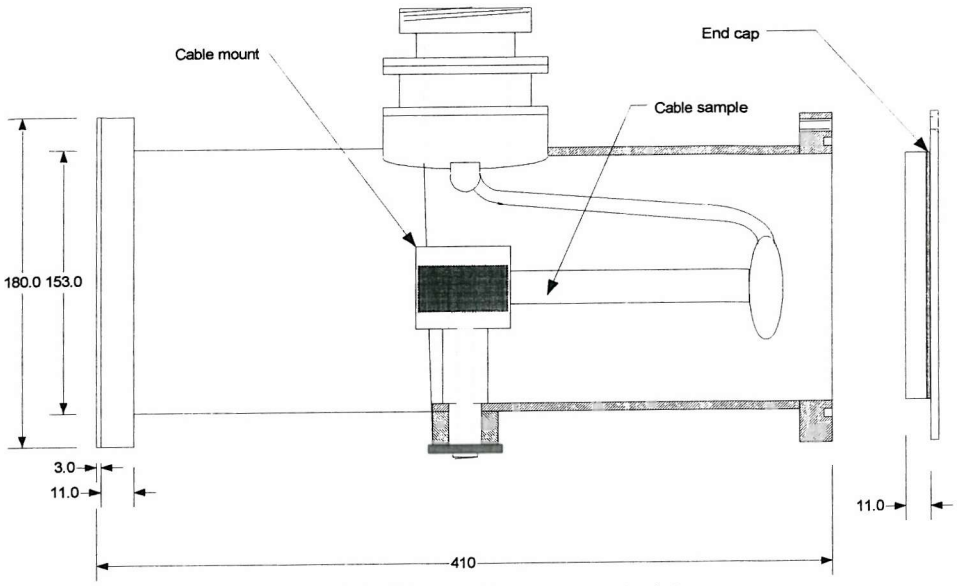

Figure A4-1 The Cable sample holder

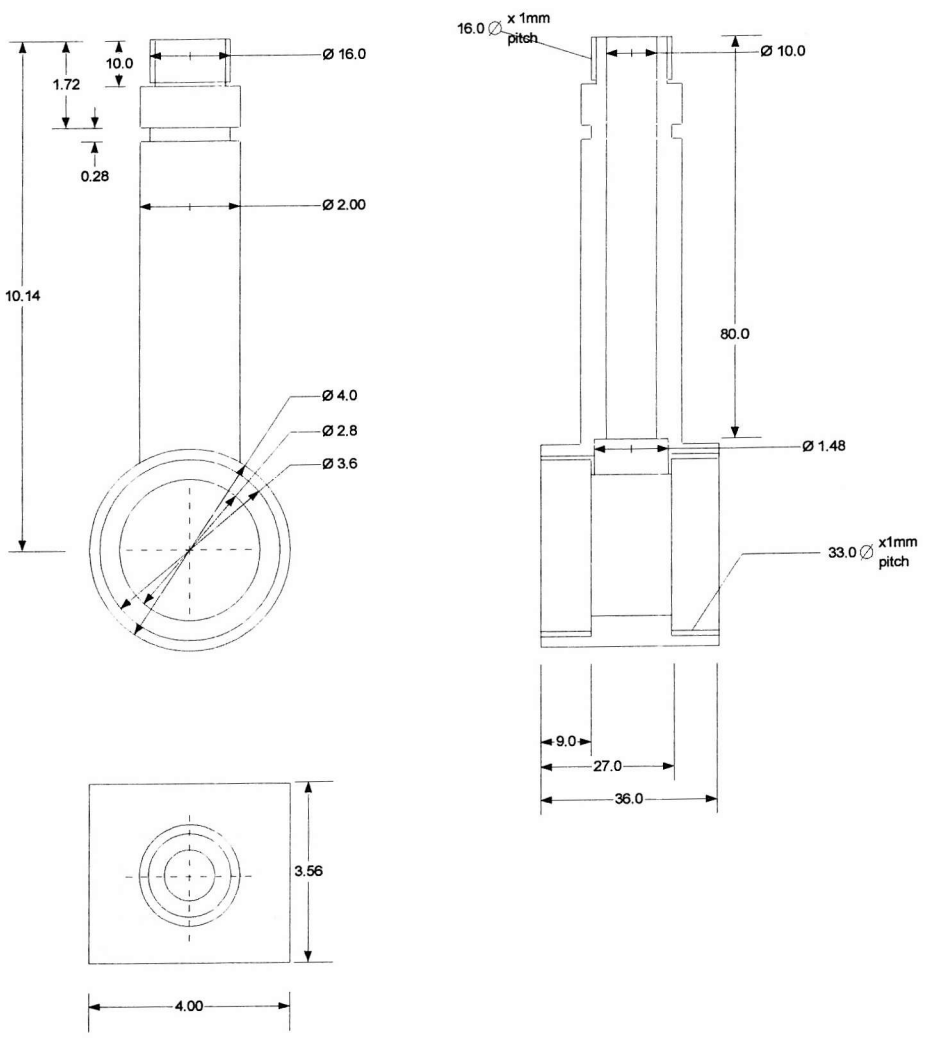

Figure A4-2. The Cable mount

Appendix 5 Technical parameters and data cable pin assessment for the online laser power measurement system

The communication parameters using in the visual program are shown as follow,

Baud rate	9600
Parity	none
Data bits	8
Stop bits	1

Data exchange and collection protocol is summarised as below,

I. Firstly, the program will tell the FieldMaster GS what to be sent to the computer,

II. The computer will check the correct "termination character" of the commands signal,

III. The command will be processed and the FieldMaster GS will send a complete response message to the computer after the process has finished, otherwise other program command cannot be sent and processed again.

Pin assignments for RS232-cable for laser power data transmission

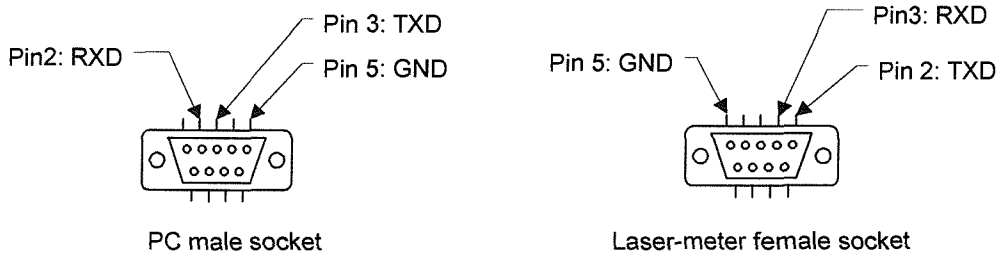

Figure A5-1 Pin assignment of connector socket on the laser power data collection cable

Appendix 6 Photos of the LIPP system

Figure A6-1 View 1 of the entire LIPP system

Figure A6-2 View 2 of the entire LIPP system

Figure A6-3 View 3 of the entire LIPP system